One Dimensional Coordination Polymers with Molecular Recognition Capability as Dynamic and Multifunctional Materials.

By

Khaled Hassanein Sayed Ahmed

Supervised by

Dr. Pilar Amo Ochoa Dr. Félix Zamora Abanades

This dissertation has been submitted to
Departamento de Química Inorgánica
Facultad de Ciencias
Universidad Autónoma de Madrid
in fulfillment of the degree of Doctorate in Chemistry

Madrid, 2016

Acknowledgements

It is difficult to decide whom to thank first, but I think it has to start with my big family, my parents and my sisters (**Iman**, **Asmaa**, and **Donia**). The support you have given me over the years with regard to my education has been invaluable. In particular, especial thank for my mother for being the only supporter in the difficult moments and for taking my responsibility as the host of my family during the last years, thank you my mother. My lovely wife (**Hind**), and my little son (**Abdelrahman**), you are the key of happiness for me in this world.

On the other hand, it was impossible to finish this thesis without the support of my advisors, **Dr**. **Pilar Amo Ochoa** and **Dr**. **Félix Zamora Abanades**. Thank you **Dr**. **Pilar Amo** for countless hours you have spent to help me through every step of my dissertation. Your advices and encouragements have been unending and invaluable, guiding me to define the direction of my research. Thank you **Dr**. **Félix Zamora**, your attentions for the details have helped me to hone my ideas and improve the quality of my dissertation.

Especial thanks for the investigators who have collaborated with us to finish this thesis. Thanks for **Dr**. **Óscar Castillo**, from Universidad del País Vasco, and **Dr**. **Josefina Perles**, from Servicio Interdepartamental de Investigación (SIDI) at Univesidad Autónoma de Madrid, for their contributions in the single crystal X-ray diffraction measurements, structural refinements, and structural descriptions. Thanks for **Dr**. **Carlos Gómez**, from Instituto de Ciencia Molecular (ICMOL), and **Dr**. **Pilar Ocon**, from Univesidad Autónoma de Madrid, for the conductivity measurements. Thanks for **Prof. Dr. Salomé Delgado**, **Dr**. **Marcos Zayat**, and **Virginia Vadillo**, from Univesidad Autónoma de Madrid, for photoluminescence measurements. Thanks for **Dr**. **José Ignacio Martínez**, from Instituto de Ciencia de Materiales, CSIC, for the DFT calculations. Thanks for **Dr**. **Álvaro Somoza, Romina Lorca**, and **Ana Latorre**, from Instituto IMDEA Nanociencia, for biological studies.

I want to thank my colleagues who participated in the experimental part of this thesis. Thank you Javier Conesa, Fatima, and Veronica.

I want to thank the present and old members of the Nanomaterials group, Cristina Hermosa, Isadora Berlanga, Mohamed Reza, Azin Hassanpour, David Rodríguez, Jesus, Pablo, Carlos, Alex, and Carmen. Thank you for my close friend Javier Troyano for being

available a lot of hours for discussions, sharing your opinions, and removing stress in hard moments.

Thank you for the workers of the Inorganic department for being always available and ready for problem solving. Thank you Miguel Angel, Ismael, and Nani.

Thank you for my Egyptian friends in Spain, with you I feel as if I am in my home country. Thank you Mohamed Moaid, Walid, Safawat, Moahmed abdel Kader, Edris, Fouad, Dr Tag, Hassan, Hitham, Imad, and Yousef.

I want to admire and address my thanks for all the professors who teach me in all my life stages especial those who forming my knowledge in chemistry.

Also, I would like to thank my dear friends living in Egypt. Mohamed Abdel Fatah, Osama, Hany, Sabry, Tamer, Mohamed Ismaeil, Khalaf, Mr. Adel Mahmoud, Hala, Nahla, and all the members of my family.

Finally, I have to mention that this work was funded by Spanish Ministry of Science and Innovation (MICINN) through grant MAT2010-20843-C02-01.

Thank you for all.

Publications and Conferences

Publications included in this thesis

- Semiconductive and Magnetic One-Dimensional Coordination Polymers of Cu(II) with Modified Nucleobases.

  Pilar Amo-Ochoa, Oscar Castillo, Carlos J. Gómez-García, Khaled Hassanein, Sandeep Verma, Jitendra Kumar and Félix Zamora. *Inorg. Chem*, **2013**, 52 (19), pp 11428–11437. dx.doi.org/10.1021/ic401758w.

- Asymmetric and symmetric dicopper(II) paddle-wheel units with modified nucleobases. Khaled. Hassanein, Pilar Amo-Ochoa, Oscar Castillo, Carlos J. Gómez-García and Félix Zamora. *Cryst. Growth Des,* **2015**, 15 (11), pp 5485–5494. DOI: 10.1021/acs.cgd.5b01110.

- Reversible stimulus-responsive Cu(I) iodide pyridine coordination polymer.

  Pilar Amo-Ochoa, Khaled Hassanein, Carlos J. Gómez-García, Samira Benmansour, Josefina Perles, Oscar Castillo, José I. Martínez, and Félix Zamora. *Chem. Commun*, **2015**, 51, pp 14306-14309. DOI: 10.1039/C5CC04746C.

- Electrical Conductivity and Strong Luminescence in Copper-Iodide Double-Chains with Isonicotinato Derivatives.

  Khaled Hassanein, Javier Conesa-Egea, Salome Delgado, Oscar Castillo, Samia Benmansour, José I. Martínez, Gonzalo Abellán, Carlos J. Gómez-García, Félix Zamora and Pilar Amo-Ochoa. *Chem. Eur. J*, **2015**, 21, pp 1 – 12. DOI: 10.1002/chem.201502131.

- Halo- and pseudohalo Cu(I)-pyridinato double chains with tunable physical properties. Khaled Hassanein, Pilar Amo-Ochoa, Carlos J. Gómez-García, Salomé Delgado, Oscar Castillo and Félix Zamora. *Inorg. Chem*, **2015**, 54 (22), pp 10738–10747. DOI: 10.1021/acs.inorgchem.5b01754.

Accepted publications included in this thesis

- Co(II)-modified nucleobases complexes. A methyl care?
  Khaled Hassanein, Félix. Zamora, Oscar Castillo and Pilar Amo-Ochoa. Inorganica chimica acta, **2016**.

Publications in progress included in this thesis

- Biocompatible Molecular Thick Nanoribbons of a Multifuntional 1D-Cu(II)-nucleobase coordination polymer showing Molecular Recognition towards Oligonucleotides.
  Khaled Hassanein, Verónica García, Romina Lorca, Ana Latorre, Álvaro Somoza, P. Amo-Ochoa, Carlos J. Gómez-García, Oscar Castillo, and F. Zamora. In preparation.

Conferences

- 40 International Conference on Coordination Chemistry" (ICCC40), Valencia, Spain, Sep. 9-13, 2012.
- The 15th Asian Chemical Congress, Singapore, Aug. 19-23, 2013.
- XXIV Symposium of the Specialized Group on Crystallography and Crystal Growth (GE3C) at Bilbao, Spain, 2014.
- 5th Molecular Materials Meeting (M3) @ Singapore An international conference on the "Next 50 Years In Materials Research" Aug. 19-23, 2015.
- First National Symposium on properties and applications of MOFs and COFs at Granada, Spain, 2015.

List of abbreviations

0D-CPs	Zero dimensional coordination polymers
1D-CPs	One dimensional coordination polymers
1D-NCPs	Nanoscale one dimensional coordination polymers
2D-CPs	Two dimensional coordination polymers
3D-CPs	Three dimensional coordination polymers
4,4'-bipy	4,4'-Bipyridine
6-MP	6-Mercaptopurine
6-TG	6-Thioguanine
AC	current
AFM	Atomic force microscopy
ANP	2-Amino-5-nitropyridine
Bio-NCPs	Nanoscale coordination polymers containing biomolecules as ligands
CAFM	Conductance atomic force microscopy
CITS	Current imaging tunneling spectroscopy
COFs	Covalent organic frameworks
CPs	Coordination polymers
DC	Direct current
DFT	Density function theory
DMA	Dimethylacetamide
DMF	Dimethylformamide
DMSO	Dimethyl sulfoxide
DNA	Deoxyribonucleic acid
E_a	Activation energy
E_g	Energy gab
EIS	Electrochemical impedance spectroscopy
Et_2O	Diethyl ether
EtIN	Ethyl isonicotinate
FESEM	Field emission scanning electron microscope

H	Applied magnetic field
H_C	Coercivity or coercive field
HDap	2,6-Diaminopurine
HE	High-energy band
HIN	Isonicotinic acid
HOPG	Highly ordered pyrolytic graphite
HS	High spin
HOMO	Highest occupied molecular orbital
IC	Internal conversion
IR	Infrared spectroscopy
ISC	Intersystem crossing
J	Magnetic exchange coupling constant
L	Liter
LC	Ligand-centered
LE	Low-energy band
LMCT	Ligand-to-metal charge transfer
LS	Low spin
LUMO	Lowest unoccupied molecular orbital
M	Magnetization
MC	Metal-center
MeCN	Acetonitrile
MeOH	Methanol
MLCT	Metal-to-ligand charge transfer
MOCNs	Metal-organic coordination networks
MOFs	Metal-organic frameworks
NBs	Nucleobases
PCPs	Porous coordination polymers
PL	Photoluminescence
SBU	Secondary building unit

SCO	Spin-crossover
SCSC	Single-crystal to single-crystal
SCXRD	Single crystal X-ray diffraction
SQUID	Superconducting quantum interference device technique
STM	Scanning tunneling microscope
STS	Scanning tunneling spectroscopy
TAcOH	Thymine-1-acetic acid
TCNQ	5,7,7,8,8-tetracyanoquinodimethane
TGA	Thermogravimetric analysis
Trans-bie	Trans-bis(N-methylimidazol-2-yl)ethylene
UAcOH	Uracil-1-acetic acid
UV-Vis	Ultraviolet-visible spectrophotometry
XLCT	Halide-to-ligand charge transfer
XRPD	X-ray Powder diffraction
θ	Angle
σ	Conductivity
λ	Wavelength
ρ	Resistivity
χ_m	Molar magnetic susceptibility
Ă	Angstroms
g	Gram

Table of contents

1. Chapter 1; Introduction to Coordination Polymers and Objectives of this Thesis.

Introduction to Coordination Polymers and their Potential Applications

This chapter provides a general overview on coordination polymers that represent the central core of this thesis. Herein, we summarize the principal aspects going from the synthesis of coordination polymers to their potential applications in many fields, in particular, electronics, magnetism, and luminescence applications. The potential uses of this class of materials for future nanotechnological applications will be illustrated.

1.1. Coordination polymers (CPs)

What are Coordination Polymers?

Coordination polymers (CPs), also known as metal-organic coordination networks (MOCNs)[1], can be defined as an extended arrays based on the self-assembly processes of metal centres (connectors or nodes) and polyfunctional organic ligands (linkers) to form 1D, 2D and 3D frameworks (**Figure 1.1**).[2] Coordination bonds and H-bonds are crucial tools for the design and constructions of CPs, with the help of other weak interactions, such as halogen bonds[3-6] and π-π bonds, due to their directionality and strength.[7-9] The selection of the starting building blocks, metal centres and polyfunctional organic ligands, as well as solvents[10], counterions, [11] and reaction conditions are crucial to rationalize the final structure, properties, dimensionality, and topology of the CPs networks.[12, 2] Properties of the new synthesized CPs, mainly, depend on their molecular components and how these components align to form crystalline solid states matter.[13]

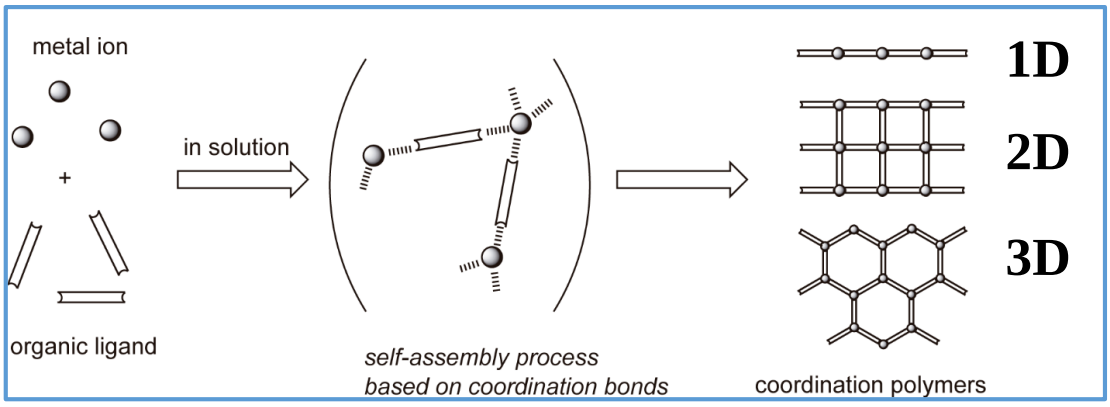

Figure 1.1. Schematic representation of coordination polymers formation.[2]

The essential building blocks for CPs constructions (connectors and linkers)

The first essential building block for CPs construction is the metal centres. In that regard, transition metals are common as versatile nodes in the construction of CPs owning to their ability to adapt various geometries depending on their oxidation states and the coordination number (**Figure 1.2**). The selection of metal ion affects the coordination geometry, i.e. the node shape, as well as the properties of the resulting CPs. For instance,

copper can have Cu(I),[14] Cu(II)[15] or mixed valance oxidation states,[16] depending on the reaction conditions. Thus, different properties (magnetism and/or photoluminescence), and different geometries (tetrahedral, trigonal or octahedral) can be obtained according to the oxidation states of copper. In addition, metal complexes can serve as nodes to construct coordination polymers with high degree of nuclearity using multi-dentate bridging ligands.[17] Recently, the term secondary building unit (SBU) has been used to coined the CPs that have been formed as a result of using metal clusters as nodes and firstly devoted for transition-metal carboxylate clusters that have been used for CPs constructions (**Figure 1.3**).[18, 19]

On the other hand, organic ligands, the second essential building blocks for CPs constructions, play critical roles to draw the topology and the final properties of the resulting networks. Organic ligands can be classified as *mono, bi, tri* dentate ligands depending on the number of the donor atoms that participate to bridge the metal centres. Ligand molecules may differ from each other in their charges: most used ligands are neutral and anionic (**Figure 1.4**).[1] Other determining points are the "body" of the organic ligands, their shapes (rigid or not), lengths (distance between the coordination functions will be important), and functionalities (further presence of heteroatoms, aromatic rings, free functional groups…). Mostly, nitrogen[20], oxygen[18, 21, 19] and sulfur[22]-donor ligands have been used in CPs construction. In that regard, biomolecules beside their potential biocompatibility, they present remarkable structural features as organic ligands.[23] They are rich with several donor atoms available for metals coordination, and consequently, they can exhibit multiple possible coordination modes. These biomolecules can be either structurally rigid or flexible, so it is predictable to present dynamic architectures. In addition, they have intrinsic self-assembly properties which can be used to direct the structure and function of CPs.[24, 25] Among these biomolecules, nucleobases and modified nucleobases (**Figure 1.5**) have received great attention as organic ligands to construct functional CPs with different dimensionality and wide range of the properties including electrical, magnetic and optical properties.[26, 27, 24, 25, 28-30]

Apart of the essential building blocks (organic ligands and metal centers), the solvent molecules may co-crystallize in the CPs, increasing the number of possible weak interactions in the final packing, and can act as guest molecules in the vacant space inside the polymers networks.[31]

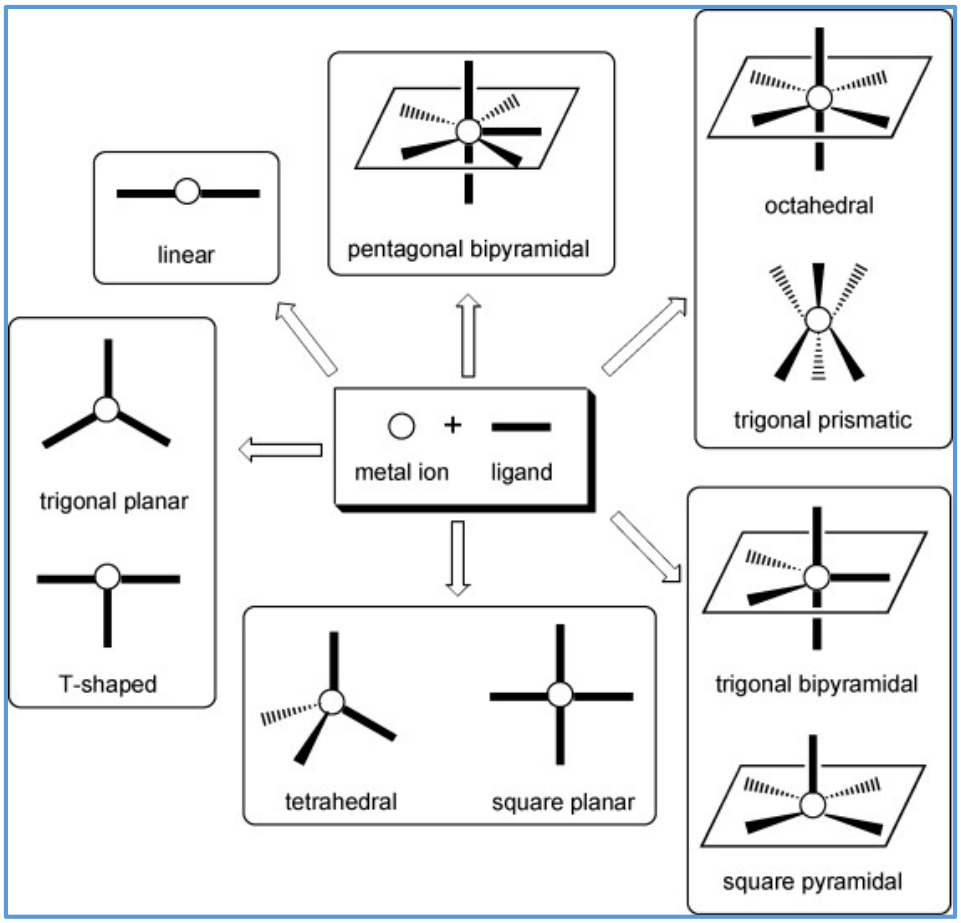

Figure 1.2. Some coordination geometries of transition metal ions.[32]

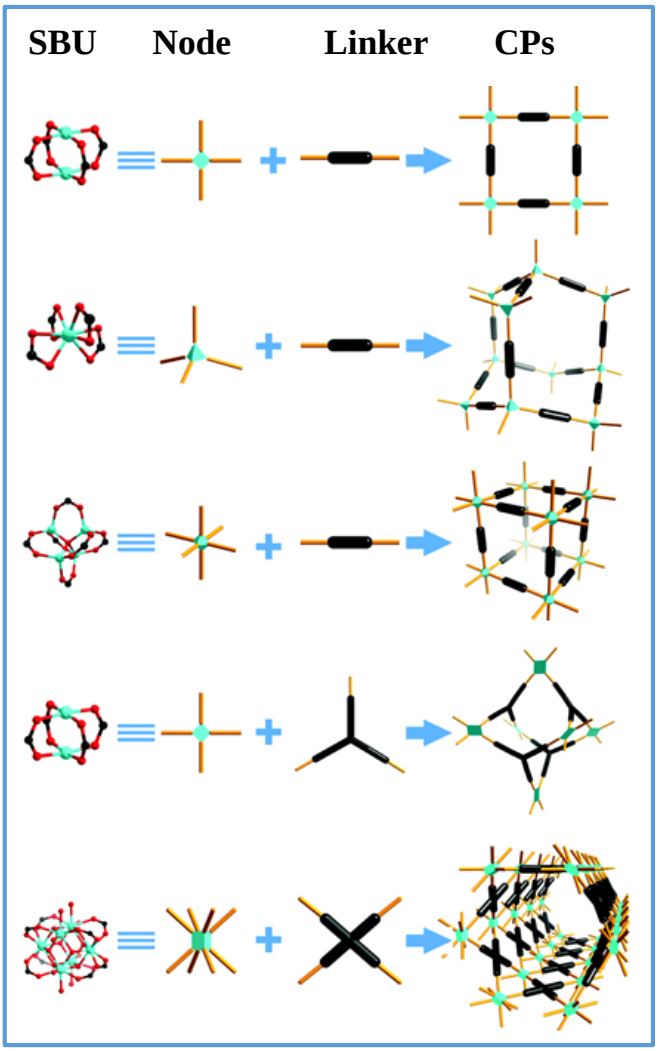

Figure 1.3. Graphical illustration of the construction of some coordination polymers from SBUs and rigid linkers.[21]

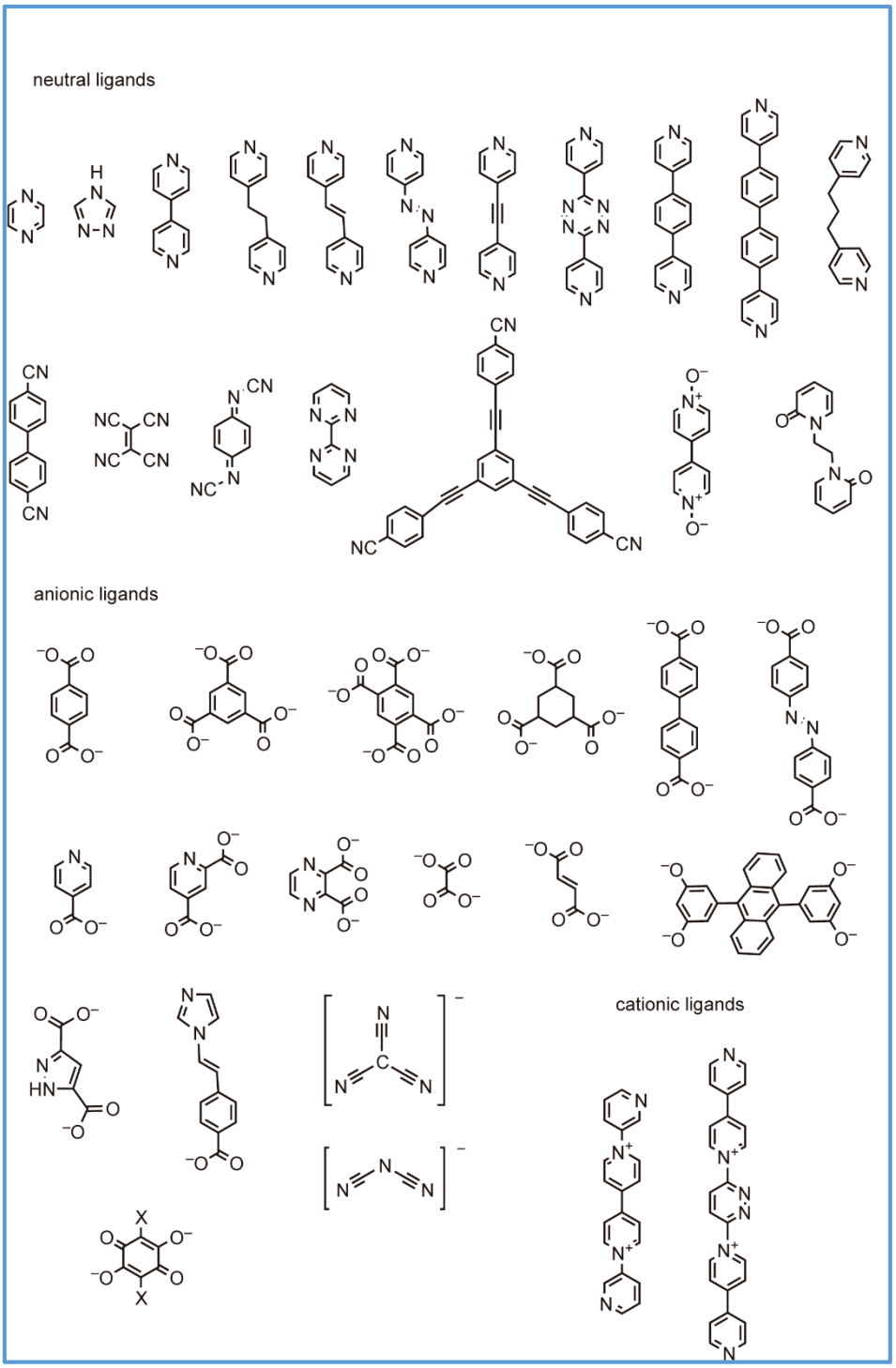

Figure 1.4. Schematic representations for some used organic ligands to construct CPs.[1]

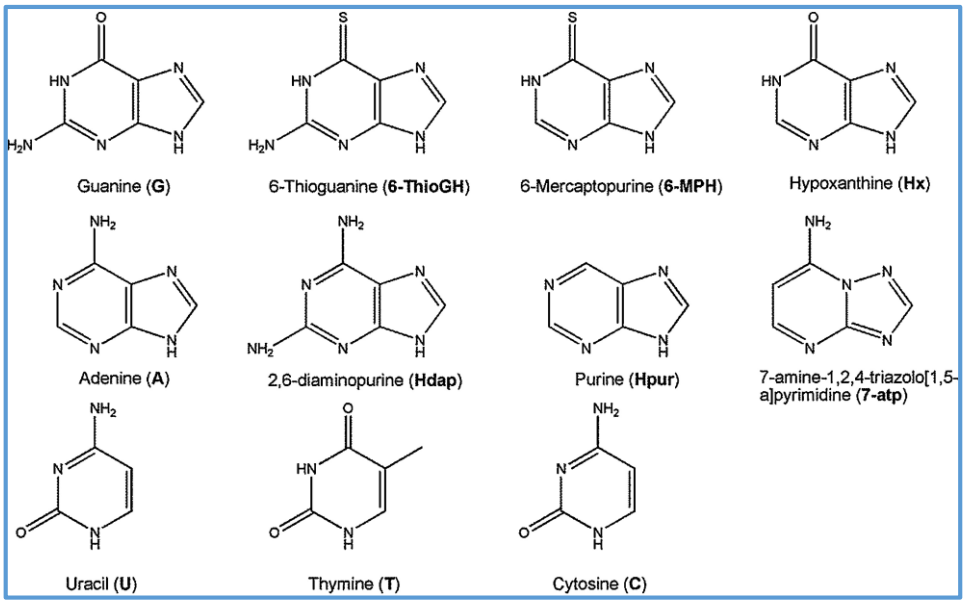

Figure 1.5. Summary of the purine (top and centre) and pyrimidine (bottom) nucleobases.[24]

Common synthetic methods of CPs

Traditionally, the goal of CPs synthesis is to obtain high quality single crystals for structural analysis and hence make it easy to understand the structure/properties relationship of CPs. However, CPs are generally insoluble in common solvents, and often the recrystallization is not available.[12] In a surprisingly short period, the structural chemistry of coordination polymers has reached a mature level, due to the application of useful crystallization and synthetic methods such as slow diffusion and solvothermal methods respectively.[22, 33]

Here we are going to describe some of the synthetic and crystallization methods that have been used for the experimental section of this thesis (**Figure 1.6**); (i). Self-assembly method where the slow evaporation of saturated solution containing the reactants may allow the growing of suitable single crystals for single crystal X-ray diffraction (SCXRD) analysis. (ii) Diffusion methods, where layers of the reactants slowly diffuse to come in contact through separate layer, are preferential to get single crystals suitable for SCXRD analysis especially, when the products are poorly soluble.[34] (iii) Hydro(solvo)thermal method where, typically, the reactions carry out at elevated temperature under autogenous pressure of the used solvents and the duration of the reactions may be extend for days.[35] (iv) Microwave irradiation, this technique has been developed as an alternative heating

technique for the hydro(solvo)thermal method to provide an efficient way to synthesize purely materials with short reaction times.[32]

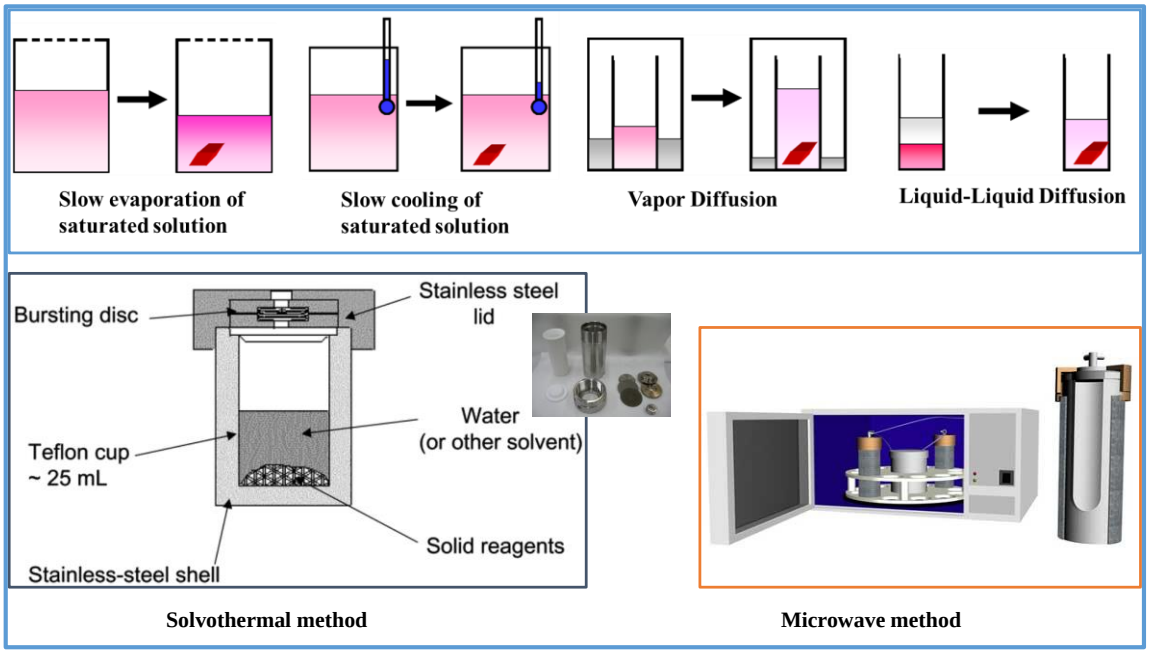

Figure 1.6. Synthetic and crystallization methods used to get single crystals during this thesis.

It is important to mention that changing the synthetic procedure and/or the reaction conditions for the same starting materials, sometimes may lead to different products and/or polymorphic species. Polymorphism defined as the existence of the same chemical substance in more than one lattice structures, in other words, materials with the same chemical composition but the forces acting in the arrangement and/or conformation of the crystalline solids lead to different networks.[36] Polymorphism is an interesting phenomenon that plays an important role in understanding crystal packing and structure–property relationships.[37, 38] One interesting example for polymorphism has been reported by Guoqi Zhang *et al*. They have synthesized one dimensional coordination polymers (1D-CP), formulated as $[CdL_2]_n$ where L is 2-mercaptopyridine-N-oxide, with two polymorphic forms (polymorph **1** and polymorph **2**). The polymorph **2** has been obtained as a result of introducing glycine as guest molecule in the starting reactants.[39] The two crystallographic polymorphs have similar 1-D polymeric chains but they are, significantly, different in the binding modes of the 2-mercaptopyridine-N-oxide ligand, and the 3-D packing modes (**Figure 1.7**)

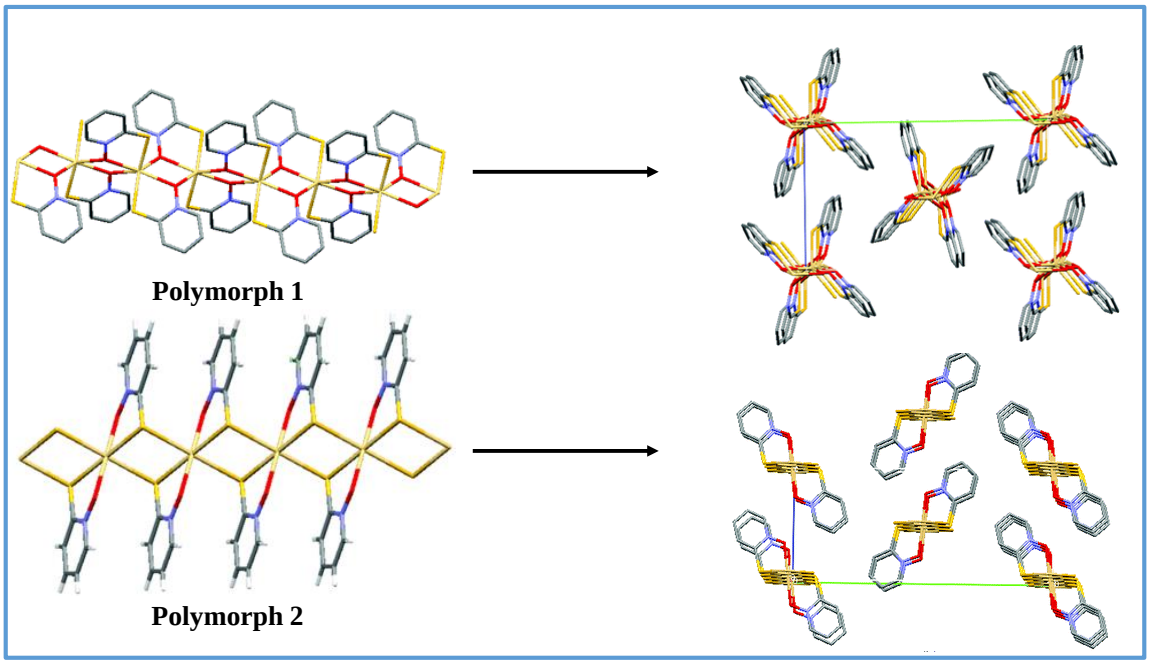

Figure 1.7. Polymorphs forms of $[CdL_2]_n$ 1D-CPs, , where L is 2-mercaptopyridine-N-oxide, and their 3-D packing modes.[39]

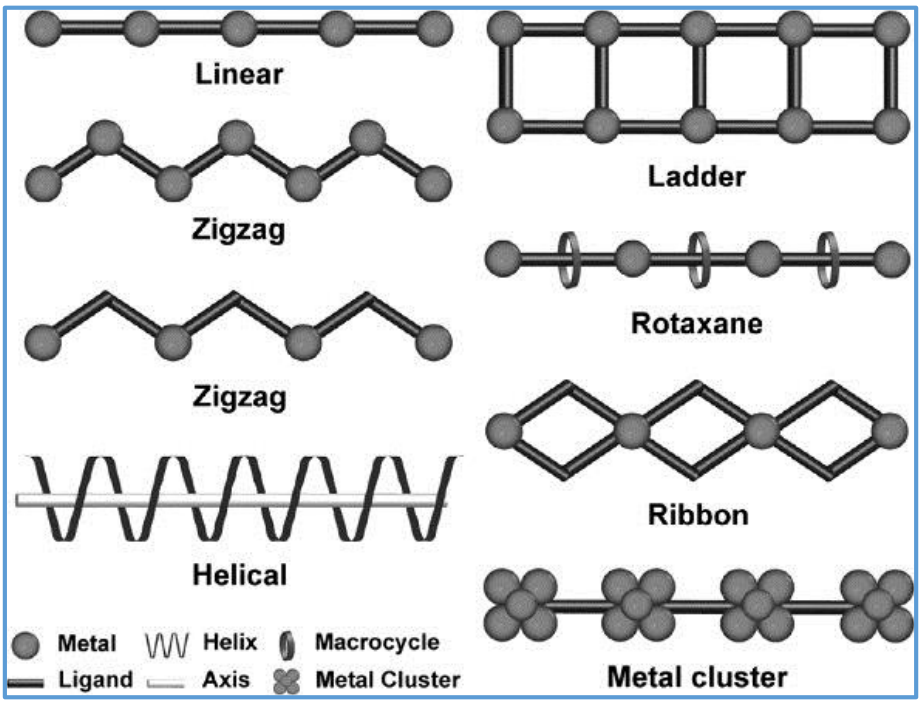

Figure 1.8. One-dimensional motifs of coordination polymers.[40]

CPs can be classified according to their dimensionalities into one dimensional coordination polymers (1D-CPs), two dimensional coordination polymers (2D-CPs), and three dimensional coordination polymers (3D-CPs). The dimensionality of CPs is often

determined by the geometry of metal centres. Interactions such as H-bond, π-π stacking, and van der Waals play an important role during the formation of the crystals, but the final compound dimensionalities is based on the coordination interactions between ligand molecules and metal ions. Of these dimensionalities, 1D-CPs are considered to be the simplest one, nevertheless they have been found to have interesting electrical, magnetic, and optical properties.[27, 41, 42, 22, 43, 44] **Figure 1.8** shows schematic representation for some common 1D-CPs motifs.

Generally, CPs show many advantages over those known as covalent-organic frameworks (COFs), porous and crystalline materials in which the building blocks are linked by strong covalent bonds, owning to the reactivity, flexibility, and reversibility of the coordinative bonds that are responsible for the arrangement of the building blocks with the aid of other supramolecular forces.[45, 46, 36] Thus, a variety of CPs can be ranging from robust frameworks of enhanced stability to flexible solids. Thus, flexible CPs can respond to external stimuli, sometimes, followed by reversible structural transformations that are intrinsically related to the structural flexibility of the ligand, the ability of the coordination sites to accept, release and/or exchange coordinating molecules.[47-49] In fact, flexible nature was observed for porous coordination polymers (PCPs), subclass of CPs, also known as metal-organic frameworks (MOFs).[50, 51] In addition, some non-porous coordination complexes show structural flexibility that was detected through single-crystal to single-crystal transformation (SCSC).[52, 53] Dynamic materials (stimuli-response) that undergo reversible structural changes as function of the applied stimulus, being exceptionally useful in the preparation of functional materials with tunable or switchable physical properties. These are, particularly, interesting for electrical[54-56], magnetic,[57] and photoluminescence applications,[58] since their physical properties are extremely sensitive to minor structural changes provoked by an external stimulus. Switching the physical properties of CPs as a result of structural transformations induced by external stimuli will be discussed in details later under CPs as responsive materials (section 1.2.4).

1.2. Properties of CPs

Currently, CPs are one of the fastest growing fields in chemistry and material science. It has attracted researchers from several areas of science due to their structural diversity, tunable properties, and the wide range of potential applications such as catalysis, electronics, magnetism, optical, opto-electronics, and nano-applications.[59-64, 12, 50, 21, 65, 66]

In the following sections, the potential uses of CPs in many applications such as electronic, magnetism, and optical applications will be presented. The dynamic nature of CPs will be discussed. Finally the potential applications of CPs as nanomaterials will be highlighted.

1.2.1. Electrical properties.

Electrical conductivity of a material is a measure of its ability to conduct electric current under certain conditions (such as temperature, pressure, applied voltages…). The measurements of the resistance (and, hence, the resistivity) of a sample require the application of a current (I) and measuring the voltage drop across the sample (V). According to Ohm's law of conductivity ($V = R \times I$; where V is the voltage, I is the current, and the proportionality constant, R, is the resistance). Since R depends on geometrical parameters (therefore, it is sample-dependent) and commonly expressed as resistivity (ρ), which is defined as $\rho = R \times (A/l)$, where A is the cross-sectional area of the conductor ($A = a \times d$) and l is the distance between the voltage-drop measuring points (**Figure 1.9**). The conductivity (σ) is inverse of the resistivity (ρ), ($\sigma = 1/\rho$), and measured in Ω^{-1} cm^{-1} = S cm^{-1} (Ω^{-1} = S = Siemens).

There are different methods to measure the electrical conductivity in solid state (crystals or pressed pellets).[62, 67] Among them, four contacts method and two contacts method have been widely used (**Figure 1.9**). Four contacts method involves the connection of four parallel in-line contacts to the sample where the two external contacts are used to apply a current ($I+$ and $I-$) and the two internal contacts are used to measure the voltage drop across the sample ($V+$ and $V-$).

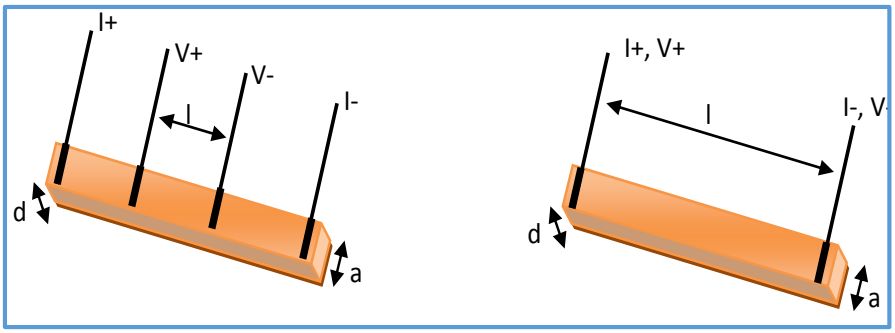

Figure 1.9. The four (left) and two (right) contacts methods for measuring electrical conductivity. Dimensions *l*, *a* and *d* are the voltage probes distance, the sample width and thickness, respectively.[62]

Two contacts method involves the connection of two parallel contacts to the sample where apply a current (*I*+ and *I*-) and measure the voltage drop across the sample (*V*+ and *V*-). These methods were developed to overcome the problems of conductivity measurements such as the effect of the electrical contacts with the sample, morphology of the sample (single crystals, pressed pellets, thin films…) and the quality of the crystals. When the sample is pressed pellet, the crystal anisotropy is removed, and in these cases the resistivity is mainly dominated by the intergrain boundary contacts, which tend to increase the resistivity, usually, between one and three orders of magnitude with respect to the values obtained in crystals, which acts as gaps that block the conductivity or as carrier accumulators. This behaviour implies that true metallic materials may appear as low band-gap semiconductors or semimetals if they are measured as pressed pellets. The four contacts method is more accurate since it only measures the resistance of the sample (R_x) but neither the resistance of the wires nor that of the contacts. In contrast, in two contacts method, the resistance of the sample and those of the wires and contacts are added in the measured resistance. Two contacts method is preferred for small size samples, typically, above *ca*. 50 μm vs. *ca*. 250 μm for the four contacts method.[62]

On the other hand, electrochemical impedance spectroscopy (EIS) technique is used to measure the impedance of a given system when apply an AC potential to an electrochemical cell. Like resistance, impedance is a measure of the ability of a sample to resist the flow of electrical current, but unlike resistance, it is frequency dependent and the current (AC) and voltage are phase shifted. The impedance (Z) of a system is generally determined by applying a voltage perturbation with a small amplitude and detecting the current response. EIS is a powerful method for analyzing the complex electrical resistance of a system and is sensitive to surface phenomena and changes of bulk properties.[68]

Therefore, it is a useful technique to measure the conductivity for the coordination polymers, in particular those that contain in the networks protonated solvent.[69]

In a linear (or pseudolinear) system, the current response to a sinusoidal potential will be a sinusoid at the same frequency but shifted in phase. Therefore, it is possible to express the impedance as a complex function. The potential is described as

$$E_t = E_0 \exp(j\omega t)$$

E_t is the potential at time t, E_0 is the amplitude of the signal, and ω is the radial frequency. The relationship between radial frequency ω (expressed in radians/second) and frequency f (expressed in hertz) is:

$$\omega = 2\pi f$$

In addition, the current response is described as

$$I_t = I_o \exp(j\omega t - \varphi)$$

An expression analogous to Ohm's law (R = E/I), where R is resistance, allows to calculate the impedance of the system. The impedance is then represented as a complex number

$$Z(\omega) = E/I = Z_0 \exp(j\varphi) = Z_0 (\cos\varphi + j \sin\varphi)$$

The impedance of a system can be expressed graphically in different ways, one of them is Nyquist plot in which the real part (Re(*Z*)) is plotted on the X-axis, and the imaginary part (Im(*Z*)) is plotted in the Y-axis of a chart (**Figure 1.10a**). On the Nyquist plot, the impedance at one frequency can be represented as a vector of length $|Z|$. The angle between this vector and the X-axis represents the phase angle (φ). Another representation for the impedance measurements is the Bode plot (**Figure 1.10b**). In this case, the logarithm of absolute values of the impedance and the phase angle are plotted in the Y-axis and the log frequency on the X-axis. The electrical conductivity can be calculated from the Nyquist plot as $\sigma = l/a \times \mathrm{Re}(Z)$, Where *l* and *a* are the thickness (cm) and cross-sectional area (cm^2) of the pellet respectively. Re(*Z*), which was extracted directly from the real impedance axis, is the bulk resistance of the sample (Ω).

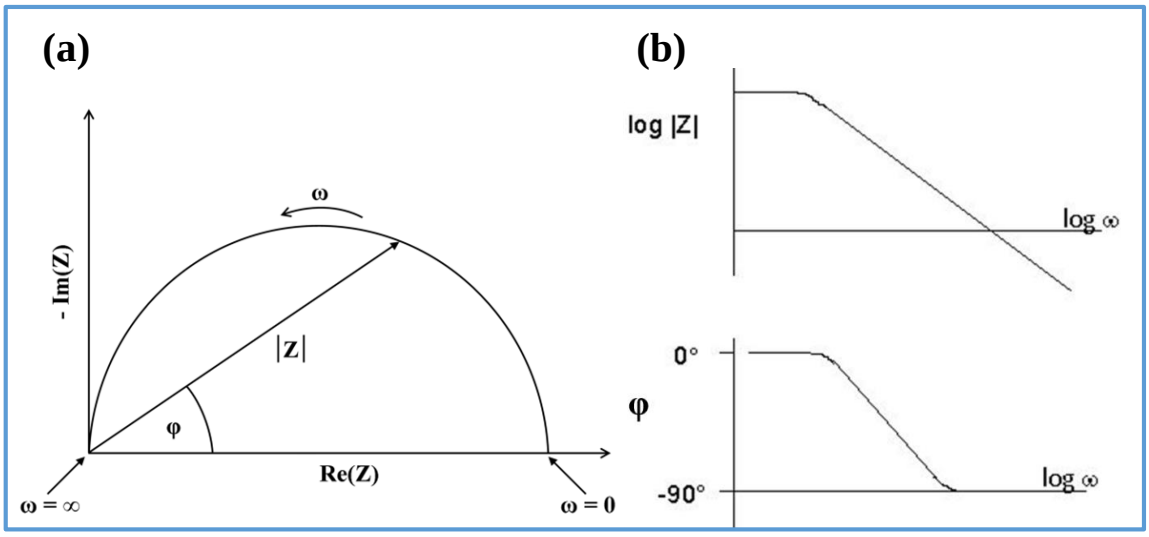

Figure 1.10. (a) Nyquist plot for a simple electrochemical system, Re(*Z*) and -Im(*Z*) refer to the real component and imaginary component, respectively. (b). Bode plots graphs.

In general, the electrical behaviors of the materials can be distinguished looking at the room temperature conductivity value which is usually in the range 10^{1}–10^{5} S cm^{-1} for metals, 10^{-10}–10^{1} S cm^{-1} for semiconductors, and below ca. 10^{-10} S cm^{-1} for insulators. The thermal variation measurements of the electrical conductivity, inside the Ohmic regime, is more reliable and give clear picture about the electrical behavior of the targeting material. For metals, the conductivity increase or the resistivity decrease with decreasing temperature and the opposite behavior was observed in semiconductors and insulators.[62]

Band theory have been used to describe the conduction in solid materials.[70] The materials can be described according to their band structure into metals, semiconductors, and insulators. Because of the very large number of atoms that interact in a solid material, the energy levels are so closely spaced where they form bands. The highest energy filled band is called the "valence band". The next higher unfilled band is called the "conduction band". The energy separation between these bands is called the "band gap", (E_g). The filling of these bands and the size of the band gap determine the electronic behavior of solid materials (**Figure 1.11**). Fermi level, usually found between the valence and conduction bands, refers to the highest occupied molecular orbital at absolute zero. The thermal activation of semiconductor lead to decrease in the gap between the conduction and valence bands (in fact, the classical insulator definition is applied when the band gap is above 3 eV). In classical semiconductors the thermal dependence of the conductivity

follows the Arrhenius law: $\sigma(T) = \sigma_0 \exp(-E_a/kT)$, where E_a represents the activation energy (corresponding to half of the band gap, $E_a = E_g/2$) and σ_0 is a pre-exponential factor. Phase transitions have been observed, in some cases, through the thermal activation of solid materials. These phase transitions, in many cases, are followed by structure rearrangements that can be detected through the structure determination techniques mainly, diffraction techniques.[68]

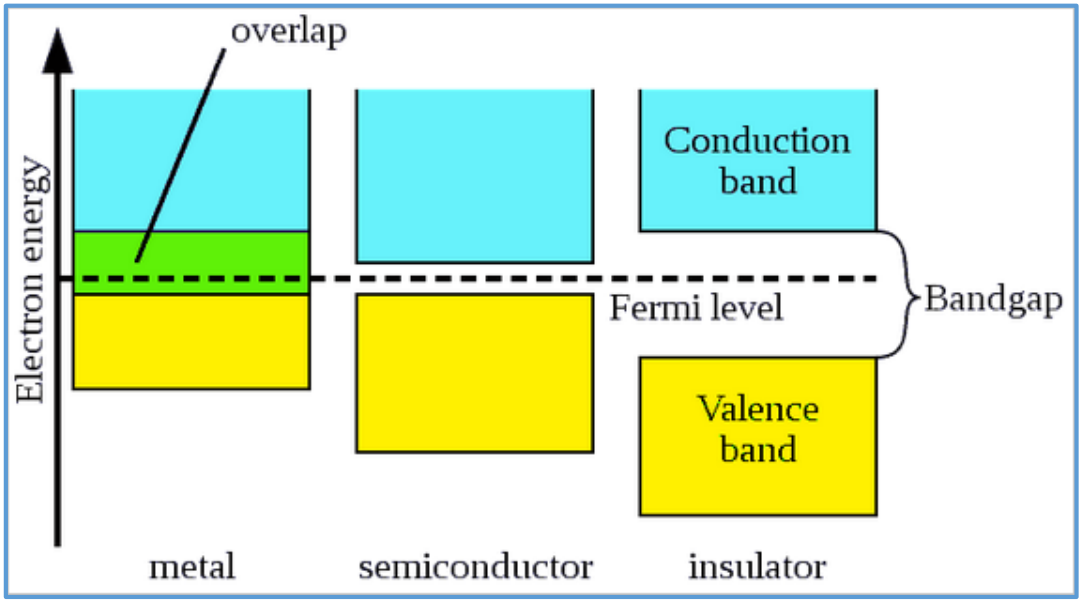

Figure 1.11. Illustrate the band structures and band gaps in different materials.

Electrical conductivity of CPs is one of the most important research areas in materials science. It is well known that electrical conductivity of organic polymers has attracted the interest of many researchers in material science, however, the research of this property in CPs is still very scarce.[62] Based on recent results, some CPs systems have shown very promising macroscopic electronic properties.[62] In addition, the gradual incorporation of theoretical calculations in CPs seem to be a powerful tool for understanding the experimental measurements and for rational design of new electrically conductive CPs.[71, 72] One possible application of CPs with electrical conductivity is the electronic one, especially, 1D-CPs that can act as electrical wires.[63] The electrical conductivity, founded in some 1D-CPs, seems to be very dependent on the composition of the starting building blocks and structural parameters,[22, 62] and require short bridging ligands to provide metal-metal distance as short as possible in the extended metal-ligand structures that may give

rise to high electrical conductivity. Here we will present the electrical conductivity studies founded in different 1D-CPs systems.

It has been reported that a family of CPs known as MMX polymers, formed by bridging dimetallic subunits (MM units M= Pt, Rh, Pd…) with halogen (X) as ligands to form 1D-CPs, have shown reasonable electronic properties.[62] Concretely, one class of MMX polymers with structural formula $[Pt_2(RCS_2)_4I]_n$, where R is alkyl groups, have shown high electrical conductivity values at room temperature. **Table 1.1** gather the electrical conductivity founded in $[Pt_2(RCS_2)_4I]_n$, MMX polymers. A careful study of structural parameters for $[Pt_2(RCS_2)_4I]_n$ MMX polymers shows that the only difference between these MMX derivatives is the alkyl chain length, which governs the interchains distances and may tune the Pt–Pt and Pt–I distances that are responsible for the observed physical properties.

Table 1.1. Summary of conductivity data obtained for $[Pt_2(RCS_2)_4I]_n$, where R is alkyl groups, chains in single crystals at RT (room temperature) and 1 bar using four contact method.[62]

Compounds	Conductivity/S cm^{-1}
$[Pt_2(CH_3CS_2)_4I]_n$	$2^{c}/10^{b,c}$ $7\times10^{-3c,d}/13$
$[Pt_2(EtCS_2)_4I]_n$	5–30
$[Pt_2(n\text{-}PrCS_2)_4I]_n$	0.23
$[Pt_2(n\text{-}BuCS_2)_4I]_n$	17–83
$[Pt_2(n\text{-}PenCS_2)_4I]_n$	0.3–1.4
$[Pt_2(n\text{-}HexCS_2)_4I]_n$	2×10^{-3}

[b] RT and 7 GPa. [c] Two probe method. [d] Pressed pellet.

As a representative example of this family, Zamora *et al*. have studied the electrical conductivity of 1D-MMX polymer formulated as $[Pt_2(n\text{-}PenCS_2)_4I]_n$, where Pen is pentyl group (**Figure 1.12a**).[68] Direct current (DC) electrical conductivity measurements carried out on crystals of $[Pt_2(n\text{-}PenCS_2)_4I]_n$, at different temperature using four contact method, have shown a metallic behavior (**Figure 1.12b**) and room temperature conductivities values in the range 0.3–1.4 S cm^{-1}. The electrical measurements on crystals of $[Pt_2(n\text{-}PenCS_2)_4I]_n$ have been carried out at three different temperatures (100 (LT), 298 (RT) and 350 (HT) K) and showed the existence of three different phases for $[Pt_2(n\text{-}PenCS_2)_4I]_n$.[68] The data collected in **Table 1.1**, summarized the excellent electrical conductive properties

that have been founded in $[Pt_2(RCS_2)_4I]_n$ 1D-CPs which open the door for these classes of materials to be applied in electronic applications.[41]

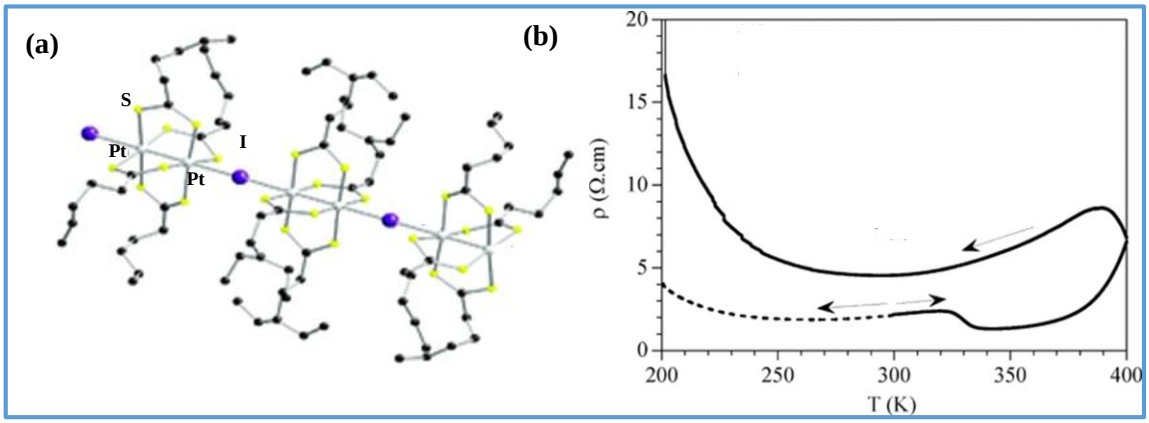

Figure 1.12. (a) A single polymer chain of $[Pt_2(n\text{-}penCS_2)_4I]$. (b) Thermal variation of the electrical resistivity of $[Pt_2(n\text{-}penCS_2)_4I]$. The dashed line shows the behavior of a non-heated sample.[68]

Another interesting CPs systems that showed reasonable electronic properties are those that are formed using S-containing ligands as bridging ligands.[62] It is well established that when the "S" atom acts as bridging ligand between the metal centers, may provide better orbital overlapping and hence gives raise for polynuclear compounds with high electrical conductivity.[73, 62] Zamora *et al*, have investigated the electrical conductivity of many 1D-CPs produced from the interactions of copper(I) salts and S-containing ligands (thiolate).[22] A novel representative 1D-CP based on S-containing ligand is $\{[Cu_9(C_5H_5NS)_8(SH)_8](BF_4)\}_n$, where C_5H_5NS = pyridine-2-thione ligand, in which Cu_9 cages bridging by S atoms (**Figure 1.13a, b**).[74] The electrical measurements of this 1D-CP have presented high room temperature conductivity value of 1.6×10^{-3} $S \cdot cm^{-1}$ and a classical semiconducting behavior with an activation energy of 110 meV (**Figure 1.13c**). The same authors studied the interactions of copper(I) halides (Br or I) with pyrimidine disulfide ligand (pym_2S_2) that led to the isolation of isostructural 1D-CPs formulated as $[Cu_3X(pymS)_2]_n$, X =Br or I anions, pymS is pyrimidine-2-thione (**Figure 1.14a**, **b**).[22] The room temperature electrical conductivity values of those two 1D-CPs are in the order of magnitude of 10^{-6} and 10^{-7} S cm^{-1} for I and Br respectively, and the thermal variation of the electrical conductivity suggested semiconducting behavior (**Figure 1.14c**, **d**).

In addition, Richard Henderson *et al*, have studied the electronic properties of 1D-CPs formulated as $[M(L)_2(X)]_n$, M= Ag or Cu, L is N-containing ligands and X = SCN or NO_3 anions.[75] Among them, 1D-CP formulated as $[Cu^I(pyridine\text{-}3,4\text{-}dicarbonitrile)_2(SCN)]_n$

(**Figure 1.15a**), presented room temperature conductivity value of 4.29×10^{-5} S cm^{-1}. In addition, the thermal variation of the electrical conductivity showed a semiconducting behavior (**Figure 1.15b)**.

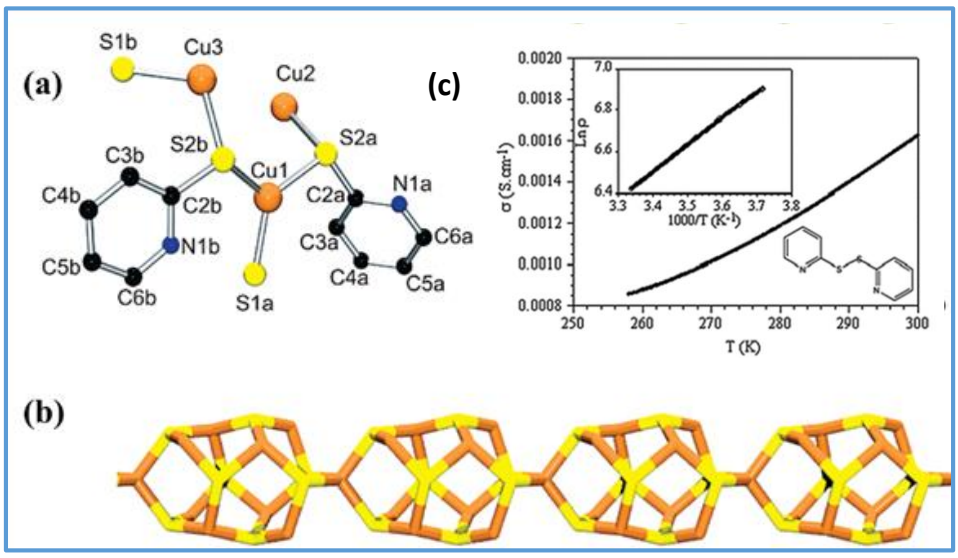

Figure 1.13. Structure details of $[Cu_9(C_5H_5NS)_8(SH)_8]^+$ cluster with an atomic numbering scheme. (a and b). Thermal variation of the electrical conductivity of compound $\{[Cu_9(C_5H_5NS)_8(SH)_8](BF_4)\}_n$ (using four contact method). The inset shows an Arrhenius plot.[74]

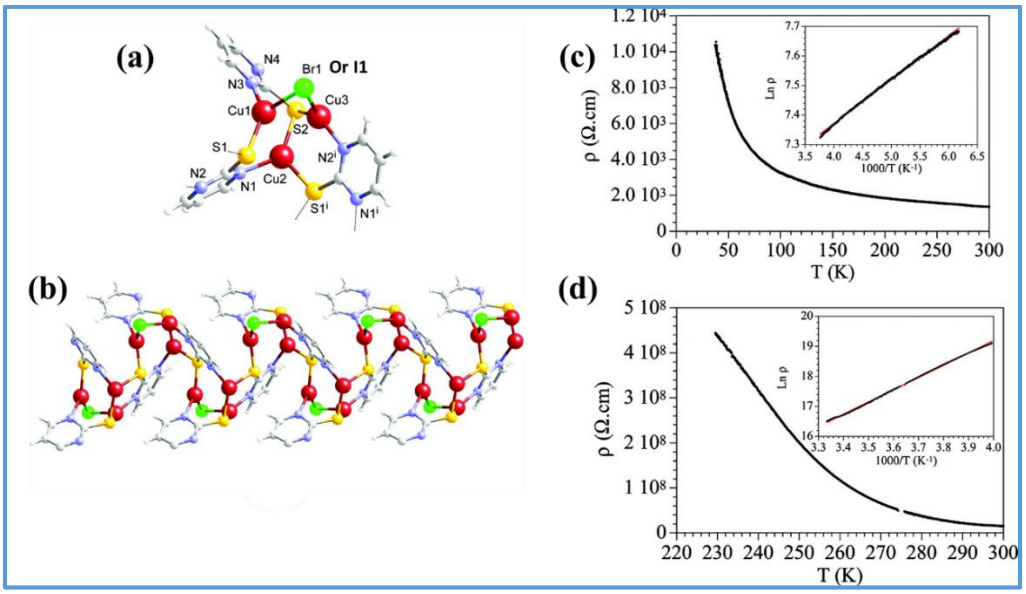

Figure 1.14. Structure details of $[Cu_3X(pymS)_2]_n$ (X = Br or I anions) with an atomic numbering scheme (a) and the helical chain of $[Cu_3X(pymS)_2]_n$ (b). Thermal variation (using four contact method) of the electrical conductivity of compounds $[Cu_3I(pymS)_2]_n$ (c) and $[Cu_3Br(pymS)_2]_n$ (d). The inset shows an Arrhenius plot.[22]

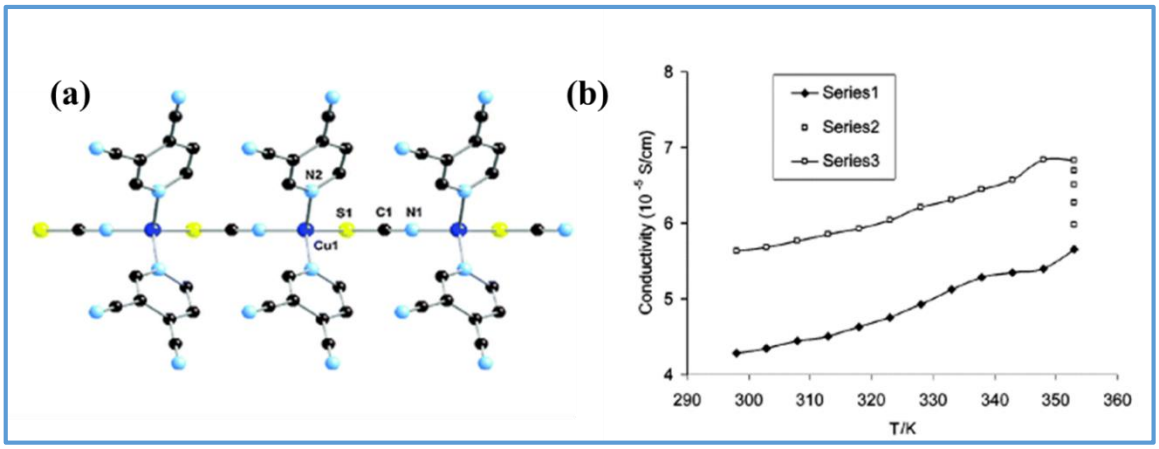

Figure 1.15. (a) A section of the polymeric chain of $[Cu^{I}(pyridine\text{-}3,4\text{-}dicarbonitrile)_2(SCN)]_n$. (b) Thermal variation of the electrical conductivity of compound $[Cu^{I}(pyridine\text{-}3,4\text{-}dicarbonitrile)_2(SCN)]_n$.

1.2.2. Magnetic properties.

Design and synthesis of attractive magnetic materials are important among all growing number of functional applications of CPs owing to the magnetic character of such class of compounds that can, easily, be tuned and controlled by changing the linkers and nodes.[76-82] As a result, large numbers of CPs exhibiting ferromagnetism[83-86], antiferromagnetism,[87-91] and ferrimagnetism interactions[92, 93], single chain magnet[94-96], single molecule magnet[97-99], spin crossover,[100-103] and spin canting[104, 105], have been synthesized and studied. In general, magnetism is based on individual spin carriers, which are paramagnetic metal centres. Thus, depending on the origin of the coupling between these spin carriers, two different magnetic materials can be distinguished: i) magnetic materials presenting long range magnetic ordering, as it occurs in general magnets; and ii) spin transition through bridging ligands. In the former, magnetic ordering is derived from the cooperative exchange interactions between the paramagnetic metal cations through superexchange pathways of, typically, diamagnetic entities. Antiferromagnetism (↑↓↑↓), ferrimagnetism (↑↓↑↓), and ferromagnetism (↑↑↑↑) are the common cooperative magnetic spin interactions observed within the solid materials. Consequently, magnetic centres need to be organized in specific topologies and linked by ligands that efficiently promote magnetic exchange interactions to achieve a long-range control of the magnetic interactions. The target is to control the magnetic exchange interactions by regulating bridging distances, angles and electronic configuration of magnetic centres. As a result, the ligands design; ligands with oxo, cyano or azido bridges show a strong coupling between the metal centres and their unpaired electrons[106, 107], is crucial, for both, to organize the paramagnetic metal ions in a desired topology and to transmit exchange interactions between the metal ions in a controlled manner.[106, 108, 107, 109-111, 86] The formation of bulk magnetic materials with non-zero spin requires a frameworks that allow parallel coupling of the spins of neighboring paramagnetic spin carriers (ferromagnetic interactions) or antiparallel coupling of unequal spins (antiferromagnetic interactions). Additionally, there is a class of magnetic CPs based on spin transition that is known as spin-crossover (SCO). SCO is a phenomenon in which electronic configurations of a transition metal ion can be switched between high-spin (HS) and low-spin (LS) states in response to external stimuli (temperature, pressure, light irradiation, magnetic field, electric field, and guest sorption) producing changes in magnetism, color and structure.[102]

Notice that, the exchange interactions are in general weak and hence, the magnetic cooperativity is only observed at very low temperatures.

Magnetic interactions for particular materials can be determined by their responses to the variations in temperature and external applied magnetic field. These responses are used to determine the specific type and strength of magnetic interactions. Typically, temperature dependent magnetism is used to draw the picture of the magnetic character of particular solid by examining the susceptibility of this solid as a function of temperature at constant applied field. Magnetic properties analysis of particular material can be carry out by examining the temperature dependence of molar susceptibility ($\chi_m = \chi_g M$ where χ_g is mass susceptibility and M is molecular weight), molar susceptibility temperature product (χ_{mT}), and inverse of molar susceptibility (**Figure 1.16**). These analyses can provide us a valuable information about the nature of magnetic interactions and the magnetic interactions strength between the active spin ions.

In order to measure the magnetic properties of CPs, SQUID technique, "superconducting quantum interference device", is a very sensitive magnetometer used to measure the magnetization of a sample with a defined mass in various applied fields (up to 7 T) and at various temperatures (as low as 1.8 K). In addition, when apply a static magnetic field, it is also possible to measure the magnetic susceptibility in an alternating (AC) field, which allows some insights into the dynamics of a magnetic system.

On the other hand, plots of M (Magnetization) vs. H (applied magnetic field) in constant temperature are also useful in magnetic characterization (**Figure 1.17**). A characteristic of the curves for ferromagnets, paramagnets, and ferrimagnets are the saturation magnetization (Ms). This is the point where all of the magnetic moments, in a material, are aligned with the field, so the magnetization of the sample cannot increase any further. This characterization is particularly important for ferromagnetic materials that show hysteresis behavior (memory effect). For ferromagnetic materials, as the field is applied starting from zero field, the sample becomes magnetized. As the field is lowered to zero, the sample retains some magnetization, which is referred to as the remanence. The sample remains magnetized until the applied field is strong enough in the negative direction to flip the spins; this field strength is referred to as the coercivity or coercive field (H_C).

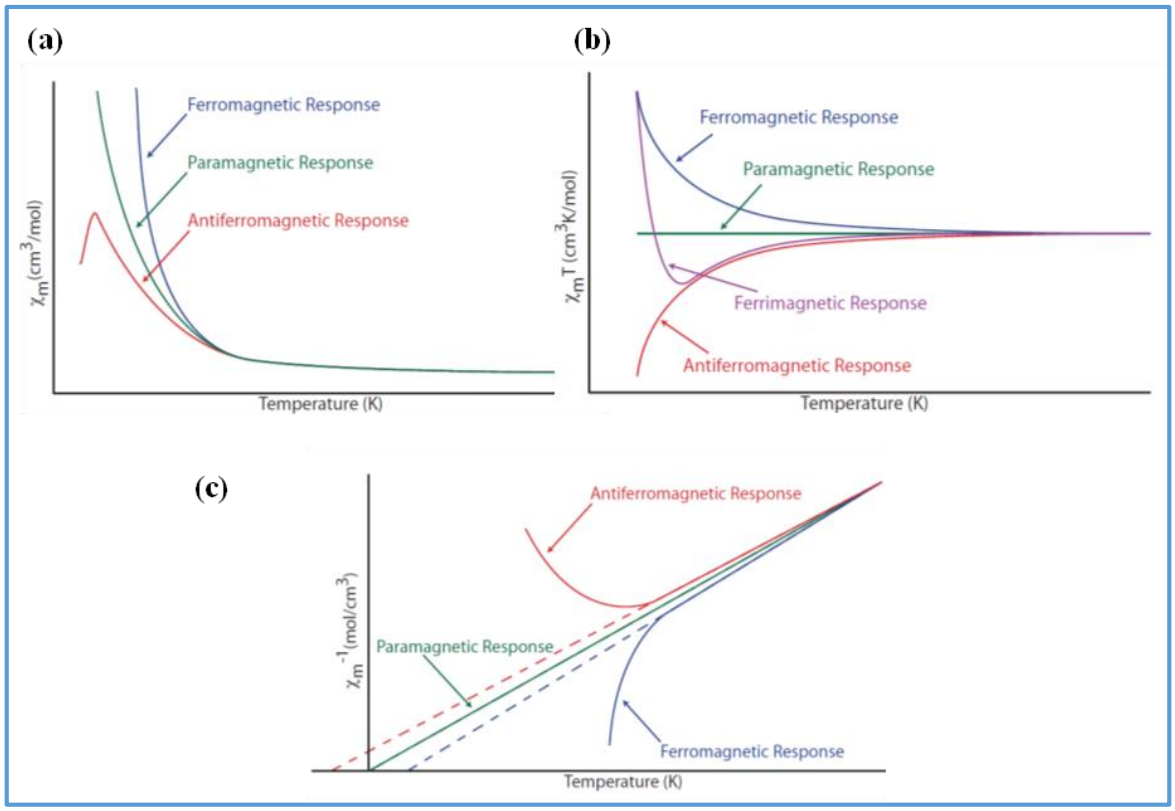

Figure 1.16. Plots of (a) χ_m vs. T, (b) Plot of χ_mT vs. T and invers of χ_m vs. T for different magnetic materials.

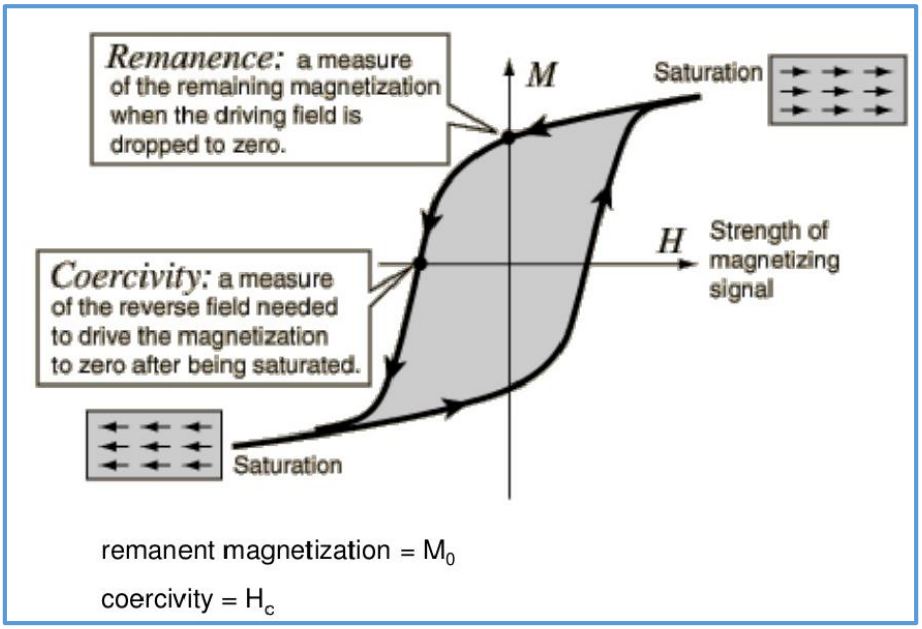

Figure 1.17. Schematic of the hysteresis loop in ferromagnetic materials showing the saturation magnetization, coercive field and remanent magnetization.

In the context of magnetism, the study of magneto-structural correlations is aiming to understand the structural and chemical factors that govern the exchange coupling between paramagnetic centers through multiatomic bridges ligands.[112, 113, 91]. Carboxylic ligands are one of the most frequently used ligands for the construction of CPs with diverse magnetic properties.[76, 87, 77, 88, 108, 90, 82, 91, 111] They can adopt different bridging modes such as syn-syn, anti-anti or syn-anti conformation. Therefore, they can bridge two or more metal ions into coordination compounds with various dimensionalities ranged from 0D complexes to infinite arrays (1D, 2D and 3D) frameworks.[114, 115, 91] Paddle-wheel carboxylate-copper systems are one of the widely studied motifs, due to their versatility and their novel magnetic systems with different dimensionalities when an appropriate coligand is used.[116-119] Generally, the experimental and theoretical studies concerning paddle-wheel species have also shown various magnetic interactions between adjacent Cu(II) ions, range from moderate or strong antiferromagnetic to ferromagnetic coupling between the unpaired electrons of the Cu(II) centers. The strength of these coupling are measured by the coupling constant *J* within the usual isotropic Heisenberg–Dirac–van Vleck model: $H= -2 \sum J_{ij} S_i S_j$; $S_i = S_j = 1/2$ ($2J$ represents the singlet–triplet energy gap). The nature of interactions, and hence magnitude of the exchange interaction, seem to be depending on the M-O-C-O-M conformation, the nature of the carboxylate ligands, the bond angles at the bridging atoms, the copper-bridge ligand bond lengths, and the apical ligands.[120, 83, 84, 87, 121, 89, 90, 122]

1.2.3. Luminescence properties.

Luminescence can be defined as the emission of light stimulated by the absorption of energy. Electron excitations result in different forms of luminescence, which include photoluminescence, thermoluminescence, electroluminescence and chemiluminescence, depend on the nature of the energy absorbed for the excitation process. Photoluminescence can be define as light emission from any form of matter because of absorption of photons (electromagnetic radiation). The processes that occur between the absorption and emission of light are usually illustrated by the Jablonski diagram (**Figure 1.18**).[123] The singlet ground electronic states are depicted by S_0. Following light absorption, several processes usually occur. A fluorophore is usually excited to some higher vibrational level of either S_1 or S_2. Molecules in higher exited states are rapidly relax to the lowest vibrational level of S_1. This process is called internal conversion (IC). IC process is nonradiative and generally occurs within 10^{-12} s or less. IC is complete prior to emission. Return to an excited vibrational state at the level of the S_0 state is the reason for the emission spectrum (fluorescence). Molecules in the S_1 state can also undergo a spin conversion to the first triplet state T_1. Emission from T_1 is termed as phosphorescence, and is generally shifted to longer wavelengths (lower energy) relative to the fluorescence emission. Conversion of S_1 to T_1 is called intersystem crossing (ISC). Transition from T_1 to the singlet ground state is forbidden, and as a result, the rate constants for triplet emission are several orders of magnitude smaller than those for fluorescence. Therefore, we can conclude that there are two basic types of luminescence: fluorescence, which is spin-allowed between the energetic states and has typical lifetimes approximately 10 ns; and phosphorescence, which is spin-forbidden and has lifetimes that can be as long as several seconds.[123]

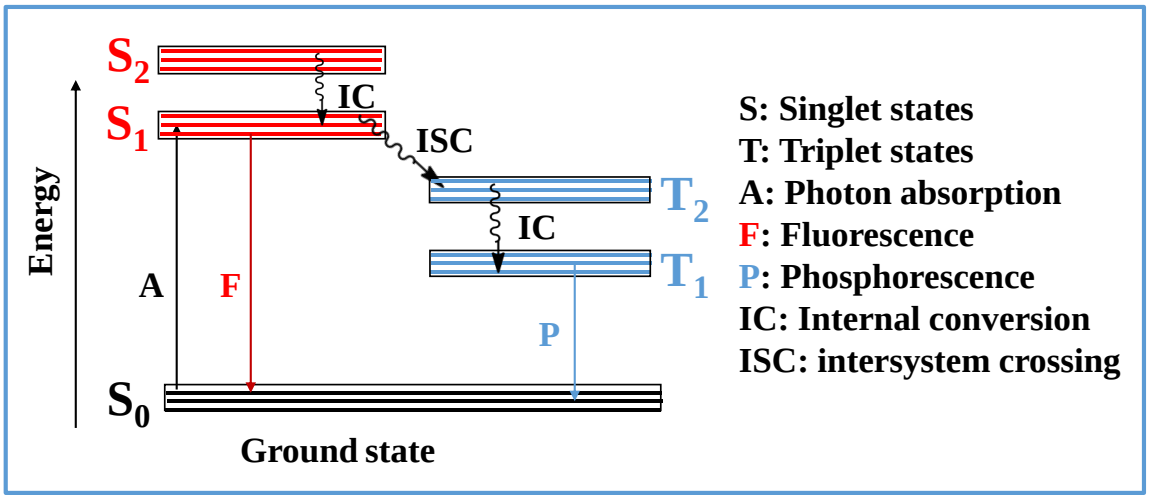

Figure 1.18. Jablonski diagram to differentiate between fluorescence and phosphorescence.

The luminescence properties can be characterized by several parameters such as luminescence spectra which defined as fluorescence intensity as a function of a wavelength. In addition, quantum yield, which gives the efficiency of the fluorescence process and is defined as the ratio of the number of emitted photons released in the process of fluorescence to the number of photons absorbed in the excitation process. Finally, lifetime, which refers to the average time the molecule stays in its excited state before emitting a photon and is determined as being inversely proportional to the sum rate constants of a radiative process and the nonradiative processes.[123]

CPs are very promising materials as photoluminescent materials where both the inorganic and the organic moieties can contribute to generate photoluminescence. Photoluminescence properties are dependent on the composition of the materials, the structure, and intermolecular packing that stabilized these materials. Currently, polynuclear d^{10} metal complexes have attracted considerable attention for their diverse structural and rich photoluminescence properties, even at ambient temperature, that give rise to potential applications as light-emitting diodes,[124-128] and as stimuli responsive materials[129-132]. One of the prominent classes of photoluminescent coordination compounds is the copper(I) halides[133, 129, 130, 134, 135, 43, 136] and pseudo-halide compounds[137-139]. The variety of available coordination numbers and the flexibility of halides coordination geometry (from terminal to μ^2- and up to μ^8- bridging modes), have introduced great structural diversity in copper(I) halides complexes.[140] Consequently, copper(I) halides can adapt various structural motifs including square Cu_2X_2 dimers,

cubane or stepped cubane Cu_4X_4 tetramers, zigzag $[CuX]_n$ chains, and double stranded $[Cu_2X_2]_n$ ladders (X = Cl, Br, or I anions, **Scheme 1.1**).[141, 142, 140] They are easily synthesized and tunable in emission color[133, 134, 143, 43, 136], with high emission quantum yields in the solid state[144-146]. From the economic point of view, copper is also more abundant, less expensive compared to noble metals and is less environmentally problematic than rare earth metals.[147]

In general, possible assignments for the excited states that are responsible for emission phenomena of Cu(I) complexes are ligand-centered (LC), $\pi \rightarrow \pi^*$ transitions and metal-center (MC). In addition, ligand-to-metal charge transfer (LMCT), transition involves the electronic transition from orbital of organic ligand to a metal-centered orbital, and metal-to-ligand charge-transfer transitions (MLCT), corresponds to the electronic transition from a metal centered orbital to an organic ligand orbital.[134, 148-152] In the presence of halides, Ford *et al*, have showed that the photoluminescent behavior and geometries of copper(I) halides aggregates are strictly related.[153-155, 136] Cu(I)-halides aggregates with tetranuclear complexes $\{Cu_4I_4L_4\}$ (L is substituted pyridine)[156-158] and rhombic $\{Cu_2(\mu\text{-}X)_2\}$ (X= halides) dimeric unit[159], are of special interest as they have been known to be emissive. Ford *et al*, studied the case of the $\{Cu_4I_4py_4\}$ (py is pyridine) cluster, where two distinct emission bands have been observed. High-energy band. (HE), dominating at low temperature 77 K, was attributed to halide-to-ligand charge transfer (XLCT) that may show up in the presence of unsaturated ligands with accessible π-orbitals.[160, 155] The low-energy band (LE), dominating at room temperature, has been assigned to an excited state known as cluster centered (CC) transitions which is mixture of halide-to-metal charge transfer (XMCT) and (d → s,p) metal centered character. The term 'metal cluster centered' was coined to emphasize that the transition is localized on the Cu_4I_4 cluster and is essentially independent of ligand. The Cu···Cu distance is a fundamental parameter to allow the presence of CC bands and must be shorter than the orbital interaction radius, estimated to be 2.8 Å.[161, 136]

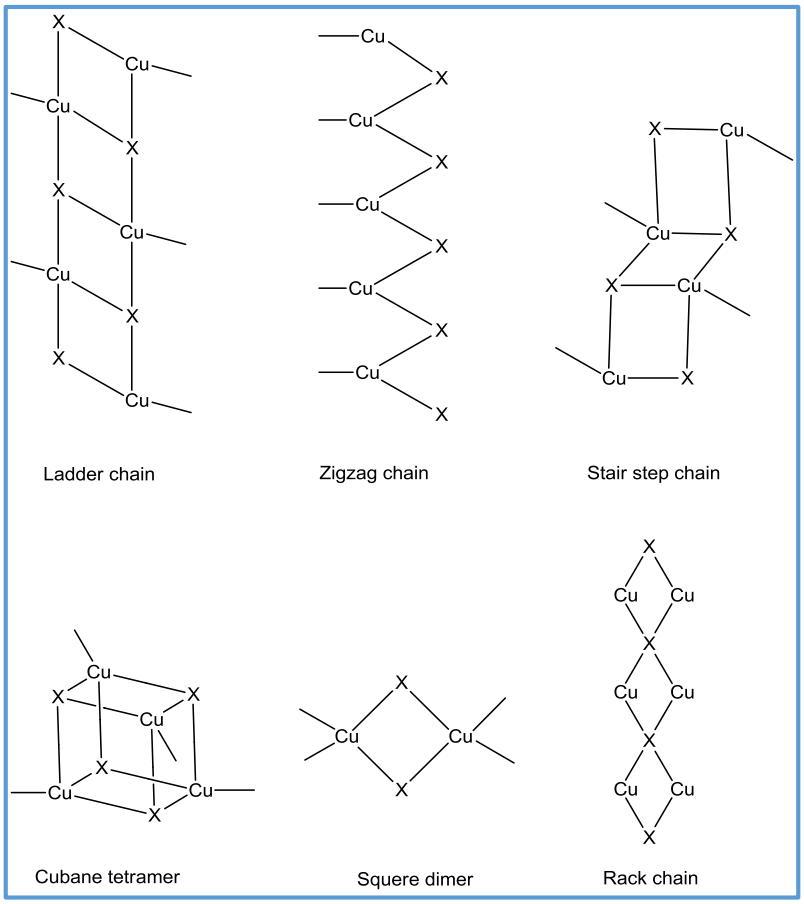

Scheme 1.1. Some coordination modes observed incopper (I) halides.

Table 1.2 Summarize of some reported double-stranded Cu(I) halides 1D-CPs and their photoluminescence properties.

Complexes	formula	$d_{Cu\cdots Cu}$ (Å)	λ_{em}/nm (298 K)	assigned to	Ref
1	$[CuI(L_1)]_n$	2.88	437	XLCT	154
2	$[CuBr(L_1)]_n$	2.91	509	XLCT	154
3	$[CuI(L_2)]_n$	2.80	454	XLCT	162
4	$[CuI(L_3)]_n$	2.89	612	XLCT	154

L_1 = pyridine (Py); L_2 = 3-methylpyridine (3-MePy); L_3 = 4-acetylpyridine (4-ActPy).

On the other hand, photoluminescence properties of polymeric "double-stranded staircase'' copper(I) halides CPs with N-containing ligands have been reported in only a few cases.[162, 153, 154, 143, 43, 136] **Table 1.2**, shows the photoluminescence assignments for a series of related, double-stranded staircase, 1D-CPs. According to **Table 1.2**, complexes **1** ($[CuI(Py)]_n$) and complex **2** ($[CuBr(Py)]_n$) adapt similar double-stranded chains with

different halide ion, I and Br anions for **1** and **2** respectively. The emissive properties have been assigned to XLCT. The emission of **2** ($[CuBr(Py)]_n$) is red shifted with respect to complex **1** ($[CuI(Py)]_n$) which doesn't follow the halides polarizability trend (I > Br). Additionally, the longer Cu···Cu distance, $d_{Cu\cdots Cu}$ of **2** > **1**, discard any contribution for CC that is very dependent on the Cu···Cu distance.[162, 154] By comparing the emissive properties of complexes **1** ($[CuI(Py)]_n$), **3** ($[CuI(3\text{-}MePy)]_n$), and **4** ($[CuI(4\text{-}ActPy)]_n$), all are structure related, one can observe that λ_{em} for **4** > **3** >**1**. The authors assumed that the electronic character of complex **4** was red shifted with respect for complexes **1** and **3** due to the electron-withdrawing effect of the acetyl group. In a recent study for the double-stranded staircase polymers with formula $[(CuX)_2L]_n$ (X = I, Br or Cl and L = pyrazine or pyrazine derivatives),[43] the authors attribute the emissive properties, in these families, to cluster centered transition, XMCT mixed with MC (copper 3d–4s). In addition, they demonstrated, using theoretical calculations, that the halides size and/or Cu–X distances play a key role in the emissive properties.

In general, the emission properties of copper(I) halides complexes are expected to assign for LMCT, MLCT, XLCT, XMCT and CC depending on the composition and the structure parameters.[154, 163, 143, 43, 164]

1.2.4. Coordination polymers as responsive materials.

Currently, the design of stimuli-responsive materials is attracting considerable interest in view of their potential applications as memories[57], or molecular sensors.[165, 166] Upon exposure the responsive materials to external stimuli (heat, light, mechanical force, remove or exchange of solvents and guest molecules, exposure to reactive vapors or more drastic by exchanging the metal ions or insertion of additional ligands), gives raise for drastic structural transformations.[167, 47] These transformations (may be attribute to new bond formation or breakage which results in a change of coordination number, geometry, dimensionality, etc.,) are often followed by changes in physical properties such as magnetism[53], luminescence[168, 166], and conductivity. Single-crystal X-ray crystallography is the principal technique to understand such structure dynamics.[48] A major source for these dynamic materials is provided by coordination polymers[57, 46, 50, 47], where they can be constructed as a result of the combination of metal ions or clusters, and organic ligands through by means of coordination bonds.

In the following paragraphs, we illustrated few interesting examples for CPs responsive materials that followed by structural modifications.

1.2.4.1. Electrical responsive coordination complexes.

Electrical responsive CPs are the materials that change their electrical state in function of external stimuli such as heat, light, electrical field, absorption of gases …etc.[169, 170]

Interesting example of electrical responsive materials has been reported by Peter McGrail1 *et al*. They have studied the electrical conductivity of one MOF formulated as Cu(TCNQ) (TCNQ is 5,7,7,8,8-tetracyanoquinodimethane). This MOF has been synthesized as two different polymorphs defined as phase **I** and phase **II** (**Figure 1.19**).[171] The electrical measurements, by two contact method, of Cu(TCNQ) phases have shown that these phases exhibiting significant difference in the charge transport properties, showing a value of 4.8×10^{-3} S cm^{-1} for phase **I** while phase **II** showed a conductivity value of 5.8×10^{-7} S cm^{-1}. Studying the electrical conductivity, on thin film, of the lower conductive phase (phase **II**) as a function of the applied electrical field (**Figure 1.20**) showed that there are an electrical switches, ongoing from less conducting phase to higher conducting phase, as the applied field increased. This process is completely reversible, the material came back to the lower conducting phase when the electrical field has been removed. X-ray powder diffraction studies have confirmed that the higher conducting phase is matching with the pattern of phase **I**. Surprisingly, this study showed that the structure transformation goes through intermediate phase, better conductor than phase **II** but less conductor than phase **I**, at lower applied potentials, 3 V (**Figure 1.19a**). The higher conducting phase (phase **II**) has been observed at higher applied potentials.[171] In fact, the authors attributed the large difference in conductivity between these two phases to structural aspect. Remarkable, the TCNQ molecules, in phase **I** network, come together to give a columnar stack with the closest distance being 3.24 Å as shown in **Figure 1.19**. In contrast, in phase **II**, the TCNQ rings are ‘‘slid’’ and no π stacking has taken place (closest distance is 6.8 Å).

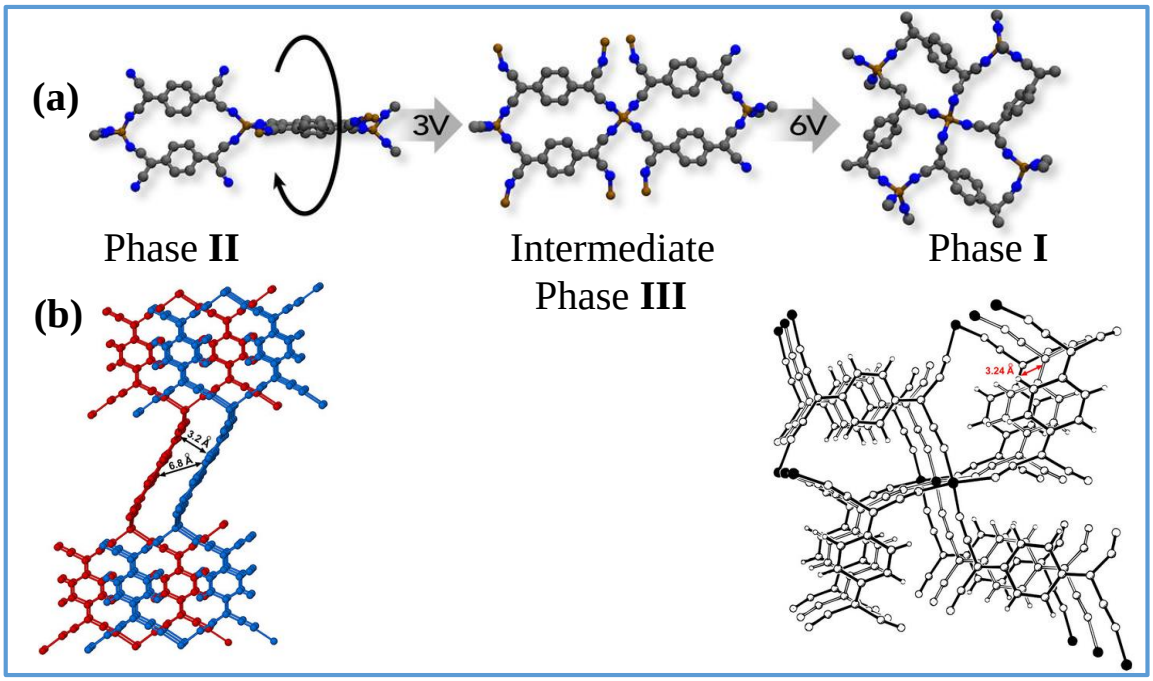

Figure 1.19. (a) Single crystal structure of Cu(TCNQ) state phase **II** (left), transitioning to a proposed new ‘‘on’’ state phase **III** (center) at 3 V followed by a transition to phase **I** at 6 V (right). (b) Interpenetrating networks in phase **II** (left) and phase **I** (right).[171]

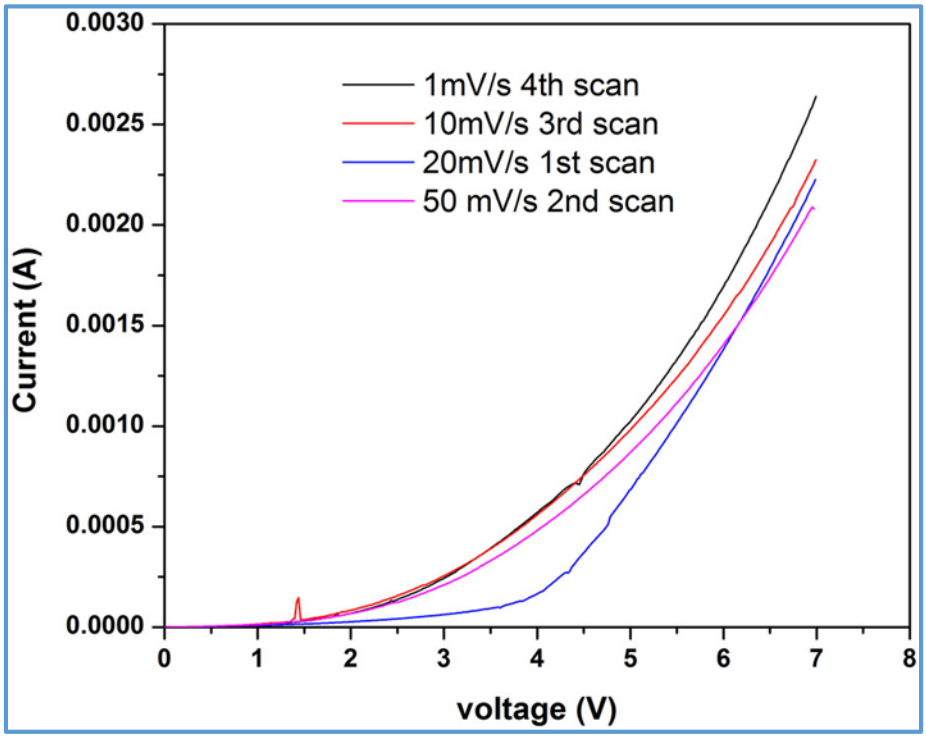

Figure 1.20. DC current-voltage plots showing bistable switching in a 10 μm-thick Cu-TCNQ (phase **II**) film placed between two electrodes in a sandwich structure. Each new scan was performed after a relaxation period of about a minute.[171]

1.2.4.2. Magnetic responsive coordination complexes.

The design of responsive magnetic materials has recently attracted considerable attention in the field of molecular magnetism.[57] In these systems, magnetic properties can be dramatically modified by the structural changes provoked by external chemical or physical stimuli such as guest molecules, temperature or pressure.[172, 79] Many examples of copper(II) carboxylates, based CPs, undergo for reversible or irreversible structural transformations in the presence of solvent molecules, temperature, and air.[79, 173, 49] The structural transformations of CPs containing paddle-wheel copper(II) carboxylates present particular interest due to these transformations are accompanied by properties modulations.[52, 174] Jean-Marc Vincent *et al*. presented a magnetic transformation, induced by humidity for fluorous copper(II) carboxylate complex formed as paddle-wheel structure and formulated as $[Cu_2(C_8F_{17}COO)_4(acetone)_2]$. By exposure the solid of complex $[Cu_2(C_8F_{17}COO)_4(acetone)_2]$ to air, a dramatic decrease of the exchange magnetic interaction within the dimer (strong antiferromagnetic) to hydrated form of complex $[Cu_2(C_8F_{17}COO)_4(acetone)_2]$, in which the copper(II) ions behave as magnetically isolated ions with small antiferromagnetic coupling, has been observed between the metal ions, $2J = -7\ cm^{-1}$, at room temperature (**Figure 1.21**). In addition, drastic changes of the spectroscopic properties (IR and EPR) have been observed.[175] The authors attributed these magnetic modifications to the change in the coordination mode of the carboxylates group. The authors proposed that the water molecules partially displaced the bridging carboxylates in the dimer units to afford a structure possessing both bridging and monodentate carboxylates to produce the hydrated form of $[Cu_2(C_8F_{17}COO)_4(acetone)_2]$ complex (**Figure 1.21**). The dehydration process (under argon gas) of the new hydrated form has led to partial recovery of the antiferromagnetic coupling between the copper(II) ions as revealed by EPR and magnetic susceptibility measurements (**Figure 1.21**).[53] These data show that the hydration/dehydration process isn't accompanied by a fully reversible structural rearrangement in the solid state as reported for other paddle wheel complexes.[52]

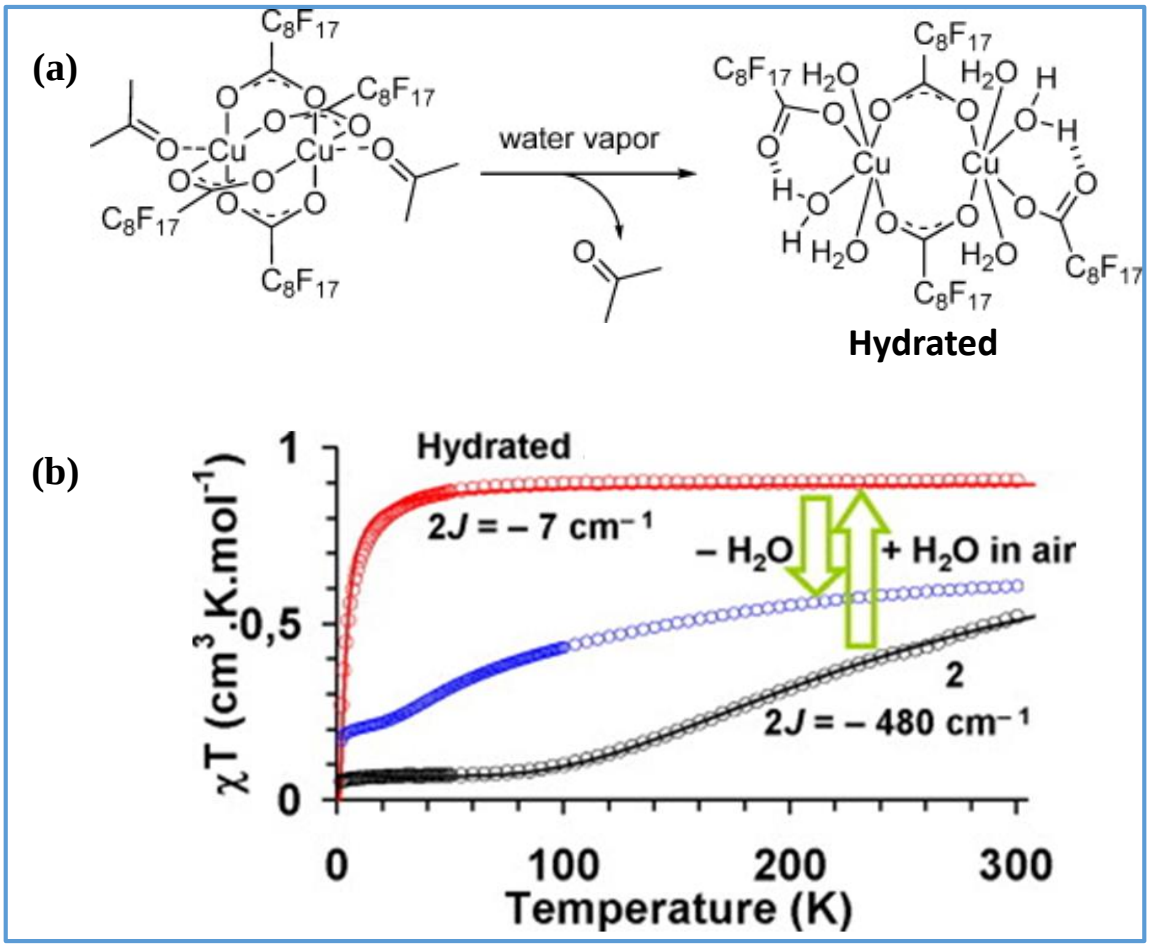

Figure 1.21. (a) Schematic representation for the expected structural rearrangement found in $[Cu_2(C_8F_{17}COO)_4(acetone)_2]$ after water vapor exposition. (b) Experimental magnetic susceptibilities plotted as χT versus T of crystals of $[Cu_2(C_8F_{17}COO)_4(acetone)_2]$. (black), the hydrated form obtained from powdered crystals of $[Cu_2(C_8F_{17}COO)_4(acetone)_2]$.exposed to the air for 24 h (red) and hydrated form that has been dehydrated under vacuum (blue).[53]

1.2.4.3. Photoluminescence responsive coordination complexes.

Photoluminescence responsive CPs are the materials that show switching in their photoluminescence properties upon exposure for external stimuli. In the literature, there are many examples where the photoluminescence properties can be switched by uptake external gas or vapors of volatile solvents which known as vapochromism.[131]

The terms thermochromism and mechanochromism were coined when the external force, responsible for switching the photoluminescence properties, are heat or mechanical forces respectively.[176] In fact, copper(I) halides have received huge attention as photoluminescent responsive materials owning their structure diversity, rich photophysical properties and adapt various geometry that can be attribute to the wide

range of their coordination numbers.[162, 134, 142, 140, 150] In a recent report, Tae *et al*. have presented a copper(I) iodide CPs that have shown dual responsive behaviors (vapochromism and thermochromism).[130] **Figure 1.22a**, presents the synthesis and crystal to crystal transformations of coordination polymers that involve Cu_4I_4 cluster bridged by organic ligand (L), L = 2-(tert-butyl-thio)-N-(pyridin-3-yl)acetamide. Upon exposure $[Cu_4I_4L_2]_n$ (defined as complex **2)** into CH_3CN (g), the CH_3CN molecules attacked the closed cubane Cu_4I_4 cluster to allow stair-step Cu_4I_4 clusters formation and gives raise to 1D, loop chain, structure formulated as $[Cu_4I_4L_2(CH_3CN)_2]_n$ (defined as complex **1)** (**Figure 1.22a**). This transformation has been followed by color change and blue shift in the photoluminescence emission spectra (**Figure 1.22a, c**). Additionally, upon exposure complex **1** ($[Cu_4I_4L_2(CH_3CN)_2]_n$) into MeOH (g), the stair-step Cu_4I_4 clusters came back to closed cubane Cu_4I_4 cluster in drastic structure change to provide 3D network of complex $\{[Cu_4I_4L_2]\cdot MeOH\}_n$ (defined as complex **3**), that is structurally analogous for complex **1** ($[Cu_4I_4L_2(CH_3CN)_2]_n$) but with MeOH molecules inside the pores of the network (**Figure 1.22a, c**). These transformations had been followed by color change and great red shift in the photoluminescence emission spectra of complex **1** ($[Cu_4I_4L_2(CH_3CN)_2]_n$). On the other hand, when solid samples of complexes **1** ($[Cu_4I_4L_2(CH_3CN)_2]_n$) and **3** ($\{[Cu_4I_4L_2]\cdot MeOH\}_n$) were heated at 130 ºC, structural transformations have been observed ongoing from complexes **1** or **3** to complex **2** and these transformations have been confirmed further by the photoluminescence study, (**Figure 1.22f, d**). This example strongly recommends photoluminescence responsive materials for applications such as chemical sensor for detecting and separating volatile harmful gases.[168, 177]

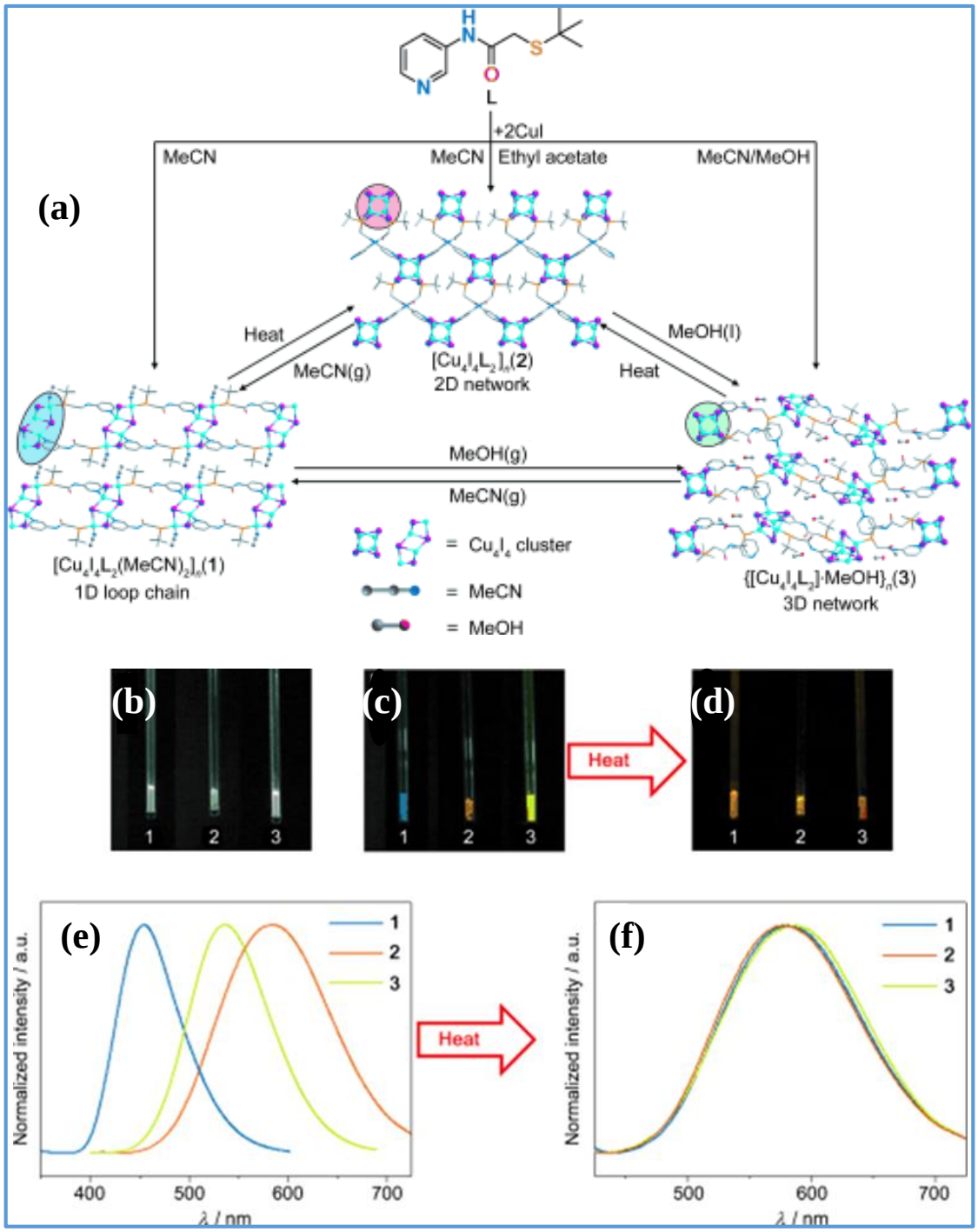

Figure 1.22. (a) Schematic representation for the preparation and crystal-to-crystal transformations of cubane and stairstep Cu_4I_4 clusters in CPs, formulated as $[Cu_4I_4L_2(CH_3CN)_2]_n$ (complex **1**), $[Cu_4I_4L_2]_n$ (complex **2**) and $\{[Cu_4I_4L_2]\cdot MeOH\}_n$ (complex **3**), by heat or solvent vapor. Photographs of complexes **1**–**3** before heating without (b) and with (c) UV irradiation, and with UV irradiation after heating (d). Photoluminescence spectra of polycrystalline complexes **1**–**3** before (e) and after (f) heating (λ_{ex}=350 nm).[130]

1.2.5. Coordination polymers as Nanomaterials and the potential applications of 1D-CPs in Nanotechnology.

The typical approaches to generate miniaturized systems in a controlled and repeatable way are 'top-down' and 'bottom-up' approaches.[178-181] The strategy of 'top-down' employs tools that mold, pattern, etch base materials to produce nanostructures with the desired geometry. This strategy facing many challenges such as complexity, size limitation around 10–15 nm, and high cost of clean rooms, operation and maintenance of the equipment.[182] On the other hand, the 'bottom-up' strategy takes the advantage of self-assemble processes of the atomic and molecular components into nanoscale structures by means of non-covalent interactions. This concept mimics the biological systems, for instance, the formation of the double helix in the deoxyribonucleic acid (DNA) molecules is made by the self-assemble of the DNA bases.

However the research efforts devoted to create CPs with novel properties, few examples of CPs nanostructures have been reported.[16, 183, 184, 68, 185-189] In that regard, miniaturization of CPs to the nanometer length scale is an area of growing interest to develop a new class of highly tailorable functional materials that maintain the classical characteristic of bulk CPs with the advantages of nanometer features. Nanoscale coordination polymers (NCPs) can be classified according to their dimensionality to: 0-D (particles)[190], 1-D (fibers, tubes, and rods)[185, 191, 192], 2-D (thin films and membranes),[193, 33] and 3D[194]. On the other hand, NCPs can be classified, based on their structural regularity, into amorphous and crystalline NCPs. Crystalline NCPs offer well understanding of their compositions, structures, and greatly facilitate the drawing of structure-property relationships in these class of nanomaterials. Indeed, many strategies have been reported to prepare crystalline NCPs by controlling the nucleation and growth of the building blocks through the self-assemble process, and their interactions at specific locations on surfaces.[183, 195, 191, 192, 188] Among these strategies, fast precipitation approach, where nanoparticles are insoluble in the solvent system whereas the individual precursors are soluble, is remarkable used for the synthesis of crystalline NCPs.[183, 185] In addition, hydrothermal synthesis and water-in-oil, or reverse, and microemulsions[196], (the micelles in the microemulsion act as "nanoreactors" that assist in controlling the kinetics of particle nucleation and growth), have been observed as powerful strategies to prepare crystalline NCPs.

There are several factors control the potential applications of the nanostructures meanly, the components, size, morphology, and the dimensionality. Huge efforts have been directed toward the development of new methods to control the formation of 1D-CPs nanostructures (1D-NCPs), such as wires, rods, tubes, and fibers, since they can play important roles in many applications, including electronics[191], optics[197], magnetic devices[198], sensor,[199, 200] and as template for functional species.[192]

In this thesis we explore the potential applications of 1D-NCPs in nanoelectronics as molecular wire. Thus, as we are planning to use biocompatible building blocks (see the objectives), we will highlight the possible biomedical applications of 1D-NCPs.

Studies of electrical conductivity in 1D-NCPs for nanoelectronics applications.

The development in the nanofabrications techniques gave rise to revolution in nanoelectronics industry by scaling down the electronic chips and electronic devices. The majority of nanotechnology interest is directed toward the precise organization of such nanostructures, of electronic chips or electronic devices, into more complex nano-architectures and devices. In order to fabricate electronic devices or integrated circuits in molecular scale, suitable technologies for establishing molecular electrical contacts (molecular wires), are required. Molecular wire candidates have to fit some requirements meanly, electronic properties, ease controllability of synthesis, and potential nanoscale self-organization (able to inter-connect and organize the individual electronic molecular components).[201, 202]

On the other hand, the field of CPs is rapidly grown due to the infinite tailorability that result from the infinite choice of building blocks and their potential applications cover broadly many fields including electronic applications.[106, 18, 61, 203, 12, 50, 204, 21, 32, 66]. Conductive nanofibers or single chain of 1D-CPs are of great importance for molecular electronics where they can act as molecular wires. The selected building blocks, metal centers and organic ligands, have to produce 1D-NCPs with two essential features, to be accessible for molecular electronics applications; (i) they have to possess electronic transport properties at nanometer scale, and (ii) they have to be able to participate in molecular recognitions processes at nanometer scale. In fact, the nanoprocessability of CPs, in general, has been limited by their poor solubility in common solvents and degradation upon heating.[12] As is essential to measure the electrical transport of an

individual chain of these 1D-NCPs, in order to test their potential applications for nanoelectronics. New methodologies have been developed to isolated single chains of 1D-NCPs on insulator substrate (**Figure 1.23**).[205, 206, 191, 187, 192, 188]. In that regard, few examples of 1D-NCPs have been tested as molecular wires.[207, 45, 68, 186, 208, 209]

Zamora *et al*, have been able to isolate nanoribbons of MMX 1D-CP, formulated as $[Pt_2I(dta)_4]_n$ (dta = dithioacetato), by direct sublimation of $[Pt_2I(dta)_4]_n$ crystals, under high vacuum conditions, on SiO_2 substrates (**Figure 1.24**).[189] This 1D-CP consists of Pt paddle wheel units, two Pt metals linked by four dithioacetate ligands that facilitate short Pt–Pt distances, and iodide ions acting as bridging ligands between the dimetallic subunits (**Figure 1.24a**). The electrical conductivity measurements of these nanoribbons, by means of conductance atomic force microscopy (CAFM), suggest an inherent metallic character (**Figure 1.24d**). These results and the conductivity founded in other MMX nanoribbons[45, 68] confirm that 1D-CPs nanostructures are very promising systems for applications in molecular electronics.

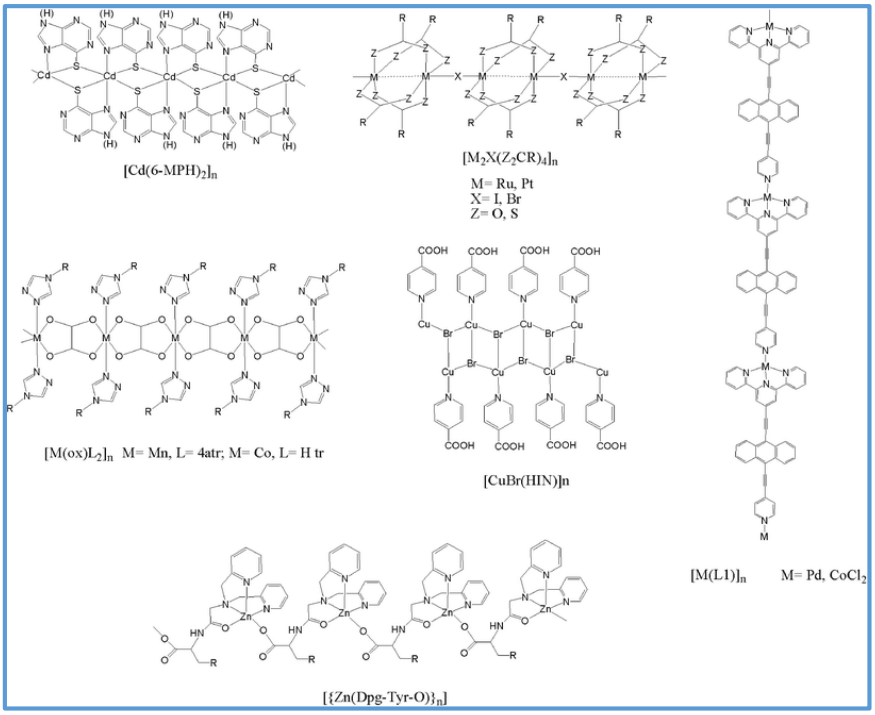

Figure 1.23. Summary of some selected inorganic systems studied as molecular wires.[191]

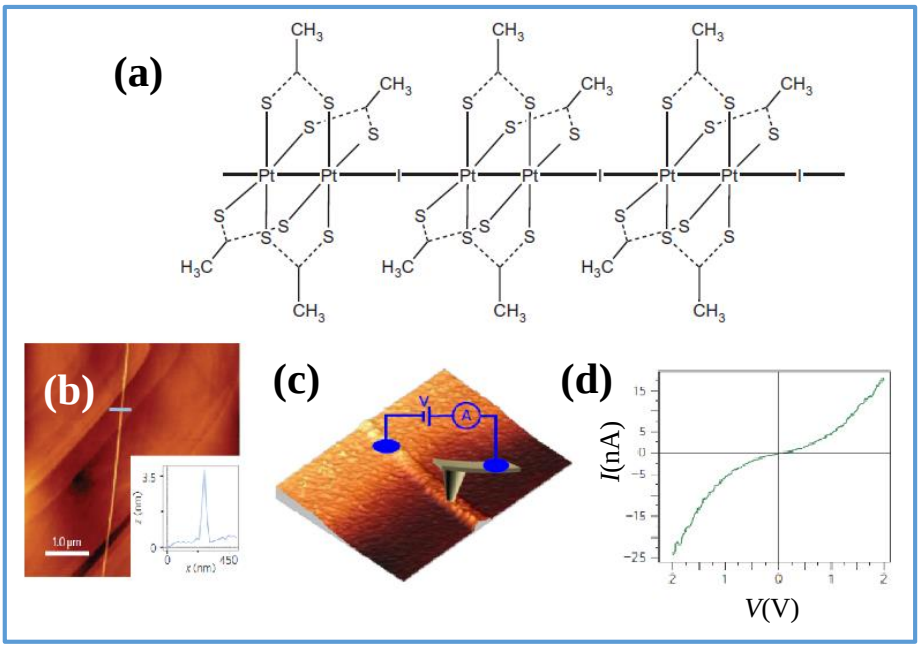

Figure 1.24. (a) Schematic representation of a single chain of $[Pt_2I(dta)_4]_n$. (b) AFM image of single nanoribbon on a highly ordered pyrolitic graphite surface directly sublimated from an MMX crystal. Inset,Height profile taken across one of the nanoribbons. (c) Scheme of the electronic circuit used to measure the current flowing through the nanoribbons. (d) Current versus voltage characteristic taken by contacting the nanoribbon 100 nm from the gold electrode.[189]

In an analogous system for MMX polymers, Paul Müller *et al*. have studied the electronic properties of single polymer strand of 1D-CP formulated as $[Cu_2(OAc)_4(trans\text{-}bie)]_n$ *trans*-bie (trans-bis(N-methylimidazol-2-yl)ethylene) is a conjugated N,N donor ligand.[210] This 1D-CP consists of paddle wheel units of copper(II) acetate and *trans*-bie acting as bridging ligands between the paddle wheel units (**Figure 1.25a**). The authors assume that such ligand (*trans*-bie) exhibit σ-donor, π-acceptor, and π-donor capacities, thus 1D MML-type CPs based on N,N donor ligands might exhibit promising physical properties related to the MMX systems. To separate single chain of this 1D-CP, acetonitrile dilute solution of $[Cu_2(OAc)_4(trans\text{-}bie)]_n$ 1D-CP was deposited on HOPG (highly ordered pyrolitic graphite surface (**Figure 1.25b**). STM/CITS (scanning tunneling microscopy/current imaging tunneling spectroscopy), have been used to characterize the electronic properties of single strand of this CP.[207] CITS is a scanning tunneling spectroscopy (STS) technique where an I-V curve is recorded at each pixel in the STM topographic map while maintaining a constant tip to surface distance. The current contrast changes significantly when, at certain bias voltages, new molecular energy levels come

into play. Therefore, these types of current imaging measurements allow spatially resolved energy spectroscopy

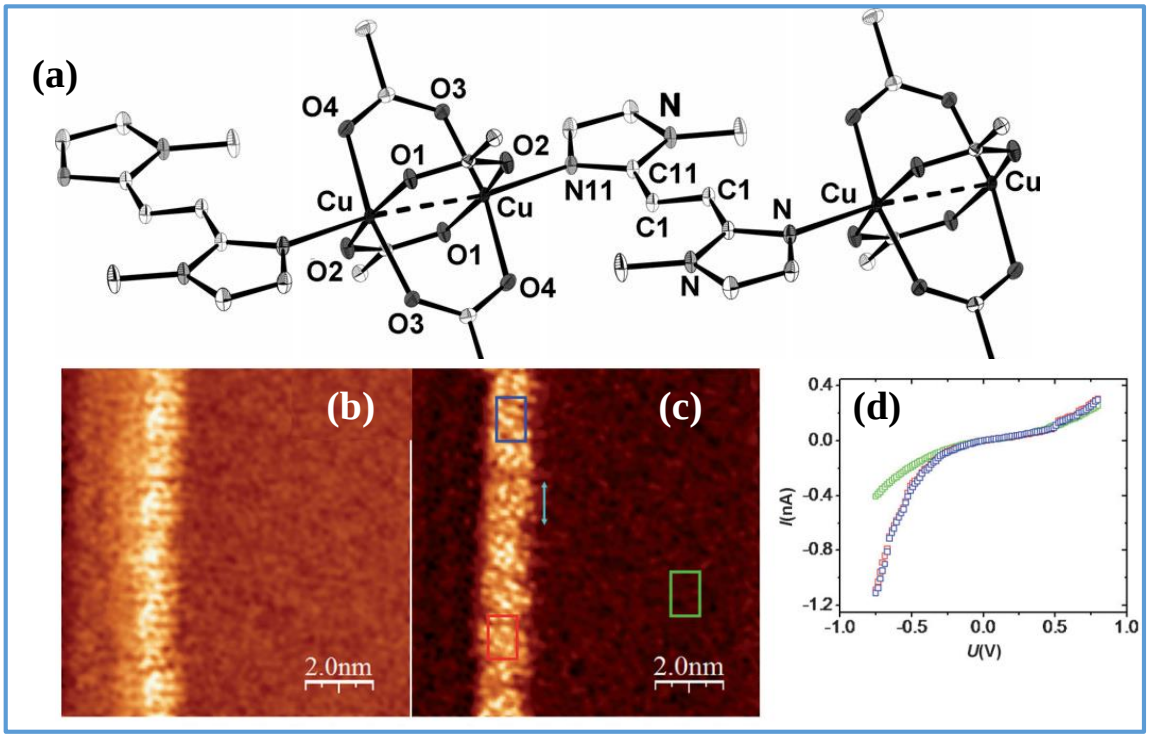

Figure 1.25. (a) Schematic representation of a single chain of $[Cu_2(OAc)_4(trans\text{-bie})]_n$. (b) and (c) STM topography and CITS current images for $Cu_2(OAc)_4(trans\text{-bie})]_n$ respectively (d) *I–V* characteristics recorded for $[Cu_2(OAc)_4(trans\text{-bie})]_n$, blue and red (polymer), and green (HOPG) regions.[210]

The authors used STM/CITS to measure *I-V* characteristics curve at three preset points from STM topograph (two along the 1D-CP, blue and red rectangular, and one point on the surface, green rectangular). The differential conductance (*dI*/*dV*) plots, calculated from the measured *I–V* measurements of the polymer and the graphite surface, are presented in **Figure 1.25d**. Three main peaks are observed approximately at -0.35, -0.55 and 0.50 V. The authors attributed these peaks to the HOMO, HOMO-1 and LUMO states and the distances between the peaks above and below 0 V define the HOMO–LUMO gap, which from these measurements, is roughly 0.8 eV. These results suggested a semiconducting behavior for single strand of $[Cu_2(OAc)_4(trans\text{-bie})]_n$.

Studies of 1D-NCPs for Bio-medical applications.

NCPs involving biomolecules (Bio-NCPs) are of great interest for nanobiological applications. Bio-NCPs present the typical structural features, as their bulk counterpart, including structural diversity and tunability, but also exhibit particle dimensions in the tens to hundreds of nanometers range, potential biocompatibility, and molecular recognition properties. Thus, the applications of Bio-NCPs were investigated in biomedical applications such as biosensor[211] and DNA delivery.[212] By this way, Li Wang *et al*, have prepared Bio-NCPs by combining (Tb^{+3}) as metal ion and adenine (Ade) as bridging ligand.[211] They demonstrated the utility of this Bio-NCP for detection of ciprofloxacin (CF) in tablet and urine samples. The Tb/Ade Bio-NCP exhibited no fluorescence emission while Tb/Ade/CF system shows fluorescence properties acquired from the fluorescence nature of CF molecule (**Figure 1.26**). These results strongly recommends the possible applications of Bio-NCP as biosensor and open the door for further investigation in the area of Bio-NCPs.

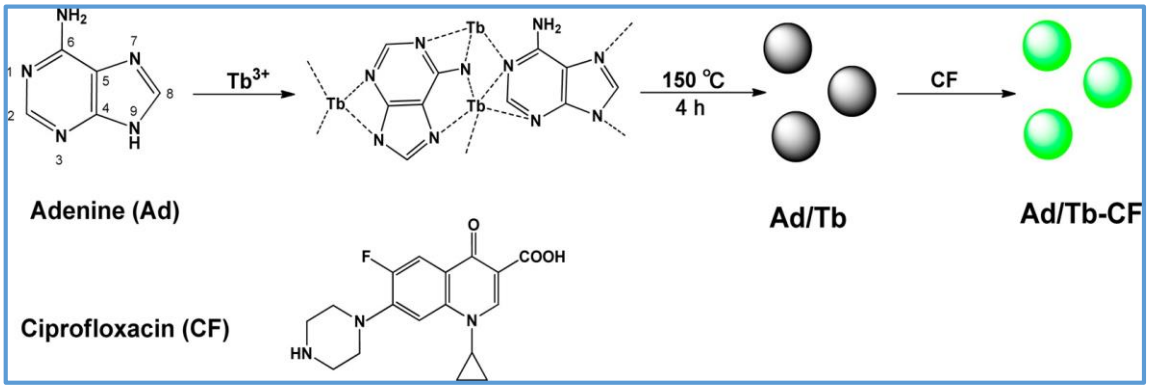

Figure 1.26. Schematic representation to illustrate the using of Tb/Ade Bio-NCP for CF detection.[211]

1.3. Thesis objectives

The objectives of the present PhD thesis are:

Design and synthesize 1D-CPs with molecular recognition capability, electronic and luminescent properties and explore their possible applications as Dynamic Materials and in nanotechnology.

To achieve these objectives, we have selected the starting building blocks to provide several features such as

- Molecular recognition capacity (coming from the organic ligands).
- Electronic and luminescent properties (coming from the metal centers and the organic ligands).

Based on these criteria, we have selected modified nucleobases, such as thymine-1-acetic acid and uracil-1-acetic acid. These biomolecules present rich molecular recognition capability (through H-bond interactions which are responsible for the well-known base pairing interactions of the DNA bases), and potential biocompatibility.

In addition, we have selected another class of ligands that can defined as pyridine derivative ligands known as 2-amino-5-nitropyridine (ANP), isonicotinic acid (HIN) and ethyl isonicotinate (EtIN). These ligands, beside that they are rich with several metal binding sites, they offer as well several functional groups available for H-bond interactions, the feature that can allow molecular recognitions processes.

Finally, we have selected some transition metals such as Cu(II), Cu(I), and Co(II) as metal ions. The combination of these metal ions with the selected organic ligands may produce 1D-CPs with molecular recognitions capacity and physical properties such as electrical conductivity, magnetism, and photoluminescence.

In that regard, the work of this thesis will divided into three dependent steps that can be summarized as following

1. **Synthesize and characterization of 1D-CPs as multifunctional and Dynamic Materials with molecular recognition capability.**

a. Synthesis and full structural characterization of the obtained coordination complexes using different techniques (IR, elemental analysis, mass spectroscopy, X-ray powder diffraction, and single crystals X-ray diffraction).
b. Study the physical properties of the obtained coordination complexes, such as electrical conductivity, magnetic, and optical properties, in macroscopic scale.
c. The flexibility and reversibility of coordination bond predict that the obtained complexes may show structural transformations as response for external stimuli. Thus, we are going to study the dynamic nature of the obtained complexes and study the changes in their properties followed by the structural transformations. These new materials can present potential applications as chemical sensors.

2. Develop strategies to prepare nanostructures, of the obtained coordination complexes, based on bottom-up approach. .

a. We are going to prepare nanostructures (nanofibers, nanoribbons, and/or nanotubes) of the obtained 1D-CPs using fast precipitation method by playing with the reaction parameters such as the concentration, pH, solvent, and/or temperature. In addition, the use of anti-solvent method to control 1D-NCPs growth can be an effective approach to control the size.[183]
b. We are going to characterize the obtained 1D-NCPs by X-ray powder diffraction technique to confirm their similarities with the bulk counterparts. In addition, we will study the size and morphology of these 1D-NCPs with field emission scanning electron microscopy (FESEM) and atomic force microscopy (AFM) techniques.

3. Exploit the molecular recognition capacity of the obtained nanostructures by the integration of our nanostructures in nanotechnology applications.

a. Once we obtain 1D-CPs with reasonable electrical conductivity value, we are going to separate single chains of these 1D-CPs on insulator surfaces and characterize their electrical behaviour by means of conductance atomic force

microscopy (CAFM) to test the electrical behaviour of single chains of these coordination polymers with the feasibility to use them as molecular wires.

b. Taking the advantage that our 1D-CPs contain free functional groups that can participate in molecular recognition processes (using meanly H-bond interactions), we aiming to explore the possible interaction of our 1D-NPCs with selected oligonucleotide sequences of DNA, exploiting the potential applications of our nanostructures for biomedical applications such as carrier for biomedical species.

References

1. O. R. Evans and W. Lin, **Crystal Engineering of NLO Materials Based on Metal−Organic Coordination Networks**, *Accounts of Chemical Research*, **2002**, 35, 511-522, http://dx.doi.org/10.1021/ar0001012.
2. S. Kitagawa and S. Noro, **Coordination Polymers: Infinite Systems**, *Comprehensive Coordination Chemistry II*, 2003, 231-261, http://dx.doi.org/10.1016/B0-08-043748-6/06192-2.
3. M. D. Allendorf and V. Stavila, **Crystal engineering, structure-function relationships, and the future of metal-organic frameworks**, *CrystEngComm*, **2015**, 17, 229-246, http://dx.doi.org/10.1039/C4CE01693A.
4. K. Biradha, **Crystal engineering: from weak hydrogen bonds to co-ordination bonds**, *CrystEngComm*, **2003**, 5, 374-384, http://dx.doi.org/10.1039/B309903B.
5. A. Mukherjee, S. Tothadi and G. R. Desiraju, **Halogen Bonds in Crystal Engineering: Like Hydrogen Bonds yet Different**, *Accounts of Chemical Research*, **2014**, 47, 2514-2524, http://dx.doi.org/10.1021/ar5001555.
6. S. Tothadi, P. Sanphui and G. R. Desiraju, **Obtaining Synthon Modularity in Ternary Cocrystals with Hydrogen Bonds and Halogen Bonds**, *Crystal Growth & Design*, **2014**, 14, 5293-5302, http://dx.doi.org/10.1021/cg501115k.
7. G. R. Desiraju, **A Bond by Any Other Name**, *Angewandte Chemie International Edition*, **2011**, 50, 52-59, http://dx.doi.org/10.1002/anie.201002960.
8. G. R. Desiraju and T. Steiner, *The Weak Hydrogen Bond: In Structural Chemistry and Biology*, Oxford University Press, 1999.
9. G. A. Jeffrey, *An Introduction to Hydrogen Bonding*, Oxford University Press, 1997.
10. C.-P. Li, J.-M. Wu and M. Du, **Exceptional Crystallization Diversity and Solid-State Conversions of CdII Coordination Frameworks with 5-Bromonicotinate Directed by Solvent Media**, *Chemistry – A European Journal*, **2012**, 18, 12437-12445, http://dx.doi.org/10.1002/chem.201200909.
11. A. J. Blake, G. Baum, N. R. Champness, S. S. M. Chung, P. A. Cooke, D. Fenske, A. N. Khlobystov, D. A. Lemenovskii, W.-S. Li and M. Schroder, **Long-range chain orientation in 1-D co-ordination polymers as a function of anions and intermolecular aromatic interactions**, *Journal of the Chemical Society, Dalton Transactions*, **2000**, 4285-4291, http://dx.doi.org/10.1039/B006202M.
12. C. Janiak, **Engineering coordination polymers towards applications**, *Dalton Transactions*, **2003**, 2781-2804, http://dx.doi.org/10.1039/B305705B.
13. E. Coronado, C. Giménez-Saiz and C. Martí-Gastaldo, in *Engineering of Crystalline Materials Properties*, eds. J. Novoa, D. Braga and L. Addadi, Springer Netherlands, 2008, 173-191, 10.1007/978-1-4020-6823-2_9.
14. J.-H. Yu, J.-Q. Xu, L. Ye, H. Ding, W.-J. Jing, T.-G. Wang, J.-N. Xu, H.-B. Jia, Z.-C. Mu and G.-D. Yang, **Hydrothermal synthesis and characterization of a copper(I) halide coordination polymer with isonicotinic acid (IN) ligand as a template possessing three-dimensional supramolecular network structure**,

Inorganic Chemistry Communications, **2002**, 5, 572-576, http://www.sciencedirect.com/science/article/pii/S1387700302004859.

15. J. Y. Lu and A. M. Babb, **An unprecedented interpenetrating structure with two covalently bonded open-frameworks of different dimensionality**, *Chemical Communications*, **2001**, 821-822, http://dx.doi.org/10.1039/B100634G.

16. P. Amo-Ochoa, L. Welte, R. Gonzalez-Prieto, P. J. Sanz Miguel, C. J. Gomez-Garcia, E. Mateo-Marti, S. Delgado, J. Gomez-Herrero and F. Zamora, **Single layers of a multifunctional laminar Cu(i,ii) coordination polymer**, *Chemical Communications*, **2010**, 46, 3262-3264, http://dx.doi.org/10.1039/B919647A.

17. W.-X. Zhang, P.-Q. Liao, R.-B. Lin, Y.-S. Wei, M.-H. Zeng and X.-M. Chen, **Metal cluster-based functional porous coordination polymers**, *Coordination Chemistry Reviews*, **2015**, 263-278, http://www.sciencedirect.com/science/article/pii/S0010854514003427.

18. M. Eddaoudi, D. B. Moler, H. Li, B. Chen, T. M. Reineke, M. O'Keeffe and O. M. Yaghi, **Modular Chemistry: Secondary Building Units as a Basis for the Design of Highly Porous and Robust Metal−Organic Carboxylate Frameworks**, *Accounts of Chemical Research*, **2001**, 34, 319-330, http://dx.doi.org/10.1021/ar000034b.

19. D. J. Tranchemontagne, J. L. Mendoza-Cortes, M. O'Keeffe and O. M. Yaghi, **Secondary building units, nets and bonding in the chemistry of metal-organic frameworks**, *Chemical Society Reviews*, **2009**, 38, 1257-1283, http://dx.doi.org/10.1039/B817735J.

20. K. Biradha, M. Sarkar and L. Rajput, **Crystal engineering of coordination polymers using 4,4[prime or minute]-bipyridine as a bond between transition metal atoms**, *Chemical Communications*, **2006**, 4169-4179, http://dx.doi.org/10.1039/B606184B.

21. W. Lu, Z. Wei, Z.-Y. Gu, T.-F. Liu, J. Park, J. Park, J. Tian, M. Zhang, Q. Zhang, T. Gentle Iii, M. Bosch and H.-C. Zhou, **Tuning the structure and function of metal-organic frameworks via linker design**, *Chemical Society Reviews*, **2014**, 43, 5561-5593, http://dx.doi.org/10.1039/C4CS00003J.

22. A. Gallego, O. Castillo, C. J. Gómez-García, F. l. Zamora and S. Delgado, **Electrical conductivity and luminescence in coordination polymers based on copper (I)-halides and sulfur-pyrimidine ligands**, *Inorganic Chemistry*, **2011**, 51, 718-727, DOI: 10.1021/ic202255w.

23. I. Imaz, M. Rubio-Martinez, J. An, I. Sole-Font, N. L. Rosi and D. Maspoch, **Metal-biomolecule frameworks (MBioFs)**, *Chemical Communications*, **2011**, 47, 7287-7302, http://dx.doi.org/10.1039/C1CC11202C.

24. P. Amo-Ochoa and F. Zamora, **Coordination polymers with nucleobases: From structural aspects to potential applications**, *Coordination Chemistry Reviews*, **2014**, 276, 34-58, http://www.sciencedirect.com/science/article/pii/S0010854514001593.

25. G. Beobide, O. Castillo, J. Cepeda, A. Luque, S. Pérez-Yáñez, P. Román and J. Thomas-Gipson, **Metal–carboxylato–nucleobase systems: From supramolecular assemblies to 3D porous materials**, *Coordination Chemistry*

Reviews, **2013**, 257, 2716-2736, http://www.sciencedirect.com/science/article/pii/S0010854513000659.

26. P. Amo-Ochoa, S. S. Alexandre, S. Hribesh, M. A. Galindo, O. Castillo, C. J. Gómez-García, A. R. Pike, J. M. Soler, A. Houlton and F. Zamora, **Coordination Chemistry of 6-Thioguanine Derivatives with Cobalt: Toward Formation of Electrical Conductive One-Dimensional Coordination Polymers**, *Inorganic Chemistry*, **2013**, 52, 5290-5299, http://dx.doi.org/10.1021/ic400237h.

27. P. Amo-Ochoa, O. Castillo, S. S. Alexandre, L. Welte, P. J. de Pablo, M. I. Rodríguez-Tapiador, J. Gómez-Herrero and F. Zamora, **Synthesis of Designed Conductive One-Dimensional Coordination Polymers of Ni(II) with 6-Mercaptopurine and 6-Thioguanine**, *Inorganic Chemistry*, **2009**, 48, 7931-7936, http://dx.doi.org/10.1021/ic900896w.

28. B. Lippert, **Multiplicity of metal ion binding patterns to nucleobases**, *Coordination Chemistry Reviews*, **2000**, 200–202, 487-516, http://www.sciencedirect.com/science/article/pii/S0010854500002605.

29. S. Sivakova and S. J. Rowan, **Nucleobases as supramolecular motifs**, *Chemical Society Reviews*, **2005**, 34, 9-21, http://dx.doi.org/10.1039/B304608G.

30. S. Verma, A. K. Mishra and J. Kumar, **The Many Facets of Adenine: Coordination, Crystal Patterns, and Catalysis**, *Accounts of Chemical Research*, **2010**, 43, 79-91, http://dx.doi.org/10.1021/ar9001334.

31. C.-P. Li and M. Du, **Role of solvents in coordination supramolecular systems**, *Chemical Communications*, **2011**, 47, 5958-5972, http://dx.doi.org/10.1039/C1CC10935A.

32. S.-i. Noro, S. Kitagawa, T. Akutagawa and T. Nakamura, **Coordination polymers constructed from transition metal ions and organic N-containing heterocyclic ligands: Crystal structures and microporous properties**, *Progress in Polymer Science*, **2009**, 34, 240-279, http://www.sciencedirect.com/science/article/pii/S0079670008000981.

33. A. Gallego, C. Hermosa, O. Castillo, I. Berlanga, C. J. Gómez-García, E. Mateo-Martí, J. I. Martínez, F. Flores, C. Gómez-Navarro, J. Gómez-Herrero, S. Delgado and F. Zamora, **Solvent-Induced Delamination of a Multifunctional Two Dimensional Coordination Polymer**, *Advanced Materials*, **2013**, 25, 2141-2146, http://dx.doi.org/10.1002/adma.201204676.

34. B. Spingler, S. Schnidrig, T. Todorova and F. Wild, **Some thoughts about the single crystal growth of small molecules**, *CrystEngComm*, **2012**, 14, 751-757, http://dx.doi.org/10.1039/C1CE05624G.

35. W.-W. Zhou, W. Zhao, X. Zhao, F.-W. Wang and B. Wei, **A New 1-D Cu(I) Pyridinate Complex [CuBr(anp)] n (anp = 2-amino-5-nitropyridine)**, *Synthesis and Reactivity in Inorganic, Metal-Organic, and Nano-Metal Chemistry*, **2013**, 43, 1171-1174, http://dx.doi.org/10.1080/15533174.2012.756899.

36. B. Moulton and M. J. Zaworotko, **From Molecules to Crystal Engineering: Supramolecular Isomerism and Polymorphism in Network Solids**, *Chemical Reviews*, **2001**, 101, 1629-1658, http://dx.doi.org/10.1021/cr9900432.

37. R. A. Heintz, H. Zhao, X. Ouyang, G. Grandinetti, J. Cowen and K. R. Dunbar, **New Insight into the Nature of Cu(TCNQ): Solution Routes to Two Distinct Polymorphs and Their Relationship to Crystalline Films That Display Bistable Switching Behavior**, *Inorganic Chemistry*, **1999**, 38, 144-156, http://dx.doi.org/10.1021/ic9812095.

38. J. Tao, R.-J. Wei, R.-B. Huang and L.-S. Zheng, **Polymorphism in spin-crossover systems**, *Chemical Society Reviews*, **2012**, 41, 703-737, http://dx.doi.org/10.1039/C1CS15136C.

39. G. Zhang, **Polymorphism in unusual one-dimensional coordination polymers based on cadmium(ii) and 2-mercaptopyridine N-oxide**, *CrystEngComm*, **2013**, 15, 6453-6456, http://dx.doi.org/10.1039/C3CE40808F.

40. W. L. Leong and J. J. Vittal, **One-Dimensional Coordination Polymers: Complexity and Diversity in Structures, Properties, and Applications**, *Chemical Reviews*, **2010**, 111, 688-764, http://dx.doi.org/10.1021/cr100160e.

41. A. Calzolari, S. S. Alexandre, F. Zamora and R. Di Felice, **Metallicity in Individual MMX Chains**, *Journal of the American Chemical Society*, **2008**, 130, 5552-5562, http://dx.doi.org/10.1021/ja800358c.

42. C.-T. Chen and K. S. Suslick, **One-dimensional coordination polymers: Applications to material science**, *Coordination Chemistry Reviews*, **1993**, 128, 293-322, http://www.sciencedirect.com/science/article/pii/0010854593800365.

43. J. Pospisil, I. Jess, C. Nather, M. Necas and P. Taborsky, **Luminescence properties of "double-stranded staircase" copper(i) halide coordination polymers with N-containing ligands**, *New Journal of Chemistry*, **2011**, 35, 861-864, http://dx.doi.org/10.1039/C0NJ00809E.

44. W. Xue, B.-Y. Wang, J. Zhu, W.-X. Zhang, Y.-B. Zhang, H.-X. Zhao and X.-M. Chen, **A one-dimensional coordination polymer exhibiting simultaneous spin-crossover and semiconductor behaviour**, *Chemical Communications*, **2011**, 47, 10233-10235, http://dx.doi.org/10.1039/C1CC12852C.

45. D. Gentili, G. Givaja, R. Mas-Balleste, M.-R. Azani, A. Shehu, F. Leonardi, E. Mateo-Marti, P. Greco, F. Zamora and M. Cavallini, **Patterned conductive nanostructures from reversible self-assembly of 1D coordination polymer**, *Chemical Science*, **2012**, 3, 2047-2051, http://dx.doi.org/10.1039/C2SC00029F.

46. S. Horike, S. Shimomura and S. Kitagawa, **Soft porous crystals**, *Nat Chem*, **2009**, 1, 695-704, http://dx.doi.org/10.1038/nchem.444.

47. G. K. Kole and J. J. Vittal, **Solid-state reactivity and structural transformations involving coordination polymers**, *Chemical Society Reviews*, **2013**, 42, 1755-1775, http://dx.doi.org/10.1039/C2CS35234F.

48. J.-P. Zhang, P.-Q. Liao, H.-L. Zhou, R.-B. Lin and X.-M. Chen, **Single-crystal X-ray diffraction studies on structural transformations of porous coordination polymers**, *Chemical Society Reviews*, **2014**, 43, 5789-5814, http://dx.doi.org/10.1039/C4CS00129J.

49. N. Zhao, F. Sun, H. He, J. Jia and G. Zhu, **Solvent-Induced Single Crystal To Single Crystal Transformation and Complete Metal Exchange of a Pyrene-Based Metal–Organic Framework**, *Crystal Growth & Design*, **2014**, 14, 1738-1743, http://dx.doi.org/10.1021/cg401887b.

50. S. Kitagawa, R. Kitaura and S.-i. Noro, **Functional Porous Coordination Polymers**, *Angewandte Chemie International Edition*, **2004**, 43, 2334-2375, http://dx.doi.org/10.1002/anie.200300610.

51. A. Schneemann, V. Bon, I. Schwedler, I. Senkovska, S. Kaskel and R. A. Fischer, **Flexible metal-organic frameworks**, *Chemical Society Reviews*, **2014**, 43, 6062-6096, http://dx.doi.org/10.1039/C4CS00101J.

52. M. Du, C.-P. Li, J.-M. Wu, J.-H. Guo and G.-C. Wang, **Destruction and reconstruction of the robust [Cu2(OOCR)4] unit during crystal structure transformations between two coordination polymers**, *Chemical Communications*, **2011**, 47, 8088-8090, http://dx.doi.org/10.1039/C1CC12184G.

53. A. Motreff, R. Correa da Costa, H. Allouchi, M. Duttine, C. Mathonière, C. Duboc and J.-M. Vincent, **A fluorous copper(II)–carboxylate complex which magnetically and reversibly responds to humidity in the solid state**, *Journal of Fluorine Chemistry*, **2012**, 134, 49-55, http://www.sciencedirect.com/science/article/pii/S0022113911000522.

54. H. Iguchi, S. Kitao, M. Seto, S. Takaishi and M. Yamashita, **Predominance of covalency in water-vapor-responsive MMX-type chain complexes revealed by 129I Mossbauer spectroscopy**, *Dalton Transactions*, **2014**, 43, 8767-8773, http://dx.doi.org/10.1039/C4DT00627E.

55. H. Iguchi, S. Takaishi, H. Miyasaka, M. Yamashita, H. Matsuzaki, H. Okamoto, H. Tanaka and S.-i. Kuroda, **Water-Vapor-Induced Reversible Switching of Electronic States in an MMX-Type Chain Complex with Retention of Single Crystallinity**, *Angewandte Chemie International Edition*, **2010**, 49, 552-555, http://dx.doi.org/10.1002/anie.200905608.

56. A. A. Talin, A. Centrone, A. C. Ford, M. E. Foster, V. Stavila, P. Haney, R. A. Kinney, V. Szalai, F. El Gabaly, H. P. Yoon, F. Léonard and M. D. Allendorf, **Tunable Electrical Conductivity in Metal-Organic Framework Thin-Film Devices**, *Science*, **2014**, 343, 66-69, http://www.sciencemag.org/content/343/6166/66.abstract.

57. E. Coronado and G. Minguez Espallargas, **Dynamic magnetic MOFs**, *Chemical Society Reviews*, **2013**, 42, 1525-1539, http://dx.doi.org/10.1039/C2CS35278H.

58. X.-C. Shan, F.-L. Jiang, L. Chen, M.-Y. Wu, J. Pan, X.-Y. Wan and M.-C. Hong, **Using cuprophilicity as a multi-responsive chromophore switching color in response to temperature, mechanical force and solvent vapors**, *Journal of Materials Chemistry C*, **2013**, 1, 4339-4349, http://dx.doi.org/10.1039/C3TC30482E.

59. J. Canivet, A. Fateeva, Y. Guo, B. Coasne and D. Farrusseng, **Water adsorption in MOFs: fundamentals and applications**, *Chemical Society Reviews*, **2014**, 43, 5594-5617, http://dx.doi.org/10.1039/C4CS00078A.

60. Y. Cui, Y. Yue, G. Qian and B. Chen, **Luminescent Functional Metal–Organic Frameworks**, *Chemical Reviews*, **2011**, 112, 1126-1162, http://dx.doi.org/10.1021/cr200101d.

61. P. Falcaro, R. Ricco, C. M. Doherty, K. Liang, A. J. Hill and M. J. Styles, **MOF positioning technology and device fabrication**, *Chemical Society Reviews*, **2014**, 43, 5513-5560, http://dx.doi.org/10.1039/C4CS00089G.

62. G. Givaja, P. Amo-Ochoa, C. J. Gómez-Garcia and F. Zamora, **Electrical conductive coordination polymers**, *Chemical Society Reviews*, **2012**, 41, 115-147, http://dx.doi.org/10.1039/C1CS15092H.

63. J. Gómez-Herrero and F. Zamora, **Coordination Polymers for Nanoelectronics**, *Advanced Materials*, **2011**, 23, 5311-5317, http://dx.doi.org/10.1002/adma.201101952.

64. S. L. James, **Metal-organic frameworks**, *Chemical Society Reviews*, **2003**, 32, 276-288, http://dx.doi.org/10.1039/B200393G.

65. S. Qiu, M. Xue and G. Zhu, **Metal-organic framework membranes: from synthesis to separation application**, *Chemical Society Reviews*, **2014**, 43, 6116-6140, http://dx.doi.org/10.1039/C4CS00159A.

66. V. Stavila, A. A. Talin and M. D. Allendorf, **MOF-based electronic and opto-electronic devices**, *Chemical Society Reviews*, **2014**, 43, 5994-6010, http://dx.doi.org/10.1039/C4CS00096J.

67. S. Tominaka, S. Henke and A. K. Cheetham, **Coordination polymers of alkali metal trithiocyanurates: structure determinations and ionic conductivity measurements using single crystals**, *CrystEngComm*, **2013**, 15, 9400-9407, http://dx.doi.org/10.1039/C3CE41150H.

68. A. Guijarro, O. Castillo, L. Welte, A. Calzolari, P. J. S. Miguel, C. J. Gómez-García, D. Olea, R. di Felice, J. Gómez-Herrero and F. Zamora, **Conductive Nanostructures of MMX Chains**, *Advanced Functional Materials*, **2010**, 20, 1451-1457, http://dx.doi.org/10.1002/adfm.200901901.

69. S. Sanda, S. Biswas and S. Konar, **Study of Proton Conductivity of a 2D Flexible MOF and a 1D Coordination Polymer at Higher Temperature**, *Inorganic Chemistry*, **2015**, 54, 1218-1222, http://dx.doi.org/10.1021/ic502098h.

70. D. A. Neamen, *An introduction to semiconductor devices*, McGraw-hill New York, 2006.

71. S. S. Alexandre, J. M. Soler, P. J. Sanz Miguel, R. W. Nunes, F. Yndurain, J. Gómez-Herrero and F. Zamora, **Design of molecular wires based on one-dimensional coordination polymers**, *Applied Physics Letters*, **2007**, 90, 193107, http://scitation.aip.org/content/aip/journal/apl/90/19/10.1063/1.2737371.

72. M. A. Castro, A. E. Roitberg and F. D. Cukiernik, **Electronic Delocalization in Coordination Polymers Based on Bimetallic Carboxylates**, *Journal of Chemical Theory and Computation*, **2013**, 9, 2609-2616, http://dx.doi.org/10.1021/ct400179t.

73. M. R. Bryce, **Recent progress on conducting organic charge-transfer salts**, *Chemical Society Reviews*, **1991**, 20, 355-390, http://dx.doi.org/10.1039/CS9912000355.

74. S. Delgado, P. J. Sanz Miguel, J. L. Priego, R. Jiménez-Aparicio, C. J. Gómez-García and F. Zamora, **A Conducting Coordination Polymer Based on Assembled Cu9 Cages**, *Inorganic Chemistry*, **2008**, 47, 9128-9130, http://dx.doi.org/10.1021/ic801314s.

75. P. Lin, R. A. Henderson, R. W. Harrington, W. Clegg, C.-D. Wu and X.-T. Wu, **New 1- and 2-Dimensional Polymeric Structures of Cyanopyridine**

Complexes of AgI and CuI, *Inorganic Chemistry*, **2004**, 43, 181-188, http://dx.doi.org/10.1021/ic030254w.

76. S. Durot, C. Policar, G. Pelosi, F. Bisceglie, T. Mallah and J.-P. Mahy, **Structural and Magnetic Properties of Carboxylato-Bridged Manganese(II) Complexes Involving Tetradentate Ligands: Discrete Complex and 1D Polymers. Dependence of J on the Nature of the Carboxylato Bridge**, *Inorganic Chemistry*, **2003**, 42, 8072-8080, http://dx.doi.org/10.1021/ic026130l.

77. S. Khullar and S. K. Mandal, **Effect of Spacer Atoms in the Dicarboxylate Linkers on the Formation of Coordination Architectures—Molecular Rectangles vs 1D Coordination Polymers: Synthesis, Crystal Structures, Vapor/Gas Adsorption Studies, and Magnetic Properties**, *Crystal Growth & Design*, **2014**, 14, 6433-6444, http://dx.doi.org/10.1021/cg501284y.

78. M. Kurmoo, **Magnetic metal-organic frameworks**, *Chemical Society Reviews*, **2009**, 38, 1353-1379, http://dx.doi.org/10.1039/B804757J.

79. Q.-Q. Li, C.-Y. Ren, Y.-Y. Huang, J.-L. Li, P. Liu, B. Liu, Y. Liu and Y.-Y. Wang, **Thermally Triggered Solid-State Single-Crystal-to-Single-Crystal Structural Transformation Accompanies Property Changes**, *Chemistry – A European Journal*, **2015**, 21, 4703-4711, http://dx.doi.org/10.1002/chem.201405984.

80. E. Pardo, R. Ruiz-Garcia, J. Cano, X. Ottenwaelder, R. Lescouezec, Y. Journaux, F. Lloret and M. Julve, **Ligand design for multidimensional magnetic materials: a metallosupramolecular perspective**, *Dalton Transactions*, **2008**, 10.1039/b801222a, 2780-2805, http://dx.doi.org/10.1039/B801222A.

81. B. Shen, P.-F. Shi, Y.-L. Hou, F.-F. Wan, D.-L. Gao and B. Zhao, **Structural diversity and magnetic properties of five copper-organic frameworks containing one-, two-, and three-types of organic ligands**, *Dalton Transactions*, **2013**, 42, 3455-3463, http://dx.doi.org/10.1039/C2DT32515B.

82. J. Suárez-Varela, A. J. Mota, H. Aouryaghal, J. Cano, A. Rodríguez-Diéguez, D. Luneau and E. Colacio, **Anion Influence on the Structure and Magnetic Properties of a Series of Multidimensional Pyrimidine-2-carboxylato-Bridged Copper(II) Complexes**, *Inorganic Chemistry*, **2008**, 47, 8143-8158, http://dx.doi.org/10.1021/ic800625w.

83. C. Biswas, P. Mukherjee, M. G. B. Drew, C. J. Gómez-García, J. M. Clemente-Juan and A. Ghosh, **Anion-Directed Synthesis of Metal−Organic Frameworks Based on 2-Picolinate Cu(II) Complexes: A Ferromagnetic Alternating Chain and Two Unprecedented Ferromagnetic Fish Backbone Chains**, *Inorganic Chemistry*, **2007**, 46, 10771-10780, http://dx.doi.org/10.1021/ic701440x.

84. F. S. Delgado, C. A. Jiménez, P. Lorenzo-Luis, J. Pasán, O. Fabelo, L. Cañadillas-Delgado, F. Lloret, M. Julve and C. Ruiz-Pérez, **Novel Malonate-Containing Coordination Compounds with Ligands Having N- and NO-Donors: Synthesis, Structures, and Magnetic Properties**, *Crystal Growth & Design*, **2012**, 12, 599-614, http://dx.doi.org/10.1021/cg200675u.

85. L. Zhang, L. Liu, C. Huang, X. Han, L. a. Guo, H. Xu, H. Hou and Y. Fan, **Polynuclear Ni(II)/Co(II)/Mn(II) Complexes Based on Terphenyl–Tetracarboxylic Acid Ligand: Crystal Structures and Research of Magnetic**

Properties, *Crystal Growth & Design*, **2015**, 15, 3426-3434, http://dx.doi.org/10.1021/acs.cgd.5b00504.

86. P.-F. Zhuang, T. Liu, X.-H. Xie, C. He and C.-Y. Duan, **A cyano-bridged tubular coordination polymer with dominant ferromagnetic interactions**, *Dalton Transactions*, **2015**, 44, 464-467, http://dx.doi.org/10.1039/C4DT02056A.

87. M. Fontanet, A.-R. Popescu, X. Fontrodona, M. Rodríguez, I. Romero, F. Teixidor, C. Viñas, N. Aliaga-Alcalde and E. Ruiz, **Design of Dinuclear Copper Species with Carboranylcarboxylate Ligands: Study of Their Steric and Electronic Effects**, *Chemistry – A European Journal*, **2011**, 17, 13217-13229, http://dx.doi.org/10.1002/chem.201101929.

88. H. Li, H. Yao, E. Zhang, Y. Jia, H. Hou and Y. Fan, **Crystal structures and magnetism of infinite alternating chains arranged by paddle-wheel dinuclear copper and mononuclear copper units**, *Dalton Transactions*, **2011**, 40, 9388-9393, http://dx.doi.org/10.1039/C1DT10822K.

89. J. Moncol, M. Korabik, P. Segl'a, M. Koman, D. Mikloš, J. Jašková, T. Glowiak, M. Melník, J. Mrozinski and M. R. Sundberg, **Preparation, Structure, Spectral, and Magnetic Properties of Copper(II) Halogenonicotinates: Crystal and Molecular Structure of Tetrakis(μ-2-chloronicotinato-O,O′)-diaquadicopper(II)**, *Zeitschrift für anorganische und allgemeine Chemie*, **2007**, 633, 298-305, http://dx.doi.org/10.1002/zaac.200600183.

90. D. L. Reger, A. Debreczeni, M. D. Smith, J. Jezierska and A. Ozarowski, **Copper(II) Carboxylate Dimers Prepared from Ligands Designed to Form a Robust π···π Stacking Synthon: Supramolecular Structures and Molecular Properties**, *Inorganic Chemistry*, **2012**, 51, 1068-1083, http://dx.doi.org/10.1021/ic202198k.

91. S. Youngme, A. Cheansirisomboon, C. Danvirutai, C. Pakawatchai, N. Chaichit, C. Engkagul, G. A. van Albada, J. S. Costa and J. Reedijk, **Three new polynuclear tetracarboxylato-bridged copper(II) complexes: Syntheses, X-ray structure and magnetic properties**, *Polyhedron*, **2008**, 27, 1875-1882, http://www.sciencedirect.com/science/article/pii/S0277538708001113.

92. W. Li, P. T. Barton, M. S. R. N. Kiran, R. P. Burwood, U. Ramamurty and A. K. Cheetham, **Magnetic and Mechanical Anisotropy in a Manganese 2-Methylsuccinate Framework Structure**, *Chemistry – A European Journal*, **2011**, 17, 12429-12436, http://dx.doi.org/10.1002/chem.201101251.

93. M.-H. Zeng, Y.-L. Zhou, M.-C. Wu, H.-L. Sun and M. Du, **A Unique Cobalt(II)-Based Molecular Magnet Constructed of Hydroxyl/Carboxylate Bridges with a 3D Pillared-Layer Motif**, *Inorganic Chemistry*, **2010**, 49, 6436-6442, http://dx.doi.org/10.1021/ic100021f.

94. L. Bogani, A. Vindigni, R. Sessoli and D. Gatteschi, **Single chain magnets: where to from here?**, *Journal of Materials Chemistry*, **2008**, 18, 4750-4758, http://dx.doi.org/10.1039/B807824F.

95. H. Miyasaka, T. Madanbashi, K. Sugimoto, Y. Nakazawa, W. Wernsdorfer, K.-i. Sugiura, M. Yamashita, C. Coulon and R. Clérac, **Single-Chain Magnet Behavior in an Alternated One-Dimensional Assembly of a MnIII Schiff-Base Complex and a TCNQ Radical**, *Chemistry – A European Journal*, **2006**, 12, 7028-7040, http://dx.doi.org/10.1002/chem.200600289.

96. L. M. Toma, C. Ruiz-Pérez, J. Pasán, W. Wernsdorfer, F. Lloret and M. Julve, **Molecular Engineering To Control the Magnetic Interaction between Single-Chain Magnets Assembled in a Two-Dimensional Network**, *Journal of the American Chemical Society*, **2012**, 134, 15265-15268, http://dx.doi.org/10.1021/ja307042z.

97. K. S. Pedersen, J. Bendix and R. Clerac, **Single-molecule magnet engineering: building-block approaches**, *Chemical Communications*, **2014**, 50, 4396-4415, http://dx.doi.org/10.1039/C4CC00339J.

98. R. Ruamps, L. J. Batchelor, R. Guillot, G. Zakhia, A.-L. Barra, W. Wernsdorfer, N. Guihery and T. Mallah, **Ising-type magnetic anisotropy and single molecule magnet behaviour in mononuclear trigonal bipyramidal Co(ii) complexes**, *Chemical Science*, **2014**, 5, 3418-3424, http://dx.doi.org/10.1039/C4SC00984C.

99. P.-F. Zhuang, Y.-J. Zhang, H. Zheng, C.-Q. Jiao, L. Zhao, J.-L. Wang, C. He, C.-Y. Duan and T. Liu, **Single-molecule magnet behavior in three cyano-bridged heterometallic FeIII-NiII clusters**, *Dalton Transactions*, **2015**, 44, 3393-3398, http://dx.doi.org/10.1039/C4DT03365E.

100. S. Brooker, **Spin crossover with thermal hysteresis: practicalities and lessons learnt**, *Chemical Society Reviews*, **2015**, 44, 2880-2892, http://dx.doi.org/10.1039/C4CS00376D.

101. J. Dugay, M. Giménez-Marqués, T. Kozlova, H. W. Zandbergen, E. Coronado and H. S. J. van der Zant, **Spin Switching in Electronic Devices Based on 2D Assemblies of Spin-Crossover Nanoparticles**, *Advanced Materials*, **2015**, 27, 1288-1293, http://dx.doi.org/10.1002/adma.201404441.

102. O. Kahn and C. J. Martinez, **Spin-Transition Polymers: From Molecular Materials Toward Memory Devices**, *Science*, **1998**, 279, 44-48, http://www.sciencemag.org/content/279/5347/44.abstract.

103. K. Murray and C. Kepert, in *Spin Crossover in Transition Metal Compounds I*, eds. P. Gütlich and H. A. Goodwin, Springer Berlin Heidelberg, 2004, vol. 233, pp. 195-228.

104. F.-P. Huang, P.-F. Yao, Q. Yu, D. Yao, H.-D. Bian, H.-Y. Li, J.-L. Tian and S.-P. Yan, **Spin canting and long-range magnetic ordering in a 2-D cobalt–organic framework incorporated with a new bent connector: 1,4-bis(5-(4-pyridyl)-1H-1,2,4-triazol-3-yl)benzene**, *Inorganic Chemistry Communications*, **2013**, 31, 18-22, http://www.sciencedirect.com/science/article/pii/S1387700313000737.

105. D. Shao, S.-L. Zhang, X.-H. Zhao and X.-Y. Wang, **Spin canting, metamagnetism, and single-chain magnetic behaviour in a cyano-bridged homospin iron(ii) compound**, *Chemical Communications*, **2015**, 51, 4360-4363, http://dx.doi.org/10.1039/C4CC10003D.

106. M. Clemente-Leon, E. Coronado, C. Marti-Gastaldo and F. M. Romero, **Multifunctionality in hybrid magnetic materials based on bimetallic oxalate complexes**, *Chemical Society Reviews*, **2011**, 40, 473-497, http://dx.doi.org/10.1039/C0CS00111B.

107. D.-F. Weng, Z.-M. Wang and S. Gao, **Framework-structured weak ferromagnets**, *Chemical Society Reviews*, **2011**, 40, 3157-3181, http://dx.doi.org/10.1039/C0CS00093K.

108. C. N. R. Rao, S. Natarajan and R. Vaidhyanathan, **Metal Carboxylates with Open Architectures**, *Angewandte Chemie International Edition*, **2004**, 43, 1466-1496, http://dx.doi.org/10.1002/anie.200300588.

109. Y.-F. Zeng, X. Hu, F.-C. Liu and X.-H. Bu, **Azido-mediated systems showing different magnetic behaviors**, *Chemical Society Reviews*, **2009**, 38, 469-480, http://dx.doi.org/10.1039/B718581M.

110. X.-M. Zhang, P. Li, W. Gao, J.-P. Liu and E.-Q. Gao, **A new cube-based dodecanuclear cobalt(ii) cluster with azide and tetrazolate ligands exhibiting ferromagnetic ordering**, *Dalton Transactions*, **2015**, 44, 13581-13585, http://dx.doi.org/10.1039/C5DT02032H.

111. Y.-Z. Zheng, Z. Zheng and X.-M. Chen, **A symbol approach for classification of molecule-based magnetic materials exemplified by coordination polymers of metal carboxylates**, *Coordination Chemistry Reviews*, **2014**, 258–259, 1-15, http://www.sciencedirect.com/science/article/pii/S0010854513001872.

112. P. W. Ball, **The magnetic properties of polynuclear transition metal complexes**, *Coordination Chemistry Reviews*, **1969**, 4, 361-383, http://www.sciencedirect.com/science/article/pii/S0010854500802106.

113. A. Rodríguez-Fortea, P. Alemany, S. Alvarez and E. Ruiz, **Exchange Coupling in Carboxylato-Bridged Dinuclear Copper(II) Compounds: A Density Functional Study**, *Chemistry – A European Journal*, **2001**, 7, 627-637, http://dx.doi.org/10.1002/1521-3765(20010202)7:3<627::AID-CHEM627>3.0.CO;2-I.

114. X. Lv, L. Liu, C. Huang, L. a. Guo, J. Wu, H. Hou and Y. Fan, **Metal-organic frameworks based on the [1,1[prime or minute]:3[prime or minute],1[prime or minute][prime or minute]-terphenyl]-3,3[prime or minute][prime or minute],5,5[prime or minute][prime or minute]-tetracarboxylic acid ligand: syntheses, structures and magnetic properties**, *Dalton Transactions*, **2014**, 43, 15475-15481, http://dx.doi.org/10.1039/C4DT02342K.

115. D. P. Martin, R. M. Supkowski and R. L. LaDuca, **A Three-Dimensional Mixed-Ligand Coordination Polymer Featuring Strongly Antiferromagnetically Coupled Dinuclear Copper Paddlewheels Linked into a 6-Connected Self-Penetrated Network**, *Crystal Growth & Design*, **2008**, 8, 3518-3520, http://dx.doi.org/10.1021/cg800743a.

116. F. S. Delgado, F. Lahoz, F. Lloret, M. Julve and C. Ruiz-Pérez, **Supramolecular Networks in Copper(II) Malonate Complexes**, *Crystal Growth & Design*, **2008**, 8, 3219-3232, http://dx.doi.org/10.1021/cg701108c.

117. M. Deniz, J. Pasan, O. Fabelo, L. Canadillas-Delgado, F. Lloret, M. Julve and C. Ruiz-Perez, **Metal-organic coordination frameworks based on mixed methylmalonate and 4,4[prime or minute]-bipiridine ligands: synthesis, crystal structure and magnetic properties**, *New Journal of Chemistry*, **2010**, 34, 2515-2527, http://dx.doi.org/10.1039/C0NJ00436G.

118. J. Pasan, J. Sanchiz, O. Fabelo, L. Canadillas-Delgado, M. Deniz, P. Diaz-Gallifa, C. Martinez-Benito, F. Lloret, M. Julve and C. Ruiz-Perez, **Influence of the coligand in the magnetic properties of a series of copper(ii)-phenylmalonate complexes**, *CrystEngComm*, **2014**, 16, 8106-8118, http://dx.doi.org/10.1039/C4CE00834K.

119. J. Pasán, J. Sanchiz, C. Ruiz-Pérez, F. Lloret and M. Julve, **Phenylmalonate-Containing Copper(II) Complexes: Synthesis, Crystal Structure and Magnetic Properties**, *European Journal of Inorganic Chemistry*, **2004**, 2004, 4081-4090, http://dx.doi.org/10.1002/ejic.200400260.

120. F. P. W. Agterberg, H. A. J. Provó Kluit, W. L. Driessen, H. Oevering, W. Buijs, M. T. Lakin, A. L. Spek and J. Reedijk, **Dinuclear Paddle-Wheel Copper(II) Carboxylates in the Catalytic Oxidation of Carboxylic Acids. Unusual Polymeric Chains Found in the Single-Crystal X-ray Structures of [Tetrakis(μ-1-phenylcyclopropane-1-carboxylato-O,O‘)bis(ethanol-O)dicopper(II)] and catena-Poly[[bis(μ-diphenylacetato-O:O‘)dicopper](μ3-diphenylacetato-1-O:2-O‘:1‘-O‘)(μ3-diphenylacetato-1-O:2-O‘:2‘-O‘)]**, *Inorganic Chemistry*, **1997**, 36, 4321-4328, http://dx.doi.org/10.1021/ic9614733.

121. D. Mikloš, M. Palicová, P. Segl'a, M. Melník, M. Korabik, T. Glowiak and J. Mrozinski, **Crystal Structures, Spectroscopic and Magnetic Behaviour of Dimeric Copper(II) 2-Methylthionicotinate Adducts with Dimethylformamide and Dimethylsulfoxide**, *Zeitschrift für anorganische und allgemeine Chemie*, **2002**, 628, 2862-2868, http://dx.doi.org/10.1002/1521-3749(200213)628:13<2862::AID-ZAAC2862>3.0.CO;2-8.

122. J. Zhou, L. Du, Z. Li, Y. Qiao, J. Liu, M. Zhu, P. Chen and Q. Zhao, **Synthesis, structure, and magnetic properties of two dimer paddle-wheel CuII toluate complexes with nitronyl nitroxide radicals**, *Journal of Coordination Chemistry*, **2013**, 66, 2166-2177, http://dx.doi.org/10.1080/00958972.2013.800485.

123. C. Albrecht, **Joseph R. Lakowicz: Principles of fluorescence spectroscopy, 3rd Edition**, *Analytical and Bioanalytical Chemistry*, **2008**, 390, 1223-1224, http://dx.doi.org/10.1007/s00216-007-1822-x.

124. F. Dumur, **Recent advances in organic light-emitting devices comprising copper complexes: A realistic approach for low-cost and highly emissive devices?**, *Organic Electronics*, **2015**, 21, 27-39, http://www.sciencedirect.com/science/article/pii/S1566119915000890.

125. W. Liu, Y. Fang, G. Z. Wei, S. J. Teat, K. Xiong, Z. Hu, W. P. Lustig and J. Li, **A Family of Highly Efficient CuI-Based Lighting Phosphors Prepared by a Systematic, Bottom-up Synthetic Approach**, *Journal of the American Chemical Society*, **2015**, 137, 9400-9408, http://dx.doi.org/10.1021/jacs.5b04840.

126. Z. Liu, M. F. Qayyum, C. Wu, M. T. Whited, P. I. Djurovich, K. O. Hodgson, B. Hedman, E. I. Solomon and M. E. Thompson, **A Codeposition Route to CuI−Pyridine Coordination Complexes for Organic Light-Emitting Diodes**, *Journal of the American Chemical Society*, **2011**, 133, 3700-3703, http://dx.doi.org/10.1021/ja1065653.

127. Z. Liu, J. Qiu, F. Wei, J. Wang, X. Liu, M. G. Helander, S. Rodney, Z. Wang, Z. Bian, Z. Lu, M. E. Thompson and C. Huang, **Simple and High Efficiency Phosphorescence Organic Light-Emitting Diodes with Codeposited Copper(I) Emitter**, *Chemistry of Materials*, **2014**, 26, 2368-2373, http://dx.doi.org/10.1021/cm5006086.

128. V. W.-W. Yam, V. K.-M. Au and S. Y.-L. Leung, **Light-Emitting Self-Assembled Materials Based on d8 and d10 Transition Metal Complexes**,

Chemical Reviews, **2015**, 115, 7589-7728, http://dx.doi.org/10.1021/acs.chemrev.5b00074.

129. E. Cariati and J. Bourassa, **Luminescence response of the solid state polynuclear copper(I) iodide materials [CuI(4-picoline)] to volatile organic compounds**, *Chemical Communications*, **1998**, 10.1039/a802805b, 1623-1624, http://dx.doi.org/10.1039/A802805B.

130. S. Cho, Y. Jeon, S. Lee, J. Kim and T. H. Kim, **Reversible Transformation between Cubane and Stairstep Cu4I4 Clusters Using Heat or Solvent Vapor**, *Chemistry – A European Journal*, **2015**, 21, 1439-1443, http://dx.doi.org/10.1002/chem.201405800.

131. O. S. Wenger, **Vapochromism in Organometallic and Coordination Complexes: Chemical Sensors for Volatile Organic Compounds**, *Chemical Reviews*, **2013**, 113, 3686-3733, http://dx.doi.org/10.1021/cr300396p.

132. G. Zeng, S. Xing, X. Han, B. Xin, Y. Yang, X. Wang, G. Li, Z. Shi and S. Feng, **Reversible photoluminescence switching behavior and luminescence thermochromism of copper(I) halide cluster coordination polymers**, *RSC Advances*, **2015**, 5, 40792-40797, http://dx.doi.org/10.1039/C5RA05157F.

133. H. Araki, K. Tsuge, Y. Sasaki, S. Ishizaka and N. Kitamura, **Luminescence Ranging from Red to Blue: A Series of Copper(I)−Halide Complexes Having Rhombic {Cu2(μ-X)2} (X = Br and I) Units with N-Heteroaromatic Ligands**, *Inorganic Chemistry*, **2005**, 44, 9667-9675, http://dx.doi.org/10.1021/ic0510359.

134. P. C. Ford, E. Cariati and J. Bourassa, **Photoluminescence Properties of Multinuclear Copper(I) Compounds**, *Chemical Reviews*, **1999**, 99, 3625-3648, http://dx.doi.org/10.1021/cr960109i.

135. M. Knorr, A. Khatyr, A. Dini Aleo, A. El Yaagoubi, C. Strohmann, M. M. Kubicki, Y. Rousselin, S. M. Aly, D. Fortin, A. Lapprand and P. D. Harvey, **Copper(I) Halides (X = Br, I) Coordinated to Bis(arylthio)methane Ligands: Aryl Substitution and Halide Effects on the Dimensionality, Cluster Size, and Luminescence Properties of the Coordination Polymers**, *Crystal Growth & Design*, **2014**, 14, 5373-5387, http://dx.doi.org/10.1021/cg500905z.

136. M. Vitale* and P. C. Ford*, **Luminescent mixed ligand copper(I) clusters (CuI)n(L)m (L=pyridine, piperidine): thermodynamic control of molecular and supramolecular species**, *Coordination Chemistry Reviews*, **2001**, 219–221, 3-16, http://www.sciencedirect.com/science/article/pii/S0010854500004148.

137. C. A. Bayse, T. P. Brewster and R. D. Pike, **Photoluminescence of 1-D Copper(I) Cyanide Chains: A Theoretical Description**, *Inorganic Chemistry*, **2009**, 48, 174-182, http://dx.doi.org/10.1021/ic801509t.

138. Y.-L. Qin, J.-J. Hou, J. Lv and X.-M. Zhang, **Organic Templated Cuprous Cyanide Open Frameworks Based on Cu2(CN)6 Dimer with Strong and Long-Lived Luminescence**, *Crystal Growth & Design*, **2011**, 11, 3101-3108, http://dx.doi.org/10.1021/cg200362c.

139. T. A. Tronic, K. E. deKrafft, M. J. Lim, A. N. Ley and R. D. Pike, **Copper(I) Cyanide Networks: Synthesis, Luminescence Behavior and Thermal Analysis. Part 1. Diimine Ligands**, *Inorganic Chemistry*, **2007**, 46, 8897-8912, http://dx.doi.org/10.1021/ic7007057.

140. R. Peng, M. Li and D. Li, **Copper(I) halides: A versatile family in coordination chemistry and crystal engineering**, *Coordination Chemistry Reviews*, **2010**, 254, 1-18, http://www.sciencedirect.com/science/article/pii/S0010854509002653.

141. C. H. Arnby, S. Jagner and I. Dance, **Questions for crystal engineering of halocuprate complexes: concepts for a difficult system**, *CrystEngComm*, **2004**, 6, 257-275, http://dx.doi.org/10.1039/B408793C.

142. P. M. Graham, R. D. Pike, M. Sabat, R. D. Bailey and W. T. Pennington, **Coordination Polymers of Copper(I) Halides**, *Inorganic Chemistry*, **2000**, 39, 5121-5132, http://dx.doi.org/10.1021/ic0005341.

143. L. Maini, D. Braga, P. P. Mazzeo, L. Maschio, M. Rerat, I. Manet and B. Ventura, **Dual luminescence in solid CuI(piperazine): hypothesis of an emissive 1-D delocalized excited state**, *Dalton Transactions*, **2015**, 44, 13003-13006, http://dx.doi.org/10.1039/C5DT02204E.

144. M. Hashimoto, S. Igawa, M. Yashima, I. Kawata, M. Hoshino and M. Osawa, **Highly Efficient Green Organic Light-Emitting Diodes Containing Luminescent Three-Coordinate Copper(I) Complexes**, *Journal of the American Chemical Society*, **2011**, 133, 10348-10351, http://dx.doi.org/10.1021/ja202965y.

145. D. Volz, A. F. Hirschbiel, D. M. Zink, J. Friedrichs, M. Nieger, T. Baumann, S. Brase and C. Barner-Kowollik, **Highly efficient photoluminescent Cu(i)-PyrPHOS-metallopolymers**, *Journal of Materials Chemistry C*, **2014**, 2, 1457-1462, http://dx.doi.org/10.1039/C3TC32347A.

146. D. Volz, D. M. Zink, T. Bocksrocker, J. Friedrichs, M. Nieger, T. Baumann, U. Lemmer and S. Bräse, **Molecular Construction Kit for Tuning Solubility, Stability and Luminescence Properties: Heteroleptic MePyrPHOS-Copper Iodide-Complexes and their Application in Organic Light-Emitting Diodes**, *Chemistry of Materials*, **2013**, 25, 3414-3426, http://dx.doi.org/10.1021/cm4010807.

147. A. Barbieri, G. Accorsi and N. Armaroli, **Luminescent complexes beyond the platinum group: the d10 avenue**, *Chemical Communications*, **2008**, 10.1039/b716650h, 2185-2193, http://dx.doi.org/10.1039/B716650H.

148. G. F. Manbeck, W. W. Brennessel and R. Eisenberg, **Photoluminescent Copper(I) Complexes with Amido-Triazolato Ligands**, *Inorganic Chemistry*, **2011**, 50, 3431-3441, http://dx.doi.org/10.1021/ic102338g.

149. T. Wen, D.-X. Zhang, J. Liu, R. Lin and J. Zhang, **A multifunctional helical Cu(i) coordination polymer with mechanochromic, sensing and photocatalytic properties**, *Chemical Communications*, **2013**, 49, 5660-5662, http://dx.doi.org/10.1039/C3CC42241K.

150. V. Wing-Wah Yam and K. Kam-Wing Lo, **Luminescent polynuclear d10 metal complexes**, *Chemical Society Reviews*, **1999**, 28, 323-334, http://dx.doi.org/10.1039/A804249G.

151. L. Yang, J.-K. Feng, A.-M. Ren, M. Zhang, Y.-G. Ma and X.-D. Liu, **Structures, Electronic States and Electroluminescent Properties of a Series of CuI**

Complexes, *European Journal of Inorganic Chemistry*, **2005**, 2005, 1867-1879, http://dx.doi.org/10.1002/ejic.200400941.

152. C. Yue, C. Yan, R. Feng, M. Wu, L. Chen, F. Jiang and M. Hong, **A Polynuclear d10−d10 Metal Complex with Unusual Near-Infrared Luminescence and High Thermal Stability**, *Inorganic Chemistry*, **2009**, 48, 2873-2879, http://dx.doi.org/10.1021/ic801840g.

153. E. Cariati, D. Roberto, R. Ugo, P. C. Ford, S. Galli and A. Sironi, **New Structural Motifs, Unusual Quenching of the Emission, and Second Harmonic Generation of Copper(I) Iodide Polymeric or Oligomeric Adducts with Para-Substituted Pyridines or trans-Stilbazoles**, *Inorganic Chemistry*, **2005**, 44, 4077-4085, http://dx.doi.org/10.1021/ic050143s.

154. E. Cariati, D. Roberto, R. Ugo, P. C. Ford, S. Galli and A. Sironi, **X-ray Structures and Emissive and Second-Order Nonlinear Optical Properties of Two Inorganic−Organic Polymeric Adducts of CuI with 4-Acetylpyridine. The Role of Both "Intrastrand" Charge Transfers and Structural Motifs on the Nonlinear Optical Response of Cu(I) Polymeric Adducts with Pseudoaromatic η1-Nitrogen Donor Ligands**, *Chemistry of Materials*, **2002**, 14, 5116-5123, http://dx.doi.org/10.1021/cm020640w.

155. F. De Angelis, S. Fantacci, A. Sgamellotti, E. Cariati, R. Ugo and P. C. Ford, **Electronic Transitions Involved in the Absorption Spectrum and Dual Luminescence of Tetranuclear Cubane [Cu4I4(pyridine)4] Cluster: a Density Functional Theory/Time-Dependent Density Functional Theory Investigation**, *Inorganic Chemistry*, **2006**, 45, 10576-10584, http://dx.doi.org/10.1021/ic061147f.

156. Q. Benito, X. F. Le Goff, S. Maron, A. Fargues, A. Garcia, C. Martineau, F. Taulelle, S. Kahlal, T. Gacoin, J.-P. Boilot and S. Perruchas, **Polymorphic Copper Iodide Clusters: Insights into the Mechanochromic Luminescence Properties**, *Journal of the American Chemical Society*, **2014**, 136, 11311-11320, http://dx.doi.org/10.1021/ja500247b.

157. F. Parmeggiani and A. Sacchetti, **Preparation and Luminescence Thermochromism of Tetranuclear Copper(I)–Pyridine–Iodide Clusters**, *Journal of Chemical Education*, **2012**, 89, 946-949, http://dx.doi.org/10.1021/ed200736b.

158. S. Perruchas, C. Tard, X. F. Le Goff, A. Fargues, A. Garcia, S. Kahlal, J.-Y. Saillard, T. Gacoin and J.-P. Boilot, **Thermochromic Luminescence of Copper Iodide Clusters: The Case of Phosphine Ligands**, *Inorganic Chemistry*, **2011**, 50, 10682-10692, http://dx.doi.org/10.1021/ic201128a.

159. K. Tsuge, Y. Chishina, H. Hashiguchi, Y. Sasaki, M. Kato, S. Ishizaka and N. Kitamura, **Luminescent copper(I) complexes with halogenido-bridged dimeric core**, *Coordination Chemistry Reviews*, http://dx.doi.org/10.1016/j.ccr.2015.03.022, http://www.sciencedirect.com/science/article/pii/S0010854515001198.

160. D. Braga, F. Grepioni, L. Maini, P. P. Mazzeo and B. Ventura, **Solid-state reactivity of copper(i) iodide: luminescent 2D-coordination polymers of CuI with saturated bidentate nitrogen bases**, *New Journal of Chemistry*, **2011**, 35, 339-344, http://dx.doi.org/10.1039/C0NJ00547A.

161. K. R. Kyle, C. K. Ryu, P. C. Ford and J. A. DiBenedetto, **Photophysical studies in solution of the tetranuclear copper(I) clusters Cu4I4L4 (L = pyridine or substituted pyridine)**, *Journal of the American Chemical Society*, **1991**, 113, 2954-2965, http://dx.doi.org/10.1021/ja00008a026.

162. E. Cariati, X. Bu and P. C. Ford, **Solvent- and Vapor-Induced Isomerization between the Luminescent Solids [CuI(4-pic)]4 and [CuI(4-pic)]∞ (pic = methylpyridine). The Structural Basis for the Observed Luminescence Vapochromism**, *Chemistry of Materials*, **2000**, 12, 3385-3391, http://dx.doi.org/10.1021/cm0010708.

163. S. Hu, F.-Y. Yu, Y. Yan, Z.-F. Hao, L. Yu and M.-L. Tong, **Two photoluminescent one-dimensional copper(I) iodide coordination polymers incorporating Cu2I2 double-stranded stair and Cu6I6 hexagonal cage chain units**, *Inorganic Chemistry Communications*, **2011**, 14, 622-625, http://www.sciencedirect.com/science/article/pii/S1387700311000426.

164. J. Vallejos, I. Brito, A. Cárdenas, M. Bolte, J. Llanos and M. López-Rodríguez, **A novel double-stranded staircase Cu(I)-iodide coordination polymer based on bis(4-pyridyl-carboxylate) ligand with flexible propyl spacer: Syntheses, crystal structure, luminescence properties and thermal stability**, *Inorganic Chemistry Communications*, **2012**, 24, 59-62, http://www.sciencedirect.com/science/article/pii/S1387700312003711.

165. Z. Hu, B. J. Deibert and J. Li, **Luminescent metal-organic frameworks for chemical sensing and explosive detection**, *Chemical Society Reviews*, **2014**, 43, 5815-5840, http://dx.doi.org/10.1039/C4CS00010B.

166. A. J. McConnell, C. S. Wood, P. P. Neelakandan and J. R. Nitschke, **Stimuli-Responsive Metal–Ligand Assemblies**, *Chemical Reviews*, **2015**, 115, 7729-7793, http://dx.doi.org/10.1021/cr500632f.

167. Y. Han, J.-R. Li, Y. Xie and G. Guo, **Substitution reactions in metal-organic frameworks and metal-organic polyhedra**, *Chemical Society Reviews*, **2014**, 43, 5952-5981, http://dx.doi.org/10.1039/C4CS00033A.

168. E. Cariati, E. Lucenti, C. Botta, U. Giovanella, D. Marinotto and S. Righetto, **Cu(I) hybrid inorganic-organic materials with intriguing stimuli responsive and optoelectronic properties**, *Coordination Chemistry Reviews*, **2016**, 306, 566–614, http://dx.doi.org/10.1016/j.ccr.2015.03.004.

169. D. Sheberla, L. Sun, M. A. Blood-Forsythe, S. Er, C. R. Wade, C. K. Brozek, A. Aspuru-Guzik and M. Dincă, **High Electrical Conductivity in Ni3(2,3,6,7,10,11-hexaiminotriphenylene)2, a Semiconducting Metal–Organic Graphene Analogue**, *Journal of the American Chemical Society*, **2014**, 136, 8859-8862, http://dx.doi.org/10.1021/ja502765n.

170. L. Sun, C. H. Hendon, M. A. Minier, A. Walsh and M. Dincă, **Million-Fold Electrical Conductivity Enhancement in Fe2(DEBDC) versus Mn2(DEBDC) (E = S, O)**, *Journal of the American Chemical Society*, **2015**, 137, 6164-6167, http://dx.doi.org/10.1021/jacs.5b02897.

171. C. A. Fernandez, P. C. Martin, T. Schaef, M. E. Bowden, P. K. Thallapally, L. Dang, W. Xu, X. Chen and B. P. McGrail, **An Electrically Switchable Metal-Organic Framework**, *Scientific Reports*, **2014**, 4, 6114, http://dx.doi.org/10.1038/srep06114.

172. E. Coronado, M. Giménez-Marqués, G. M. Espallargas and L. Brammer, **Tuning the magneto-structural properties of non-porous coordination polymers by HCl chemisorption**, *Nat Commun*, **2012**, 3, 828, http://dx.doi.org/10.1038/ncomms1827.

173. N. Singh, P. Vishnoi and G. Anantharaman, **Coordination polymers based on copper carboxylates and angular 2,5-bis(imidazol-1-yl)thiophene (thim2) ligand: sequential structural transformations**, *CrystEngComm*, **2015**, 17, 2153-2161, http://dx.doi.org/10.1039/C4CE02428A.

174. J. Seo, C. Bonneau, R. Matsuda, M. Takata and S. Kitagawa, **Soft Secondary Building Unit: Dynamic Bond Rearrangement on Multinuclear Core of Porous Coordination Polymers in Gas Media**, *Journal of the American Chemical Society*, **2011**, 133, 9005-9013, http://dx.doi.org/10.1021/ja201484s.

175. A. Motreff, R. Correa da Costa, H. Allouchi, M. Duttine, C. Mathonière, C. Duboc and J.-M. Vincent, **Dramatic Solid-State Humidity-Induced Modification of the Magnetic Coupling in a Dimeric Fluorous Copper(II)−Carboxylate Complex**, *Inorganic Chemistry*, **2009**, 48, 5623-5625, http://dx.doi.org/10.1021/ic9005218.

176. S. Perruchas, X. F. L. Goff, S. Maron, I. Maurin, F. Guillen, A. Garcia, T. Gacoin and J.-P. Boilot, **Mechanochromic and Thermochromic Luminescence of a Copper Iodide Cluster**, *Journal of the American Chemical Society*, **2010**, 132, 10967-10969, http://dx.doi.org/10.1021/ja103431d.

177. P. Kumar, A. Deep, K.-H. Kim and R. J. C. Brown, **Coordination polymers: Opportunities and challenges for monitoring volatile organic compounds**, *Progress in Polymer Science*, **2015**, 45, 102–118, http://dx.doi.org/10.1016/j.progpolymsci.2015.01.002.

178. J. V. Barth, G. Costantini and K. Kern, **Engineering atomic and molecular nanostructures at surfaces**, *Nature*, **2005**, 437, 671-679, http://dx.doi.org/10.1038/nature04166.

179. A. Biswas, I. S. Bayer, A. S. Biris, T. Wang, E. Dervishi and F. Faupel, **Advances in top–down and bottom–up surface nanofabrication: Techniques, applications & future prospects**, *Advances in Colloid and Interface Science*, **2012**, 170, 2-27, http://www.sciencedirect.com/science/article/pii/S0001868611001904.

180. D. Mailly, **Nanofabrication techniques**, *The European Physical Journal Special Topics*, **2009**, 172, 333-342, http://dx.doi.org/10.1140/epjst/e2009-01058-x.

181. A. Santos, M. J. Deen and L. F. Marsal, **Low-cost fabrication technologies for nanostructures: state-of-the-art and potential**, *Nanotechnology*, **2015**, 26, 042001-042021, http://stacks.iop.org/0957-4484/26/i=4/a=042001.

182. A. Allan, D. Edenfeld, W. H. Joyner, A. B. Kahng, M. Rodgers and Y. Zorian, **2001 technology roadmap for semiconductors**, *Computer*, **2002**, 35, 42-53.

183. A. Carne, C. Carbonell, I. Imaz and D. Maspoch, **Nanoscale metal-organic materials**, *Chemical Society Reviews*, **2011**, 40, 291-305, http://dx.doi.org/10.1039/C0CS00042F.

184. J. Della Rocca, D. Liu and W. Lin, **Nanoscale Metal–Organic Frameworks for Biomedical Imaging and Drug Delivery**, *Accounts of Chemical Research*, **2011**, 44, 957-968, http://dx.doi.org/10.1021/ar200028a.

185. I. Imaz, M. Rubio-Martínez, W. J. Saletra, D. B. Amabilino and D. Maspoch, **Amino Acid Based Metal−Organic Nanofibers**, *Journal of the American Chemical Society*, **2009**, 131, 18222-18223, http://dx.doi.org/10.1021/ja908721t.

186. E. Mateo-Marti, L. Welte, P. Amo-Ochoa, P. J. Sanz Miguel, J. Gomez-Herrero, J. A. Martin-Gago and F. Zamora, **Direct evidence of nanowires formation from a Cu(i) coordination polymer**, *Chemical Communications*, **2008**, 8, 945-947, http://dx.doi.org/10.1039/B711416H.

187. D. Olea, U. García-Couceiro, O. Castillo, J. Gómez-Herrero and F. Zamora, **Nanoprocessability of a one-dimensional oxalato-bridged cobalt(II) complex with 1,2,4-triazole**, *Inorganica Chimica Acta*, **2007**, 360, 48-54, http://www.sciencedirect.com/science/article/pii/S0020169306004725.

188. A. M. Spokoyny, D. Kim, A. Sumrein and C. A. Mirkin, **Infinite coordination polymer nano- and microparticle structures**, *Chemical Society Reviews*, **2009**, 38, 1218-1227, http://dx.doi.org/10.1039/B807085G.

189. L. Welte, A. Calzolari, R. Di Felice, F. Zamora and J. Gomez-Herrero, **Highly conductive self-assembled nanoribbons of coordination polymers**, *Nat Nano*, **2010**, 5, 110-115, http://dx.doi.org/10.1038/nnano.2009.354.

190. M. Oh and C. A. Mirkin, **Chemically tailorable colloidal particles from infinite coordination polymers**, *Nature*, **2005**, 438, 651-654, http://dx.doi.org/10.1038/nature04191.

191. R. Mas-Balleste, J. Gomez-Herrero and F. Zamora, **One-dimensional coordination polymers on surfaces: towards single molecule devices**, *Chemical Society Reviews*, **2010**, 39, 4220-4233, http://dx.doi.org/10.1039/C001965H.

192. J. Puigmartí-Luis, M. Rubio-Martínez, U. Hartfelder, I. Imaz, D. Maspoch and P. S. Dittrich, **Coordination Polymer Nanofibers Generated by Microfluidic Synthesis**, *Journal of the American Chemical Society*, **2011**, 133, 4216-4219, http://dx.doi.org/10.1021/ja110834j.

193. P. J. Beldon, S. Tominaka, P. Singh, T. Saha Dasgupta, E. G. Bithell and A. K. Cheetham, **Layered structures and nanosheets of pyrimidinethiolate coordination polymers**, *Chemical Communications*, **2014**, 50, 3955-3957, http://dx.doi.org/10.1039/C4CC00771A.

194. S. Furukawa, J. Reboul, S. Diring, K. Sumida and S. Kitagawa, **Structuring of metal-organic frameworks at the mesoscopic/macroscopic scale**, *Chemical Society Reviews*, **2014**, 43, 5700-5734, http://dx.doi.org/10.1039/C4CS00106K.

195. W. Lin, W. J. Rieter and K. M. L. Taylor, **Modular Synthesis of Functional Nanoscale Coordination Polymers**, *Angewandte Chemie International Edition*, **2009**, 48, 650-658, http://dx.doi.org/10.1002/anie.200803387.

196. K. M. L. Taylor, A. Jin and W. Lin, **Surfactant-Assisted Synthesis of Nanoscale Gadolinium Metal–Organic Frameworks for Potential Multimodal Imaging**, *Angewandte Chemie International Edition*, **2008**, 47, 7722-7725, http://dx.doi.org/10.1002/anie.200802911.

197. X. Zhang, Z.-K. Chen and K. P. Loh, **Coordination-Assisted Assembly of 1-D Nanostructured Light-Harvesting Antenna**, *Journal of the American Chemical Society*, **2009**, 131, 7210-7211, http://dx.doi.org/10.1021/ja901041d.

198. E. Coronado, J. R. Galán-Mascarós, M. Monrabal-Capilla, J. García-Martínez and P. Pardo-Ibáñez, **Bistable Spin-Crossover Nanoparticles Showing Magnetic Thermal Hysteresis near Room Temperature**, *Advanced Materials*, **2007**, 19, 1359-1361, http://dx.doi.org/10.1002/adma.200700559.

199. J. An, C. M. Shade, D. A. Chengelis-Czegan, S. Petoud and N. L. Rosi, **Zinc-Adeninate Metal−Organic Framework for Aqueous Encapsulation and Sensitization of Near-infrared and Visible Emitting Lanthanide Cations**, *Journal of the American Chemical Society*, **2011**, 133, 1220-1223, http://dx.doi.org/10.1021/ja109103t.

200. S. Guo and E. Wang, **Functional Micro/Nanostructures: Simple Synthesis and Application in Sensors, Fuel Cells, and Gene Delivery**, *Accounts of Chemical Research*, **2011**, 44, 491-500, http://dx.doi.org/10.1021/ar200001m.

201. D. James and J. Tour, in *Molecular Wires and Electronics*, Springer Berlin Heidelberg, 2005, 257, 33-62, DOI.10.1007/b136066.

202. N. Robertson and C. A. McGowan, **A comparison of potential molecular wires as components for molecular electronics**, *Chemical Society Reviews*, **2003**, 32, 96-103, http://dx.doi.org/10.1039/B206919A.

203. C. H. Hendon, D. Tiana and A. Walsh, **Conductive metal-organic frameworks and networks: fact or fantasy?**, *Physical Chemistry Chemical Physics*, **2012**, 14, 13120-13132, http://dx.doi.org/10.1039/C2CP41099K.

204. S. Kitagawa and S. Noro, **Coordination polymers: infinite systems**, *ChemInform*, **2004**, 35,

205. U. García-Couceiro, D. Olea, O. Castillo, A. Luque, P. Román, P. J. de Pablo, J. Gómez-Herrero and F. Zamora, **Scanning Probe Microscopy Characterization of Single Chains Based on a One-Dimensional Oxalato-Bridged Manganese(II) Complex with 4-Aminotriazole**, *Inorganic Chemistry*, **2005**, 44, 8343-8348, http://dx.doi.org/10.1021/ic0505302.

206. Y. Liu and Z. Tang, **Nanoscale Biocoordination Polymers: Novel Materials from an Old Topic**, *Chemistry – A European Journal*, **2012**, 18, 1030-1037, http://dx.doi.org/10.1002/chem.201101520.

207. N. V. Fischer, U. Mitra, K.-G. Warnick, V. Dremov, M. Stocker, T. Wölfle, W. Hieringer, F. W. Heinemann, N. Burzlaff, A. Görling and P. Müller, **High Resolution Scanning Tunneling Microscopy of a 1D Coordination Polymer with Imidazole-Based N,N,O Ligands on HOPG**, *Chemistry – A European Journal*, **2014**, 20, 11863-11869, http://dx.doi.org/10.1002/chem.201302379.

208. D. Olea, S. S. Alexandre, P. Amo-Ochoa, A. Guijarro, F. de Jesús, J. M. Soler, P. J. de Pablo, F. Zamora and J. Gómez-Herrero, **From Coordination Polymer Macrocrystals to Nanometric Individual Chains**, *Advanced Materials*, **2005**, 17, 1761-1765, http://dx.doi.org/10.1002/adma.200401687.

209. F. Zamora, M. Pilar Amo-Ochoa, P. J. Sanz Miguel and O. Castillo, **From metal-nucleobase chemistry towards molecular wires**, *Inorganica Chimica Acta*,

2009, 362, 691-706, http://www.sciencedirect.com/science/article/pii/S0020169308000844.

210. N. V. Fischer, M. S. Alam, I. Jum'h, M. Stocker, N. Fritsch, V. Dremov, F. W. Heinemann, N. Burzlaff and P. Müller, **trans-1,2-Bis(N-methylimidazol-2-yl)ethylene: Towards Building Blocks for 2D Fabrics and MML-Type 1D Molecular Strands**, *Chemistry – A European Journal*, **2011**, 17, 9293-9297, http://dx.doi.org/10.1002/chem.201101053.

211. H. Tan, L. Zhang, C. Ma, Y. Song, F. Xu, S. Chen and L. Wang, **Terbium-Based Coordination Polymer Nanoparticles for Detection of Ciprofloxacin in Tablets and Biological Fluids**, *ACS Applied Materials & Interfaces*, **2013**, 5, 11791-11796, http://pubs.acs.org/doi/abs/10.1021/am403442q.

212. F. Wang, B. Liu, P.-J. J. Huang and J. Liu, **Rationally Designed Nucleobase and Nucleotide Coordinated Nanoparticles for Selective DNA Adsorption and Detection**, *Analytical Chemistry*, **2013**, 85, 12144-12151, http://pubs.acs.org/doi/abs/10.1021/ac4033627.

2. Chapter 2; Metal-Nucleobases Coordination Complexes

Metal-Nucleobases Coordination Complexes as Potential Candidates for Nanotechnology Applications.

In this chapter, we present the state of art in using metal-nucleobases chemistry to design and construct conductive one dimensional coordination polymers.

To devolve the work in this chapter, we use, as organic ligands, two modified nucleobases known as thymine-1-acetic acid (TAcOH) and uracil-1-acetic acid (UAcOH), and Cu(II) and Co(II) ions as metal centres. The direct reactions between these two building blocks allow us to separate several complexes ranged from mononuclear to extended 1D-CPs.

The electrical and magnetic properties of the synthesized complexes will be discussed.

The nanoprocessability of one selected complex has been investigated and its possible nanotechnological application has been demonstrated.

2.1. Introduction to Metal Nucleobases Coordination Polymers and its Potential Applications for Nanotechnology.

Recently, metal–nucleobase coordination chemistry has been an active research area of coordination chemistry that currently spreads into new fields of material science and nanoscience.[1-6]

Nucleobases (NBs) are key constituents of nucleic acids that are normally involved in base-pairing: adenine binds to thymine or uracil via two H-bonds, whereas guanine specifically recognizes cytosine through three H-bonds. Nucleobases are ligands that in combination with metal ions show a high capacity to generate a large structural variety due to the different available donor sites positions for metal coordination as well as their H-bonding capabilities and potential π–π stacking, similar to that observed in helical duplex DNA.[7] These bond-making characteristics provide a rich basis for a variety of supramolecular architectures.[8] NBs, like other biomolecules, present many metal binding sites, diverse structures, intrinsic self-assembly properties to direct the formation of biologically compatible CPs with outstanding functionalities, and probably good biocompatibility.[3, 9, 10] Because of these unique properties and functionalities of NBs, it is expected that they can replace the conventional synthetic molecules, as organic ligands, to construct more biologically coordination polymers (Bio-CPs). Moreover, the construction of Bio-CPs will be paramount not only for development of new materials with novel properties but also for understanding of many biorelated self-assembly processes.[11] A diverse choice of metal nodes and biomolecule building blocks may produce novel Bio-CPs with a broad range of compositions and properties. More important, these high degree of structural and functional tailorabilities may lead to biological nanoscale coordination polymers (Bio-NCPs) with interesting characteristics for a variety of applications in many fields, especially in biology.[3, 10] So far, although only a few Bio-NCPs have been synthesized, the multifunctionality, and application value of these type of novel materials have been broadly recognized.[12, 13]

Here, we will discuss the possible uses of Bio-CPs (using nucleobases or modified nucleobases as organic ligands) in molecular electronic and bio-medical applications.

Biological Inspiration for using Metal-Nucleobases in Molecular Electronic Application.

DNA nanotechnology provides one of the most interesting approaches to form tailored complex structures with precise control over molecular features.[14] Seeman, the father of DNA nanotechnology, proposed the possibilities to use DNA and its nanostructures as structural materials for bottom-up self-assembly.[15] Since this date, the field of DNA nanostructures became a hot topic for material science and nanotechnology,[16] and many DNA nanostructures, linear, branched, and complex motifs have been fabricated.[17-19]

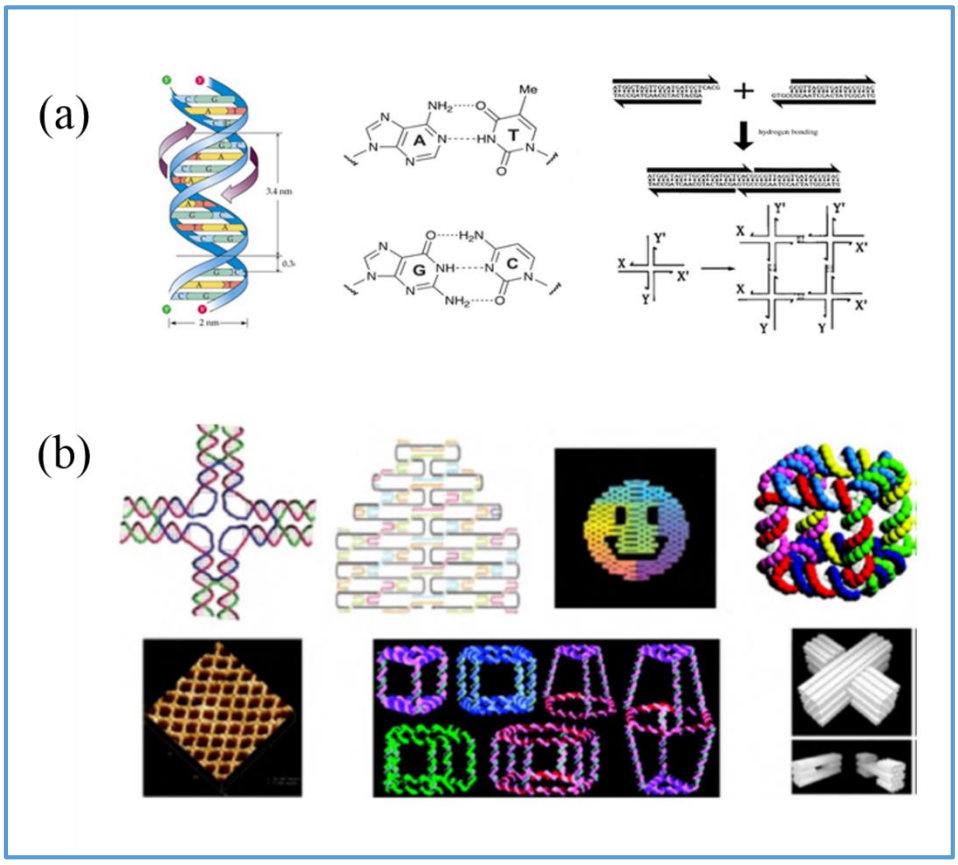

Figure 2.1. (a) Structural features of DNA. (b) 2D and 3D objects constructed by manipulate DNA strands.[20]

DNA molecule and DNA nanostructures gather several structural features making this molecule and its motifs as unique constructing materials for molecular electronics.[21-23] These structural features can be summarized as following:

1. DNA presents a well-known nanoscale dimensions of the double-stranded helix, 2 nm diameter and a 3.4 nm helical repeat (10.5 base pairs) and ease of automated synthesis (**Figure 2.1a**).
2. DNA is the molecule whose intermolecular interactions are the most readily programmed and reliably predicted where G (guanine) pairs with C (cytosine) and A (adenine) pairs with T (thymine) (**Figure 2.1a**).
3. It is available to generate and manipulate long DNA strands with variety sequence and tie DNA molecules together by programming sticky ends to construct complex architectures by the aid of noncovalent interactions (**Figure 2.1b**).
4. The self-organizing and molecular recognition capability of DNA and its nanostructures, may allow the design and formation of self-assembling complex architectures such as nano-circuits.

By this way, DNA and its nanostructures can contribute for molecular electronics applications as templates or as an active wiring system. Unfortunately, the electronic properties of DNA hinder its applications in molecular electronics.[24, 25] The conductivity measurements through the DNA molecule have been reported[26] and it seem to be quite dependent on the measurements methods[27] and DNA base sequence[28, 29]. It has been concluded that DNA molecule can be described as a wide-gap semiconductor.[30, 27] Therefore, many attempts have been proposed to enhance the electrical conductivity of DNA molecule and/or construct molecular wires based on DNA or its nanostructures. These models can be classified as following, depend on the participation nature of DNA:

1. Templating conducting materials on duplex DNA.[31-33]
    a. Incorporate metal nanoparticles in the DNA duplex by the reduction of metal salts into its zero-valent state. This strategy allows the formation of DNA based nanowires < 10 nm.[34]
    b. Electrostatic attractions and noncovalent interactions between cationic conducting polymers such as pyrrole and indole, synthesis through oxidative polymerization process, and the anionic DNA template can provide electrically conducting nanowires based on DNA.[35, 36]
2. M-DNA model, the incorporate divalent cations in the DNA duplex by substitution reaction of the protons of the nucleotides of the DNA lead to new form of DNA named as M-DNA. This M-DNA has been proposed as molecular wire candidate by Prof. Lee.[37, 23] This model of molecular wire, based on DNA,

facing many problems in particular its instability at acidic or neutral pH, unclear position of the metal ions,[38] unclear electronic properties.[39, 40]

3. Using DNA as scaffold for conducting polymers. In this model the self-recognition, self-assembly and sequence programmability of DNA could enable the production of unique nanoscale materials with tailored electronic properties.[41]

One interesting approach to create hybrid materials with better electronic properties and possible applications in nanoelectronic is based on using DNA and/or DNA nanostructures, taking the advantage of their intrinsic molecular recognition capacity, as scaffold for conductive one dimensional coordination polymers (1D-CPs).[6] The selected 1D-CPs have to maintain molecular recognition capability, provide reasonable electronic properties, and accessible to be processed at nanometer scale. In fact, conductivity studies of coordination polymers in macroscopic scale (single crystals or powder)[42] suggested, in some cases, the possible metallic or semi-conductive behavior of isolated chains.[43] Therefore, it is quite important to develop strategies to separate single chains of 1D-CPs on an insulated surface to measure the electrical transport in individual chain in order to test their potential applications for nano-electronics.[44, 45] On the other hand, the selected organic ligands, to design conductive 1D-CPs, have to allow the molecular recognition process between DNA and/or DNA nanostructures with the conductive 1D-CPs. By this way, nucleobases (NBs) or modified NBs can be consider as a potential candidates as organic ligands to construct 1D-CPs with structural diversity and molecular recognition capability.

NBs contain several heteroatoms, allowing them to act as multidentate organic ligands, as well as they maintain the base pairing complementarity, the same structural feature of DNA, that make them a powerful and skillful building blocks to construct conductive 1D-CPs, with the visibility to fabricate well-defined hybrid complex nanostructure by the molecular recognition between DNA and/or DNA nanostructures and single chains of 1D-CPs (**Figure 2.2**).

As a proof of concept, Zamora *et al*, have selected 1D-CP (involve a nucleobase as ligand) formulated as $[Cd(6\text{-}MP)_2]_n$, 6-MP is 6-mercaptopurine, for its structure similarity with the proposed structure of M-DNA (**Figure 2.3a**).[5] They were able to isolate single chain of this 1D-CP over insulator surface and studied the electrical conductivity of single chain (**Figure 2.3b**). Unfortunately, single chain of this polymer has shown insulating behaviour.[5]

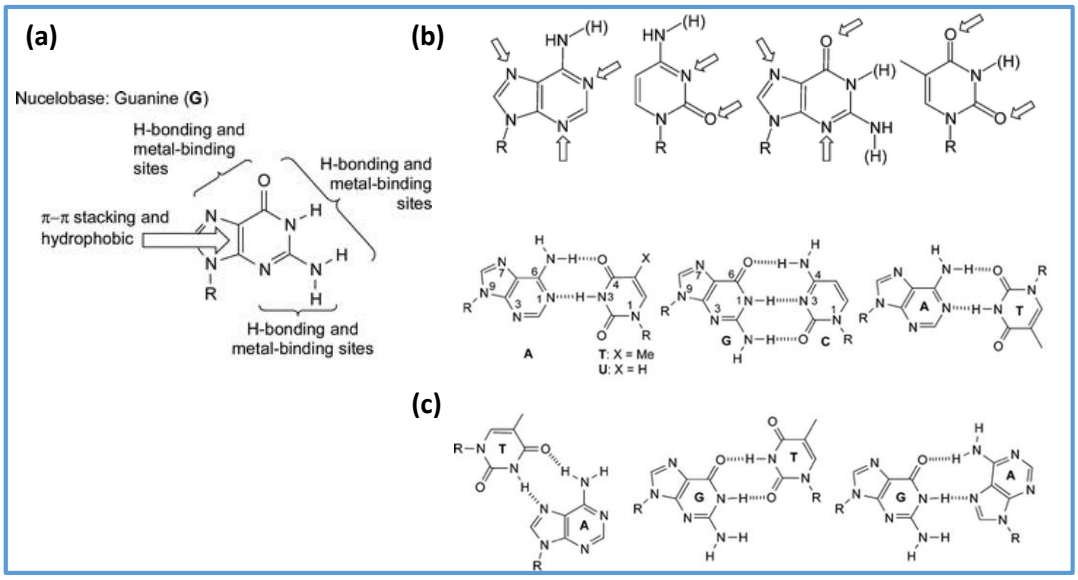

Figure 2.2. (a) Some of the non-covalent interactions, which are present in the nucleobase guanine. (b) Arrows showing the major metal-binding sites on the some nucleobases. The H atoms in parentheses are attached to additional sites which can be involved in metal binding upon removal of the hydrogen. (c) The base-pairing interactions founded for some nucleobases.

As a motivation by these results, the same authors used density functional theory (DFT) to study the electronic structure of other coordination polymers analogues to the $[Cd(6\text{-}MP)_2]_n$ system with different 3*d* transition metal cations, aiming at identifying candidates for a rational synthesis of molecular wires. These calculations have carried out using the X-ray data of $[Cd(6\text{-}MP)_2]_n$ polymer by replacing the Cd atoms with the respective 3*d* transition metals. The calculations suggested that polymers with Fe^{II}, Ni^{II}, and Co^{II} ions are semiconductors while polymer containing Cu^{II} ion shows a metallic behavior (**Table 2.1**).[46] Following with this calculation, the same group reported the synthesis and electrical conductivity measurements for several 1D-CPs similar to $[Cd(6\text{-}MP)_2]_n$ (**Table 2.1**). The reported 1D-CPs showed a semiconductive behaviors and the band gap that have been founded for them fitted perfectly with the calculated ones (**Table 2.1**). It seems that theoretical calculations are suitable tools to understand experimental measurements.

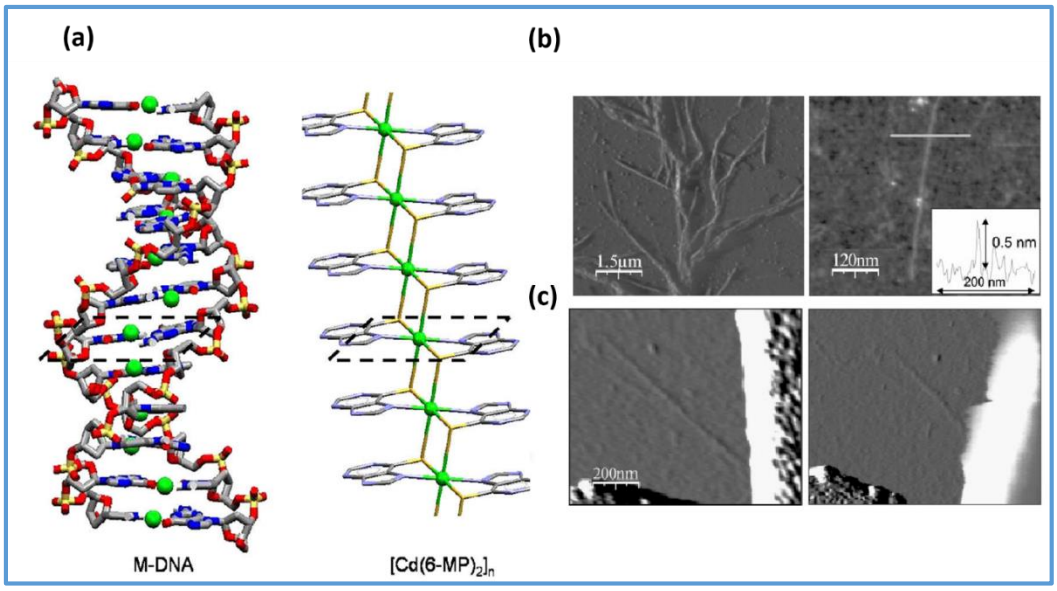

Figure 2.3. (a) Schematic representations of the suggested M-DNA structure and $[Cd(6\text{-}MP)_2]_n$ coordination polymer.[6] (b) AFM images of $[Cd(6\text{-}MP)_2]_n$ fibres (right) and the size of individual chain (left). (c) AFM images of a single chain connected to gold electrode (right) and applying a tip-sample bias voltage of 4 V (left).[5]

Table 2.1. The calculated band gap for $[M(L)_2]_n$ polymers and the metal-metal distances. L is 6-mercaptopurine (6-MP) or 6-thioguanine (6-TG).

Metals (II)	**L**	**M-M (Å)**		**σ S/cm (273K)**	**σ S/cm (400K)**	**Eg**		**Ref**
		Cal	Exp			Cal	Exp	
Cd	6-MP	3.92	3.91	Insulator	Insulator	2.30	Insulator	47
Co	6-MP	3.60	a	a	a	0.78	a	48
Co	6-TG	a	3.66	10^{-11}	10^{-6} (f)	a	0.8	49
Ni	6-MP	3.60	3.68	1.1 10^{-5} (t)	a	0.77	0.66	1
Ni	6-TG	a	3.65	1.3 10^{-4} (t)	a	66	0.69	1
Cu	6-MP	3.47	a	a	a	0	a	48
Fe	6-MP	3.65	a	a	a	0.36	a	48

a; means that these measurements did not realize yet. t; means two contacts method. f; means four contacts method.

The same authors demonstrated the nanoprocessability for $[Cd(6\text{-}MP)_2]_n$ and $[Ni(6\text{-}MP)_2]_n$ polymers.[1, 5] These results suggested that the uses of 1D-CPs, using organic

ligands, that allow molecular recognition with DNA, such as nucleobases or nucleobases derivatives, might allow the construction of nanocircuits based on molecules through the molecular recognition of 1D-CPs on well-organized nanoarrays of DNA via H-bonding interactions.

Bio-medical applications of Coordination Polymers based on Metal Nucleobases

Constructing CPs using biomolecules, as bridging ligands, will open the door for a new class of materials with important applications such as biomedical applications or novel sensors.[12, 13] Compared with nonbiological components, biomolecules have good biocompatibility and are environmentally friendly. These intrinsic properties might lead to bulk production of biologically and environmentally compatible nanoscale bio-coordination polymers (Bio-NCPs) that can be easily incorporated into biological systems. To this end, many challenges need to be overcome,[10] including the design and construction of Bio-CPs with different dimensions, the chemical and physical functionalization of these Bio-CPs for potential bio-applications, and, finally, preparing nanostructures of these Bio-CPs.

Bio-CPs have major advantages that make them as novel sensors. First, the interactions between guest molecules and Bio-CPs might induce changes in their physical properties. Second, some biomolecules (e.g. nucleobases) have the ability to recognize specific analytes. However, the selectivity of CPs remains quite challenging. One important strategy to overcome the selectivity is introducing more specific intermolecular forces. In that regard, Bio-CPs that involve, for instance, nucleobases can interact with materials via a number of intermolecular forces mainly, H-bond. Taking into account the well-known base pairing of nucleobases[7, 8], these Bio-CPs can be specifically used for developing biosensors for DNA detection. Juewen Liu *et al*, have used this strategy, using CPs nanoparticles, for DNA detection.[50] They used nanoparticle of a coordination complex formed by the reaction of adenine and Au metal ion. These Au/adenine nanoparticles have been used and tested for DNA detection. Several DNA with a random sequence have been tested and fluorescence intensities have been recorded upon the combinations with Au/adenine nanoparticles. For all DNA sequences the absorption has been confirmed by the fluorescence quenching (**Figure 2.4**). In addition, these

nanoparticles have shown high selectivity for poly-T DNA with respect to poly-G DNA. The author demonstrated also that these Au/adenine nanoparticles can be used for DNA sensing and for delivery DNA into cells.[50]

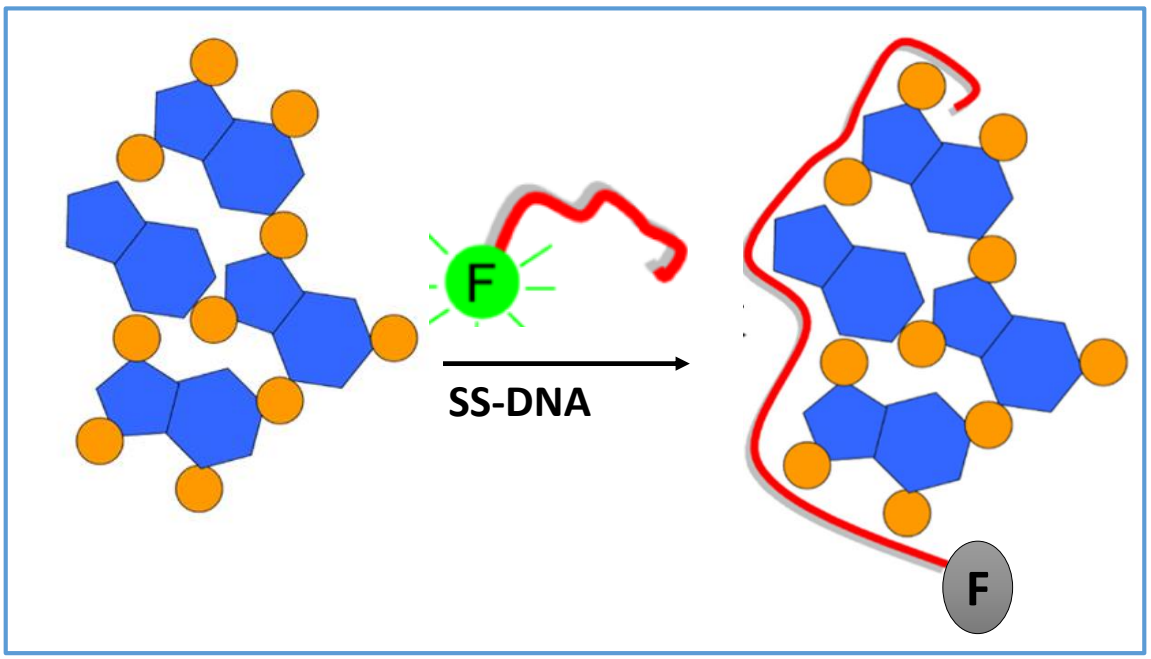

Figure 2.4. Schematics of the adenine/Au complex binding to ss-DNA, where the DNA can interact with both the base (blue polygons) and the metal ion (orange dots). Adsorption of ss-DNA probe induces fluorescence quenching.[50]

On the other hand, some Bio-CPs have been directly used as drug carriers owing to their good biocompatibility and tunable structures. For instance, Nathaniel L. Rosi *et al*,[12] controlled the drug release from $[Zn_8(Ade)_4(bpdc)_6.O.2Me_2NH_2]$. (**Bio-MOF-1**, Ade = adeninate; bpdc = biphenyldicarboxylate). They exploited the anionic nature of this Bio-MOF by demonstrating that it can host cationic drug molecules. In addition, this Bio-MOF is biocompatibility, stable in water and biological buffers for several weeks. These features allow its applications in cation-triggered drug release for the first time. Procainamide, which is a cationic drug molecule, was loaded into the pores of MOF-1 via cationic exchange with the dimethylammonium cations that initially reside inside the pores. As shown in **Figure 2.5**, the procainamide release from the zinc–adeninate framework was triggered by exogenous cations, such as Na^+ ions from biological buffers, owing to the ionic interactions between procainamide and the framework. It is impressive

that the crystalline integrity of the framework could be maintained throughout the whole release process.

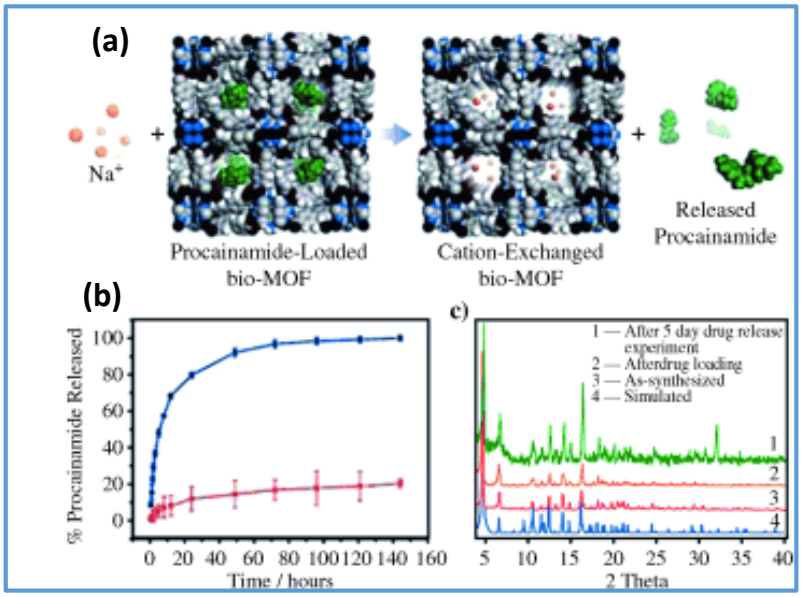

Figure 2.5. (a) Scheme depicting cation-triggered procainamide release from $[Zn_8(Ade)_4(bpdc)_6.O.2Me_2NH_2]$. (b) Procainamide release profiles from $[Zn_8(Ade)_4(bpdc)_6.O.2Me_2NH_2]$. (c) X-ray powder diffraction patterns for $[Zn_8(Ade)_4(bpdc)_6.O.2Me_2NH_2]$ before and after drug loading.[12]

In this chapter, we have selected two modified nucleobases known as thymine-1-acetic acid (TAcOH) and uracil-1-acetic acid (UAcOH) (**Figure 2.6a**), as essential ligands to construct multifunctional 1D-CPs. These ligands contain different functional groups that can participate in metal binding as well as in H-bond interactions and π…π stacking through the pyrimidine moieties (**Figure 2.6a**). In addition, the presence of the carboxylic group add advantages by increasing the diversity and tunability of the coordination to the metal ions. The carboxylic group can adapt various coordination modes (**Figure 2.6b**).[51, 52] Additionally, we have tried to obtain extended coordination polymers using auxiliaries ligands such as 2,6 diaminopurine (HDap) and 4,4′-bipyridine, (4,4′-bpy) (**Figure 2.6c**).

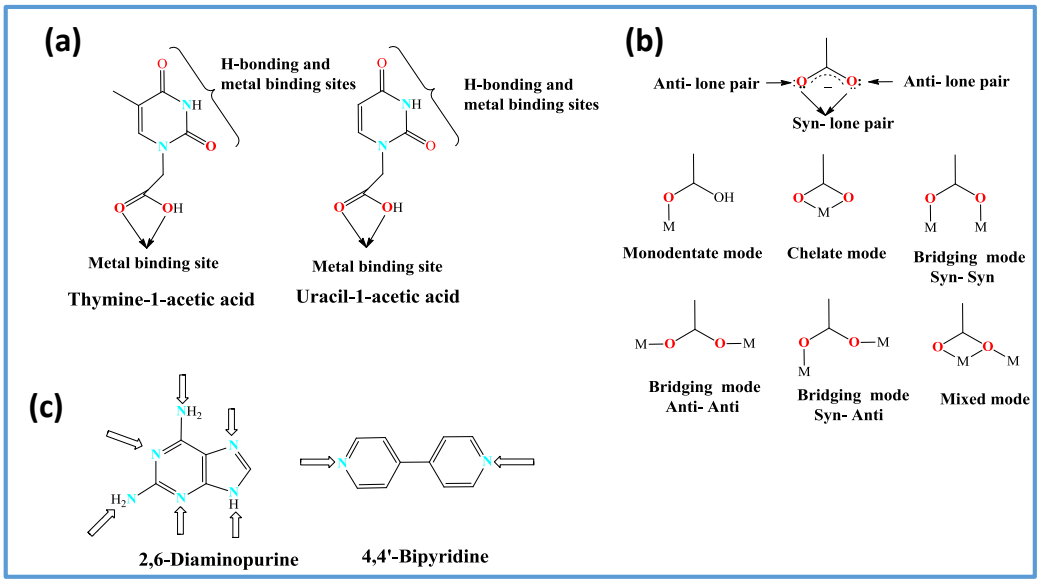

Figure 2.6. (a) Schematic representations showing the main ligands, TAcOH and UAcOH, used in this chapter. (b) The common coordination modes of the carboxylates group. (c) Selected auxiliaries ligands known as 2,6 diaminopurine (HDap) and 4,4′-bipyridine, (4,4′-bpy). The arrows indicate to the metal binding sites.

2.2. Results and discussion

2.2.1. Synthesis and Structural Characterization

The reactions of metal(II) salts with the two modified nucleobases TAcOH and/or UAcOH at different conditions give raise to the isolation of complexes **1-18**. The synthetic part of this chapter can be divided into two blocks depending on the used metal center.

Block A: This block involve the complexes obtained with Cu(II) salts and (TAcOH) and/or (UAcOH) as ligands. The synthesis and the reaction conditions of the obtained complexes is summarized in **Scheme 2.1**. playing with the reactions conditions such as, the starting metal salt, temperature, pH and solvents, the direct reactions of TAcOH and/or UAcOH in the presence of copper(II) salts lead to the formation of different complexes ranged between (i) mononuclear complexes, **[Cu(TAcO)$_2$(H$_2$O)$_4$]·4H$_2$O** ***(1)*** and **[Cu(UAcO)$_2$(H$_2$O)$_4$]** ***(2)***, (ii) dimetallic complexes, **[Cu$_2$(TAcO)$_4$(DMF)$_2$]·2DMF** ***(3)***, **[Cu$_2$(TAcO)$_4$(DMF)$_2$][Cu$_2$(TAcO)$_4$(DMF)(H$_2$O)]** ***(4)***, **[Cu$_2$(TAcO)$_4$(DMSO)$_2$]·6DMSO** ***(5)***, **[Cu$_2$(TAcO)$_4$(DMA)$_2$]·DMA** ***(6)***, **[Cu$_2$(TAcO)$_2$(UAcO)$_2$(DMF)$_2$]** ***(7)*** and **[Cu$_2$(UAcO)$_4$(DMSO)$_2$]·2DMSO** ***(8)*** and (iii) 1D-CPs, **[Cu(TAcO)$_2$(H$_2$O)$_2$]$_n$** ***(9)*** and **[Cu$_{1.5}$(TAcO)$_2$(H$_2$O)(OH)]$_n$·4H$_2$O** (***10***). Moreover, the reactions of copper(II) nitrate trihydrate with TAcOH in the presence of 4,4'-bipyridine (4,4'-bipy) as linear bridging ligand (auxiliary ligand), lead to the formation of two different complexes, **[Cu(TAcO)$_2$(4,4'-bipy)(H$_2$O)]$_n$·2H$_2$O** ***(11)*** and **[Cu$_2$(TAcO)$_2$(4,4'-bipy)]$_n$** ***(12)***.

The purity of all the complexes have been confirmed by powder X-ray diffraction (PXRD), (see appendix **B**).

The IR spectrum of complexes **1-12** have shown significant shifts in the υ(C=O) and υ(C-O) stretching vibrations with respect to the free ligands that confirm the coordination of the carboxylate groups of the TAcOH or/and UAcOH ligands to copper(II) ion. Additionally, the coordination mode for the carboxylate groups can be inferred from the difference between the asymmetric and symmetric vibrations of the COO^- groups ($\Delta = \upsilon COO_{asym} - \upsilon COO_{sym}$) **Table 2.2**.[51, 53-56]

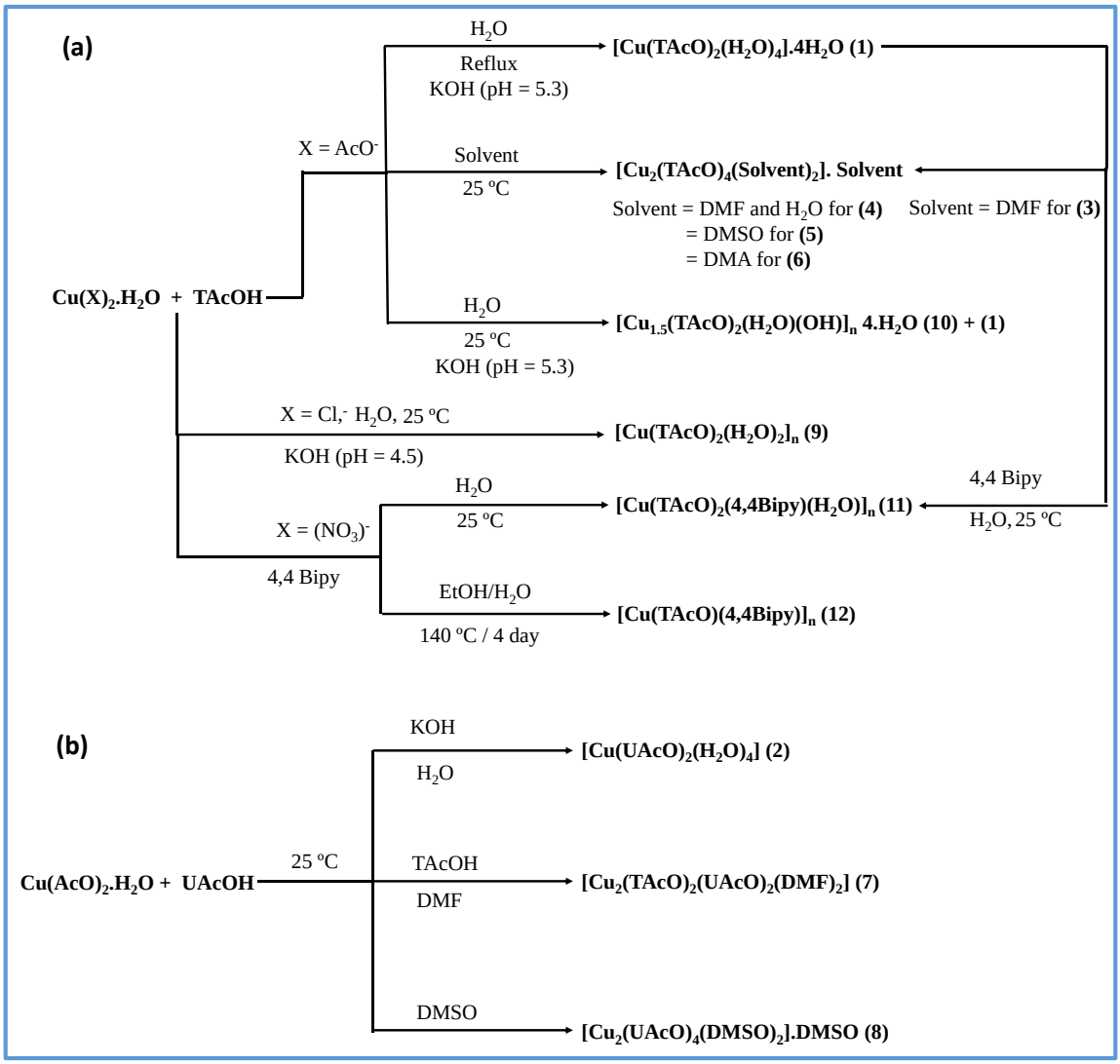

Scheme 2.1. Schematic representation of complexes (**1-12**) obtained by the reactions of Cu(II) salts with TAcOH and /or UAcOH ligands.

Table 2.2. Shows the Δ values of complexes **1-12** correlated with the coordination mode of the carboxylate groups.

Complexes	$\upsilon(COO)_{asym}$ (cm^{-1})	$\upsilon(COO)_{sym}$ (cm^{-1})	$\Delta(\upsilon_{asym} - \upsilon_{sym})$ (cm^{-1})	Coordination modes
1	1678	1404	274	monodentate mode
2	1711	1411	300	monodentate mode
3	1626	1475	151	bridging mode (syn-syn)
4	1630	1467	163	bridging mode (syn-syn)
5	1645	1468	177	bridging mode (syn-syn)
6	1602	1436	166	bridging mode (syn-syn)
7	1630	1456	174	bridging mode (syn-syn)
8	1651	1459	192	bridging mode (syn-syn)
9	1647	1428	219	bridging mode
10	1696	1402/1475	294/221	bridging and monodentate modes
11	1704	1419	285	monodentate mode
12	1643	1427	216	bridging mode

Structure descriptions

The crystal structure of complex **1** consists of discrete complex with the formula $[Cu(TAcO)_2(H_2O)_4]$ and crystallization water molecules (**Figure 2.7**). On the other hand, the structural characterization of complex **2** indicates that its crystal structure is isostructural with complex **1** and formulated as $[Cu(UAcO)_2(H_2O)_4]$ (**Figure 2.8**). The metal center, for complexes **1** and **2**, present a CuO_6 coordination environment with the usual Jahn-Teller tetragonally elongated octahedral geometry. The basal plane implies two carboxylate oxygen atoms from, two TAcO ligands for complex **1** or from two UAcO ligands for complex **2**, and two coordinated water molecules (O1w and $O1w^i$) for everyone in the both complexes (**1** and **2**). The two apical positions for both complexes are occupied by additional coordination water molecules (O2w and $O2w^i$) with longer coordination bond distances (2.53(14) *vs.* 1.94(14) and 1.96(13) Å) in complex **1** and (2.59(2) *vs.*1.94 (14) and 1.87(13) Å) for complex **2**. The functionalized thymine moiety in complex **1** and functionalized uracil moiety in complex **2** coordinate only through one of its carboxylic oxygen atoms whereas the other are involved in an intramolecular hydrogen bonding interaction with the apical coordination water molecules (**Figure 2.7c** and **Figure 2.8c**). The thymine base in complex **1** and uracil base in complex **2** that are not involve in metal coordination leading to an intricate network of hydrogen bonding interactions with the water molecules that provided cohesion to the 3D crystal building. There is no evidence of direct hydrogen bonding or aromatic interaction among the nucleobases in complexes **1** and **2**.

X-ray studies for complexes (**3**-**8**) confirm that all these complexes present a paddle-wheel $[Cu_2(RAcO)_4(solvent)_2]$ entities where R = thymine (T) (**3**-**6**), R = T and uracil-1-methyl (U) (**7**) and R = U (**8**); solvent = water and dimethylformamide (DMF) **4**), (DMF, **3** and **7**), dimethylacetamide (DMA, **6**) and dimethyl sulfoxide (DMSO, **5** and **8**) (**Figure 2.9**).

For complexes (**3**-**8**), four bridging carboxylate ligands are linked to the copper(II) atoms, through a *syn-syn* μ-1κ*O*:2κ*O'* coordination mode, to provide the core of the paddle-wheel shaped dinuclear units. Two solvent molecules occupy the apical positions resulting in an elongated square pyramidal coordination environment of the metal centres. **Figure 2.9** shows a perspective view of the dimeric entity together with the labelling scheme, which is conventionally, accepted for thymine and uracil nucleobases for

chemical and biological purposes, while the coordination bonds and angles are gathered in (**Table A.6**, Appendix **A**).

In complexes (**3-8**), the intradinuclear copper···copper distances are between 2.64 to 2.68 Å. The major differences come from the supramolecular assembly through complementary hydrogen bonding interactions involving the thymine and uracil residues of the carboxylate ligands.

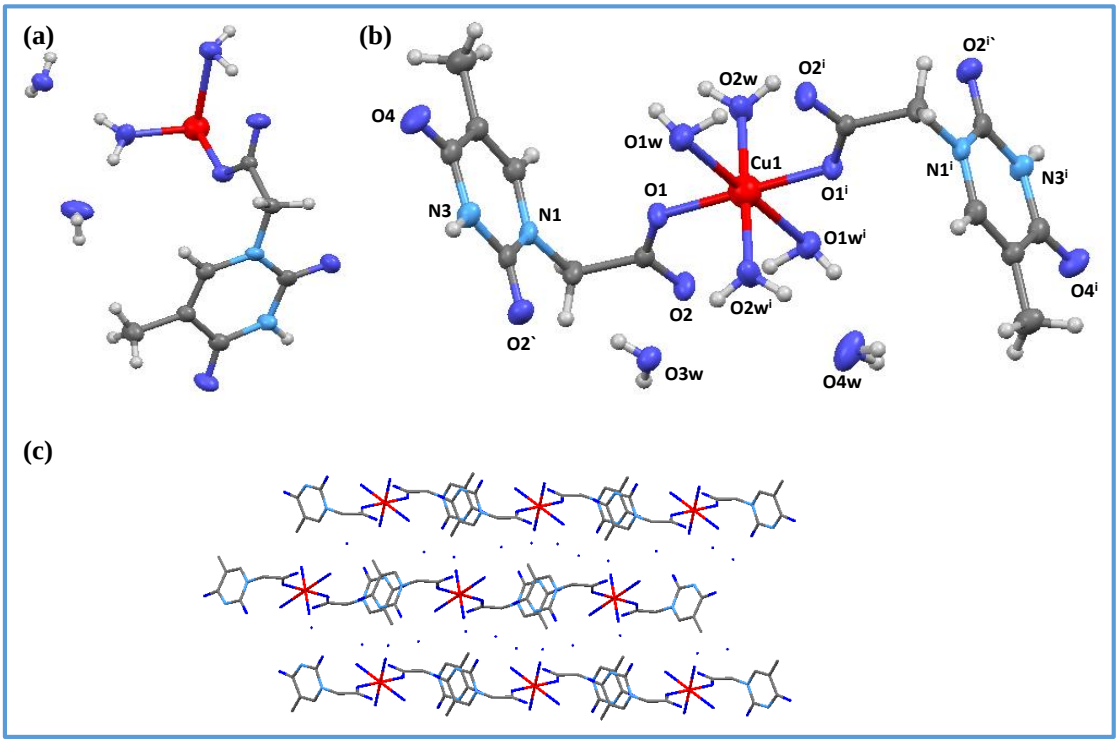

Figure 2.7. Asymmetric unit (a), monomeric entity (b), and view of the crystal packing along the crystallographic c axis (c) of complex **1**. Hydrogens have been omitted for clarify**.** General colour code in this chapter is; O, light blue, N, dark blue, Cu, red, C, grey and H, white.

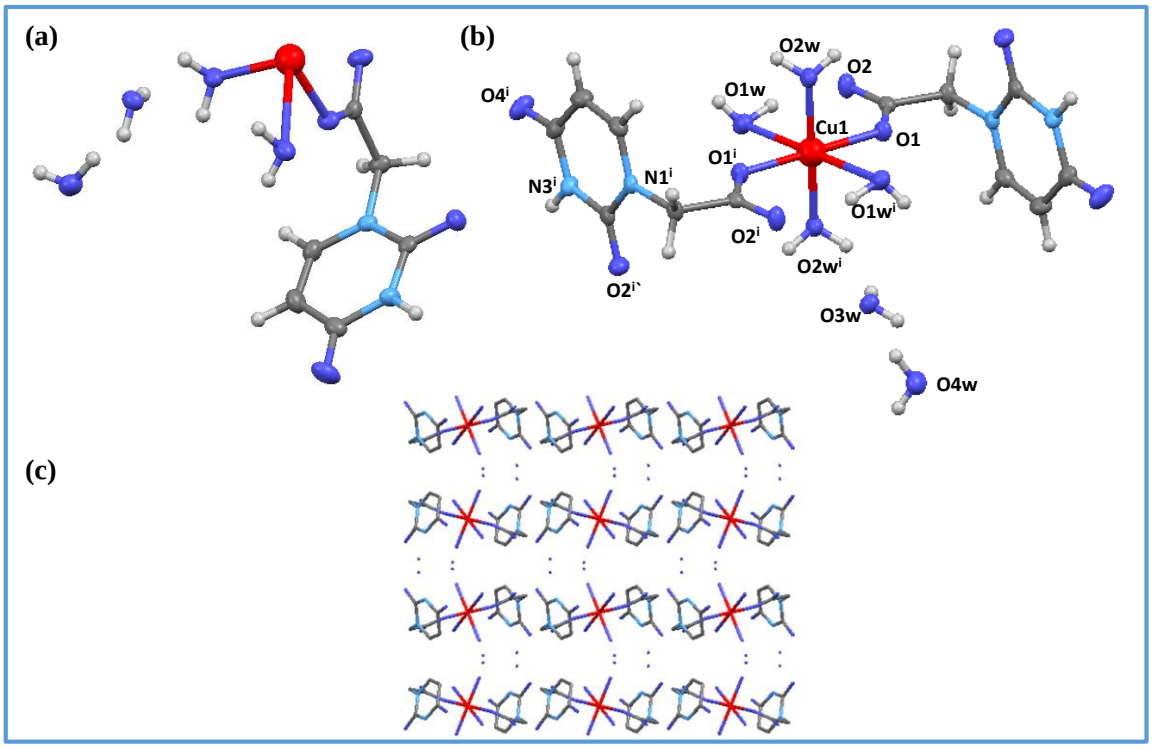

Figure 2.8 Asymmetric unit (a), monomeric entity (b), and view of the crystal packing along the crystallographic c axis (c) of complex **2**. Hydrogens have been omitted for clarify.

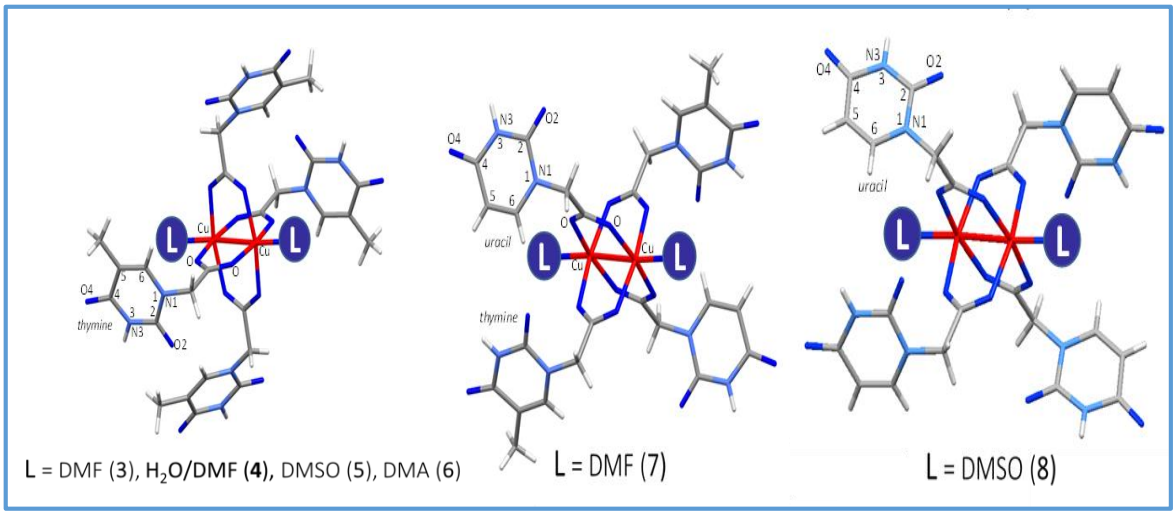

Figure 2.9. Dimeric entities found in complexes **3**-**8**. The usually accepted numbering scheme of the pyrimidinic nucleobases is indicated.

The crystal structure of complex **3**, $[Cu_2(TAcO)_4(DMF)_2]\cdot DMF$, consists from a paddle-wheel dimeric entity that is formed by the coordination of $TAcO^-$ ligands through its carboxylate groups and having DMF capping the apical positions (**Figure 2.10**). The thymine residue is neither involved in metal coordination nor in a complementary hydrogen bonding interaction between thymine residues. Instead of that, it presents

double N3-H···$O_{carboxylate}$ hydrogen bonds involving two *trans* arranged thymine-1-acetato ligands, giving rise to a supramolecular linear chain that runs along the crystallographic *b* axis. This supramolecular assembly is reinforced by π-π stacking interactions between the thymine residues (**Table A. 7**, Appendix **A**). The two remaining thymine-1-acetato ligands are hydrogen bonded through the N3-H donor position to the oxygen atom of the crystallization DMF molecules.

The crystal structure of complex **4** (**Figure 2.11a**) comprises two different dimeric entities that differ in the solvents molecules occupying the apical positions. The first dimer involve two DMF molecules coordinated through its oxygen atom to both apical positions (similar to complex **3**), but the second dimer presents a water molecule and a DMF molecule occupying the two apical positions of the dimer.

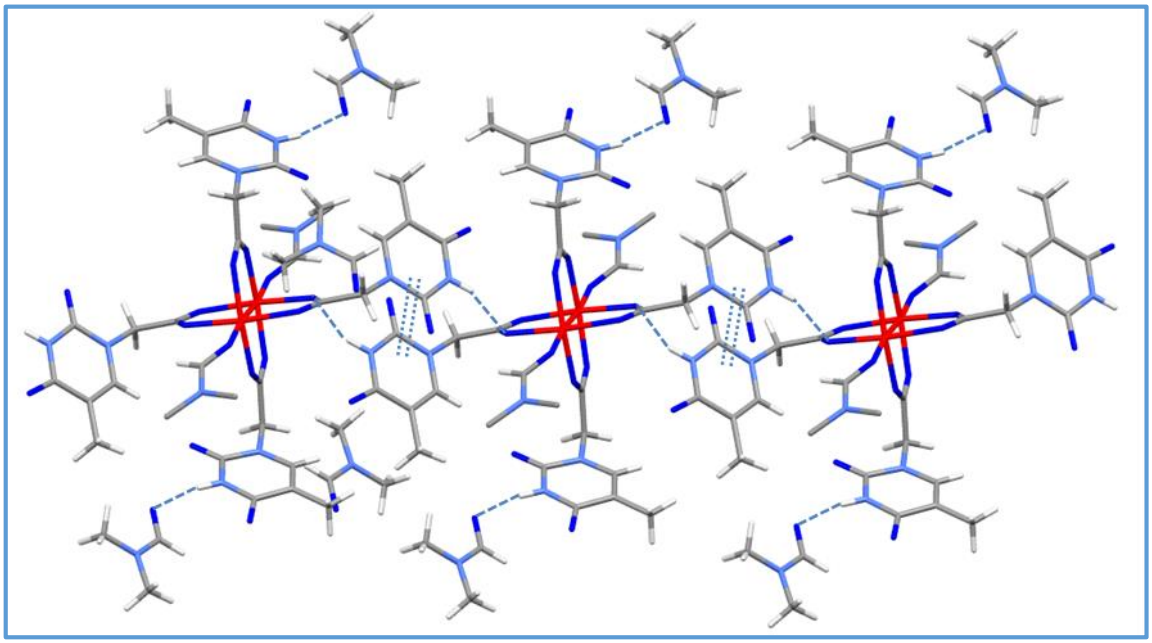

Figure 2.10. Hydrogen bond sustained 1D supramolecular chain of dimeric entities found in complex **3**. Double dashed lines indicate π−π stacking interactions.

The thymine residue is not involved in metal coordination and exposes its Watson-Crick edge, ready to establish a recognition process with other thymines from adjacent dimeric complexes. These interactions imply double N3-H···O2 and N3-H···O4 hydrogen bonds involving the N3-H donor group and O2/O4 acceptor positions. These interactions provide a supramolecular structure containing a 2D interconnected channel system

comprising 71.1% of the unit cell volume (**Figure 2.11b**). However, the real crystal structure implies two of these supramolecular networks mutually interpenetrated. Interestingly, these two interpenetrated networks still left space for channels running along the crystallographic *a* axis that represent 42.2% of the total volume. This void volume in the channels implies a possible porosity in this complexes. In order to check this possibility we have performed two different kinds of experiments. In the first one, taking into account the thermogravimetric analysis of complex **4** (**Figure 2.12a**) and, in order to check the stability of the crystal structure after removing the solvent molecules from the pores, the sample has been subjected to vacuum at 90 °C for 24 h. This experiment has resulted in an amorphous solid (**Figure 2.12b**), suggesting that the structure has collapsed after removal of the guest solvents. In a second experiment, the sample has been exposed to EtOH vapours for several days in order to check possible solvent exchange. TGA analyses and X-ray powder diffraction data (**Figure 2.12c**, **d**) have shown that after one week in these conditions there is no solvent exchange.

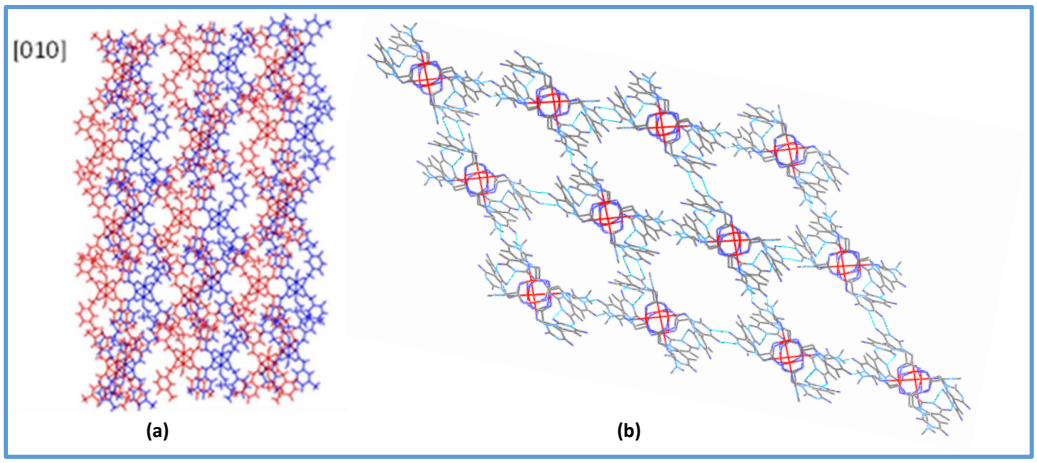

Figure 2.11. Complex **4**: (a) Double interpenetrated supramolecular final structure. (b) Supramolecular network sustained by base pairing interactions between the thymine residues showing 1D channels in the interpenetrated final structure. Dashed lines indicate hydrogen bonding interactions.

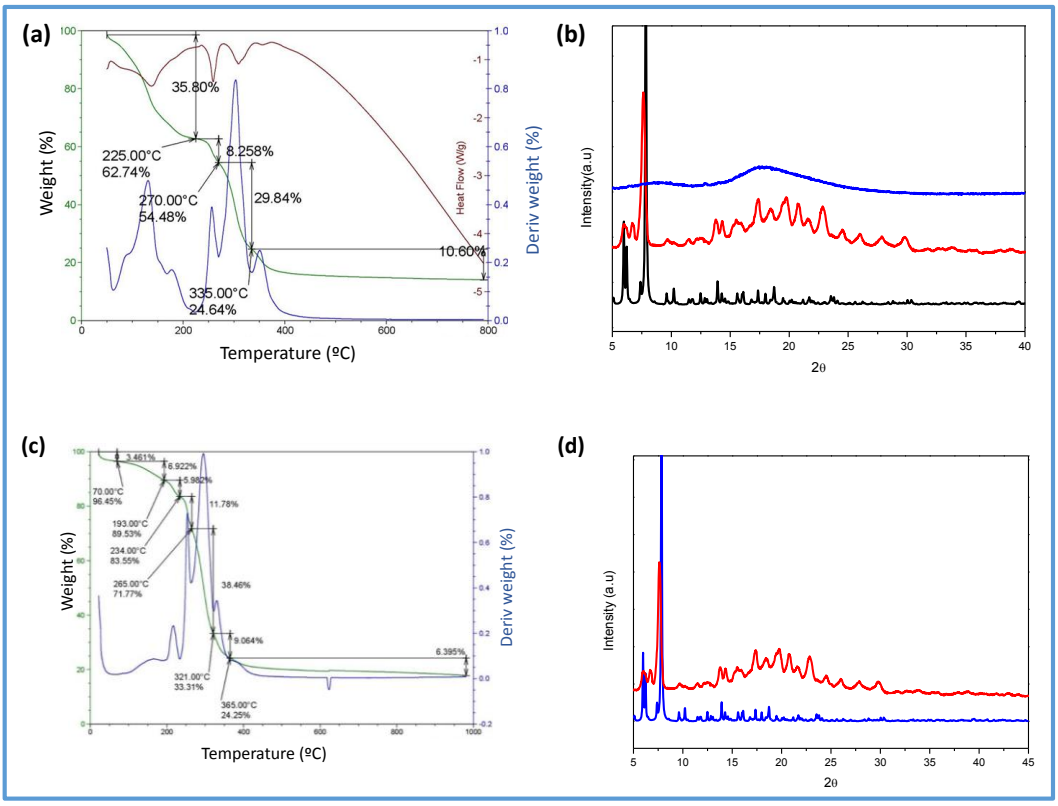

Figure 2.12. Thermogravimetric analysis of complex under nitrogen gas with flow rate 90 mL/min and heating rate 10 ºC/min for complex **4** (a), and after exposed to ethanol gas for 3 days (c). (b) DRX powder diffractogram of simulated and solid of complex **4** (black and red lines respectively) and after making vacuum 24 h heating at 90ºC (blue line). (d) Simulated X-ray powder diffractogram of complex **4** (blue line) and X-ray powder diffractogram of a polycrystalline sample of complex **4** after exposure for ethanol gas for one week (red line).

Complex $[Cu_2(TAcO)_4(DMSO)_2]\cdot 4.5DMSO$ (**5**) presents again an assembly of $[Cu_2(TAcO)_4(DMSO)_2]$ dimeric units into supramolecular chains through hydrogen bonding interactions. Albeit, there are not direct hydrogen bonds between the dimeric entities but crystallization DMSO mediated N3-H···O_{DMSO}···H-N3 ones (**Figure 2.13**). Nevertheless, there are clear evidences of π-π stacking interactions between the thymine residues that reinforce the 1D supramolecular aggregate (**Table A. 7**, Appendix **A**). The final 3D supramolecular structure of complex **5** is only sustained by weak van der Waals interactions.

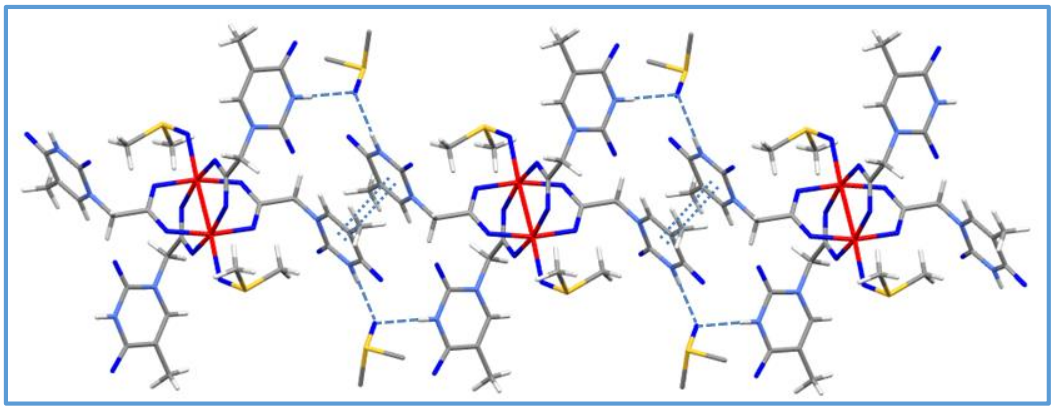

Figure 2.13. Hydrogen bonded supramolecular 1D chain founded in complex **5**. Double dashed lines indicate π-π stacking interactions.

The crystal structure of complex $[Cu_2(TAcO)_4(DMA)_2]\cdot DMA$ (**6**) is more complex as two crystallographically independent $[Cu_2(TAcO)_4(DMA)_2]$ dimeric entities are coexisted. The first one establishes complementary N3-H···O4 hydrogen bonding interactions through two *trans* arranged thymine-1-acetato ligands. The remaining carboxylato ligands are involved in a double N3-H···$O_{carboxilato}$ intermolecular hydrogen bond that is reinforced by π-π stacking interactions between the thymine residues (**Table A. 7**, Appendix **A**). The combination of all these interactions generates a 2D rectangular grid of dimeric entities (**Figure 2.14a**). The crystallographically independent second $[Cu_2(TAcO)_4(DMA)_2]$ dimeric units are held together into linear supramolecular chains, through N3-H···$O_{carboxilato}$ intermolecular hydrogen bonds involving two *trans* arranged thymine-1-acetato ligands (**Figure 2.14b**). These hydrogen bonds are reinforced by π-π stacking interactions between the thymine residues. The two remaining thymine-1-acetato ligands are hydrogen bonded through the N3-H donor position to the oxygen atom of the crystallization DMA molecules. These supramolecular chains are sandwiched between the previously described supramolecular sheets but there is no structural evidence of additional interactions apart from weak van der Waals interactions.

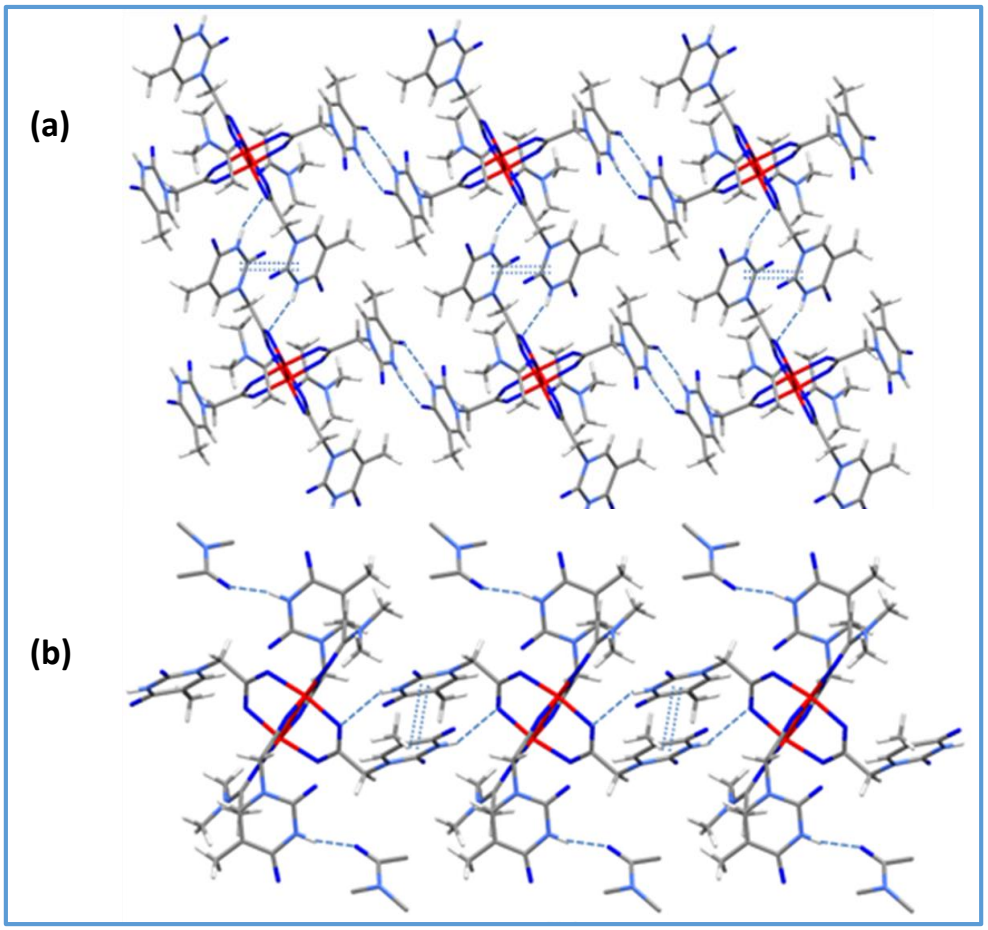

Figure 2.14. Supramolecular assemblies found in complex **6**: (a) 2D rectangular grid of dimeric entities and (b) supramolecular linear chains. Double dashed lines indicate π-π stacking interactions.

The building unit of complex **7**, $[Cu_2(TAcO)_2(UAcO)_2(DMF)_2]$, is similar to all the previous cases, a paddle-wheel shaped dimeric complex, but now replacing two of the thymine-1-acetato ligands by uracil analogues. The dimeric complex establishes complementary N3-H···O4 hydrogen bonding interactions through two *trans* arranged thymine-1-acetato ligands, whereas the remaining uracil-1-acetato ligand are involved in a double N3-H···$O_{carboxilato}$ intermolecular hydrogen bond that is reinforced by π-π stacking interactions between the aromatic rings of the uracil residues (**Table A. 7**, Appendix **A**). The combination of both supramolecular interactions generated a 2D rectangular grid of dimeric entities (**Figure 2.15a**). These sheets are held together by means of weak van der Waals interactions.

Similar to all the previous cases, complex **8**, $[Cu_2(UAcO)_4(DMSO)_2]\cdot DMSO$, is forming from a paddle-wheel shaped dimeric unit where all the uracil residue forming the dimeric entities of $[Cu_2(UAcO)_4(DMSO)_2]$, are involved in base pairing interactions (double N3-

H···O2 hydrogen bond) to provide supramolecular sheets of the dimeric complex entities (**Figure 2.15b**). Solvation DMSO molecules are placed in the space between adjacent sheets.

Complex **9** presents 1D polymeric complex in which the copper(II):water ratio is less with respect to complex **1**, being the TAcO ligand forced to occupy the empty coordination sites of the elongated octahedral geometry (**Figure 2.16**). The carboxylato group of the thymine adopted a μ-1κ*O*:2κ*O´* coordination mode in such a way it is coordinated through O1 to the equatorial plane of one copper(II) atom and through O2 to the apical position of an adjacent copper(II) atom, 1.945(2) and 2.624(2) Å respectively. The carboxylate group is almost coplanar with the Cu1-O1 bond but almost perpendicular to Cu1^{ii}-O2. Two *trans* water molecules completed the coordination equatorial plane. These coordinated water molecules further contributed to the cohesion within the chain by means of intrachain hydrogen bonds that they established as donors with the thymine O2´ and the carboxylate O2 oxygen atoms as acceptors. The copper···copper distance within the chain is 4.5896(3) Å. The thymine bases are projected outward the 1D chain allowing the establishment of complementary hydrogen bonding interactions (N3-H···O4) between thymine fragments belonging to adjacent chains. This interaction provided 2D supramolecular sheets of complex chains that are held together by means of weak van der Waals interactions.

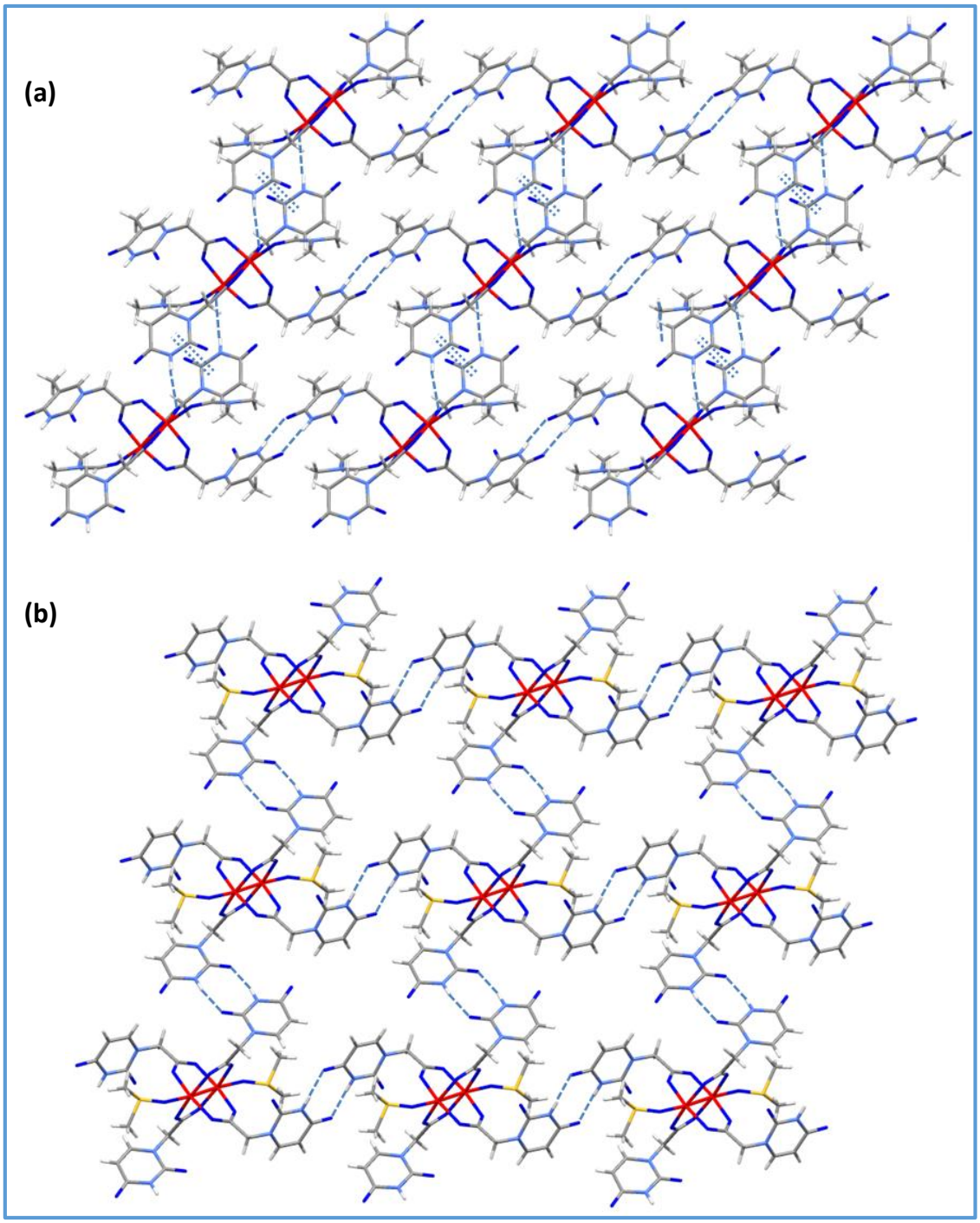

Figure 2.15. Supramolecular 2D rectangular grid of dimeric entities found in complex **7** (a) and **8** (b). Double dashed lines indicate π-π stacking interactions.

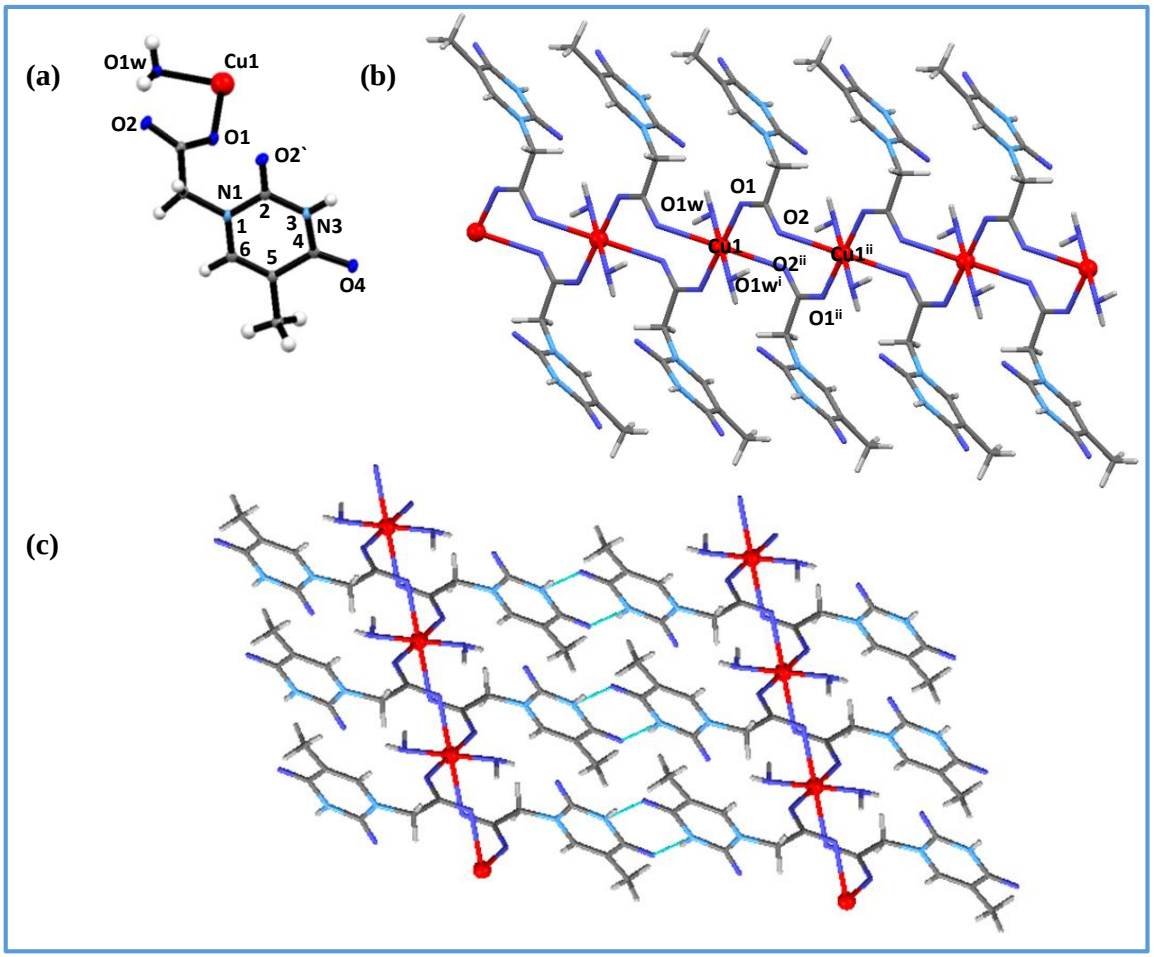

Figure 2.16. (a) Asymmetric unit of complex **9**. (b) Fragment of the polymeric chain of complex **9**. (c) Supramolecular 2D network resulting from the base pairing between adjacent polymeric chains of complex **9**.

Complex **10** corresponds to a 1D polymeric complex in which hydroxide anions help the TAcO ligands to connect the copper(II) metal centers. In fact, two crystallographically independent copper(II) centers are presented in the crystal structure of this complex (**Figure 2.17a-c**). Both are octahedrally coordinated but Cu1, sited on a symmetry center, is bonded to two hydroxide anions and four oxygen atoms belonging to the carboxylate group of four TAcO ligands, whereas Cu2, located in a general position, completed its coordination polyhedron with two hydroxide anions, a water molecule and three oxygen carboxylate atoms from three TAcO ligands. Both the hydroxide and the TAcO ligands act as bridges to link the metal centers within the chain. The hydroxide anion connects three metal centers in an almost symmetrical fashion (bond distances: 1.963-1.966 Å). There are two crystallographically independent TAcO ligands (TAcO-1 and, TAcO-2) that bridge the adjacent metal centers showing different coordination modes

(**Figure 2.17a**). The first ligand, TAcO-1, uses its two carboxylate oxygen atoms to bridge three metal centers (μ_3-1κ*O*:2κ*O*:1κ*O'*), whereas the second ligand, TAcO-2 uses only one carboxylate oxygen atom to bridge two metal centers (μ-1κ*O*:2κ*O*). The equatorial positions of the Cu coordination spheres are occupied by the carboxylato oxygen atoms of the TAcO-1 ligand, the hydroxide anion and the water molecule with short coordination bond distances (1.93-1.99 Å). The TAcO-2 ligand and one carboxylato oxygen atom from the TAcO-1 ligand occupy the apical positions (2.34-2.68 Å). This connectivity scheme leads to a linear array of fused metal triangles that share an edge and the opposite vertex of each triangle where three different metal···metal distances could be identified (Cu1···Cu2: 3.003(2); Cu1···Cu2^{ii}: 3.302(2) and Cu2···Cu2^{ii}: 2.9734(14) Å) (**Figure 2.17c**-**b**). The thymine residue of the TAcO ligands remains free to establish additional supramolecular interactions that ensure the 3D cohesiveness of the crystal structure. These supramolecular interactions comprise two different supramolecular recognition processes involving thymines residues that hold chains together: i) a double hydrogen bond (N3-H···O4^{i}) between the TAcO-2 ligands and ii) two hydrogen bonds established between the TAcO-1 ligand, and the coordinated water molecule and a carboxylate oxygen atom from another TAcO-1 ligand. The crystallization water molecules also reinforce previously described interactions by means of an extensive network of hydrogen bonds (**Figure 2.17d**).

Complexes **11** and **12** have been obtained through a simple one-pot reaction between Cu(II) nitrate, TAcOH, and 4,4´-bipy by hydrothermal reactions (see section 5.3).

Crystal structure of complex **11** is composed of linear 1D chains in which the metal centers are bridged by 4,4´-bipyridine (4,4´-bipy) ligands that impose a Cu···Cu distance of 11.124 Å. The coordination sphere of the copper(II) metal center adopts an axially elongated square pyramid geometry (**Figure 2.18**). The basal plane being occupied by the two carboxylate oxygen atoms from two TAcO ligands in *trans* arrangement. The apical position is occupied by a water molecule with a significantly longer coordination bond distance than those placed in the basal plane (2.31 Å *vs* 1.97-2.01 Å). The metal center is displaced 0.140 Å from the basal plane towards the apical position. The 4,4´-bipy bridging ligand is twisted 61.20º with respect to the mean basal plane. The shape of the coordination polymer in the solid state is best described as a linear ribbon of dimensions 1.9 x 0.8 nm (**Figure 2.18**). The supramolecular 3D structure is sustained by a complex network of hydrogen bonds (**Figure 2.18**). The stronger hydrogen bonds involve the

water molecules as donor of hydrogen bonds to the carboxylate oxygen atoms and as acceptor from the thymine N3-H position. There are also less strong C-H···O hydrogen bonds involving the aromatic C-H positions of the 4,4´-bipy bridging ligand and thymine residue as donors and the thymine ketone groups as acceptors. It is worth to note that there is no base pairing interactions between the thymine residues probably due to the presence of water molecules that disrupt these interactions. There is no evidence of π-π stacking interactions.

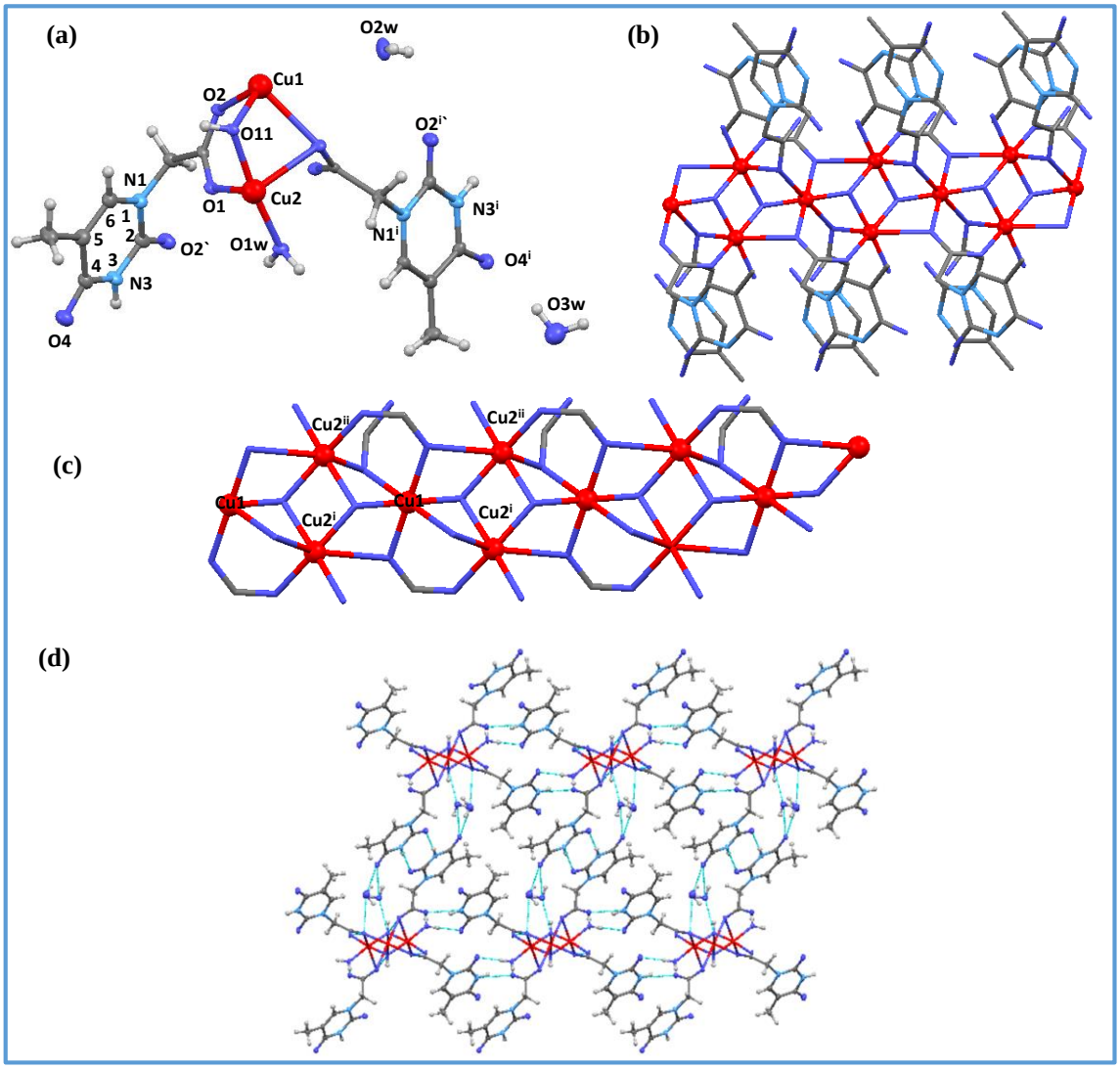

Figure 2.17. (a) Asymmetric unit of complex **10**, (b) Fragment of the polymeric chain of complex **10**. (c) Schematic representation of the chain topology. The rest of the TAcO ligand has been removed for clarity. (d) Supramolecular structure founded in complex **10**.

Crystal structure of complex **12** is composed of linear 1D chains where the coordination sphere of the copper(I) metal centers adopt trigonal geometry. The coordination sphere of the Cu(I) ion consists of one nitrogen atom from 4,4´-bipy and two oxygen atoms from two TAcO ligands (**Figure 2.19a**). Dimeric Cu_2O_2 core was formed by bridging copper (I) centers by two oxygen atoms from carboxylate groups of two TAcO ligands ($\mu_{1,1}$-oxo bridging mode) and this dimer species are extended into 1D chains by linear ligands (4,4´-bipy) (**Figure 2.19b**). The Cu···Cu distance is about 3.17 Å through the Cu_2O_2 dimeric species, indicative of no direct Cu···Cu bonding, whereas the 4,4´-bipy ligands impose the Cu···Cu distance between the dimeric species to 10.90 Å. The thymine bases are projected outward the 1D chain allowing the establishment of complementary hydrogen bonding interactions (N3-H···O4) between thymine fragments belonging to adjacent chains. This interaction provided 2D supramolecular sheets of complex chains that are held together by means of weak van der Waals interactions (**Figure 2.19c**).

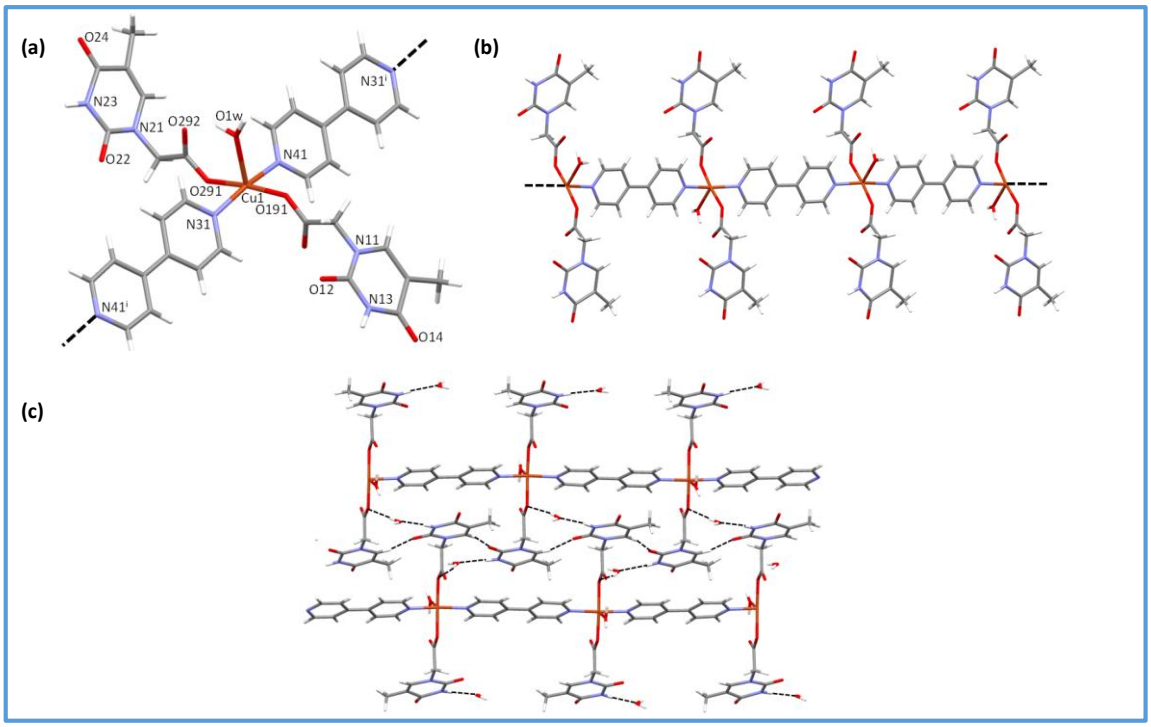

Figure 2.18. (a) Coordination sphere around the copper(II) metal centre. (b) Views of a fragment of the infinite coordination polymer. (c) Fragment of the crystal packing showing some of the most relevant hydrogen bonding interactions. The disorder of the thymine residues has been omitted for clarity.

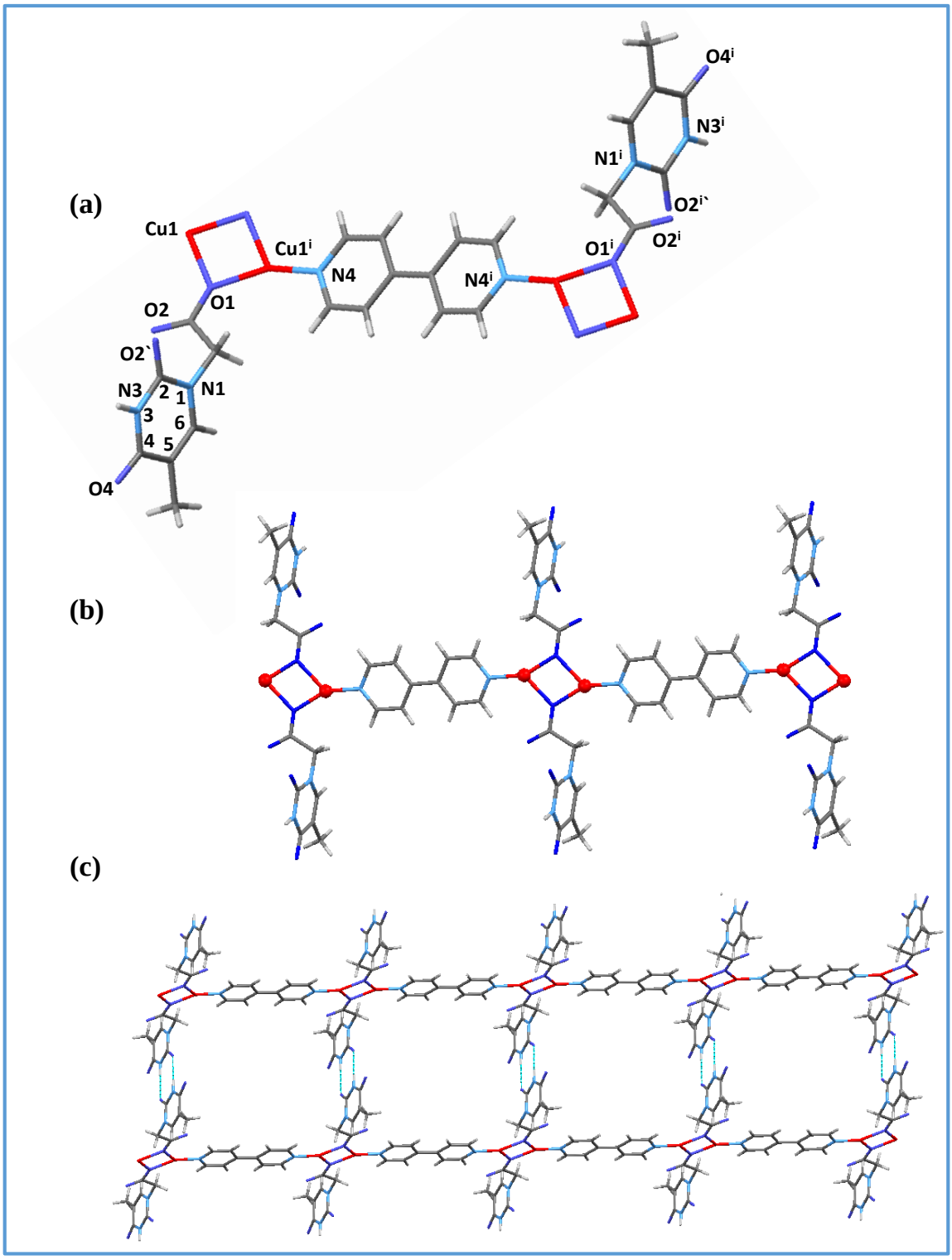

Figure 2.19. (a) Coordination sphere around the copper(I) metal centre of complex **12**. (b) Polymeric chain of complex **12**. (c) Supramolecular 2D network resulting from the base pairing between adjacent polymeric chains of complex **12**.

Structural interconversion study involve the mononuclear, dimetallic and 1D-CP complexes

Interestingly, when a microcrystalline sample of $[Cu_2(TAcO)_4(DMF)_2]_3[Cu_2(TAcO)_4(DMF)(H_2O)]$ (**4**) is exposed to a saturated humidity atmosphere it undergoes, within few hours, a quantitative non-trivial crystal-to-crystal transformation, to the blue 1D coordination polymer $[Cu(TAcO)_2(H_2O)_2]_n$ (**9**) (**Figure 2.20c**, **d**). However the treatment of microcrystals of **4** with large excess of water, immediately and quantitatively reverse to the starting mononuclear complex $[Cu(TAcO)_2(H_2O)_4]\cdot 2H_2O$ (**1**) (**Figure 2.20a**, **b**). The last transformation is also corroborated for complexes **5** and **8**, which after water addition transformed to complexes $[Cu(TAcO)_2(H_2O)_4]\cdot 2H_2O$ (**1**) and $[Cu(UAcO)_2(H_2O)_4]\cdot 4H_2O$ (**2**), respectively (**Figure 2.21**).

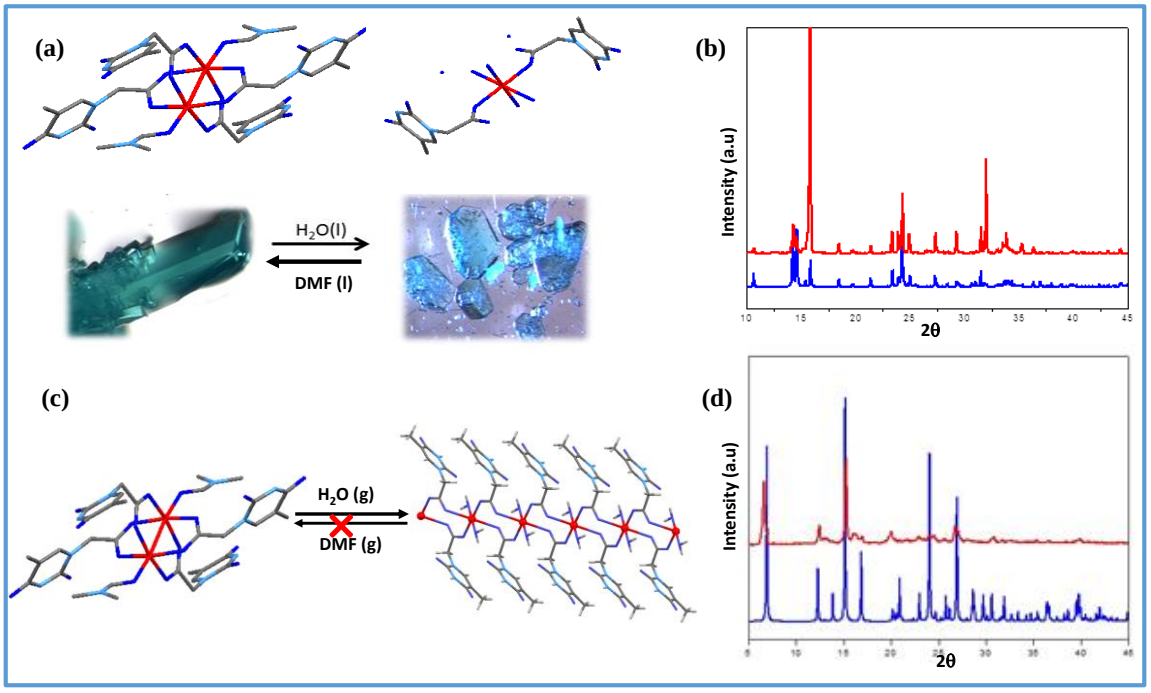

Figure 2.20. Schematic representation of exposure of the dimetallic units fragment $[Cu_2(TAcO)_4(DMF)_2]$ in (**4**) to liquid water (a) or vapor of water (c) induced destruction of the $[Cu_2(TAcO)_4(DMF)_2]$ (**4**) to produce $[Cu(TAcO)_2(H_2O)_4].2H_2O$ (**1**) or $[Cu(TAcO)_2(H_2O)_2]_n.2H_2O$ (**9**) respectively. (b) X-ray powder diffractogram of complex $[Cu(TAcO)_2(H_2O)_4].2H_2O$ (blue) and X-ray powder diffractogram of complex **4** after add liquid water (red line). (c) X-ray powder diffractogram of complex $[Cu(TAcO)_2(H_2O)_4].2H_2O$ (blue line) and X-ray powder diffractogram of complex **4** after exposure to water vapor (red line).

It is remarkable the significant structural changes induced by water in the coordination sphere of the copper(II) ions going from paddle-wheel dimetallic units in complexes **4**, **5**, and **8** to an octahedral coordination sphere of $[Cu(RAcO)_2(H_2O)_4]\cdot nH_2O$ with R = Thymine (**1**) or Uracil (**2**) (n= 2 (**1**), 4 (**2**)). The reversibility of these transformations were proved by adding dry DMSO for complexes **1** and **2** that lead to the formation of complexes **5** and **8** respectively (**Figure 2.21**)

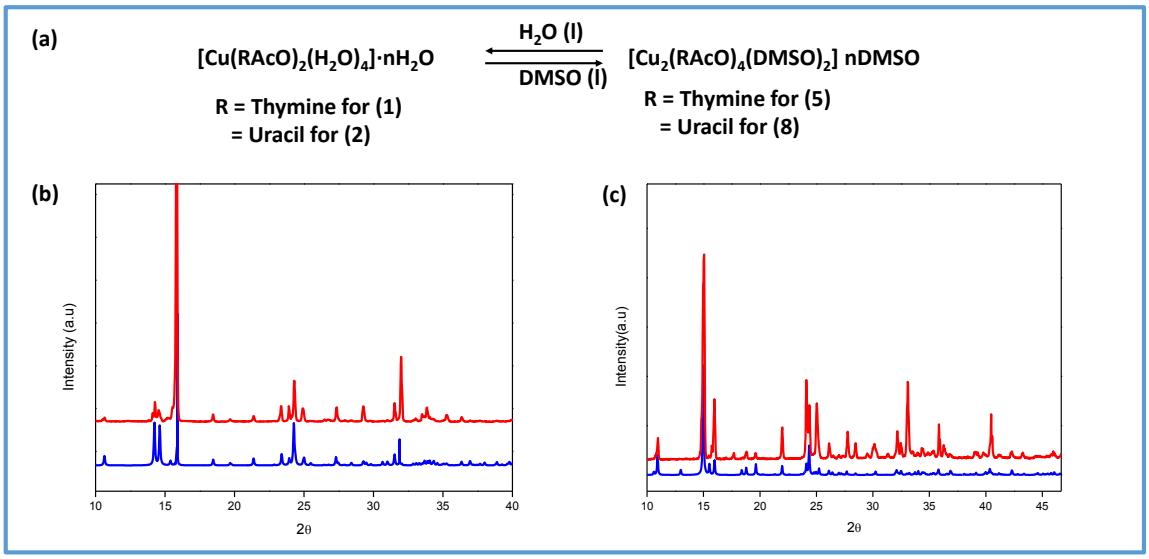

Figure 2.21. (a) Schematic representation of the reversible transformations, induced by solvents, of the paddle wheel complexes (**5** and **8**) to the mononuclear complexes (**1** and **2** respectively) and the reverse. X-ray powder diffractograms of mononuclear complex **1** (b) and **2** (c) (blue lines) and X-ray powder of polycrystalline samples of complex **5** (b) and **8** (c) (red lines) after water addition.

Block B; This block involves the complexes that have been obtained from the reactions of Co(II) salts and TAcOH or UAcOH as ligands (**Scheme 2.2**). The direct reactions of TAcOH or UAcOH in the presence of cobalt acetate monohydrate give raise to the formation of mononuclear complexes (**13** and **14** respectively). On the other hand, the direct reactions of TAcOH or UAcOH with cobalt acetate monohydrate in the presence of another nucleobase, 2,6-diaminopurine (HDap), with the idea to obtain extended 1D polymers and to get insights into possible molecular recognitions between complementary nucleobases, allow the formation of mononuclear complexes (**15** and **16** respectively). In addition, we extended our attempts to obtain extended 1D polymer using 4,4'-bipyridine (4,4'-bipy) as linear bridging ligand but we have gotten mononuclear complex (**17**).

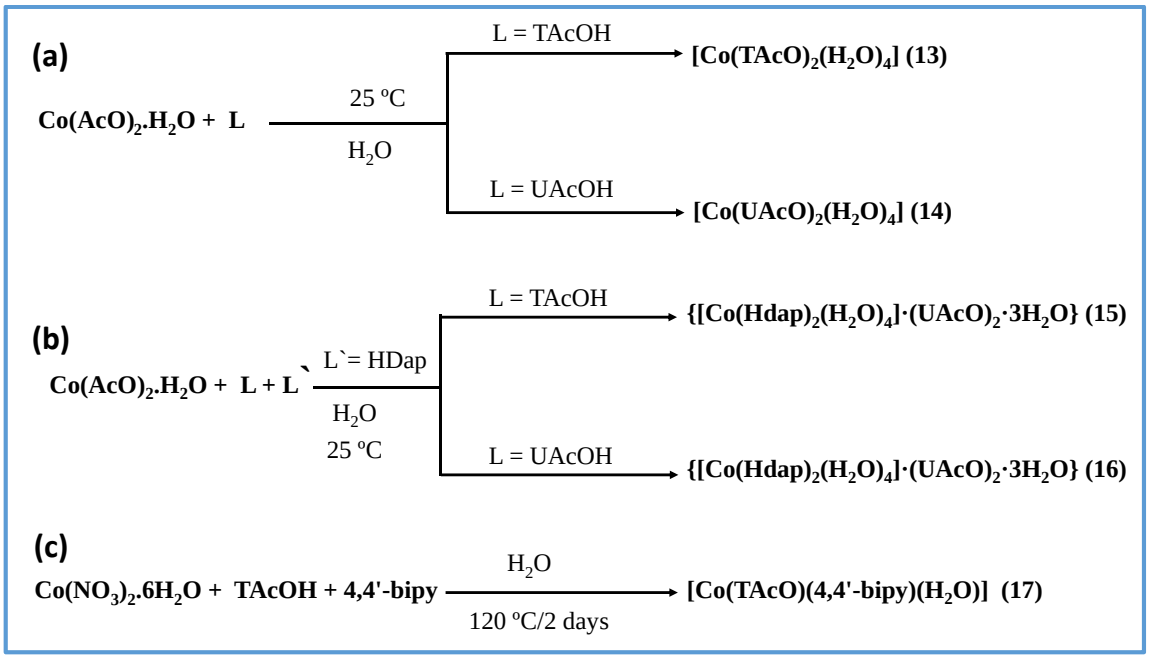

Scheme 2.2. Schematic representation of synthetic methods of complexes (**13-17**).

The crystal structures of complexes **13** and **14** consist of discrete *trans*-$[Co(XAcO)_2(H_2O)_4]$ units, (X=Thymine or Uracil for **13** and **14** respectively). The metal centre in complexes **13** and **14** present a MO_6 coordination environment that has been formed from two carboxylate oxygen atoms from two ligands and four oxygen atoms from water molecules (**Figure 2.22**). Complex **13** shows usual Jahn-Teller tetragonally octahedral geometry with the coordination bond distance established by the carboxylate oxygen atom being slightly shorter than those with the water molecules (2.07 *vs* 2.12 Å).

Complex **14** shows less regular environment than that observed in complex **13** with a bond distance difference of *ca*. 0.1 Å between the two crystallographically independent water molecules (2.14 and 2.05 Å, respectively), whereas the carboxylate oxygen atom coordination bond lies in between (2.10 Å). The functionalized nucleobase moieties coordinated only through one of its carboxylic oxygens whereas the other is involved in an intramolecular hydrogen bonding interaction with coordinated water molecules (**Figure 2.22)**. Therefore, the nucleobase substituents of these ligands are not involved in the metal coordination but they are a key factor that determines the assembling of the discrete complex entities through supramolecular interactions.

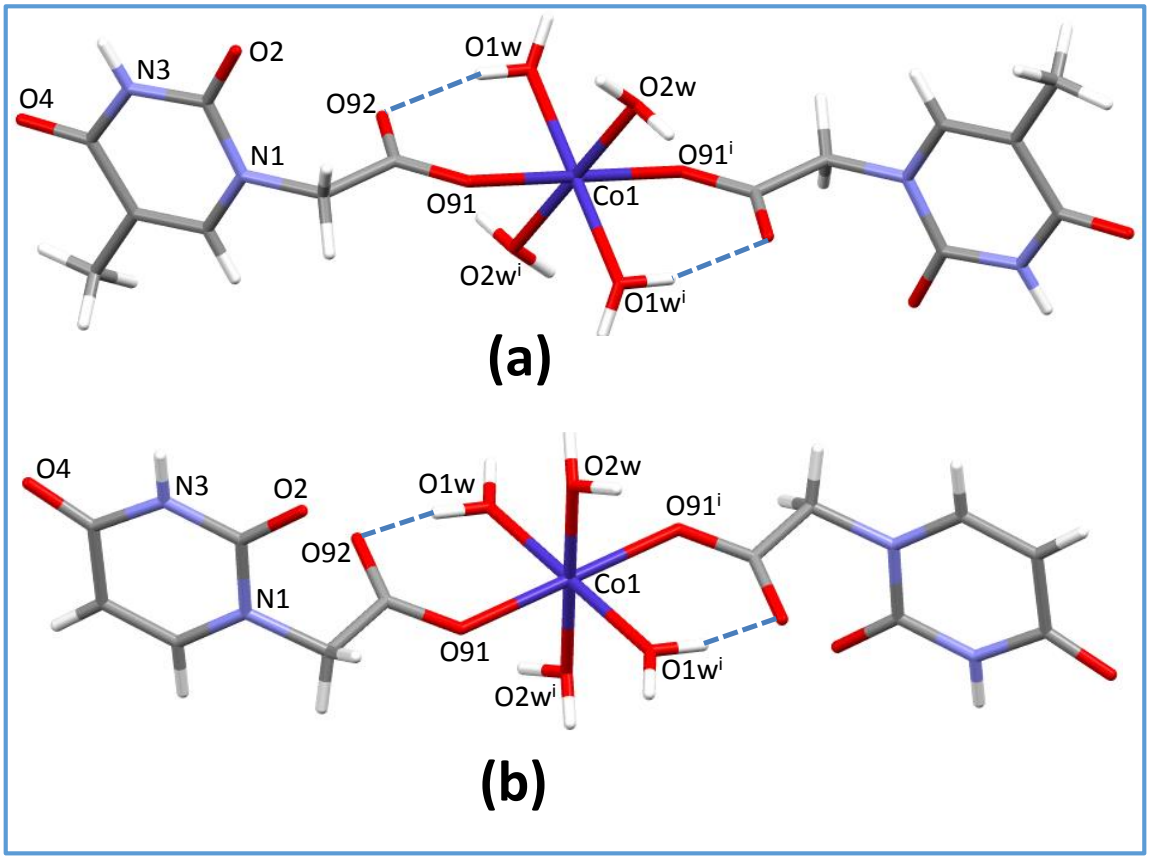

Figure 2.22. Molecular structure of complexes **13** (a) and **14** (b). Dashed lines indicate to the intra H-bonds between the coordinated waters molecules and the oxygens of the carboxylate group. Colours code are; O, red, N, dark blue, Co, blue, C, grey and H, white.

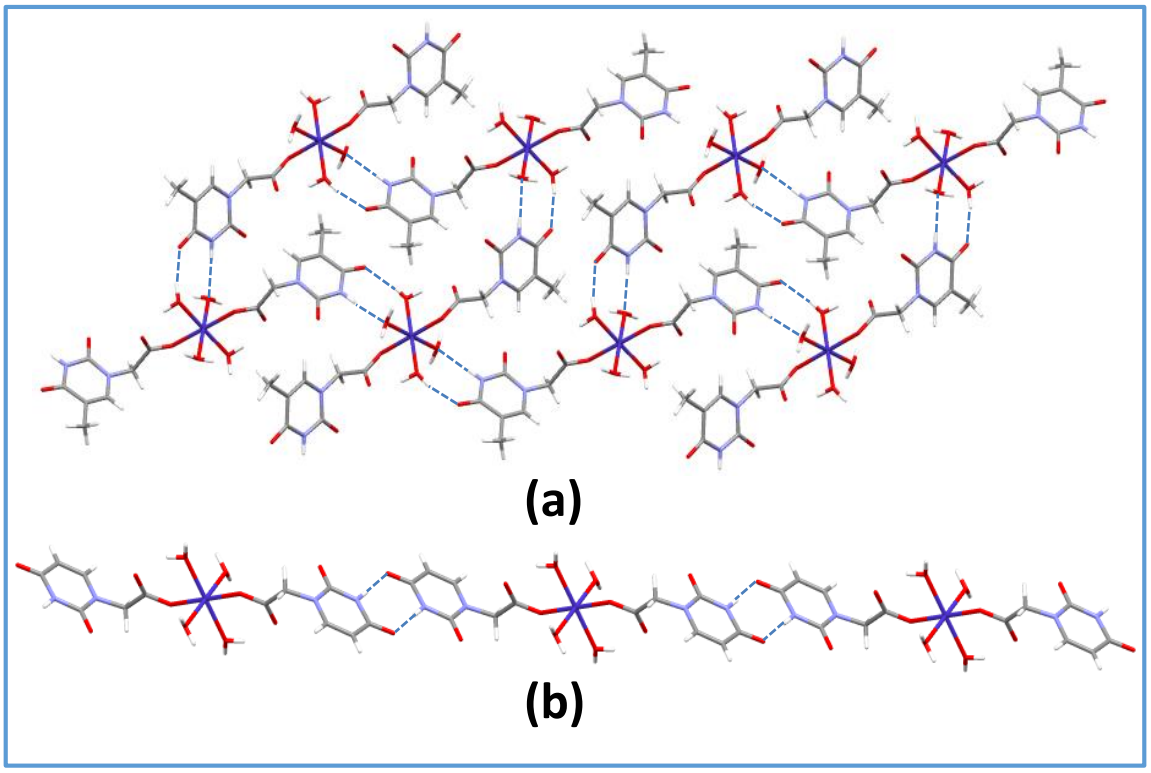

Figure 2.23. Complementary hydrogen bonding interactions involving the thymine residue in complex **13** (a) and the uracil residue in complex **14** (a). Dashed lines indicate to the H-bond.

In fact, there is a significant difference when analysing the supramolecular architectures of complexes **13** and **14**. The assembling of the discrete entities in complex **13** involves the interaction of the thymine residue with the water molecules of the adjacent entities without the presence of direct hydrogen bonding between the nucleobases. These interactions involve the major groove N3-H and O4 positions to establish the double hydrogen bond with two coordinated water molecules of an adjacent monomeric entity, leading to a 2D supramolecular sheet (**Figure 2.23a**). Supramolecular architecture is completed through additional water···water hydrogen bonds that held these supramolecular sheets into a 3D crystal structure.

On the contrary, in complex **14** the uracil residues are able to establish direct complementary hydrogen bonds through its major groove N3-H and O4 positions. It gives rise to 1D supramolecular chains (**Figure 2.23b**) that are held together through additional Ow-H···O2 hydrogen bonds. The different supramolecular assemblies present in both complexes and similarly of their synthesis, seems indicate a stronger uracil···uracil base pairing interaction than the thymine···thymine one.

In complexes **15** and **16**, the coordination environment of the metal centre is quite different with respect to complexes **13** and **14**, as two 2,6-diaminopurine ligands are coordinated to the metal centre in a *trans* arrangement, whereas the $TAcO^-$/$UAcO^-$ anions remain non-coordinated (**Figure 2.24**). The coordination sphere (in both complexes) is completed by four water molecules to form a cationic $[Co(HDap)_2(H_2O)_4]^{2+}$ entities that exhibit octahedral environment (CoN_2O_4). Two of the water molecules help stabilizing the 2,6-diaminopurine coordination mode through N9 position by establishing an intramolecular hydrogen bond with the N3 position of the purine as acceptor.

The difference of supramolecular crystal structure between complexes **14** and **15** coming from the different regimen of H-bond interactions established between Hdap, H_2O, and $TAcO^-$ ion in **15** or $UAcO^-$ ion for **16**.

In case of complex **15**, three H-bonding interactions are responsible for the supramolecular crystal structure: (*i*) double hydrogen bond involving two *cis*-arranged water molecules as donors and the two oxygen atoms of the TAcO carboxylate group, (*ii*) base pairing interaction between the major groove edge of the thymine residues, and (*iii*) base pairing interaction between the HDap N1 and N6-H positions. The combination of these three recognition H-bond interactions leads to 2D supramolecular assemblies (**Figure 2.25a**) which are piled up through additional N7-H$\cdots O_{carboxylate}$ hydrogen bonds. In complex **16**, two H-bonding interactions are responsible for the supramolecular crystal structure: (*i*) double hydrogen bond involving two *cis*-arranged water molecules as donors and the two oxygen atoms of the UAcO carboxylate group (the same observed for complex **15**), and (*ii*) base pairing interaction between the uracil residue and the N1/N6-H positions of the 2,6-diaminopurine ligand involving three hydrogen bonds (uracil: O12, N13-H, O14 and 2,6-diaminopurine: N2-H, N1, N6-H). The combination of these two supramolecular complementary interactions generates 1D supramolecular chains (**Figure 2.25b**) that are connected through additional Ow-H$\cdots O_{carboxylate}$ and N7-H$\cdots O_{carboxylate}$ hydrogen bonds.

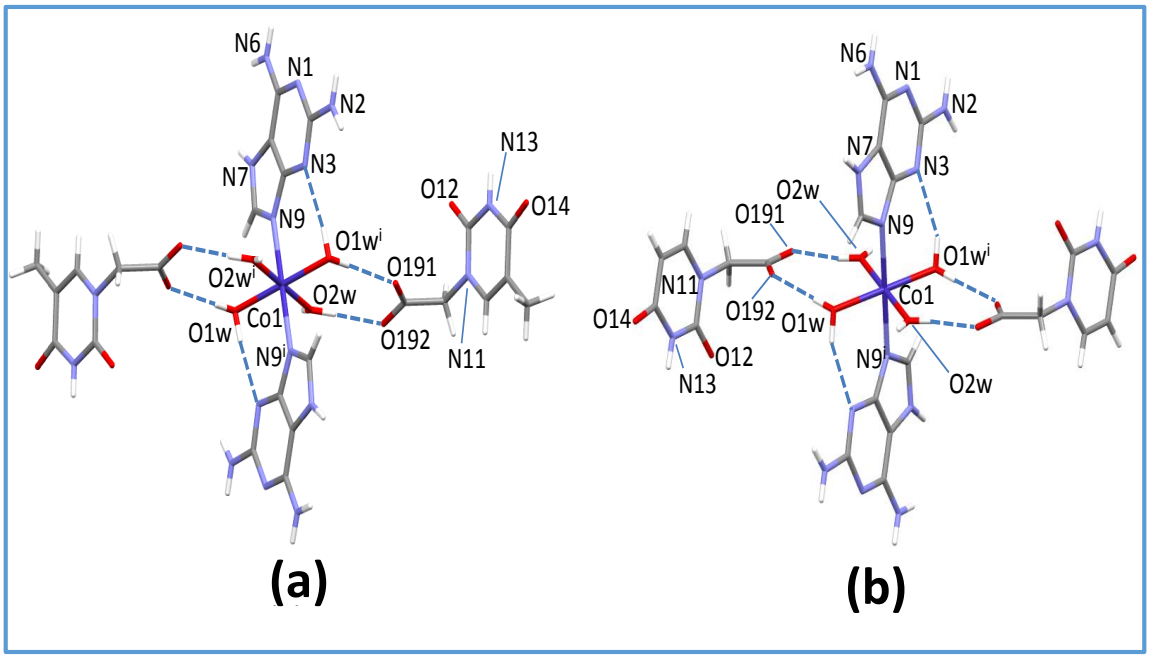

Figure 2.24. Molecular structure of complexes **15** (a) and **16** (b). Dash lines represent the H-bonds.

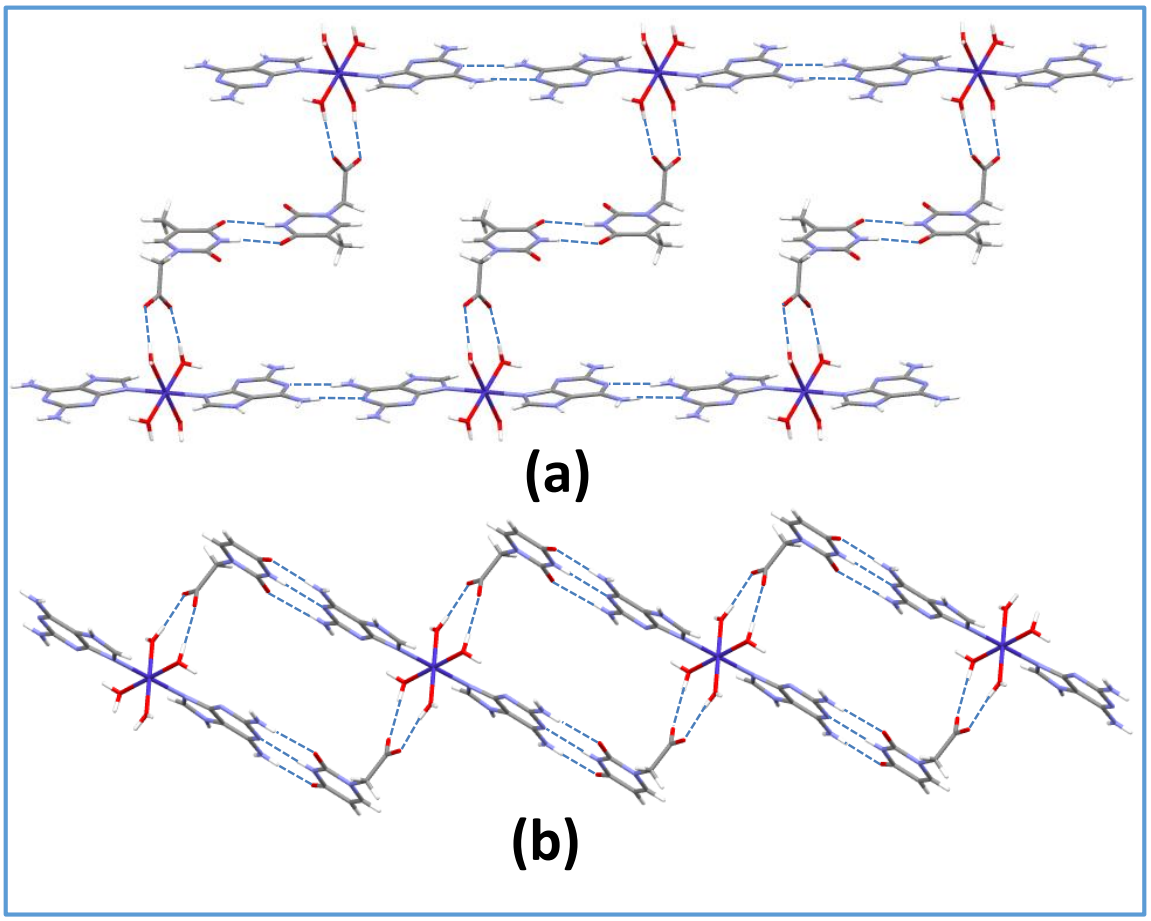

Figure 2.25. Complementary hydrogen bonding interactions involving the thymine residue in complex **15** (a) and the uracil residue in complex **16** (b). Dash lines represent the H-bonds.

For complex **17**, as shown in **Figure 2.26,** similar to **13** and **14**, TAcOH coordinate to Co(II) ion as monodentate ligand through the carboxylate group. The Co(II) atom is six-coordinated by four oxygen atoms, from two water molecules and two TAcO anions, and two nitrogen atoms from two 4,4'-bipy ligands (**Figure 2.26a**, **b**). The Co-O1 bond length [2.081 Å] is close to Co-O bond length that was observed for some monodentate carboxylate ligands.[57] The Co-N [2.195 Å] bond length is longer than those of other Co(II) complexes with 4,4'-bipy bridging linker. The O-H···N hydrogen bonds between thymine residues allow the formation of supramolecular 1D chains in the direction of *a* axis (**Figure 2.26c**). Additionally, the O-H···N hydrogen bonds between oxygen atoms of water molecules and nitrogen atoms of 4,4'-bipy, from the adjacent supramolecular chain, lead to a 2D layer supramolecular structure (**Figure 2.26d**).

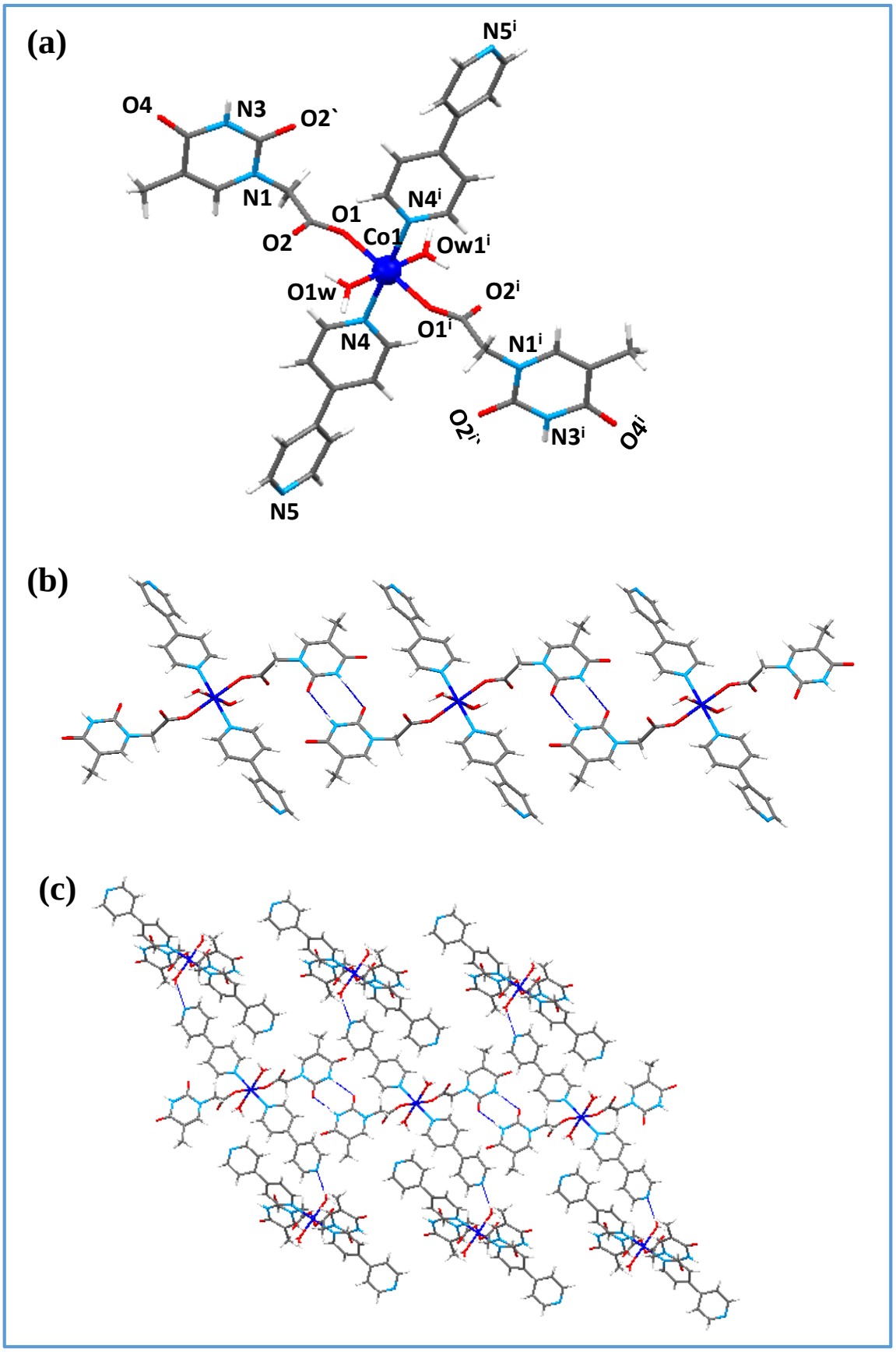

Figure 2.26. (a) Molecular structure of **17** with atoms labeling. (c) Supramolecular 1D chain resulting from the base pairing of thymine fragments. (d) 2D supramolecular network established in complex **17**. Dash lines represent the H-bonds established in complex **17**.

Insights in the H-bonding interactions in complexes 13-16.

The study of crystal structures in complexes **13-16** allow us to make comparative study and conclude some insights in H-bond directionality, in the presence of strong donor/acceptor molecules such as water molecules, *versus* the molecular recognitions between complementary nucleobases through the well-known base pairing and/or between pairs of the same nucleobase.

Although double stranded DNA structure is a clear example of the stability of complementary nucleobases interactions, previous works have shown that water molecules can disrupt these direct hydrogen bonds between the nucleobases.[58] The underlying issue seems to be a competition between the strength of the nucleobase···nucleobase and nucleobase···water hydrogen bonding interactions

The four Co(II)-nucleobase complexes (**13-16**) show a close structural resemblance at the molecular level (**13-14** and **15-16**, respectively) but slight different in the supramolecular arrangements. The methyl group present in the thymine residue (the only difference between TAcOH and UAcOH) leads to the formations of different supramolecular synthons that organize the crystal structure in different ways in these complexes and providing the opportunity to estimate the relative strength of the H-bonding supramolecular interactions (**Figure 2.27**). It allows determining their hierarchy among the supramolecular synthons that we believe could be a useful tool for the design of novel crystal architectures based on this type of biologically active ligands.

Complexes **13-16** show a constant structural feature: the presence of two *cis* coordinated water molecules that play a predominant role in the hydrogen-bonding network. Complex **13** presents direct hydrogen bonds between the thymine and water molecules (H_2O-T) but not thymine-thymine (T-T) interactions, while complex **14** shows non-canonical uracil-uracil (U-U) base pairing interactions. This fact suggests that T-T interactions are weaker than those established between H_2O-T and probably even weaker than those between U-U (**Figure 2.27**).

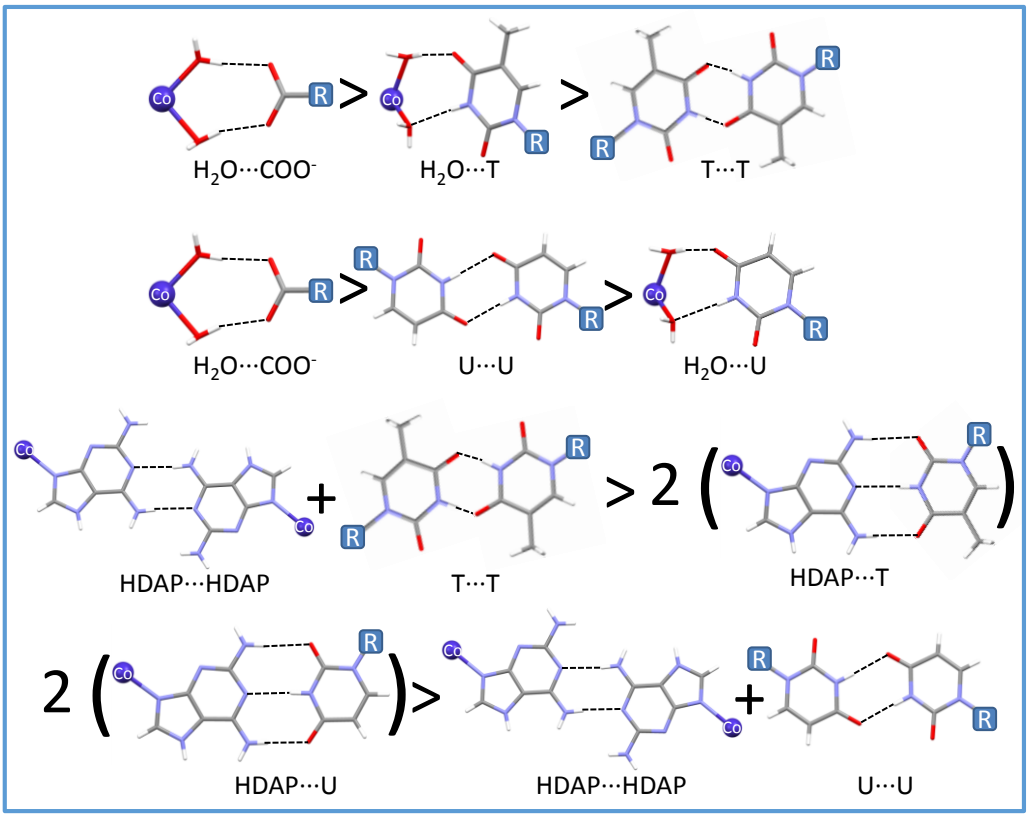

Figure 2.27. Relative supramolecular synthon strength as deduced from the crystal structures of complexes **13-16**.

In fact, one of the reason proposed by the biologists for the replacement of uracil by thymine in the DNA is the greater tendency of uracil not only to pair with adenine but also with any other base, including self-pairing [59]. Probably, the presence of the hydrophobic methyl group in the thymine is responsible of this behaviour as it is repelled by the rest of the DNA[60].

On the other hand, complexes **15** and **16** also display a *cis* arrangement of the coordinated water molecules but the hydrogen bonding interactions take place between the water ligands and the free carboxylate group of the modified nucleobases (H_2O-COO^-). It implies that this interaction is stronger than those established between the pyrimidines (T or U) and the coordinated water molecules. Additionally, the HDap-U interactions are stronger than the HDap-HDap and U-U combination but the HDap-HDap and T-T combination is stronger than the HDap-T interactions. It also seems indicate that the HDap-U interaction is stronger than the HDap-T one.

2.2.2. Physical properties measurements.

2.2.2.1. Electrical properties.

Two probe direct current (dc) electrical conductivity measurements at 300 K were performed in several single crystals of complexes **9-12** (see section 5.1.6). The conductivity values at 300 K were obtained applying voltages from +10 V to –10 V. The room temperature DC conductivity values, for complexes **9-12**, suggesting a semiconductor behavior in all cases (**Table 2.3**). **Table 2.3**, shows the conductivity of complexes (**9-12**). The conductivity values founded in these four 1D-CPs can be explained looking at the copper···copper distances. Complexes **9** and **10** present shorter copper···copper distances than these founded in complexes **11** and **12**. These difference, of the copper···copper distances, can be attributed to the nature of the bridging ligands that interconnect the Cu atoms. $TAcO^-$ ligand, the acting bridging ligand in complex **9**, and $TAcO^-$ and OH^- ion, the responsible bridging ligands in complex **10**, lead to shorter copper···copper distances comparing with complexes **11** and **12** where 4,4'-bipy is the bridging ligand.. The better conductivity of complex **10** comparing with complex **9** can be attribute to the existence of small bridging ligand such as OH- ion beside $TAcO^-$ ligand making the copper···copper distances shorter and hence better electrical conductivity (**Table 2.3**).

For complexes **9** and **10**, we have also performed dc electrical measurements with the four contacts method in the temperature range 300-400 K in order to confirm the semiconducting behavior and determine the activation energy. These measurements showed a semiconductor behaviour (**Figure 2.28**) and activation energies of *ca*. 1.3 eV for both complexes. As expected for semiconductors, at 400 K the conductivity is higher with values of $1x10^{-6}$ and $5x10^{-7}$ $S \cdot cm^{-1}$ in complexes **9** and **10** respectively with to the conductivity values at 300 K (**Table 2.3**).

Table 2.3. The dc electrical conductivity measurements at 300 K and 400 K for complexes **9**-**12**.

Complexes	Cu···Cu (Å)	σ S/cm (300 K) (t)	σ S/cm (400 K) (f)
9	4.59	1.1×10^{-9}	1.0×10^{-6}
10	3.00, 3.30, 2.97	6.8×10^{-6}	5×10^{-7}
11	11.12	1.78×10^{-9}	-
12	3.18, 10.90	1.9×10^{-9}	-

t: mean tow contact method, f; mean four contact method, -: mean that we didn't perform these measurements.

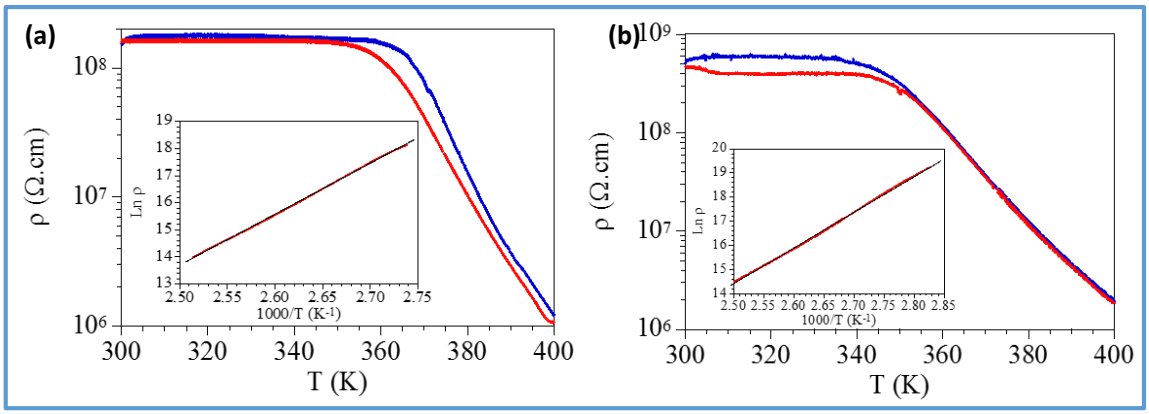

Figure 2.28. Thermal variation of the dc conductivity of single crystals of complexes (a) **9** and (b) **10** in the warming (red points) and cooling scans (blue points). Inset shows the corresponding Arrhenius plot.

2.2.2.2. Magnetic properties.

The magnetic measurements of Cu(II) monomeric complexes **1** and **2** containing isolated CuO_6 monomers present χ_mT values at room temperature of ca. 0.43-0.45 cm^3 K mol^{-1} (**Figure 2.29a**), which are the expected values for isolated S = ½ Cu(II) complexes with *g* slightly higher than complexes **3-8** (**Table 2.4**). The χ_mT product remains constant in complexes **1** and **2**, down to very low temperatures (ca.10 K) where it presents a smooth decrease to reach values of ca. 0.41-0.42 cm^3 K mol^{-1} at 2 K. This behaviour clearly indicates that both complexes are essentially paramagnetic although there is a very weak antiferromagnetic interaction as suggested by the decrease in χ_mT at low temperatures. Since the structure of both complexes shows the presence of π-π interactions connecting the monomers along the [101] direction, giving rise to a regular chain, we have used the model proposed by Hatfield *et al*. for a regular S = ½ chain.[61] This model reproduced very satisfactorily the magnetic properties of both complexes in the whole temperature range with the parameters displayed in **Table 2.4** (solid lines in **Figure 2.29a**). As expected, both complexes showed similar *g* and *J* values, given their very close structures.

The thermal variation of the molar magnetic susceptibility per Cu dimer (χ_m) for complexes **3-8** shows very similar behavior (**Figure 2.29b**). They present a rounded maximum near room temperature and a decrease with decreasing temperature to reach a minimum at *ca.* 50 K and a divergence at lower temperatures. This behavior suggests the presence of a strong antiferromagnetic Cu-Cu interaction, as expected from the structure of complexes **3-8**. The divergence at low temperatures indicates the presence of a paramagnetic contribution arising from monomeric Cu(II) units resulting from defects and vacancies in the Cu dimers or from other Cu(II) monomeric complexes. The confirmation of the strong antiferromagnetic coupling in these dimers is provided by the thermal variation of the χ_mT product (**Figure 2.29c**) that shows at room temperature a value of *ca.* 0.6 cm^3 K mol^{-1}, well below the expected one for two non-interacting Cu(II) ions (*ca.* 0.75 cm^3 K mol^{-1}). When the temperature is decreased, the χ_mT value decreases and reaches a value close to zero below *ca.* 50 K. The very small residual value agrees with the presence of a small paramagnetic contribution.

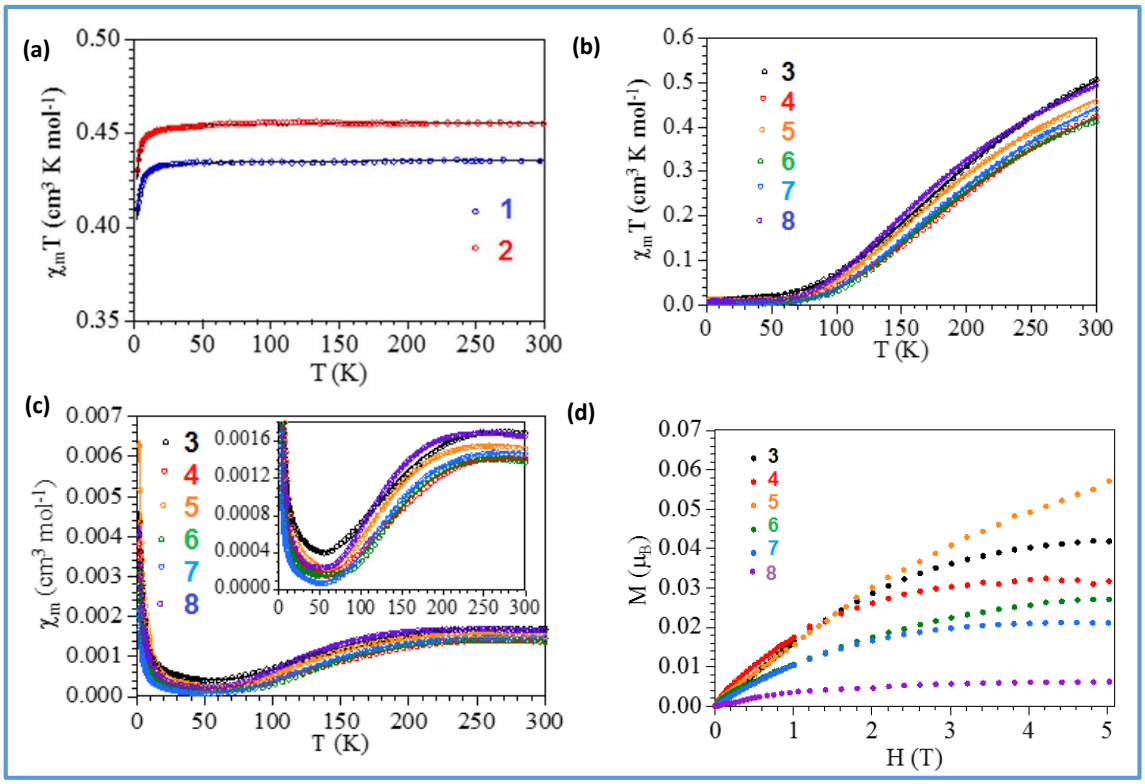

Figure 2.29. Thermal variation of the $\chi_m T$ product for complexes **1** and **2** (a) and for complexes **3-8** (b). Solid lines are the best fit to the S = ½ dimer model (see text) for complexes **3-8**. (c) Thermal variation of χ_m for complexes **3-8**. Solid lines are the best fit to the S = ½ dimer model (see text). Inset shows the low region. (d) Isothermal magnetization at 2 K of complexes **3-8**.

As already indicated in the structural description of complexes **3-8**, they all present the same dimeric $[Cu_2(OOCR)_4]$ core and, accordingly, we have fitted the magnetic properties of complexes **3-8** to the classical Bleaney and Bowers S = ½ dimer model.[62] In order to reproduce the divergence at low temperatures, we have included a paramagnetic S = ½ contribution (ρ) with the same g value that the Cu(II) ions in the dimer. This model reproduces very satisfactorily the magnetic properties of complexes **3-8** in the whole temperature range, including the divergence at low temperatures with the parameters displayed in **Table 2.4** (solid lines in **Figure 2.29b**, **c**; the Hamiltonian is written as $H = -JS_1S_2$). As expected, the S = 0 spin ground state of complexes **3-8** as a result of the strong intradimer antiferromagnetic coupling is confirmed by the isothermal magnetizations at 2 K (**Figure 2.29d**) that show, in all cases, very low values arising from the weak paramagnetic contribution observed in the low temperature χ_m data.

Table 2.4. Magnetic parameters of complexes **1**-**10**.

Complex	*g*	*J* (cm^{-1})[a]
1	2.156	-0.16
2	2.205	-0.15
3	2.094	-320
4	2.066	-311
5	2.099	-298
6	2.099	-326
7	2.104	-313
8	2.096	-278
9	2.14	-0.2
10		28, 36, -8

As can be seen in **Table 2.4**, the coupling constants in the six paddle-wheel complexes are very similar (in the range -278 cm^{-1} to -326 cm^{-1}), in agreement with the almost identical dimeric structure observed in all cases. These values also agree with the reported values for many other similar Cu(II) paddle wheel dimers including the original acetate complex (J = -296 cm^{-1}) and with the values obtained from DFT calculations.[63] Interestingly, these theoretical calculations also show that changing the axial ligand L (**Figure 2.9)** is not expected to produce big variations in the exchange constants of the copper dimer, in agreement with our observations. Thus, in complexes **3**-**8**, changes in L (DMF in **4**, H_2O/DMF in **4,** DMSO in **5**, DMA in **6**, DMF in **7** and DMSO in **8**) only give rise to slight changes in the *J* values (**Table 2.4**). These *J* values suggest that the effect of DMSO is to decrease *J* (the two lowest *J* coupling constant in absolute value are found in **5** and **8**, both with DMSO as axial ligand). DMA seems to increase *J* (the highest *J* value is found in **6**, the only dimer with DMA) and DMF has an intermediate effect as shown by the intermediate *J* values found in **3**, **4** and **7**). Note that these changes have to be attributed to structural effects of the axial ligands rather to electronic ones since, due to symmetry reasons, the orbitals of the axial ligands do not participate in the SOMO of the Cu(II) dimer (which has a δ character).

Complex **9** presents a typical magnetic behavior of isolated copper(II) metal centers, the $\chi_m T$ curve remains constant upon cooling (0.425 $cm^3.K.mol^{-1}$) and only at temperatures below 15 K decreases slightly (0.410 $cm^3.K.mol^{-1}$ at 5 K) (**Figure 2.30a**). Considering the structural features, the experimental data were least-squared fitted with a numerical expression proposed for an antiferromagnetic copper(II) uniform chain[64] that leads to *J* (triplet-singlet gap) = –0.2 cm^{-1}, *g* = 2.14 and R = $1.7 \cdot 10^{-6}$, R being the agreement factor defined as $\sum_i \left[(\chi_M T)_{obs}(i) - (\chi_M T)_{calc}(i)\right]^2 / \sum_i \left[(\chi_M T)_{obs}(i)\right]^2$. This almost negligible antiferromagnetic coupling can be understood in terms of the nature of the orbital involved in the exchange interactions, together with the arrangement of the bridging ligand. The unpaired electron of the copper(II) ion is essentially described by a magnetic orbital built from the $d_{x^2-y^2}$ metallic orbital and located mainly in the basal plane. The carboxylato, with a basal (short, 1.945(2) Å)-axial (long, 2.624(2) Å) bridging mode leads to an almost nil overlap between the two metal centered magnetic orbitals, resulting in a weak anti- or ferromagnetic (when the overlap is zero, accidental orthogonality) coupling.[65, 66]

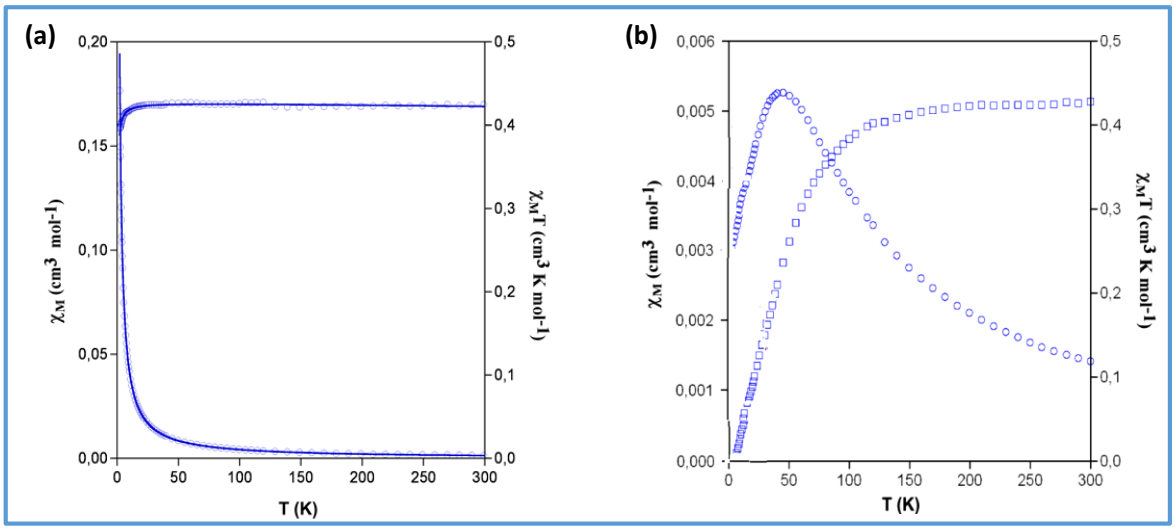

Figure 2.30. Thermal variation of the $\chi_m T$ product for complexes (a) **9** and (b) **10**.

The $\chi_m T$ value per copper(II) atom for complex **10** at room temperature is 0.430 $cm^3.K.mol^{-1}$. This value remained almost constant until 120 K and shows a sharp decrease upon cooling to reach a value of 0.012 $cm^3.K.mol^{-1}$ at 2 K. The thermal evolution of the magnetic susceptibility shows the presence of a rounded maximum around 43 K

(**Figure 2.30b**). This behavior is indicative of dominant moderate antiferromagnetic interactions between the Cu(II) atoms. **Figure 2.31** depicts the different exchange coupling constants taking place in complex **10** that should be taken into account in order to model its magnetic behavior. As far as we know, no available mathematical expression could account for the scheme of magnetic interactions taking place within the polymeric chains of these kind of complexes. Therefore, we have estimated the individual *J* magnetic coupling constant for each magnetic exchange pathway (J_1, J_2, J_3) from quantum computational calculations performed over simplified fragments of the polymeric chains.

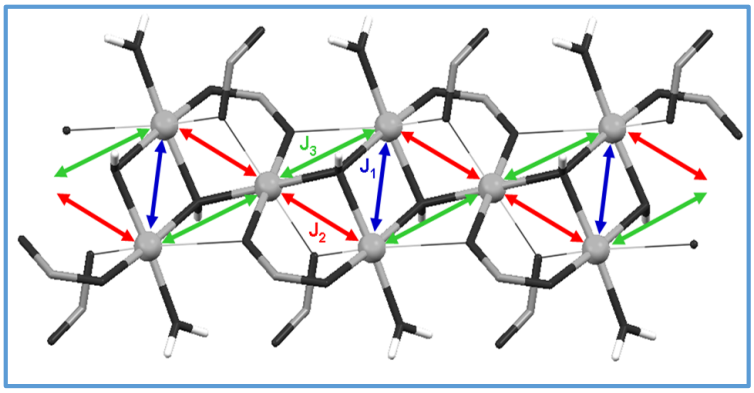

Figure 2.31. Magnetic exchange pathways in complex **10**. Thinner bonds represent the elongated coordination bonds due to the Jahn-Teller effect of the copper(II) metal centers. Only the carboxylate group of the $TAcO^-$ ligands are represented for clarity.

The results indicate that the double hydroxide bridge mediated exchange interaction (J_1) should be weakly ferromagnetic (J_1 = +28 cm^{-1}) for complex **10** according to the computational simulation. These results are in good agreement with previous experimental results that show the exchange coupling constants mediated by hydroxide ligands range from -700 to +300 cm^{-1}.[67-69] For di-μ-hydroxido-bridged Cu(II) binuclear complexes the classical magneto-structural correlation between the Cu-O-Cu bond angle (φ) and the experimental exchange constant (*J*) (J= –74.538 φ + 7270 cm^{-1}) indicates that this complex is antiferromagnetic for φ > 98º, but ferromagnetic for smaller angles.[70] However, more recently advanced theoretical calculations using different density functional methods have demonstrated that another structural parameters, such as small variances in the Cu-O (bridge) distances, the out of plane displacement of the hydroxo hydrogen atoms, the non-planarity of the Cu_2O_2 core and the distance from copper atom

to the basal plane, can play an important role on the fine tuning of the exchange coupling.[71, 72] On the other hand the ferromagnetic interaction predicted in complex **10** for the second exchange pathway (J_2) is explained by means of the orbital counter-complementary between the μ-carboxylato-κO:κO´ bridge and the hydroxide bridge with $\varphi > 98^{o}$. [73]

2.2.3. Nano-processability of complex 11.

The electrical conductivity of the obtained 1D-CPs (**9-12**) are too low to investigate their incorporations in nanoelectronic applications. However, the molecular recognition capacity and their biological nature encourage us to focus our attention on their potential use in bio-nanotechnology area. Therefore, it is important to find the procedure to scale down these 1D-CPs into nanometer scale. To this end, we have been able to prepare nanoribbons by means of fast precipitation reaction, of complex **11** under similar synthetic conditions that have been used to prepare the macroscopic counterpart but at lower concentration, 0.05 M (see section 5.3). The X-ray powder diffraction, as well as spectroscopic and analytical data, confirm that the composition and structure of these nanoribbons are in agreement with those observed for the as-synthesized bulk counterparts (**Figure 2.33**). In order to study the morphology of these nanoribbons, we carried out field emission scanning electron microscopy (FESEM) (**Figure 2.32**) and atomic force microscopy (AFM) analyses (**Figure 2.34**) for the solid obtained upon fast precipitation. The FESEM images confirm a nanoribbon-like structure with a high homogeneity in dimensions. **Figure 2.32** clearly show nanoribbons with *ca*. 100-150 nm width and length of microns.

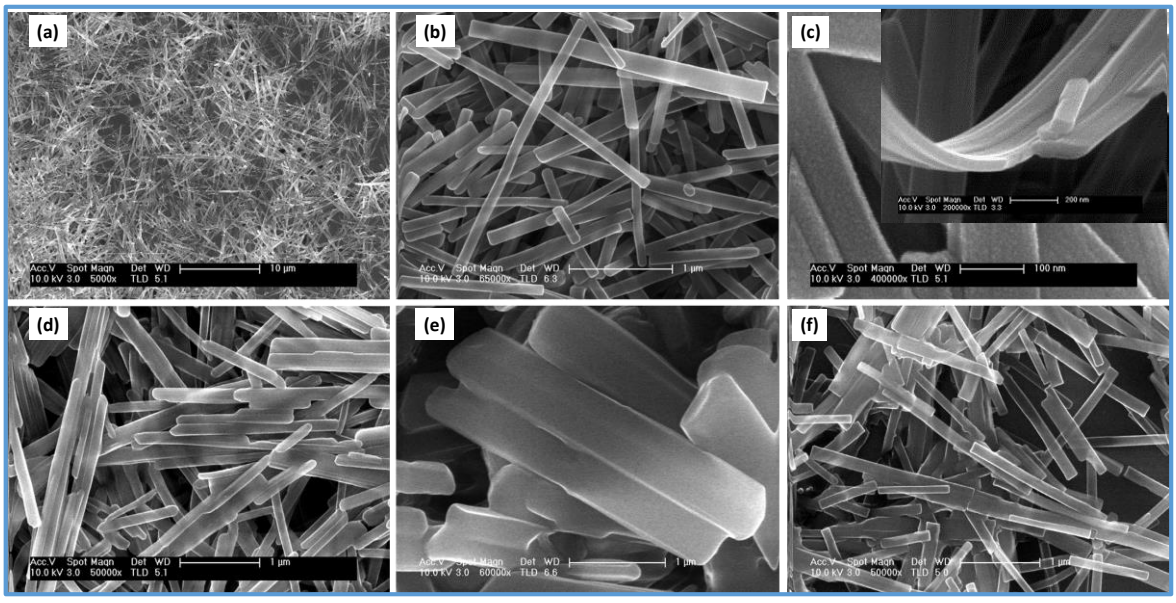

Figure 2.32. FESEM images of **11**. Pictures (a-c) taken at time 0 (recently prepared) to show the general size and homogeneity of the sample at different zooms.(a)10 µm, (b) 500 nm and (c) 100 nm, showing the medium diameter size of 100-150 nm. The inset in (c) shows the thickness of the nanoribbons. (d and e) Show the FESEM images of nanoribbons for complex **11** recorded at time 48 h and one month respectively. (f) FESEM images for the preparation carried out with Cu(II) concentration of 0.1 M at time 0.

We doesn't observe significant changes neither in the width nor in shape nanoribbons upon varying the concentration of the reactants from 0.05 to 0.1 mol/L, however, the length become shorter (**Figure 2.32b**, **f**). We observe that upon standing the colloid in contact with solution from time 0 to 1 month the width increases in about one order of magnitude while length decrease (**Figure 2.32b**, **d-f**). Finally, the AFM images (see section 5.1.10) obtained upon deposition, by drop casting, of a diluted suspension of the initial colloid on mica surface confirm the width of the nanoribbons while allowed to measure a minimum height of *ca*. 3.5 nm for the nanoribbons and shows a very smooth roughness (**Figure 2.34a**). The height of 3.5 nm is in agreement with the isolation of a ribbon consisting of just one-two molecules by comparison with the X-ray diffraction data (**Figure 2.34b**). Additionally, based on the X-ray structure we assume that the nanoribbons are formed by means of complementary thymine hydrogen bonds interactions between the chains (**Figure 2.18**).

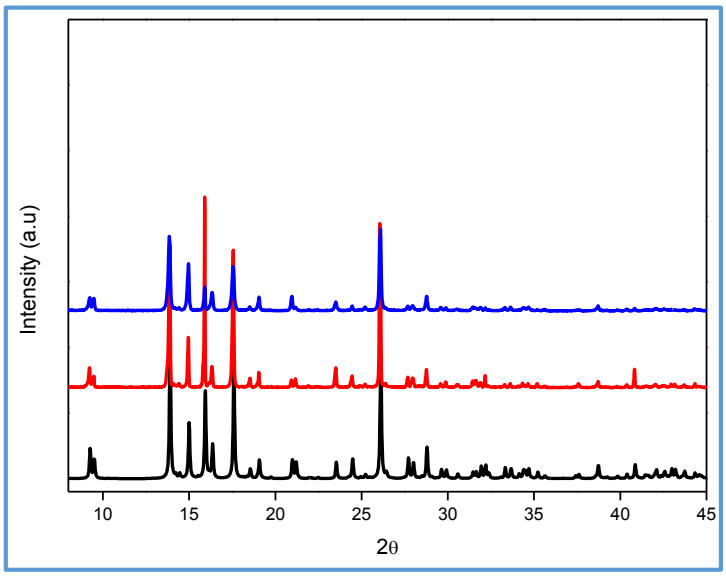

Figure 2.33. X-Ray powder diffraction patterns of simulated pattern of complex **11 (black)**, as-synthesized bulk counterpart (red), and nanoribbons (blue).

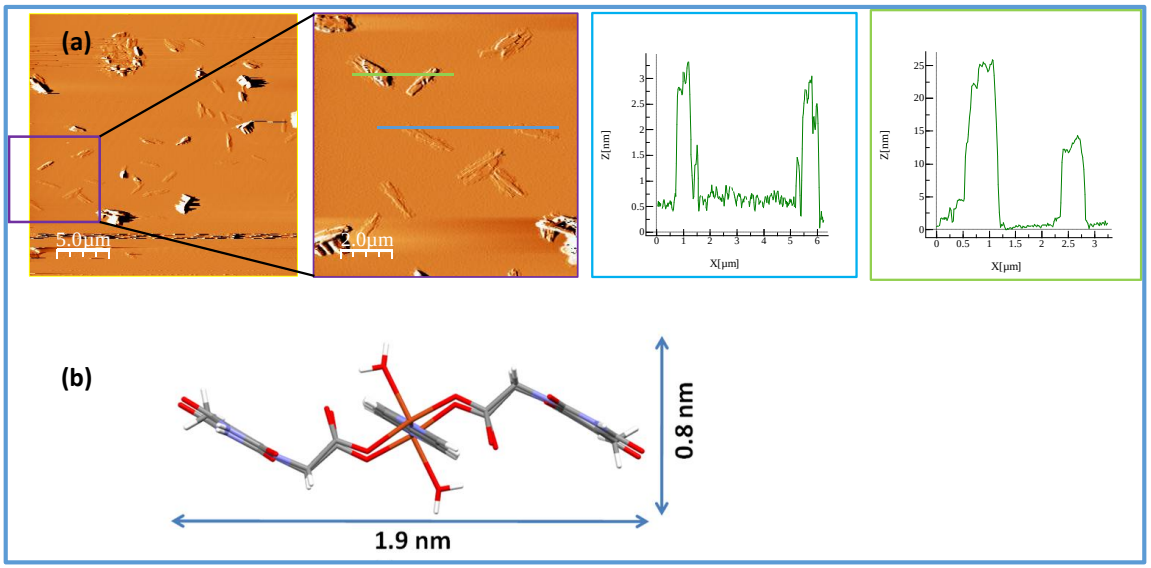

Figure 2.34. AFM images of nanoribbons from complex **11** on mica surface recorded at time 0 for the preparation carried out with Cu(II) concentration of 0.05 M.

Once we are able to isolate and manipulate nanoribbons of complex **11** and based on the structure understanding, we decided to evaluate the interaction of the nanoribbons with biomolecules, particularly with oligonucleotides. In this sense, the presence of thymines in the structure could be exploited to bind selectively DNA sequences containing adenines easing the functionalization of the nanoribbons. Therefore, as a proof-of-concept, we studied the interaction of the nanoribbons with oligonucleotides containing different nucleobases, particularly we used the sequences detailed in **Table 2.5**.

Table 2.5. Selected oligonucleotides sequences.

Name	Sequence
PolyA	5'-dAdAdAdAdAdAdAdAdA-3'
PolyC	5'-dCdCdCdCdCdCdCdCdC-3'
PolyG	5'-dGdGdGdGdGdGdGdGdG-3'
PolyT	5'-dTdTdTdTdTdTdTdTdT-3'

The interaction between the nanoribbons and the sequences was evaluated. The corresponding mixtures were incubated at room temperature for two hours. Then, the mixtures were centrifuged using standard dialysis eppendorfs (Amicon10 kDa, 0.5 mL) to remove the unbound material, then, the eluted solutions were used to quantify the

unbound amount of oligonucleotides. We found that the nanoribbons had selectivity for the PolyA sequence, where a 38% of the oligonucleotide was unbound during the washing step (**Figure 2.35**). When PolyT, PolyC and PolyG were used, the amount of the unbound sample increased to 68%, 59% and 53% respectively. These results suggested that the interaction of the nanoribbons with an oligonucleotide bearing adenines is much stronger than in the other cases. In the case of PolyG, it bounds the polymer better than PolyT and PolyC, which might be due to the formation of a wobble base pairing between the guanines and thymines stabilized through two hydrogen bonds. The results obtained highlight the potential applications of CPs with nucleobases or modified nucleobases, since these CPs could be easily functionalized with oligonucleotides bearing a PolyA sequence, such as RNA derivatives involved in gen regulation (microRNA or siRNAs). Interestingly, this type of sequence (PolyA) is presented in messenger RNA (mRNA) and has implications in its stability. For this reason, we envision that some of the future applications of these type of CPs might deal with the delivery of nucleic acids to control biological processes. However, the presence of copper in the polymer might limit this use due to its potential toxicity. For this reason, we decided to evaluate the toxicity of this material in MCF-7 cells (see section 5.1.12). Interestingly, we only observed high toxicity when the concentration of the polymer was high (>100 µM). On the other hand, concentrations below this threshold did not affect dramatically the viability of the cells, (**Figure 2.36**).

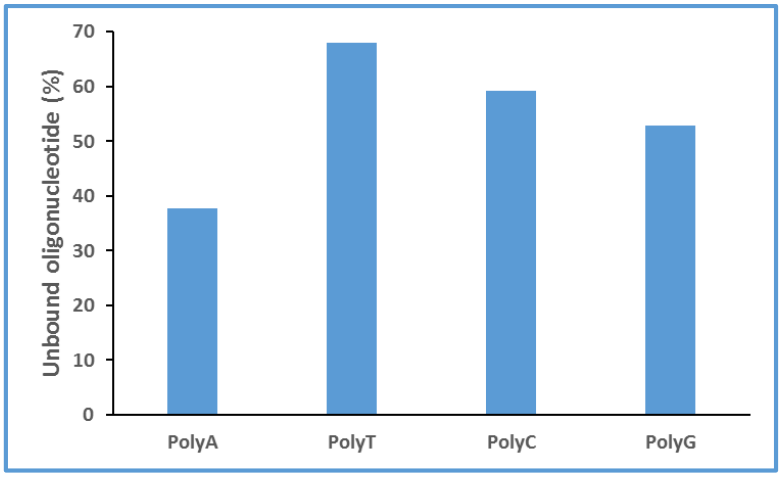

Figure 2.35. The affinity of the different sequences represented as % of the unbound material. The PolyA sequence has the highest affinity for the polymer due to the efficient interaction between thymines and adenines.

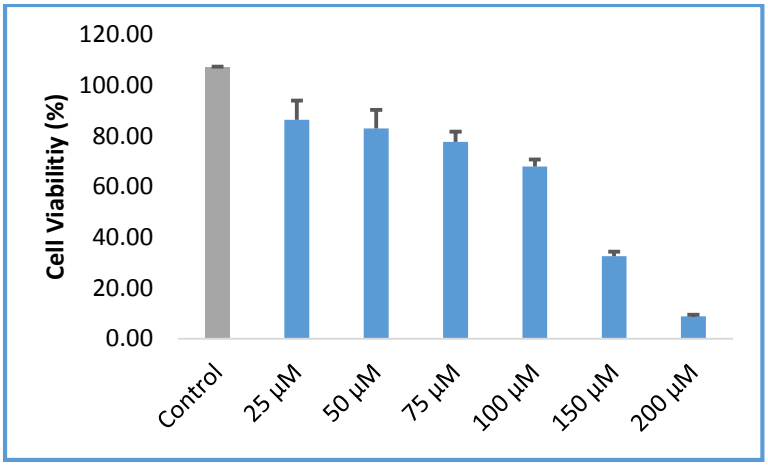

Figure 2.36. Cell viability study in MCF7 using different concentrations of the polymer.

References

1. P. Amo-Ochoa, O. Castillo, S. S. Alexandre, L. Welte, P. J. de Pablo, M. I. Rodríguez-Tapiador, J. Gómez-Herrero and F. Zamora, **Synthesis of Designed Conductive One-Dimensional Coordination Polymers of Ni(II) with 6-Mercaptopurine and 6-Thioguanine**, *Inorganic Chemistry*, **2009**, 48, 7931-7936, http://dx.doi.org/10.1021/ic900896w.
2. P. Amo-Ochoa and F. Zamora, **Coordination polymers with nucleobases: From structural aspects to potential applications**, *Coordination Chemistry Reviews*, **2014**, 276, 34-58, http://www.sciencedirect.com/science/article/pii/S0010854514001593.
3. I. Imaz, M. Rubio-Martinez, J. An, I. Sole-Font, N. L. Rosi and D. Maspoch, **Metal-biomolecule frameworks (MBioFs)**, *Chemical Communications*, **2011**, 47, 7287-7302, http://dx.doi.org/10.1039/C1CC11202C.
4. R. Mas-Ballesté, O. Castillo, P. J. Sanz Miguel, D. Olea, J. Gómez-Herrero and F. Zamora, **Towards Molecular Wires Based on Metal-Organic Frameworks**, *European Journal of Inorganic Chemistry*, **2009**, 10.1002/ejic.200801090, 2885-2896, http://dx.doi.org/10.1002/ejic.200801090.
5. D. Olea, S. S. Alexandre, P. Amo-Ochoa, A. Guijarro, F. de Jesús, J. M. Soler, P. J. de Pablo, F. Zamora and J. Gómez-Herrero, **From Coordination Polymer Macrocrystals to Nanometric Individual Chains**, *Advanced Materials*, **2005**, 17, 1761-1765, http://dx.doi.org/10.1002/adma.200401687.
6. F. Zamora, M. Pilar Amo-Ochoa, P. J. Sanz Miguel and O. Castillo, **From metal-nucleobase chemistry towards molecular wires**, *Inorganica Chimica Acta*, **2009**, 362, 691-706, http://www.sciencedirect.com/science/article/pii/S0020169308000844.
7. B. Lippert, **Multiplicity of metal ion binding patterns to nucleobases**, *Coordination Chemistry Reviews*, **2000**, 200–202, 487-516, http://www.sciencedirect.com/science/article/pii/S0010854500002605.
8. S. Sivakova and S. J. Rowan, **Nucleobases as supramolecular motifs**, *Chemical Society Reviews*, **2005**, 34, 9-21, http://dx.doi.org/10.1039/B304608G.
9. I. Imaz, M. Rubio-Martínez, W. J. Saletra, D. B. Amabilino and D. Maspoch, **Amino Acid Based Metal−Organic Nanofibers**, *Journal of the American Chemical Society*, **2009**, 131, 18222-18223, http://dx.doi.org/10.1021/ja908721t.
10. Y. Liu and Z. Tang, **Nanoscale Biocoordination Polymers: Novel Materials from an Old Topic**, *Chemistry – A European Journal*, **2012**, 18, 1030-1037, http://dx.doi.org/10.1002/chem.201101520.
11. H. Wei, B. Li, Y. Du, S. Dong and E. Wang, **Nucleobase−Metal Hybrid Materials: Preparation of Submicrometer-Scale, Spherical Colloidal Particles of Adenine−Gold(III) via a Supramolecular Hierarchical Self-Assembly Approach**, *Chemistry of Materials*, **2007**, 19, 2987-2993, http://dx.doi.org/10.1021/cm070028a.
12. J. An, S. J. Geib and N. L. Rosi, **Cation-Triggered Drug Release from a Porous Zinc−Adeninate Metal−Organic Framework**, *Journal of the American Chemical Society*, **2009**, 131, 8376-8377, http://dx.doi.org/10.1021/ja902972w.
13. J. An, C. M. Shade, D. A. Chengelis-Czegan, S. Petoud and N. L. Rosi, **Zinc-Adeninate Metal−Organic Framework for Aqueous Encapsulation and Sensitization of Near-infrared and Visible Emitting Lanthanide Cations**, *Journal of the American Chemical Society*, **2011**, 133, 1220-1223, http://dx.doi.org/10.1021/ja109103t.

14. A. V. Pinheiro, D. Han, W. M. Shih and H. Yan, **Challenges and opportunities for structural DNA nanotechnology**, *Nat Nano*, **2011**, 6, 763-772, http://dx.doi.org/10.1038/nnano.2011.187.
15. N. C. Seeman, **Nucleic acid junctions and lattices**, *Journal of Theoretical Biology*, **1982**, 99, 237-247, http://www.sciencedirect.com/science/article/pii/0022519382900029.
16. M. Zahid, B. Kim, R. Hussain, R. Amin and S. Park, **DNA nanotechnology: a future perspective**, *Nanoscale Research Letters*, **2013**, 8, 1-13, http://dx.doi.org/10.1186/1556-276X-8-119.
17. A. Condon, **Designed DNA molecules: principles and applications of molecular nanotechnology**, *Nat Rev Genet*, **2006**, 7, 565-575, http://dx.doi.org/10.1038/nrg1892.
18. T. H. LaBean and H. Li, **Constructing novel materials with DNA**, *Nano Today*, **2007**, 2, 26-35, http://www.sciencedirect.com/science/article/pii/S1748013207700567.
19. N. C. Seeman, **An Overview of Structural DNA Nanotechnology**, *Molecular biotechnology*, **2007**, 37, 246-257, http://www.ncbi.nlm.nih.gov/pmc/articles/PMC3479651/.
20. H. Yang, K. L. Metera and H. F. Sleiman, **DNA modified with metal complexes: Applications in the construction of higher order metal–DNA nanostructures**, *Coordination Chemistry Reviews*, **2010**, 254, 2403-2415, http://www.sciencedirect.com/science/article/pii/S0010854510000664.
21. E. L. Albuquerque, U. L. Fulco, V. N. Freire, E. W. S. Caetano, M. L. Lyra and F. A. B. F. de Moura, **DNA-based nanobiostructured devices: The role of quasiperiodicity and correlation effects**, *Physics Reports*, **2014**, 535, 139-209, http://www.sciencedirect.com/science/article/pii/S0370157313003797.
22. J. P. Patwardhan, C. Dwyer, A. R. Lebeck and D. J. Sorin, **Circuit and System Architecture for DNA-Guided Self-Assembly of Nanoelectronics**, *Foundations of Nanoscience*, **2004**, 344-358,
23. N. Sergiy, B. Marcelo and S. L. Jeremy, **A field-effect transistor from M-DNA**, *Nanotechnology*, **2007**, 18, 095205, http://stacks.iop.org/0957-4484/18/i=9/a=095205.
24. J. C. Genereux and J. K. Barton, **Mechanisms for DNA Charge Transport**, *Chemical Reviews*, **2010**, 110, 1642-1662, http://dx.doi.org/10.1021/cr900228f.
25. D. Porath, N. Lapidot and J. Gomez-Herrero, in *Introducing Molecular Electronics*, eds. G. Cuniberti, K. Richter and G. Fagas, Springer Berlin Heidelberg, 2005, vol. 680, pp. 411-444.
26. M. Waleed Shinwari, M. Jamal Deen, E. B. Starikov and G. Cuniberti, **Electrical Conductance in Biological Molecules**, *Advanced Functional Materials*, **2010**, 20, 1865-1883, http://dx.doi.org/10.1002/adfm.200902066.
27. M. Taniguchi and T. Kawai, **DNA electronics**, *Physica E: Low-dimensional Systems and Nanostructures*, **2006**, 33, 1-12, http://www.sciencedirect.com/science/article/pii/S1386947706000543.
28. E. Meggers, M. E. Michel-Beyerle and B. Giese, **Sequence Dependent Long Range Hole Transport in DNA**, *Journal of the American Chemical Society*, **1998**, 120, 12950-12955, http://dx.doi.org/10.1021/ja983092p.
29. H. A. Wagenknecht and H. B. Gray, *Charge Transfer in DNA: From Mechanism to Application*, Wiley, 2006.
30. F. F. Maia, V. N. Freire, E. W. S. Caetano, D. L. Azevedo, F. A. M. Sales and E. L. Albuquerque, **Anhydrous crystals of DNA bases are wide gap**

semiconductors, *The Journal of Chemical Physics*, **2011**, 134, 175101, http://scitation.aip.org/content/aip/journal/jcp/134/17/10.1063/1.3584680.

31. T. Catherall, D. Huskisson, S. McAdams and A. Vijayaraghavan, **Self-assembly of one dimensional DNA-templated structures**, *Journal of Materials Chemistry C*, **2014**, 2, 6895-6920, http://dx.doi.org/10.1039/C4TC00460D.
32. A. Houlton and S. M. D. Watson, **DNA-based nanowires. Towards bottom-up nanoscale electronics**, *Annual Reports Section "A" (Inorganic Chemistry)*, **2011**, 107, 21-42, http://dx.doi.org/10.1039/C1IC90017J.
33. S. M. D. Watson, A. R. Pike, J. Pate, A. Houlton and B. R. Horrocks, **DNA-templated nanowires: morphology and electrical conductivity**, *Nanoscale*, **2014**, 6, 4027-4037, http://dx.doi.org/10.1039/C3NR06767J.
34. J. Pate, F. Zamora, S. M. D. Watson, N. G. Wright, B. R. Horrocks and A. Houlton, **Solution-based DNA-templating of sub-10 nm conductive copper nanowires**, *Journal of Materials Chemistry C*, **2014**, 2, 9265-9273, http://dx.doi.org/10.1039/C4TC01632G.
35. S. M. D. Watson, M. A. Galindo, B. R. Horrocks and A. Houlton, **Mechanism of Formation of Supramolecular DNA-Templated Polymer Nanowires**, *Journal of the American Chemical Society*, **2014**, 136, 6649-6655, http://dx.doi.org/10.1021/ja500439v.
36. S. M. D. Watson, J. H. Hedley, M. A. Galindo, S. A. F. Al-Said, N. G. Wright, B. A. Connolly, B. R. Horrocks and A. Houlton, **Synthesis, Characterisation and Electrical Properties of Supramolecular DNA-Templated Polymer Nanowires of 2,5-(Bis-2-thienyl)-pyrrole**, *Chemistry – A European Journal*, **2012**, 18, 12008-12019, http://dx.doi.org/10.1002/chem.201201495.
37. P. Aich, S. L. Labiuk, L. W. Tari, L. J. T. Delbaere, W. J. Roesler, K. J. Falk, R. P. Steer and J. S. Lee, **M-DNA: a complex between divalent metal ions and DNA which behaves as a molecular wire**, *Journal of Molecular Biology*, **1999**, 294, 477-485, http://www.sciencedirect.com/science/article/pii/S0022283699932345.
38. S. S. Alexandre, B. J. Murta, J. M. Soler and F. Zamora, **Stability and electronic structure of <math display="inline"><mrow><mi>M</mi></mrow></math>-DNA: Role of metal position**, *Physical Review B*, **2011**, 84, 045413, http://link.aps.org/doi/10.1103/PhysRevB.84.045413.
39. K. Mizoguchi, S. Tanaka, T. Ogawa, N. Shiobara and H. Sakamoto, **Magnetic study of the electronic states of <math display="inline"><mi>B</mi></math>-DNA and <math display="inline"><mi>M</mi></math>-DNA doped with metal ions**, *Physical Review B*, **2005**, 72, 033106, http://link.aps.org/doi/10.1103/PhysRevB.72.033106.
40. M. Nagatori, M. Ojima, Y. Ibuki, H. Sakamoto and K. Mizoguchi, **Electronic States of Metal Ions Incorporated in Mn-DNA**, *Journal of the Physical Society of Japan*, **2011**, 80, 114803, http://dx.doi.org/10.1143/JPSJ.80.114803.
41. B. Datta, G. B. Schuster, A. McCook, S. C. Harvey and K. Zakrzewska, **DNA-Directed Assembly of Polyanilines: Modified Cytosine Nucleotides Transfer Sequence Programmability to a Conjoined Polymer**, *Journal of the American Chemical Society*, **2006**, 128, 14428-14429, http://dx.doi.org/10.1021/ja0648413.
42. G. Givaja, P. Amo-Ochoa, C. J. Gómez-Garcia and F. Zamora, **Electrical conductive coordination polymers**, *Chemical Society Reviews*, **2012**, 41, 115-147, http://dx.doi.org/10.1039/C1CS15092H.

43. A. Guijarro, O. Castillo, L. Welte, A. Calzolari, P. J. S. Miguel, C. J. Gómez-García, D. Olea, R. di Felice, J. Gómez-Herrero and F. Zamora, **Conductive Nanostructures of MMX Chains**, *Advanced Functional Materials*, **2010**, 20, 1451-1457, http://dx.doi.org/10.1002/adfm.200901901.
44. J. Gómez-Herrero and F. Zamora, **Coordination Polymers for Nanoelectronics**, *Advanced Materials*, **2011**, 23, 5311-5317, http://dx.doi.org/10.1002/adma.201101952.
45. R. Mas-Balleste, J. Gomez-Herrero and F. Zamora, **One-dimensional coordination polymers on surfaces: towards single molecule devices**, *Chemical Society Reviews*, **2010**, 39, 4220-4233, http://dx.doi.org/10.1039/C001965H.
46. S. S. Alexandre, J. M. Soler, P. J. Sanz Miguel, R. W. Nunes, F. Yndurain, J. Gómez-Herrero and F. Zamora, **Design of molecular wires based on one-dimensional coordination polymers**, *Applied Physics Letters*, **2007**, 90, -, http://scitation.aip.org/content/aip/journal/apl/90/19/10.1063/1.2737371.
47. P. Amo-Ochoa, M. I. Rodríguez-Tapiador, O. Castillo, D. Olea, A. Guijarro, S. S. Alexandre, J. Gómez-Herrero and F. Zamora, **Assembling of Dimeric Entities of Cd(II) with 6-Mercaptopurine to Afford One-Dimensional Coordination Polymers: Synthesis and Scanning Probe Microscopy Characterization**, *Inorganic Chemistry*, **2006**, 45, 7642-7650, http://dx.doi.org/10.1021/ic060384f.
48. S. S. Alexandre, J. M. Soler, P. J. Sanz Miguel, R. W. Nunes, F. Yndurain, J. Gómez-Herrero and F. Zamora, **Design of molecular wires based on one-dimensional coordination polymers**, *Applied Physics Letters*, **2007**, 90, 193107, http://scitation.aip.org/content/aip/journal/apl/90/19/10.1063/1.2737371.
49. P. Amo-Ochoa, S. S. Alexandre, S. Hribesh, M. A. Galindo, O. Castillo, C. J. Gómez-García, A. R. Pike, J. M. Soler, A. Houlton and F. Zamora, **Coordination Chemistry of 6-Thioguanine Derivatives with Cobalt: Toward Formation of Electrical Conductive One-Dimensional Coordination Polymers**, *Inorganic Chemistry*, **2013**, 52, 5290-5299, http://dx.doi.org/10.1021/ic400237h.
50. F. Wang, B. Liu, P.-J. J. Huang and J. Liu, **Rationally Designed Nucleobase and Nucleotide Coordinated Nanoparticles for Selective DNA Adsorption and Detection**, *Analytical Chemistry*, **2013**, 85, 12144-12151, http://pubs.acs.org/doi/abs/10.1021/ac4033627.
51. G. B. Deacon and R. J. Phillips, **Relationships between the carbon-oxygen stretching frequencies of carboxylato complexes and the type of carboxylate coordination**, *Coordination Chemistry Reviews*, **1980**, 33, 227-250, http://www.sciencedirect.com/science/article/pii/S0010854500804555.
52. M. Nara, H. Torii and M. Tasumi, **Correlation between the Vibrational Frequencies of the Carboxylate Group and the Types of Its Coordination to a Metal Ion: An ab Initio Molecular Orbital Study**, *The Journal of Physical Chemistry*, **1996**, 100, 19812-19817, http://dx.doi.org/10.1021/jp9615924.
53. U. Kumar, J. Thomas and N. Thirupathi, **Factors Dictating the Nuclearity/Aggregation and Acetate Coordination Modes of Lutidine-Coordinated Zinc(II) Acetate Complexes**, *Inorganic Chemistry*, **2009**, 49, 62-72, http://dx.doi.org/10.1021/ic901100z.
54. M. F. R. Moita, M. L. T. S. Duarte and R. Fausto, **Investigation of the structure of the columnar liquid-crystalline phase of copper(II) carboxylates. An FTIR spectroscopic study**, *Journal of the Chemical Society, Faraday Transactions*, **1994**, 90, 2953-2960, http://dx.doi.org/10.1039/FT9949002953.

55. M. Wriedt, A. A. Yakovenko, G. J. Halder, A. V. Prosvirin, K. R. Dunbar and H.-C. Zhou, **Reversible Switching from Antiferro- to Ferromagnetic Behavior by Solvent-Mediated, Thermally-Induced Phase Transitions in a Trimorphic MOF-Based Magnetic Sponge System**, *Journal of the American Chemical Society*, **2013**, 135, 4040-4050, http://dx.doi.org/10.1021/ja312347p.
56. V. Zeleňák, Z. Vargová and K. Györyová, **Correlation of infrared spectra of zinc(II) carboxylates with their structures**, *Spectrochimica Acta Part A: Molecular and Biomolecular Spectroscopy*, **2007**, 66, 262-272, http://www.sciencedirect.com/science/article/pii/S1386142506001430.
57. M. Indrani, R. Ramasubramanian, S. Kumaresan, S. K. Kang, M. Chen and M. Du, **Hydrothermal synthesis, crystal structures, and properties of CoII and NiII supramolecular complexes with 2,4,6-trimethyl benzoate and 4,4′-bipyridyl**, *Polyhedron*, **2008**, 27, 3593-3600, http://www.sciencedirect.com/science/article/pii/S0277538708004622.
58. J. Thomas-Gipson, G. Beobide, O. Castillo, M. Fröba, F. Hoffmann, A. Luque, S. Pérez-Yáñez and P. Román, **Paddle-Wheel Shaped Copper(II)-Adenine Discrete Entities As Supramolecular Building Blocks To Afford Porous Supramolecular Metal–Organic Frameworks (SMOFs)**, *Crystal Growth & Design*, **2014**, 14, 4019-4029, http://dx.doi.org/10.1021/cg500634y.
59. B. G. Vertessy and J. Toth, **Keeping Uracil Out of DNA: Physiological Role, Structure and Catalytic Mechanism of dUTPases**, *Accounts of Chemical Research*, **2009**, 42, 97-106, <Go to ISI>://WOS:000262616700010.
60. R. Olinski, M. Jurgowiak and T. Zaremba, **Uracil in DNA-Its biological significance**, *Mutation Research-Reviews in Mutation Research*, **2010**, 705, 239-245, <Go to ISI>://WOS:000285808300009.
61. D. B. Brown, J. A. Donner, J. W. Hall, S. R. Wilson, R. B. Wilson, D. J. Hodgson and W. E. Hatfield, **INTERACTION OF HYDRAZINE WITH COPPER(II) CHLORIDE IN ACIDIC SOLUTIONS - FORMATION, SPECTRAL AND MAGNETIC-PROPERTIES, AND STRUCTURES OF COPPER(II), COPPER(I), AND MIXED-VALENCE SPECIES**, *Inorganic Chemistry*, **1979**, 18, 2635-2641, <Go to ISI>://WOS:A1979HM96400001.
62. B. B. Bleaney, K. D., *Proc. R. Soc. Lond. A.* , **1952**, 214, 451-465,
63. A. Rodríguez-Fortea, P. Alemany, S. Alvarez and E. Ruiz, **Exchange Coupling in Carboxylato-Bridged Dinuclear Copper(II) Compounds: A Density Functional Study**, *Chemistry – A European Journal*, **2001**, 7, 627-637, http://dx.doi.org/10.1002/1521-3765(20010202)7:3<627::AID-CHEM627>3.0.CO;2-I.
64. J. C. Bonner, Fisher, M. E., *Phys. Rev.*, **1964**, 135, 640,
65. Z. Han, Y. Zhao, J. Peng and C. J. Gómez-García, **Unusual Oxidation of an N-Heterocycle Ligand in a Metal−Organic Framework**, *Inorganic Chemistry*, **2007**, 46, 5453-5455, http://dx.doi.org/10.1021/ic700432p.
66. D.-C. Wen, S.-X. Liu and J. Ribas, **Syntheses, structures and magnetic property of two copper complexes with cyclic dimer and 2D herringbone-like network built from helical motif**, *Inorganic Chemistry Communications*, **2007**, 10, 661-665, http://www.sciencedirect.com/science/article/pii/S1387700307000755.
67. E. D. Coronado, P. Gatteschi, D. Miller, J.S., **Magnetic Molecular Materials: From Molecular Assemblies to the Devices, Kluwer, Dordrecht,**, **1996**, 321,
68. O. Kahn, **Molecular Magnetism**, *VCH Publishers, New York,*, **1993**,

69. D. M. Miller J.S., **Magnetism: Molecules to Materials**, , *Wiley-VCH, Weinheim*, **2001-2005**, 1-5,
70. V. H. Crawford, H. W. Richardson, J. R. Wasson, D. J. Hodgson and W. E. Hatfield, **Relation between the singlet-triplet splitting and the copper-oxygen-copper bridge angle in hydroxo-bridged copper dimers**, *Inorganic Chemistry*, **1976**, 15, 2107-2110, http://dx.doi.org/10.1021/ic50163a019.
71. E. Ruiz, P. Alemany, S. Alvarez and J. Cano, **Toward the Prediction of Magnetic Coupling in Molecular Systems: Hydroxo- and Alkoxo-Bridged Cu(II) Binuclear Complexes**, *Journal of the American Chemical Society*, **1997**, 119, 1297-1303, http://dx.doi.org/10.1021/ja961199b.
72. E. Ruiz and S. Alvarez, **Theoretical search for new ferromagnetically coupled transition metal complexes**, *Chemical Communications*, **1998**, 0, 2767-2768, http://dx.doi.org/10.1039/A807973K.
73. S. Pérez-Yáñez, O. Castillo, J. Cepeda, J. P. García-Terán, A. Luque and P. Román, **Analysis of the Interaction between Adenine Nucleobase and Metal-Malonato Complexes**, *European Journal of Inorganic Chemistry*, **2009**, 2009, 3889-3899, http://dx.doi.org/10.1002/ejic.200900124.

3. Chapter 3; Copper(I) Coordination Polymers and their Potential Applications

Copper(I) Coordination Polymers with Pyridine Derivatives Ligands

---

In this chapter, we present the potential use of Cu(I) metal ions to construct 1D-CPs with multifunctional properties. In that regard, the synthesis and structural characterization of a family of 1D-CPs formulated as $[CuX(L)]_n$, L = 2-amino-5-nitropyridine (ANP) and X = Cl, Br, I, CN and SCN ions, will be discussed. Additionally, the synthesis and structural characterization of two isostructural 1D-CPs, formulated as $[CuI(L)]_n$, L = ethyl-isonicotinate (EtIN) or isonicotinic acid (INH), will be discussed. For all complexes, the electrical and photoluminescence properties have been clarified.

The DFT calculations will be used to rationalize the electrical conductivity founded for all these complexes. Therefore, the dynamic nature of $[CuX(ANP)]_n$ 1D-CPs, X = Br or I, and their reversible structural transformation as a response of absorption/desorption processes of the gas of volatile organic solvents, will be explored. This feature strongly recommend these class of materials for sensing applications.

Finally, the nanoprocessability of one selected complex formulated as $[CuI(ANP)]_n$ will be investigated.

3.1. Introduction

The field of compounds containing two or more metal atoms separated by a shorter distance than the sum of their covalent radii, termed a metallophilic interactions, has attracted much attention during last years in materials science area, because this shorter distance can act as a driving force to form one dimensional structures with unusual electronic and optoelectronic properties.[1, 2] However, the metallophilic interactions have been observed for closed shell d^{10} metal ions, mostly for Au and Ag centres[3-5], but it was pointed out that, even for $Cu^{I}\cdots Cu^{I}$ separations as short as 2.35 Å[6], the existence of a weak bonding interaction between copper(I) atoms remains controversial[7-9], and the effect of the bridging ligands on $Cu^{I}\cdots Cu^{I}$ separations is crucial.[10-12]

In fact, 1D-CPs based on copper(I) halides attract great attention as potential candidates for electronic and optoelectronic applications[13-19] owning to their remarkable structural diversities[20, 21], originating from the soft acceptor characteristics of copper(I) ion that give rise to relatively flexible coordination sphere and the flexibility of halides as inorganic bridging ligands as they can adapt μ_2-, μ_3-, or μ_4-bridging modes with tunable $Cu^{I}\cdots Cu^{I}$ distances. Consequently, halides play an important role in fine-tuning the $Cu^{I}\cdots Cu^{I}$ separation, make copper(I) halides complexes excellent candidates as multi-stimuli responsive materials as they can respond to various external stimuli that associated with marked changes in their physical properties.[22] In that regard, copper(I) halides stimuli-responsive luminescent materials have received great attention as chemical sensors.[23, 24] The stimuli-responsive luminescence behaviour of copper(I) halides complexes have been reported and it depend on the external stimuli such as, thermal treatment (thermochromism)[25, 26], mechanical grinding (mechanochromism)[27] or vapochromism[28, 29], that give rise for switching of the luminescence properties. The stimuli-responsive phenomena that observed for non-porous copper(I) complexes, provided by structure transformations in the targeting material, result in mostly changes in the $Cu^{I}\cdots Cu^{I}$ distance[27], coordination core (breaking and forming of new bond around the metal center)[23], geometry and/or the packing forces[28, 25].

The resulting properties and final structure of copper(I) halides complexes depend crucially on the molar ratio, reactions conditions, and selected organic ligands.[30, 22, 21, 31] In particular, the photoluminescence of copper(I) halides with N-organic ligands have been studied experimental and theoretical.[14, 15, 19] On the other hand, the electrical

conductivities in some 1D-CPs based on copper(I) halides with sulfur-containing ligands have been reported.[17] In addition, the electrical conductivities found in some of the CuX-double chains with N-organic ligands have suggested their potential use as electronic materials.[32] Recently, Amo *et al*, have studied the accessibility of 1D-CP([CuBr(INH)]n), based on copper(I) bromide and isonicotinic acid (INH) as terminal ligand, as nano-wire (**Figure 3.1**).

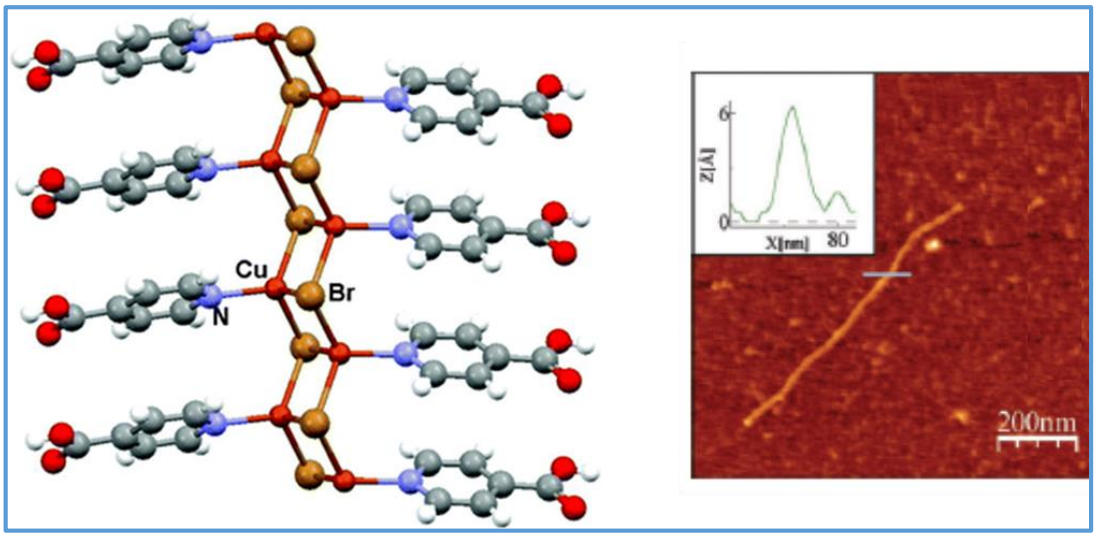

Figure 3.1. Schematic representation of a $[CuBr(INH)]_n$ polymer chain (right). AFM topography image of $[CuBr(INH)]_n$ deposited on polylisine treated mica surface (left).[32]

The authors rationalized the selection of isonicotinic acid because this ligand can bind to the metal center through the carboxyl group and/ or pyridine nitrogen atom keeping, in the last case, the carboxylic group free to participate in molecular recognition process through H-bond interactions with others molecules as for example DNA or DNA nanostructures, the feature that may allow the construction of electronic circuit based on new hybrid DNA-CPs material.[32] These results prompted us to investigate the electronic properties of further 1D-CPs based on copper(I) halides with functionalized N-organic ligands, keeping in the account the molecular recognition as an essential factor, to study their interactions with DNA or DNA nanostructures. In addition, single chains of these 1D-CPs can serve as molecular wire.[33]

In this chapter, we study the self-assemble of CuX or CuX_2 salts (X = Cl, Br, I, CN or SCN anions) and pyridine derivatives ligands (**Figure 3.2**), named as 2-amino-5-

nitropyridine (ANP), Ethyl-isonicotinate (EtIN) and Isonicotinic acid (INH), that give rise to a series of halides and pseudo halides 1D-CPs with general formula $[CuXL]_n$. (L= pyridine organic ligands and X = X = Cl, Br, I, CN or SCN anions) . The selection of the ligands coming on the basis of their capabilities to participate in the formation of supramolecular structures by means of weak interactions mostly H-bonds that are highly desirable for the molecular recognition interactions with others biological structures as DNA nanostructures.

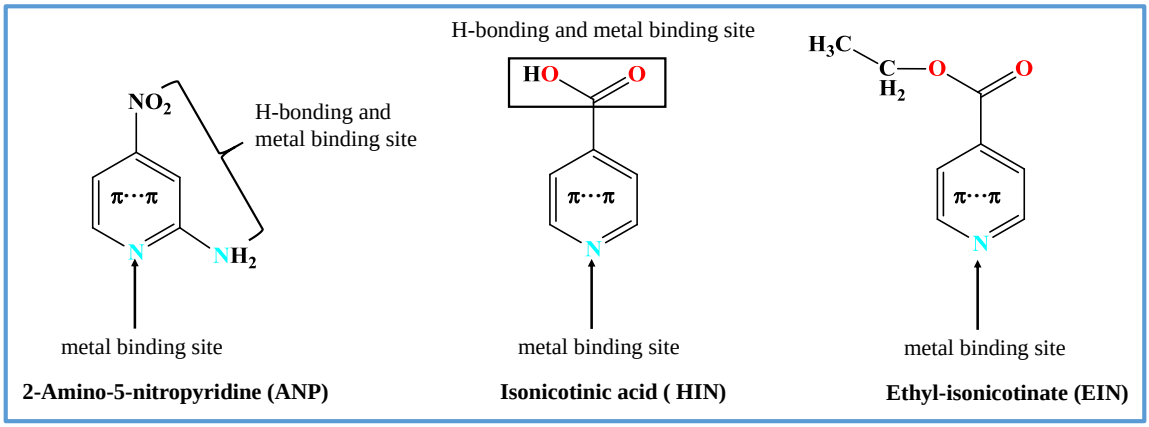

Figure 3.2. Schematic representation of the selected ligands for this chapter with their metals and H-bond binding sites.

3.2. Results and discussion

3.2.1. Synthesis and Structural Characterization

Due to the instability of copper (I) halides and lack of solubility in common organic solvents except acetonitrile, hydro(solvo)thermal methods remarkably have been used as synthetic method for this family.[34] It is well established that copper (II) salts may undergo for a reduction reactions in the presence of pyridine like ligands or N-containing heteroaromatic ligands under hydro(solvo)thermal conditions.[35-37] In some cases, these methods produce mixed-valence copper coordination polymers.[38] In addition, saturated alkali metal halide aqueous solutions have been used to dissolve the copper (I) halide.[39] In this chapter, prepare a series of 1D-CPs, based on copper(I) halides, using different synthetic procedure.

The reactions of CuX (where X is Cl, Br I, CN or SCN anions) and pyridine derivatives ligands at different conditions allow the separation of complexes **18**-**24** (**Scheme 3.1**). Complexes **18** and **19** have been synthetized by direct reactions between the corresponding CuX or CuX_2 salts (X= Cl, Br anions for complexes **18** and **19** respectively) with ANP under solvothermal or microwave conditions (**Figure 3.3**), (see section 5.3). When CuX_2 have been used, reduction of Cu(II) ions were taken place in presence of pyridine ligand (ANP), and under these energetic conditions as in many reported examples.[36] The direct reaction carried out between CuI and ANP in acetonitrile at 25 ºC leads to the isolation of complex (**20^{RT}**) (**Figure 3.3**). A similar reaction between CuI and ANP but using solvothermal conditions in acetonitrile-water (2:1) affords the structural polymorph (**20a**) (**Figure 3.3**). Additionally, the study of the physical properties of complex **20** indicates a phase transition at ca. 267 K. This transition has been studied in detail by solving the structure of **20** at 200 K (**20^{LT}**) and at 298 K (**20^{RT}**). In a reaction carried out under similar synthetic solvothermal conditions to those used for complex **20a**, but with an oxygen saturated acetonitrile-water (2:1) solution, a few crystals of complex **20b** are isolated (**Figure 3.4**). Complexes **21** and **22** have been synthetized by direct reactions between the corresponding CuX salts (X= CN, SCN anions for complexes**21** and **22** respectively) and ANP under mild conditions.

On the other hand, the reactions between CuI and EtIN or HIN lead to the separation of complexes **23** and **24** respectively (**Scheme 3.1**).

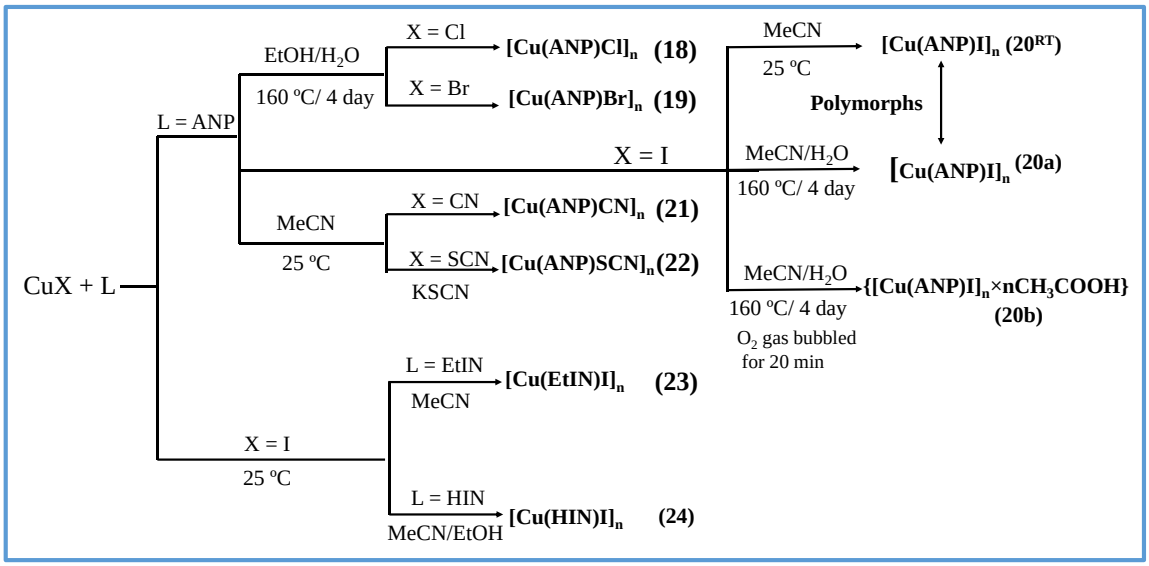

Scheme 3.1. Schematic representation of complexes (**18**-**24**) obtained by the reactions of Cu(I) salts with pyridine derivatives ligands.

All the complexes have been characterized by single crystals X-ray diffraction and their purity have been confirmed by X-ray powder diffraction techniques (see appendices **A** and **B**).

Complexes **18**, **19**, **20^{LT}**, **20^{RT}** and **20a** present a similar structural feature where they consist of a double-stranded stair motif (**Figure 3.3**), in which copper(I) metal centers are bridged by μ_3-halides. Three bridging halides and the iminic nitrogen atom of the ANP ligand complete the tetrahedral coordination environment around the metal center. Whereas complex **20b** shows a similar double-stranded stair chain with the incorporation of acetic acid molecules in its crystal backing (**Figure 3.4**). All the complexes (**18**-**20**) show an almost identical Cu-X double-chain structure with the expected lengthening along the propagation direction, affecting the dimension of the unit cell *a* edge as the bridging halide size increases. The *a* edge are 3.7060(2) Å for X = Cl (**18**), 3.7808(1) Å for X = Br (**19**), and 4.2284(1), 4.1982(1), 4.0708(1), 4.1444(1) Å for X = I in complexes **20^{LT}**, **20^{RT}**, **20a**, and **20b** respectively (see appendix **A**). The copper-halides and copper-pyridine nitrogen bond distances are similar to those of other known $[CuX(L)]_n$ stairs.[40-44] **Figure 3.5** and **Table 3.1** collect the Cu-X, Cu-N, and Cu···Cu distances for complexes **18**, **19**, and **20**. Most of the intra-chain Cu···Cu distances found are close to the sum of the van der Waals radii (2.80 Å)[45], indicating the possible metallic Cu···Cu interactions that could explain the conductivity results founded in some of these complexes (see electrical properties section).

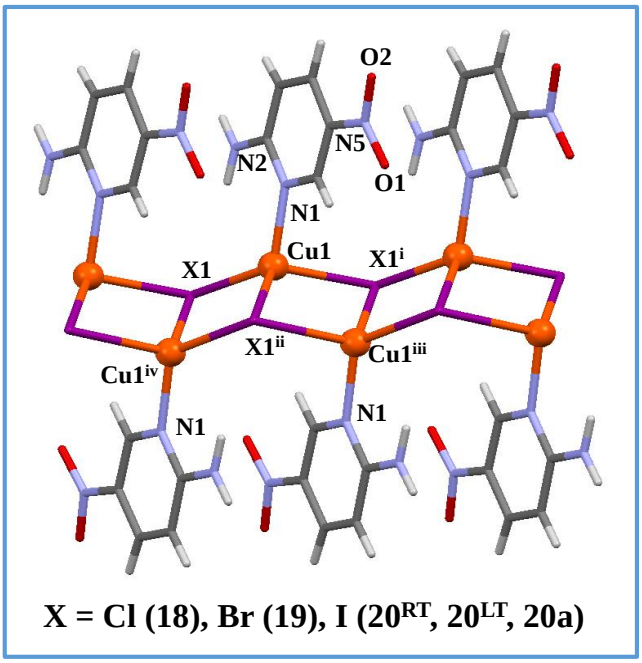

Figure 3.3. View of the polymeric chain $[CuX(ANP)]_n$ in complexes **18**, **19**, **20^{RT}**, **20^{LT}** and **20a**.

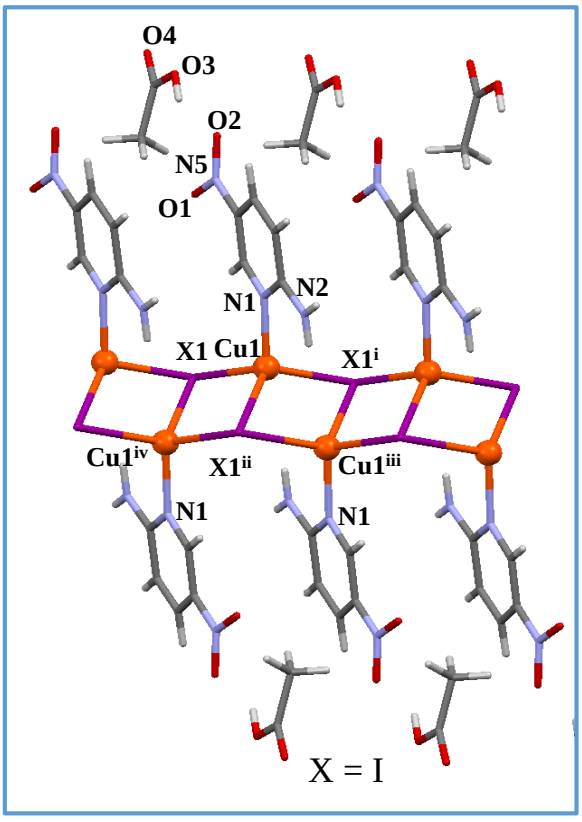

Figure 3.4. View of the polymeric chain $\{[CuI(ANP)]_n \times nCH_3COOH\}$ in **20b**.

The halides are tricoordinated in a distorted pyramidal geometry. The bond distances asymmetry decreased on going from chloride to iodide as can be seen in (**Figure 3.5** and **Table 3.1**). The stair type chain can be also described as formed by planar Cu_2I_2 squares that share two opposite sides with dihedral angles show slight variations between these complexes. These differences observed mainly between the polymorphs of complex **20** and **20b** (117.4º for **20^{RT}**, 117.3º and 116.8º for **20^{LT}**, 114.1º for **20a**, and 112.2º for **20b**) suggest that the inter-chain interactions are important in determining the overall structure of these complexes and these data support the idea that the ANP ligand plays a crucial structural role. Surprisingly, the intra-chain Cu-X-Cu and X-Cu-X angles did not show the expected increase as the size of halide anions (X) increase. Thus, these angles decrease from 104.9º to 98.7º when passing from Cl (**18**) to Br (**19)** and then increase for I to, 105.3º for (**20^{RT}**), 104.55º for (**20^{LT}**), 100.1º for (**20a**), and 101.8º for (**20b**). This lack of size-angle trend indicates that in this series of complexes, the halogen size is not the only factor determining the geometry of the chain but strongly suggests that the packing forces and interchain interactions are also important in determining the structure of these complexes.

Table 3.1. Bond lengths (Å) and bond angles (°) for **18**, **19**, **20^{RT}**, **20^{LT}**, **20a**, and **20b**.

	18 (X=Cl)	**19 (X=Br)**	**20^{RT} (X=I)**	**20^{LT} (X= I)**	**20a (X= I)**	**20b (X= I)**
Cu1—X1	2.2902(8)	2.4561(7)	2.6220(1)	2.6180(8)	2.6205(7)	2.6930(1)
Cu1—X1^{i}	2.3854(8)	2.5260(8)	2.6970(1)	2.6895(8)	2.6886(7)	2.6490(1)
Cu1—Cu1^{iii}	2.7641(8)	2.7678(12)	2.8490(2)	2.8020(8)	2.7722(9)	2.7140(1)
Cu1—Cu1^{iv}	3.1774(8)	2.7793(12)	3.1610(2)	3.1660(8)	2.8994(9)	3.2780(1)
Cu1—X1^{ii}	2.5256(9)	2.5260(8)	2.6980(1)	2.6576(8)	2.6517(7)	2.6500(1)
X1—Cu1—X1^{i}	104.85**(3)**	98.72(3)	105.30(30)	104.55(3)	100.12(2)	101.76(3)
X1^{i}—Cu1—X1^{ii}	111.56(3)	113.48(3)	116.24(4)	117.97(3)	117.46(2)	118.39(6)
π···π	3.297	3.374	3.332	3.307	3.520	3.464

Symmetry codes for complex **18**: (i) -1+x, y, z; (ii) 3-x, -y, 2-z; (iii) 2-x, -y, 2-z; (iv) 1+x, y, z.; for complex **19**: (i) 2-x, 1-y, 1-z; (ii) 1+x, y, z; (iii) -1+x, y, z; (iv) 1-x, 1-y, 1-z; for complex **20^{RT}**: i) x+1, y, z; ii) -x+1, -y+1, -z; iii) -x, -y+1, -z; **20^{LT}**: (i) 1+x, y, z; (ii) -x, 2-y, 1-z; (iii) 1-x, 2-y, 1-z; (iv) -1+x, y, z. for complex **20a**: i) -x+2, -y, -z+1; ii) -x+3, -y, -z+1; i) -x+2, -y, -z+1; ii) -x+3, -y, -z+1; for complex **20b**: i) x+1, y, z; ii) -x, -y+2, -z+1; iii) -x+1, -y+2, -z+1; iv) -x, -y+2, -z+1.

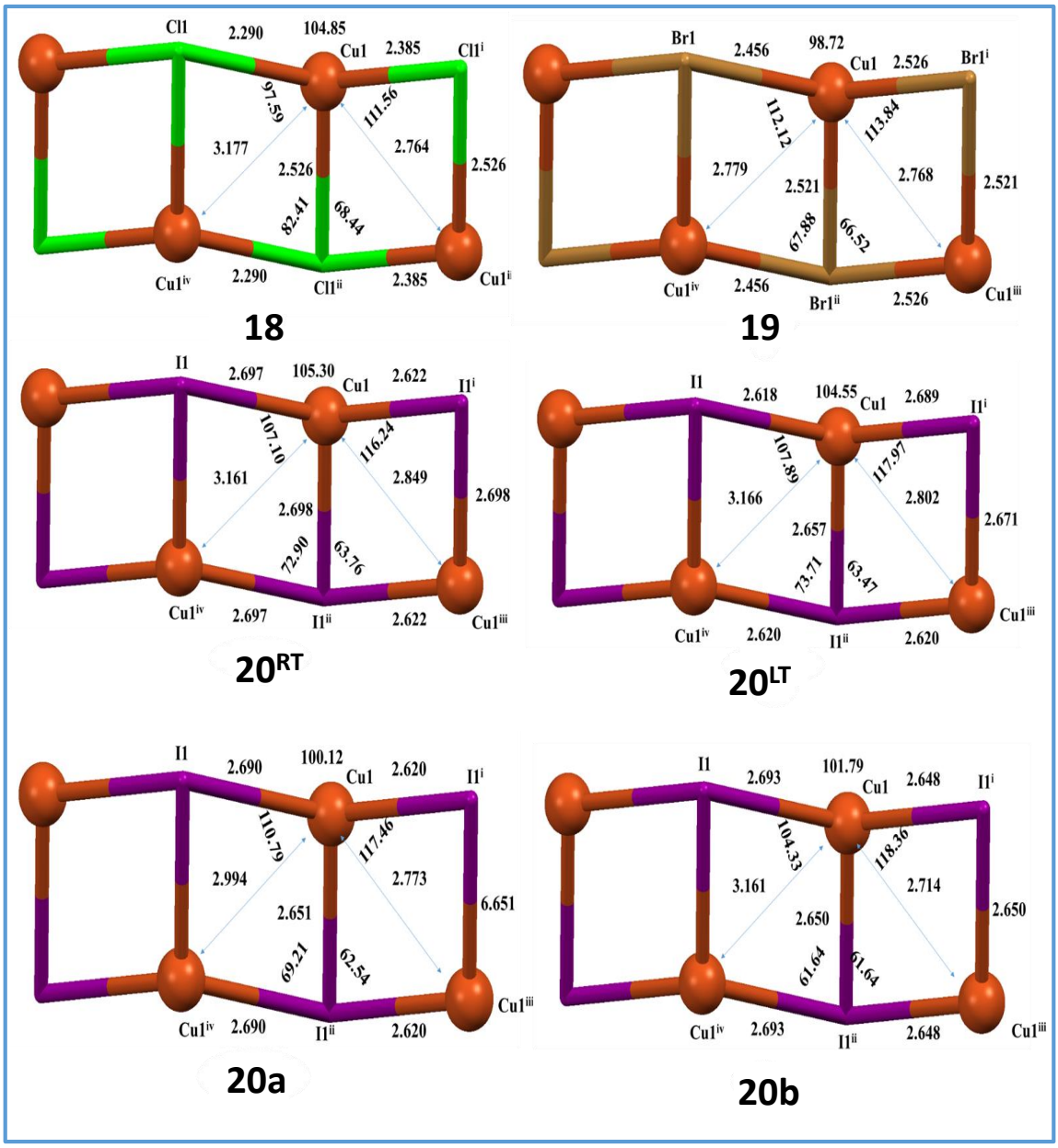

Figure 3.5. Fragment of the double-stranded stair in complexes **18**.**19**, **20**^{RT}, **20**^{LT}, **20a**, and **20b** showing the bond angles (°) and distances (Å).

Note that the main change between the structures of **20**^{LT}, **20**^{RT}, and **20a** reside in the CuI double chain: in **20**^{LT}, this chain contains two crystallographically independent Cu and I atoms resulting in a dimerized chain, whereas in **20**^{RT} and **20a** the chains contain only one Cu and I independent atoms. Interestingly, the average intra-chain Cu···Cu distances are shorter in the dimerized phase (**20**^{LT}) that in the regular one (**20**^{RT}) (**Figure 3.5** and **Table 3.1**). Complex **20a** shows intra-chain Cu···Cu distances shorter than **20**^{LT} and **20**^{RT}, but longer than those found in **20b**.

The ANP ring is tilted (78.2º for **18**, 80.9º for **19**, 78.2º for **20^{RT}**, 79.0º for **20^{LT}** 77.6º for **20a**, and 89.3º for **20b**) and twisted (57.4º for **20^{RT}**, 56.0º for **20^{LT}**, and 67.1º for **20a**) relative to the propagation direction of the chain. The chain cohesion is also ensured by the presence of π···π stacking interactions at each side of the chain between the adjacent ANP ligands with interplanar distances of 3.297 Å (**18**), 3.374 Å (**19**), 3.332 Å (**20^{RT}**), 3.307 Å (**20^{LT}**), 3.520 Å (**20a**), and 3.464 Å (**20b**) (**Table 3.1**). Note again that these interplanar distances do not always follow the expected increase when the halogen size increases since the complexes are not isostructural and, as noted before, the Cu-X-Cu and X-Cu-X angles do not vary in a regular form. Additionally, all complexes show weak intra-chain hydrogen bonds involving the halide as acceptor and the NH_2/CH groups as donor thanks to the twisting of the ANP ligands.

Despite the great similarity between the chains of complexes **18**, **19**, **20^{RT}**, **20^{LT}**, and **20a**, the overall crystal structure clearly shows the influence of the different hydrogen bond acceptor capacity of the halides (**Figure 3.6**, **Figure 3.7** and **Figure 3.8**). In complexes **19**, **19**, **20^{RT}**, **20^{LT}**, and **20a**, the supramolecular architectures are directed by the hydrogen bonding interactions established between the NH_2 and C-H donor groups and the NO_2 and halide acceptor groups of neighboring chains. In fact, the number of hydrogen bond donor positions of the ANP ligand involved in the supramolecular hydrogen bonding scheme reduces on going from **18** to **20**, in agreement with the weaker hydrogen bond acceptor capacity of the halides on going from chloride to iodide.

In complex **20b**, the inclusion of acetic acid molecules, a strong hydrogen bond donor and acceptor molecule, between the $[CuI(ANP)]_n$ chains, disrupts the previous described hydrogen bonding schemes. The intramolecular π-π stacking and N-H···I interactions are retained, but the C-H···I ones are removed (**Figure 3.8**). The inter-chain interactions are dominated by the hydrogen bonds established between the amino group of the ANP ligands and the acetic acid molecules, giving rise to a crystal packing with 1D channels, occupied by highly disordered solvent molecules. These channels of ca. 5 Å diameter occupy a 14.0 % of the total volume. No evidence of inter-chain I···I or π-π interactions are observed.

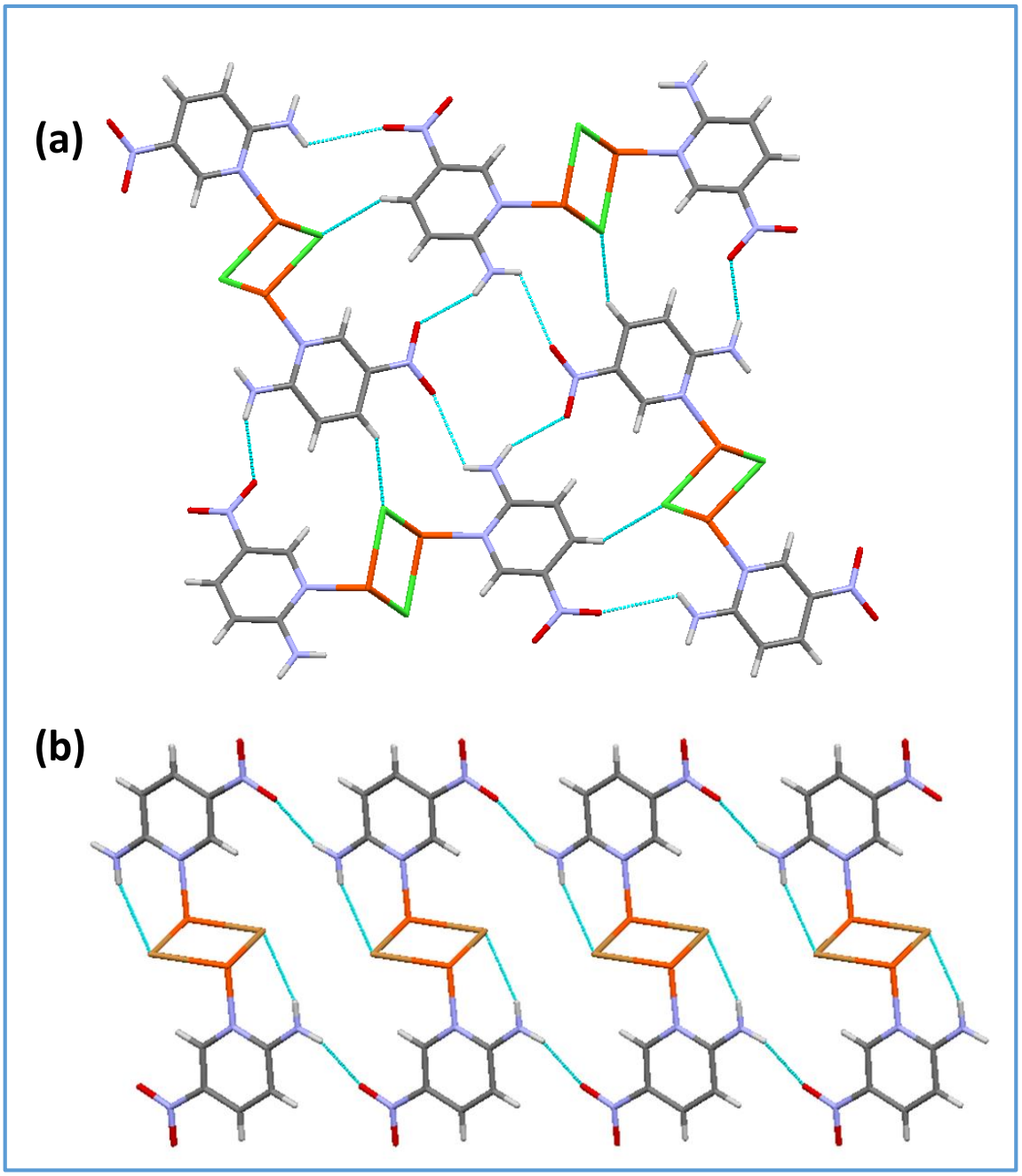

Figure 3.6. Packing of complexes **18** (a), and **19** (b), viewed along the *a* axis. Dashed lines indicate hydrogen bonding interactions. Colour code: C; grey, O; red, N; blue, Cl; green, Br; brown, Cu; orange.

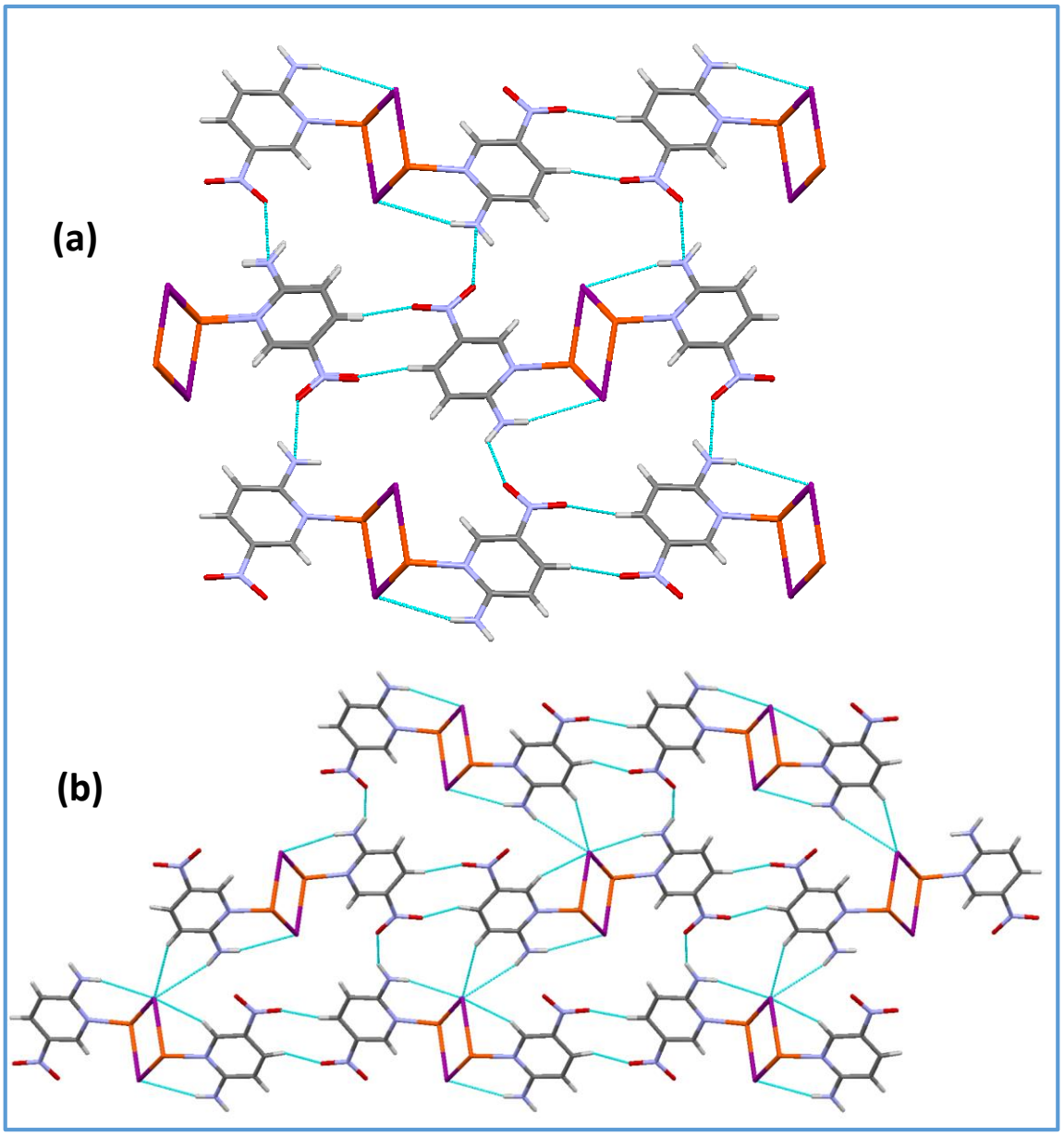

Figure 3.7. Packing of complexes **20**^{RT} (a), and **20**^{LT} (b), viewed along the *a* axis. Dashed lines indicate hydrogen bonding interactions. Colour code: C; grey, O; red, N; blue, I; violet, Cu; orange.

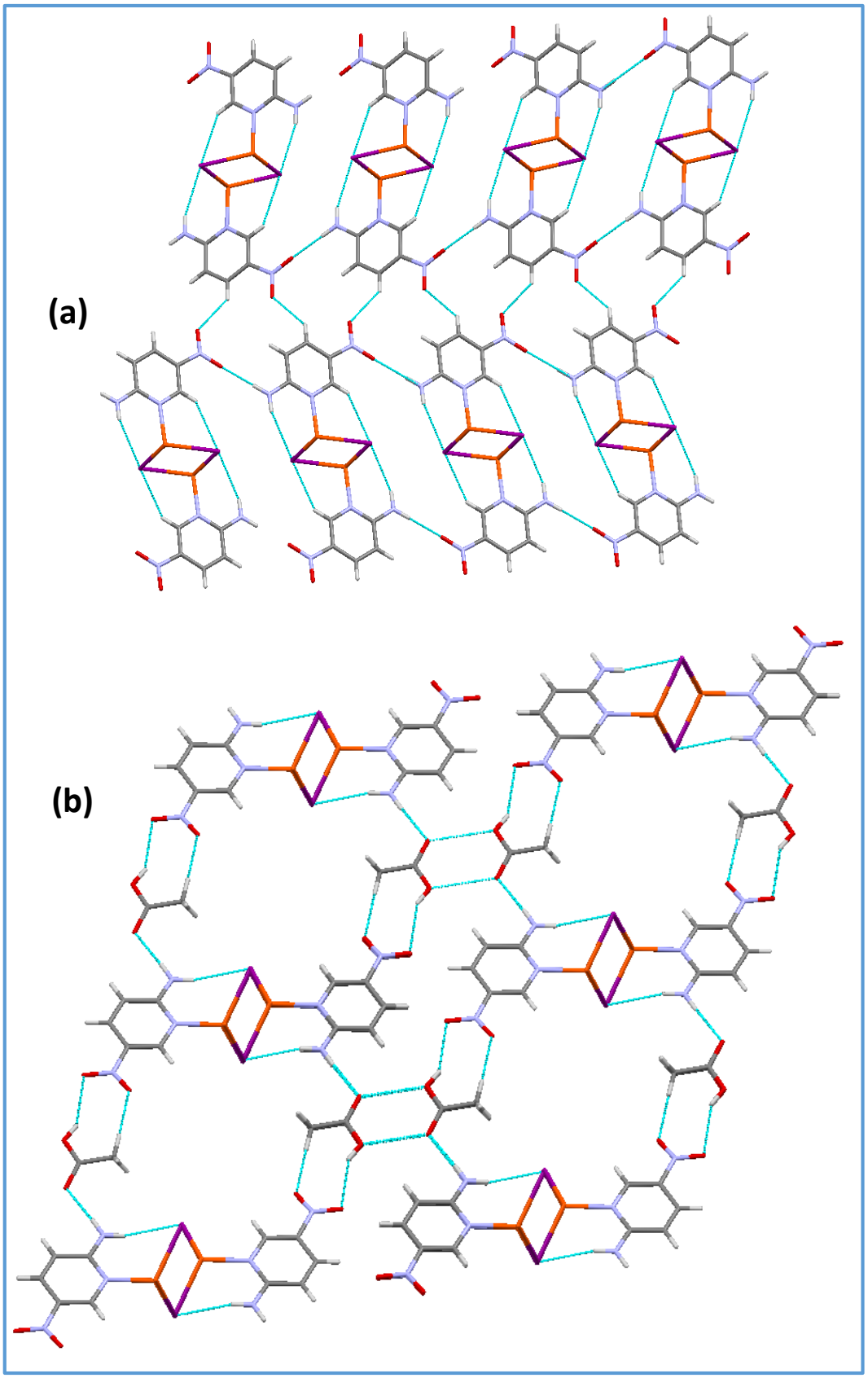

Figure 3.8. Packing of complexes **20a** (a), and **20b** (b), viewed along the *a* axis. Dashed lines indicate hydrogen bonding interactions. Colour code: C; grey, O; red, N; blue, I; violet, Cu; orange.

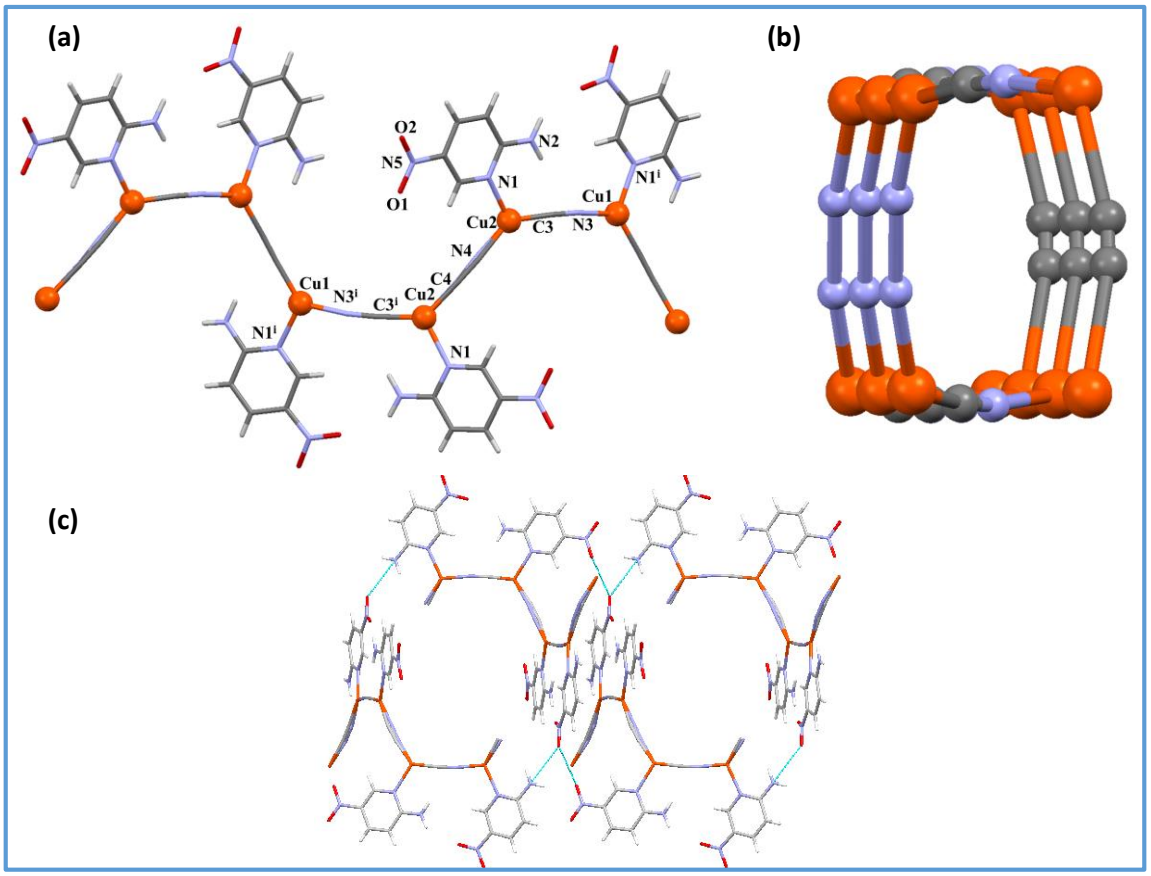

Figure 3.9. Fragment of the polymeric chain of complex **21** (a) and detail of the helical shape of the chain core b), where ANP ligands have been omitted for clarify. Packing of complex **21** viewed along the *a* axis (c). Dashed lines indicate hydrogen bonding interactions. Colour code: C; grey, O; red, N; blue, Cu; orange.

Complex **21** crystallizes in the monoclinic *P2/n* space group with cell parameters *a* = 14.6169(3) Å, *b* = 7.2367(2) Å, *c* = 16.1212(3) Å, and β = 110.554(1) °. Its crystal structure is formed by helical polymeric chains $[CuCN(ANP)]_n$ running parallel to the [100] direction (**Figure 3.9**). The packing of these chains is accomplished through a dense net of hydrogen interactions involving the NO_2 and NH_2 groups from neighbouring chains. The copper atoms within the same chain are located at longer distances than the ones found in complexes bridged by halides due to the longer length of the CN ligand that coordinates in a linear Cu-CN-Cu mode: Cu1-Cu1 = 4.866 Å, Cu2-Cu2 = 4.930 Å and Cu1-Cu2 = 4.946 Å. Some statistical disorder can be found in two of the three crystalographicaly independent CN groups acting as bridging ligands (involving atoms C4-N4 and $C4^i$-$N4^i$).

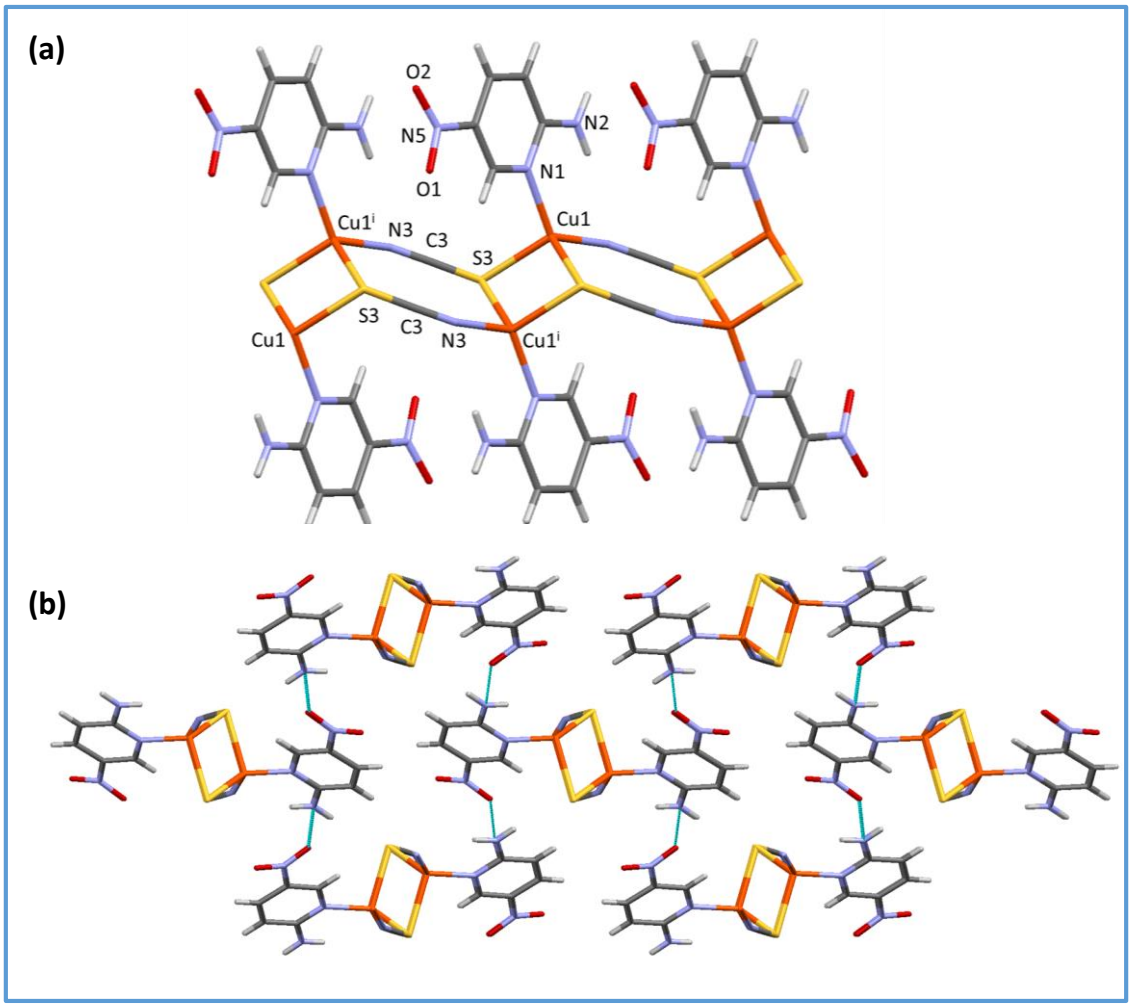

Figure 3.10. Fragment of the polymeric chain of complex **22** (a). Packing of complex **22** viewed along the *a* axis (b). Dashed lines indicate hydrogen bonding interactions. Colour code: C; grey, O; red, N; blue, S; yellow, Cu; orange.

Complex **22** crystallizes in the monoclinic $P2_1/n$ space group with cell parameters a = 5.8985(1) Å, b = 14.2513(3) Å, c = 10.8843(2) Å, and β = 105.129(1) °. The crystal structure is formed by chains (**Figure 3.10a**) similar to the ones found in complexes **18-20** with the double-stranded stair motif. In this case the copper(I) metal centers are bridged by μ_3-1κ*N*, 2:3κ^{2}S ligands, where the sulphur atom is bridging two neighbor copper centers to form Cu_2S_2 squares, and the nitrogen atom is coordinated to a metal atom from another Cu_2S_2 square. This coordination mode gives rise to alternating long and short rectangles along the chain. The corresponding short and long Cu···Cu distances within the chain are 2.861 Å and 5.245 Å, much longer than the ones found in complexes **18-20** (**Figure 3.5** and **Table 3.1**). The packing of the chains is achieved through hydrogen bonds involving the NH_2 groups from the ANP ligand and the SCN bridges of

adjacent chains (**Figure 3.10c**). There are also intrachain hydrogen bonds between the other amino hydrogen atom and the SCN ligand.

As we have previously mentioned that the reactions of CuI with EtIN or HIN have produced complexes **23** and **24** respectively. These complexes present the common feature of their double-stranded stair motif formulated as $[CuI(L)]_n$ similar to those observed in complexes **18**-**20**, with L = EtIN, for (**23**) (**Figure 3.11a**), or HIN, for (**24**) (**Figure 3.12a**), where copper(I) metal centers are bridged by μ_3-iodides. Three bridging iodides and the iminic nitrogen atom of the pyridinic ligands formed the tetrahedral coordination environment around the metal centers. These complexes are not isostructural but the core of the chains is almost identical. The copper-iodide and copper-pyridinic nitrogen bond distances are similar to those of other known similar $[CuI(L)]_n$ stairs.[40-44] **Table 3.2** collects the most relevant Cu-I, Cu-N and Cu···Cu bond distances and angles for complexes **23** and **24**. The Cu···Cu distances within the chains found in these complexes are close to or above the sum of the van der Waals radii (2.80 Å). The iodide is tricoordinated in a distorted pyramidal geometry. The stair type chain can also be described as composed of planar Cu_2X_2 squares, as found in polymorphs of complex **20**, that share two opposite sides with angles between adjacent squares of 120.9º (**23**) and 119.3º (**24**), respectively. The EtIN, and HIN ligands are arranged in such a way that they are tilted [82.0º (**23**), and 90.6º (**24**)] and twisted [63.5º (**23**), and 61.0º (**24**)] (**Table 3.2**) relative to the propagation direction of the chain. Despite the similarity of the double ladder polymeric chains of complexes **23** and **24**, their supramolecular architecture differs considerably. The ethoxy residue of the pyridinic ligand in complex **23**, precludes a close approach of the chains to establish π-π stacking interactions between the pyridinic rings. Therefore, the final 3D cohesiveness is achieved only by means of weak van der Waals interactions (**Figure 3.11b**). On the other hand, complex **24** presents a supramolecular crystal structure directed by the presence of complementary hydrogen bonds between the carboxylic groups of adjacent isonicotinic acids, giving rise to 2D supramolecular sheets parallel to the (102) plane that assemble together by means of weak van der Waals interactions (**Figure 3.12b**). This complementary hydrogen bonding scheme between carboxylic groups is a well-known supramolecular synthon that usually directs the supramolecular crystal structure of organic molecules containing carboxylic groups.[46]

Table 3.2. Selected distances (Å) bond angles (°) for complexes **23** and **24**.

Complexes	23	24
Cu-I1	2.7056(6)	2.6323(10)
Cu-I1^{i}	2.6180(6)	2.6313(10)
Δ[Cu-I1$_{rail}$] = [(C-I1) – (Cu-I1^{i})]	0.0876	0.0010
Cu-I1^{ii}	2.6432(6)	2.6583(10)
Cu-N1	2.044(4)	2.054(5)
Cu···Cu^{ii}	2.7971(11)	2.8715(12)
Cu···Cu^{iii}	2.8133(11)	2.8715(12)
Δ[Cu···Cu]	0.0162	0.0000
I1-Cu1-I1^{i}	102.69(2)	103.01(3)
I1-Cu1-I1^{ii}	116.95(2)	114.24(3)
I1^{i}-Cu1-I1^{ii}	115.35(2)	114.27(4)
Cu1-I1-Cu1^{ii}	63.05(2)	65.74(3)
Cu1-I1-Cu1^{iii}	102.69(2)	103.01(3)
Cu1^{ii}-I1-Cu1^{iii}	64.65(2)	65.75(3)
dihedral angle[a]	120.9	118.3
tilt angle[b]	82.0	90.6
twist angle[c]	63.5	61.0

Symmetry codes for **23**: i) x-1, y, z; ii) -x+1, -y+2, -z-1; iii) -x, -y+2, -z-1; for 2: i) x-1, y, z; ii) x, -y, -z+1; iii) -x+1, -y, -z+1and for **24**: i) x, y+1, z; ii) -x+1, y+1/2, -z+3/2; iii) -x+1, y 1/2, -z+3/2. [a]Dihedral angle between adjacent Cu_2I_2 squares. [b,c]Tiling and twist angles of the pyridinic ring relative to the propagation direction of the chain.

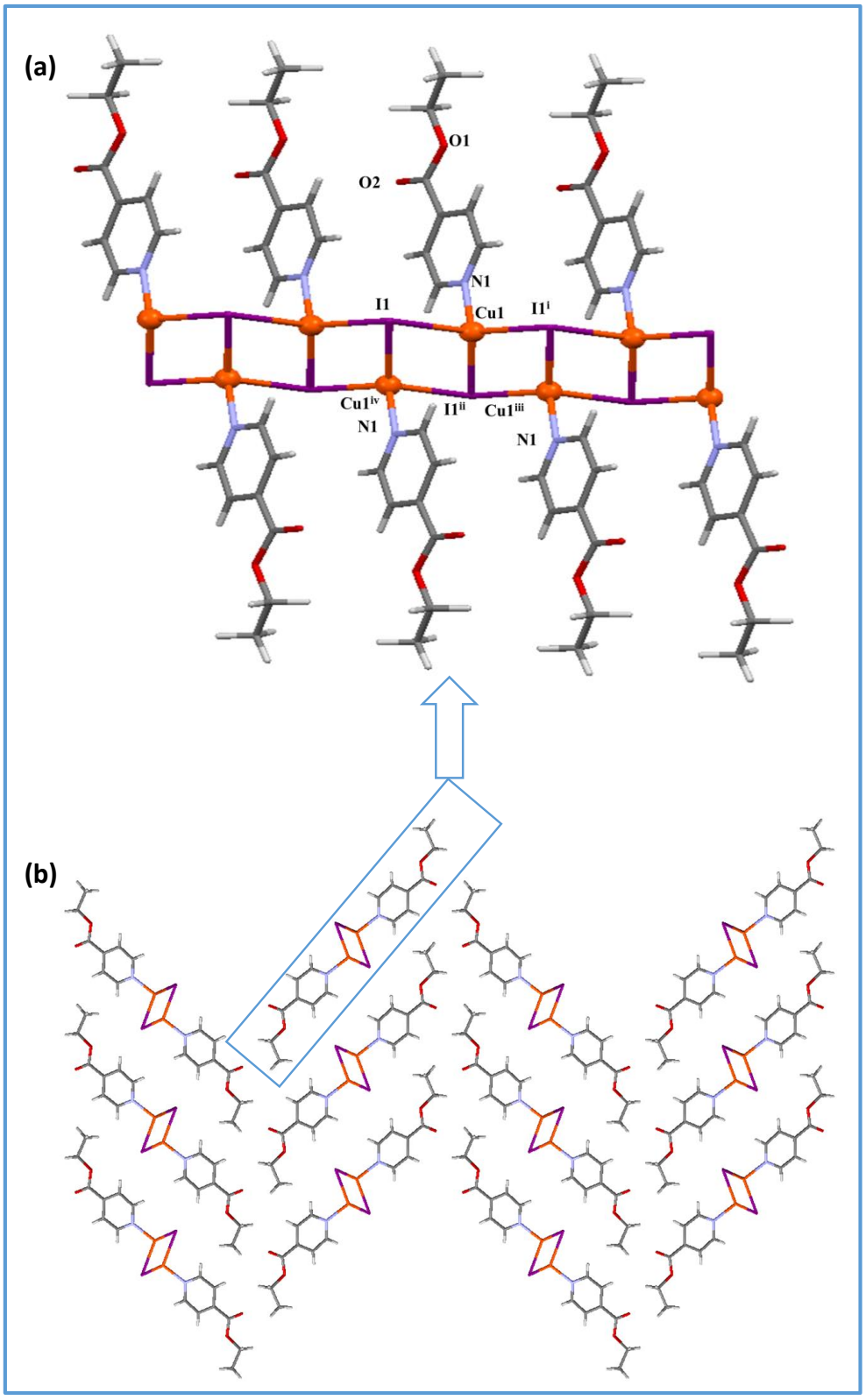

Figure 3.11. Fragment of the polymeric of complex **23** (a). Weak van der Waals interactions predominate the packing of complex **23** (b). Colour code: C; grey, O; red, N; blue, I; violet, Cu; orange.

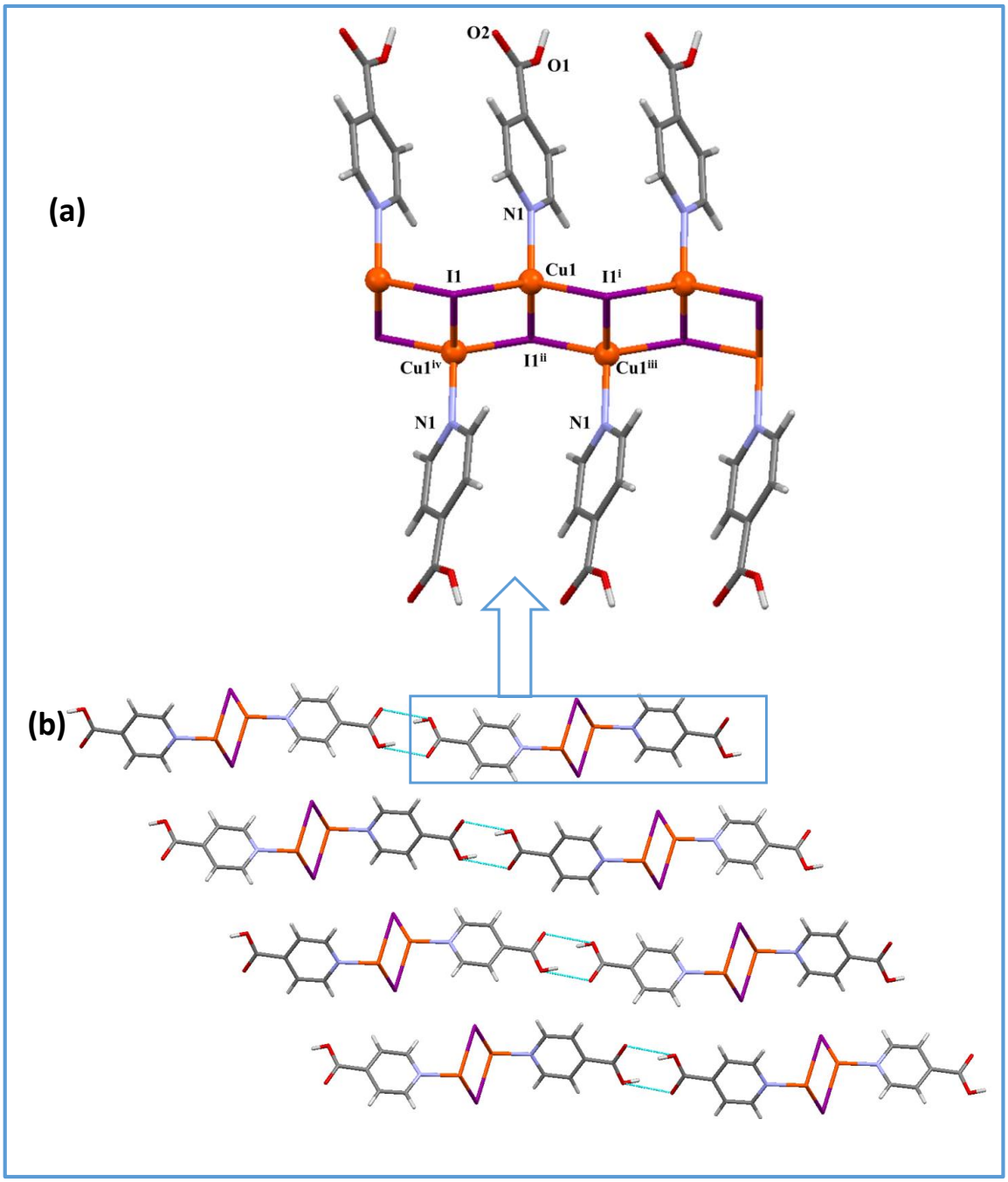

Figure 3.12. Fragment of the polymeric of complex **24** (a). Packing of complex **24** viewed along the *a* axis (b). Dashed lines indicate hydrogen bonding interactions. Colour code: C; grey, O; red, N; blue, I; violet, Cu; orange.

3.2.2. Physical properties measurements.

3.2.2.1. Electrical properties.

Two probe direct current (d c) electrical conductivity measurements at 300 K are performed in several single crystals of complexes **18-24**. The conductivity values at 300 K are obtained applying voltages from +10 V to -10 V.

The room temperature average dc conductivity values for complexes **18**-**20** are strongly dependent on the structure and on the bridging ligand. The variation observed in the conductivity values: σ (**18**) < σ (**19**) < σ (**20**) < σ (**20a**) < σ (**20b**), (**Table 3.3**), suggesting, in all cases, that this family of polymers are semiconductors. In order to confirm this behaviour and to determine their activation energies, we performed a dc conductivity measurements as a function of temperature for at least four single crystals of each complex. These measurements show that complexes **18**,**19**, **21**, and **22**, with X = Cl, Br, CN, and SCN ions, respectively, display very similar thermal behaviors (**Figure 3.13**) where the resistivity decrease with increasing the temperature and following a classical Arrhenius law above ca. 350 K (Inset in **Figure 3.13**). The activation energies determined for the four complexes are also very close to each other and in range 1.09-1.37 eV (**Table 3.3**).

Complex **20** presented a reversible semiconducting-semiconducting transition with an abrupt transition at ca. 267 K in the cooling scan and ca. 282 K in the heating one and a hysteresis of ca. 15 K (**Figure 3.14**). Interestingly, this transition implies a decrease in the resistivity by a factor of ca. 30 when passing from high to low temperature. Although the sample remains semiconducting before and after the transition, the activation energy decreases from ca. 0.40 eV at high temperatures to ca. 0.08 eV at low temperatures (**Table 3.3**).

These values indicate that the low temperature phase is a better conductor and has a lower activation energy, in contrast with the usual behavior observed in chain complexes, where the Peierls transitions imply a decrease of the resistivity and an increase of the energy gap in the low temperature phase.[47-51]

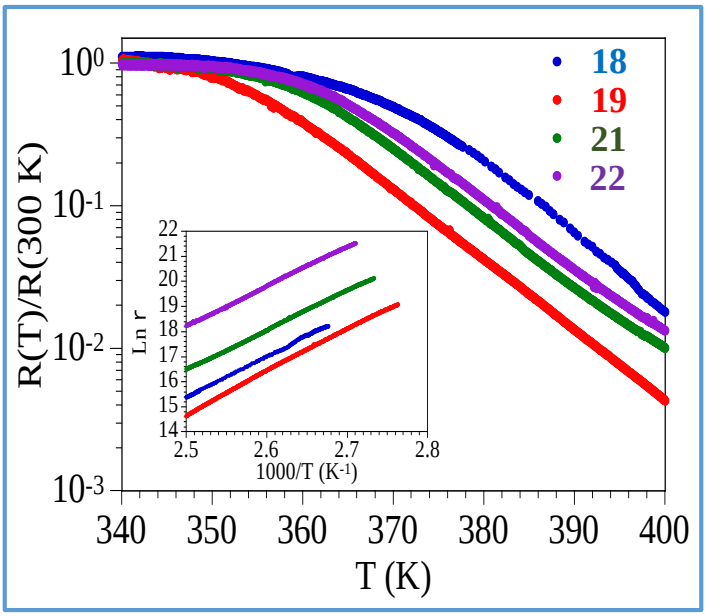

Figure 3.13. Thermal variation of the resistivity (logarithmic scale) of complexes **18** (blue), **19** (red), **21** (green) and **22** (violet) in the temperature range 350-400 K. Inset shows the Arrhenius plot for the same complexes.

This unexpected result can be easily explained with the structural data obtained for **20^{LT}** and **20^{RT}** above and below the transition temperature. The main difference between **20^{RT}** and **20^{LT}** is the presence of two independent Cu and I atoms in **20^{LT}**, compared to only one in **20^{RT}** and **20a**, resulting in a dimerized chain in **20^{LT}**. A second interesting result shown by the electrical conductivity of complex **20** is the presence of strong oscillations in the resistivity when the sample is heated above ca. 370 K, suggesting that some kind of degradation or transformation is taking place at high temperatures (**Figure 3.14**). This transformation leads to a state with a much higher conductivity and even a metallic-like behavior from 400 K down to ca. 300 K. At lower temperatures, the crystals show again a semiconducting behavior with a very small activation energy of ca. 10 meV. In the successive heating and cooling scans the samples show similar semiconducting behaviors from low temperatures to ca. 300 K and metallic-like behaviors above ca. 300 K. In the metallic-like phase, the conductivity is four to six orders of magnitude higher than the original values. This behavior is observed in at least four different crystals of complex **20**. Complexes **20**, **20a** and **20b** show very similar behaviours except for the transition at ca. 267-282 K, that is only observed in complex **20** (**Figure 3.14** and **Figure 3.15**). Thus, **20a** and **20b** show semiconducting behaviours with activation energies of 0.37 and 0.20 eV (**Table 3.3**) respectively but no transition around 275 K (**Table 3.3** and **Figure 3.15**). Similar to complex **20**, complexes **20a** and **20b** also show an important increase in the

conductivity of ca. four orders of magnitude after heating at 400 K and display a metallic-like behaviour at high temperatures and semiconducting regimes with lower activation energies at low temperatures (**Table 3.3**). Unfortunately, the crystals loos the crystallinity when heated to 400 K, precluding a structural study of this highly conducting phase. Nevertheless, given the relative easiness of the CuI chain to slightly modify its structure and the important consequences of these small modifications on the electrical properties, we can anticipate that the transition that taken place at high temperatures must imply a change inside the CuI chain. This change would lead to shorter Cu···Cu distances and better overlaps of the copper orbitals, resulting in the enhanced conductivity observed experimentally.

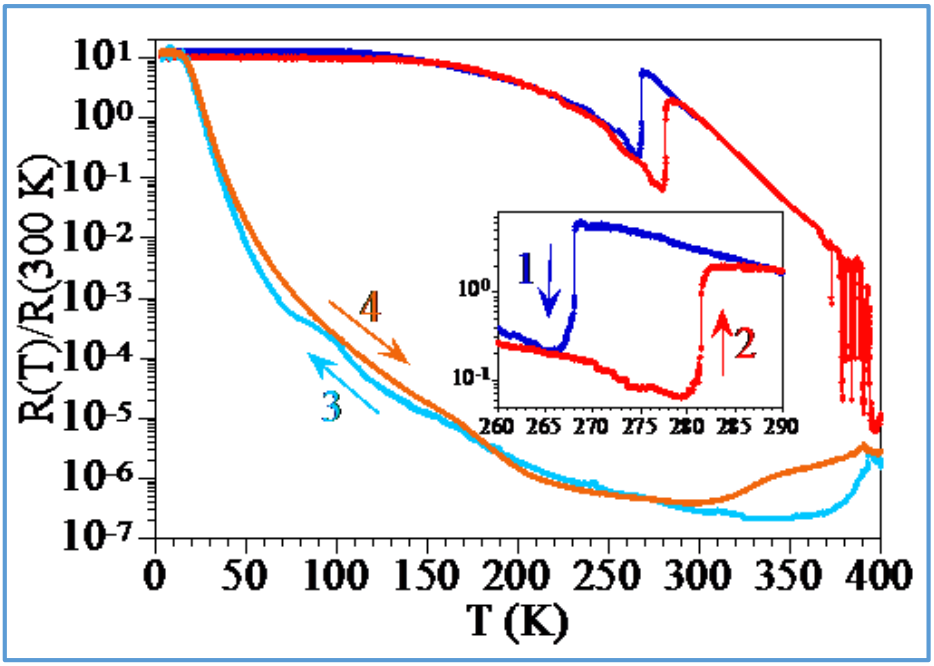

Figure 3.14. Thermal variation of the normalized resistance (logarithmic scale) of complex **20**^{RT} after successive heating and cooling scans (1-4) in the 2-400 K range. Inset shows the transition taking place at 268-281 K.

In complexes **20** (**20**^{RT} and **20**^{LT}), **20a**, and **20b**, the variations observed in the conductivity values, σ(**20**) < σ (**20a**) < σ (**20b**), (**Table 3.3**), suggest that the main factors determining the conductivity must be the structural parameters in these chains as the average Cu···Cu distance (3.01 Å in **20**^{RT}, 2.98 Å in **20**^{LT}, 2.88 Å in **20a** and 2.714 Å in **20b**) and the dihedral angle between adjacent Cu_2I_2 units which is closer to 90º in **20a** (114.1º) than in **20**^{RT} (116.8-117.4º) (**Table 3.3**), resulting in a better orbital overlap in

20a. Furthermore, the high conductivity values displayed by complexes **20a** and **20b**, where the Cu···Cu distances are shorter than the sum of the van der Waals radii (2.8 Å), confirm that this short Cu···Cu distances play a key role in the electronic properties. At 400 K the conductivities reach values in the range $1x10^{-8}$ to $1x10^{-3}$ S cm^{-1} (**Table 3.3**).

Table 3.3. DC conductivity values at 300 and 400 K and experimental and calculated activation energies in complexes **18**-**24**.

Complexes	σ_{300} (S/cm)	σ_{400} (S/cm)	E_a (eV) exp.	E_a (eV) calc.
18	$2.0x10^{-9}$	$2.1x10^{-7}$	1.09	1.17
19	$3.0x10^{-9}$	$4.4x10^{-7}$	1.34	0.75
20^{RT}	$1.1x10^{-8}$	$1.0x10^{-5}$ *	0.40	0.59
20^{LT}			0.08	0.18
20a	$5.0x10^{-6}$	$1.0x10^{-4}$ *	0.37	0.31
20b	$1.4x10^{-3}$	$5.0x10^{-3}$ *	0.20	0.29
21	$2.9x10^{-10}$	$6.7x10^{-8}$	1.25	1.26
22	$2.0x10^{-12}$	$1.2x10^{-8}$	1.37	2.31
23	$2.0x10^{-6}$		0.08	0.04
24	3×10^{-3}		0.2	0.13

* The crystals decompose at 400 K and show a metallic-like behaviour in the cooling scan from 400 to ca. 250 K.

In complexes **18**-**20** the conductivity values follow the expected order from orbital overlap considerations (Cl < Br < I)[52] and Cu···Cu and Cu-X bond distances. Albeit, the conductivity for complex **19** is only 1.5 times higher than that of the complex **18** derivative. Furthermore, in the Br derivative the Cu-X bond distances are more regular than in the Cl derivative and, therefore, its conductivity should be much better than that of the Cl complex. This unexpected small increase may be attributed to the significantly smaller Cu-X-Cu bond angle observed in the Br derivative (98.7º) compared with the one observed in the Cl derivative (104.9º). Complex **20** is better conductor than complexes **18** and **19** since the orbital overlap is larger for X = I.

Complexes **21** and **22** present, as expected, the lower conductivities since both bridges give rise to much larger Cu···Cu distances. The order σ (**22**) < σ (**21**) also agrees with a longer Cu···Cu distance (5.245 Å) and the longer bridge along the chain in the SCN- derivative (**22**) compared with the CN- one.

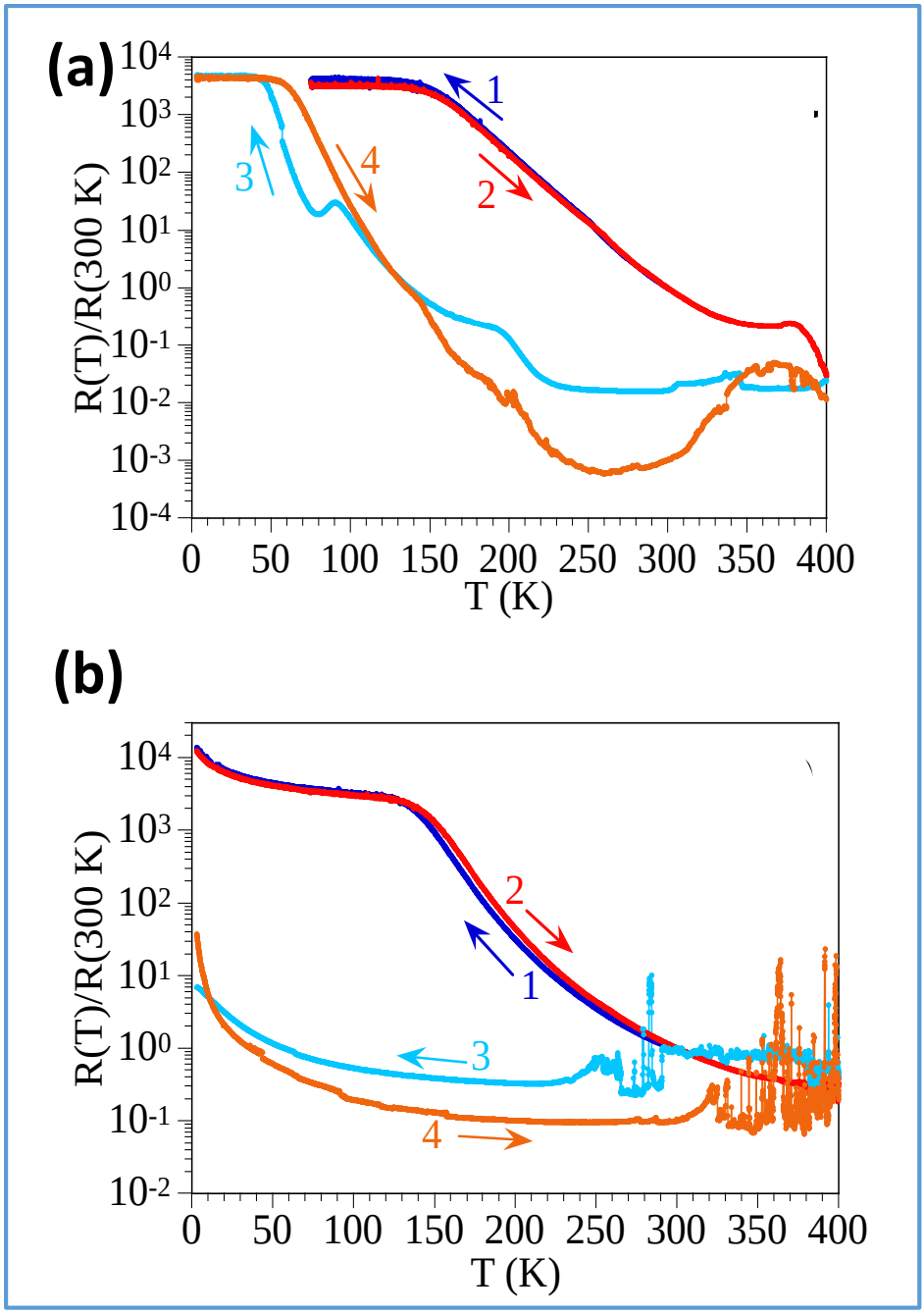

Figure 3.15. Thermal variation of the normalized resistance (logarithmic scale) for complexes **20a** (a) and **20b** (b) after successive heating and cooling scans (1-4) in the 2-400 K range.

Complex **23** shows a dc conductivity of *ca*. 2×10^{-6} S/cm at room temperature and a classical semiconducting behavior (the resistivity increases as the temperature is decreased, (**Figure 3.16a**) with an activation energy of *ca*. 80 meV. When the crystals of complex **23** are heated to 400 K they all show an abrupt and irreversible drop of the resistivity of more than four orders of magnitude at *ca*. 360 K (**Figure 3.16a**). After the transition, the conductivity of the sample at room temperature observed in the successive cooling and warming scans is also *ca*. four orders of magnitude higher (*ca*. 5×10^{-2} S/cm at 300 K). Besides the increase of the conductivity, complex **23** shows a quasi-metallic behavior in the temperature range of 400-250 K and a classical semiconducting behavior below 250 K with a very low activation energy of *ca*. 20 meV. This behavior suggests that complex **23** suffers an irreversible transition to a highly conducting state at high temperatures and remains in this state in the successive scans. Once the sample has been heated to 400 K the transparent yellow crystals become opaque and white. Furthermore, as can be observed in **Figure 3.16a**, after the transition the conductivity shows large oscillations. These facts suggest that the transition could consists of a partial degradation/transformation of the crystals due to the irreversible release of some CO_2 at high temperatures. The released CO_2 would be formed by oxidation of the carboxylate groups of the ligands and would imply the reduction of some Cu(I) centers to Cu(0). This hypothesis is confirmed by TGA analysis coupled to a mass spectrometer (**Figure 3.19**) and explains the irreversible formation of a highly conducting phase with a quasi-metallic behavior. The amount of released CO_2 must be small since the overall crystallinity is kept after the transition at 380 K, as clearly demonstrated by the X-ray powder diffractogram at 380 K which is identical to the experimental and simulated ones from the structure at 296 K (**Figure 3.17**). An additional proof of the reduction of a small fraction of Cu(I) into Cu(0) is provided by magnetic measurements performed at 400 K on a sample of complex **23** (**Figure 3.21**).

Complex **24** shows a dc room temperature conductivity of *ca*. 3×10^{-3} S/cm (**Figure 3.16b**) and a semiconducting behaviour with an activation energy of *ca*. 200 meV. When the crystals of **24** are heated up to 400 K they remain semiconductors although at *ca*. 380 K they show a small increase of the resistivity probably due to sample degradation or disorder induced in the sample. When the sample is cooled again, complex **24** remains semiconducting although with a much lower activation energy 25 meV. Additionally, complex **24** shows higher resistivity values in the temperature range 400-150 K and a small transition at *ca*. 288 K only observed in the cooling scan. When the sample is heated

again, it shows lower resistivity values in the temperature range 160-390 K. At *ca*. 390 K, it shows again a smooth increase in the resistivity (as the one observed in the first heating scan) and at 400 K it recovers the resistivity value observed in the first heating scan. This behaviour contrasts with the one observed in complex **23** and suggests that complex **24** has a much higher thermal stability (probably due to the presence of the strong H-bonds between adjacent chains), in agreement with the thermogravimetric analysis (**Figure 3.20**). Unfortunately, the crystals of complex **24** also partially decompose upon heating, precluding a structural analysis at high temperatures. Nevertheless, we can suppose that after heating at 400 K the crystals of **24** release very small amounts of CO_2 with the simultaneous formation of Cu(0). The presence of very small amounts of Cu(0) would be responsible for the decrease of the activation energy but would not result in a sharp increase of the conductivity nor in a quasi-metallic behaviour (as observed in **23**) probably because the amount of Cu(0) is well below the percolation limit. Although the two structures are very similar, their room temperature conductivities are quite different (**24** is almost three orders of magnitude better conductor than **23** before the high temperature transition).These differences in conductivity values can be rationalized taken into account the small variations in the Cu-I bond distances and angles and/or the Cu···Cu distances (**Table 3.2**). As can be seen in **Table 3.2**, the Cu···Cu distances are significantly shorter in complexes **23** (average values of 2.805 Å) than in **24** (average value of 2.872 Å). These Cu···Cu distances disagree with the conductivity values observed in complex **23**. Although it could be argued that the dimerization of the Cu···Cu distances (measured as the difference between the two Cu···Cu distances, **Table 3.2**) agrees with the observed conductivity values, both Cu···Cu distances are longer in **24** than in **23**. Therefore, the most plausible pathway for the electronic delocalization must be the Cu-I_{rail} [(Cu-I1) and (Cu-I1^{i})] bonds along the chain (**Table 3.2**). These bond distances are shorter in **24** (average value 2.632 Å) than in **23** (2.659 Å), in agreement with the lower resistivity value found in **24**. Furthermore, the dimerization of these Cu-I_{rail} bonds along the chain is also much shorter in **24** (0.001 Å) than in **23** (0.0876 Å), also in agreement with the observed conductivity values. Additionally, although the differences are shorter, the I-Cu-I bond angle along the chain is larger in **24** (103.01(3) º) than in **23** (102.69(2) º) (**Table 3.2**). This larger angle is expected to lead to a better orbital overlap and, therefore, to a high electrical conductivity, again in agreement with the observed values. Finally, the dihedral angle between the Cu_2I_2 rectangular units forming the chain also suggests that complex **24** should be a better

conductor since this angle is shorter in **24** (119.3º) than in **23** (120.9º), **Table 3.2**, giving rise to a better orbital overlap in **24** (**Figure 3.18**).

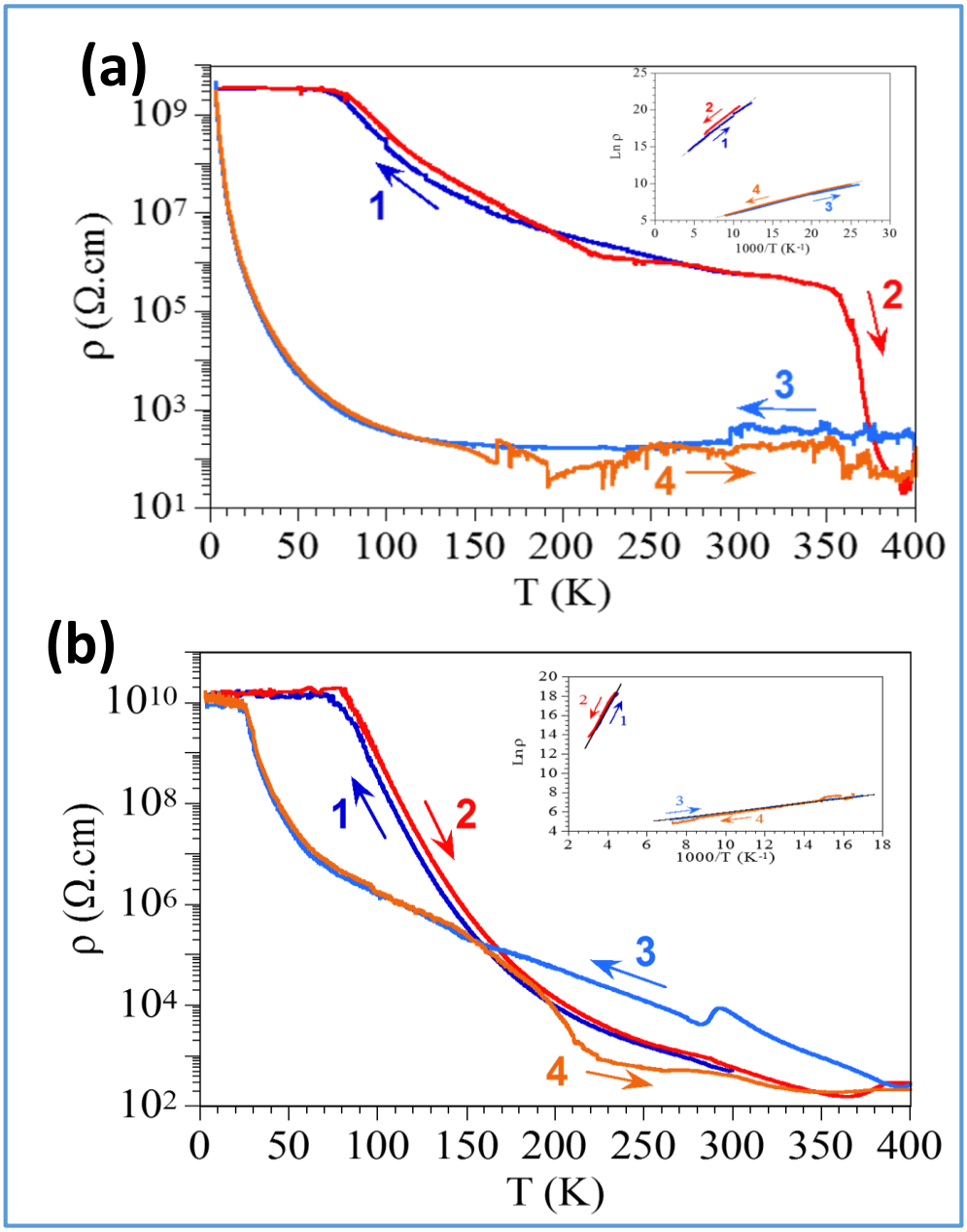

Figure 3.16. Thermal variation of the electrical conductivity in four successive scans (1-4). The horizontal resistivity values indicate that the resistance has reached the measuring limit of our equipment (5x1011 Ω) with inset, Arrhenius plot (Ln ρ vs 1/T) for the successive cooling and heating scans (1 4) in complex **23** (a) and **24** (b).

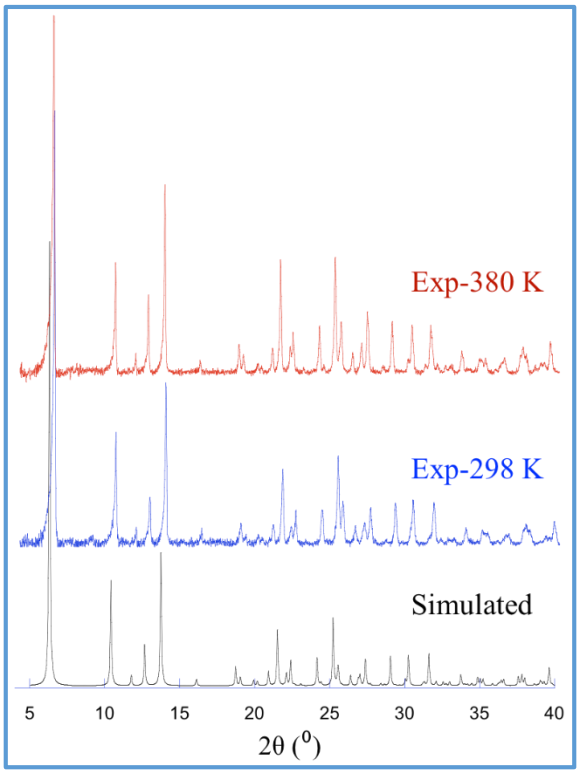

Figure 3.17. Experimental (at 298 and 380 K) and simulated powder diffractograms of **23**.

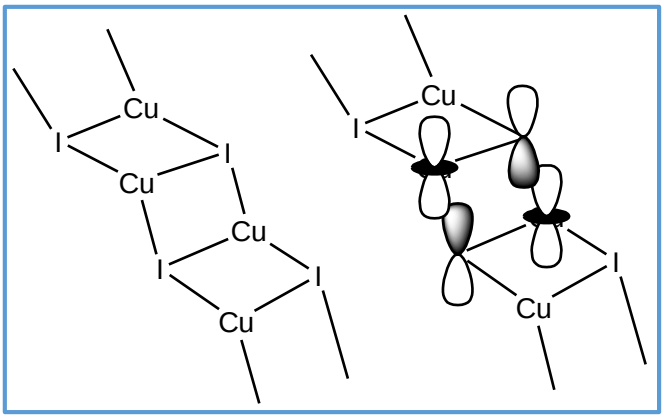

Figure 3.18. Schematic representation of the Overlap simulation between the d_z^2 orbitals of Cu center and the p_z orbitals of iodine.

In order to gain insights into the chemical processes taking place during the thermal treatment of complexes **23** and **24** and how they influence their conductivity, we have characterized samples of complexes **23** and **24** with TGA-MS under an inert atmosphere of helium. It was hence possible to unambiguously identify the fragments cleaved from the isonicotinato derivatives at moderate temperatures (**Figure 3.19** and **Figure 3.20**). Analysis of complex **23** from room temperature to 300 °C revealed an abrupt mass loss

around 180 °C. Continuous MS enabled the allocation of the molecular fragments that were being detached from the sample as a function of temperature. Four characteristic fragments of the ethyl isonicotinate ligands with *m/z* = 78, 106, 123, and 151, were found to cause the mass reduction. Moreover, an intense continuous release of CO and CO2 was detected during all the studied temperature range, probably arising from the carboxylic moieties, highlighting the smaller thermal stability of complex **23**. In stark contrast, complex **24** exhibited a remarkable higher stability with almost no appearance of any peak in the total ion current until about 250 ºC (523 K), with the characteristic fragments of the isonicotinic ligands at *m/z* =78, 106 and 123 the being detected; moreover, a less intense evolution of CO and CO2 (*m/z* =44) was detected, probably arising from the cleavage of carboxylic moieties of the pyridinic ring.

On the other hand, in order to confirm the possible reduction of a fraction of Cu(I) to Cu(0), we have performed magnetic measurements with two different samples of complex **23**, using a plastic bag and a porous paper bag. These measurements indicate that complex **23** is, as expected, diamagnetic, but when it is heated to 400 K, it shows the appearance of a paramagnetic signal that increases with time (**Figure 3.21**). This increase is much faster when the sample is placed in a paper bag than in a non-sealed plastic one, suggesting that the increase is related with a gas release that is more effective in the paper bag. The signal initially increases in a linear way and reaches saturation after *ca*. 1 hour (more than 5 hours in the plastic bag) at a magnetic moment of *ca*. 0.03 cm^3 K mol^{-1}, corresponding to *ca*. 8 % of the contribution of one electron. These measurements agree with the formation of paramagnetic Cu(0), with one unpaired electron, and CO_2 release, suggesting that this redox reaction is probably limited by diffusion of the CO_2 in the solid. In fact, the appearance of the weak paramagnetic contribution may be explained by the reduction of Cu(I) to Cu(0), which has one unpaired electron. The delocalization of the Cu(0) unpaired electron would give rise, on one hand, to the very high conductivity and the quasi metallic behavior observed in this complex after the transition and, on the other hand, to a Pauli-type paramagnetic contribution accounting for the increase in the paramagnetic signal with time.

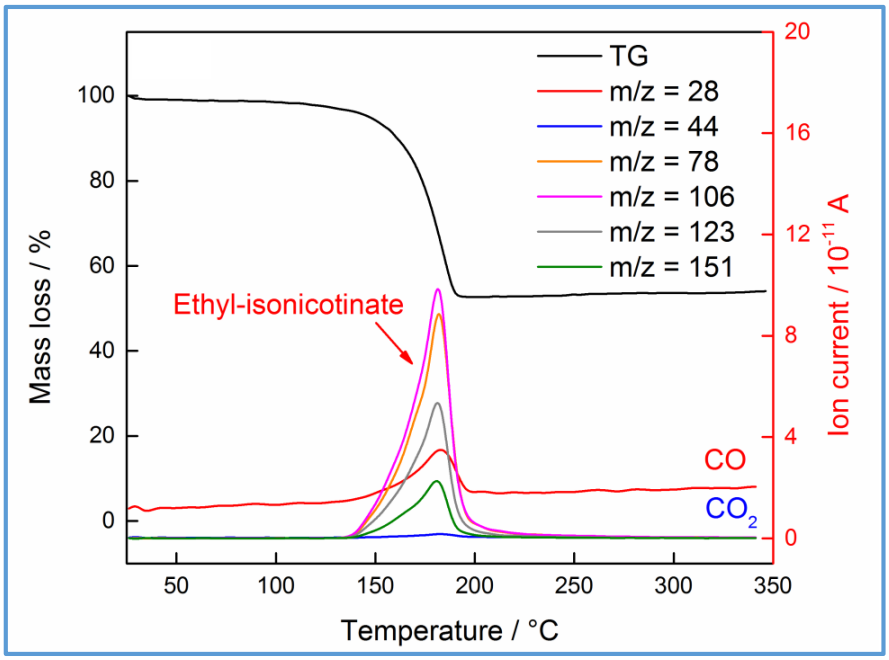

Figure 3.19. TGA-MS analysis of the complex **23** using a heating rate of 10K/min under helium. A continuous release of CO (m/z = 28) and CO2 (m/z = 44) can be detected. The intense peak mass loss takes place at ca. 180 °C. Depicted MS traces can be attributed to the ethyl isonicotinate fragments – m/z (78, 106, 123, and 151).

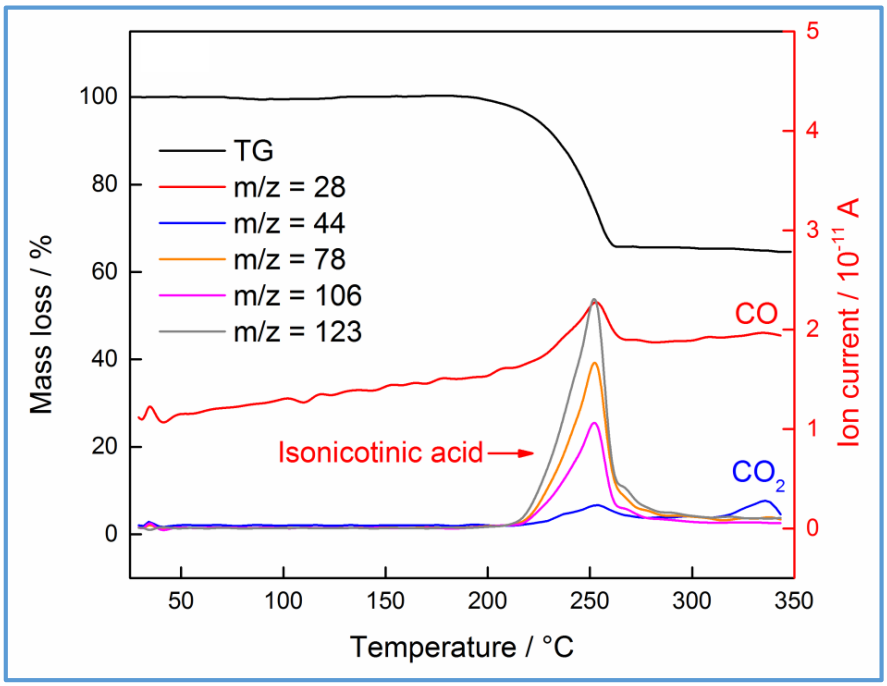

Figure 3.20. TGA-MS analysis of the complex **24** using a heating rate of 10 K/min under helium. A continuous release of CO (m/z = 28) and CO2 (m/z = 44) can be detected. The first peak mass loss takes place at ca. 250 °C. Depicted MS traces can be attributed to the isonicotinic acid fragments – m/z (78, 106, and 123).

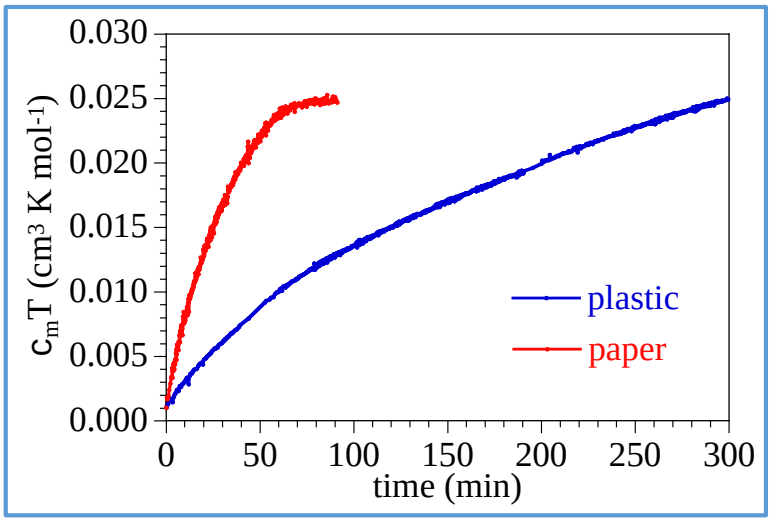

Figure 3.21. Temporal evolution of the product of the magnetic susceptibility times the temperature for complex **23** at 400.

3.2.2.2. Electrical responsive properties of $[Cu(X)ANP]_n$ polymers.

Attempts to reproduce complex **20b**, through single-crystal-to-single-crystal transformation from $\mathbf{20^{RT}}$ to **20b** using acetic acid vapours, failed. This is probably consequence of the non-porous nature of $\mathbf{20^{RT}}$. However, when a microcrystalline powder of $\mathbf{20^{RT}}$ is immersed in glacial acetic acid the colour of crystals changed from yellow to orange and loose the crystallinity, becoming amorphous (**Figure 3.22**). This can be explained as a sorption process that has taken place thanks to structure flexibility of $\mathbf{20^{RT}}$ associated with the presence of ANP ligand with donor and acceptor H-bonds groups. Surprisingly, this change is reversible and when the acetic acid is removed and the sample is dried in air during several days, the crystals become yellow and recover the crystallinity, and the dried sample presents a powder X-ray diffractogram very similar to the original (**Figure 3.22**). This reversible interaction has also been proven by the change in the electrical conductivity of $\mathbf{20^{RT}}$. Thus, a device was built up consisting of a pellet of $\mathbf{20^{RT}}$ electrically contacted with two copper wires (**Figure 3.23**). Electrical characterization of this pellet (complex $\mathbf{20^{RT}}$**)** was done at room temperature by Electrochemical Impedance Spectroscopy (EIS) measurements (**Figure 3.24**). The samples were exposed to HAcO vapour at different times and the total pellet resistance (R) was obtained from the intercept of the arc (at the low frequency end) on the Z' axis. The conductivity σ in S cm^{-1} is calculated from Z' value by using Eq. (3.1), where "l" is the pellet thickness in cm, "R" is the resistance in Ω and "A" is the electrode area in cm^2. The calculated conductivities of the samples are presented in **Table 3.4.**

$$\sigma = \frac{l}{R \cdot A} \qquad \text{Eq (3.1)}$$

Typical Nyquist plot for complex $\mathbf{20^{RT}}$, after 24 h exposed to HAcO vapour, in the frequency range 1 Hz-1 MHz is shown in **Figure 3.24a**. A careful observation indicates the presence of depressed semicircular arc at high-medium frequencies (1 MHz-30 Hz) that is attributed to the bulk properties of the complex and a line in the low frequency region typical of materials that show the capacitive behavior occurring between the mobile ion (that are blocked by the electrode-electrolyte interphase).[53]

The Nyquist plots recorded after different exposure times (45, 20 and 15 min) are similar to those obtained after 24 h exposure (**Figure 3.25**) but the intercept of the semicircle with the Z' axis shifts towards higher values. The pristine sample of $\mathbf{20^{RT}}$ (t = 0 min in

HAcO vapour), loses the semicircle shape and, in addition, the experimental measurements have a lot of dispersion from 100 Hz (**Figure 3.25**), suggesting that the material does not possess any inherent route for electrical conduction.

Table 3.4. AC conductivity values of complex **20**^{RT} at room temperature and different exposition times to HAcO or $CHCl_3$ (vapour).

$HAcO_{(g)}$ time	$_{298K}$ (Scm^{-1})	Time in the air	$_{298K}$ (S/cm)
0 min	$\sim10^{-11}$		
15 min	2.2×10^{-7}		
20 min	9.6×10^{-7}		
45 min	2.2×10^{-6}	60 min	$\sim10^{-11}$
24 h	2.5×10^{-6}	30 min	4.5×10^{-10}
$CHCl_{3(g)}$ time	σ_{298K} (Scm^{-1})		
24 h	3.59×10^{-10}		

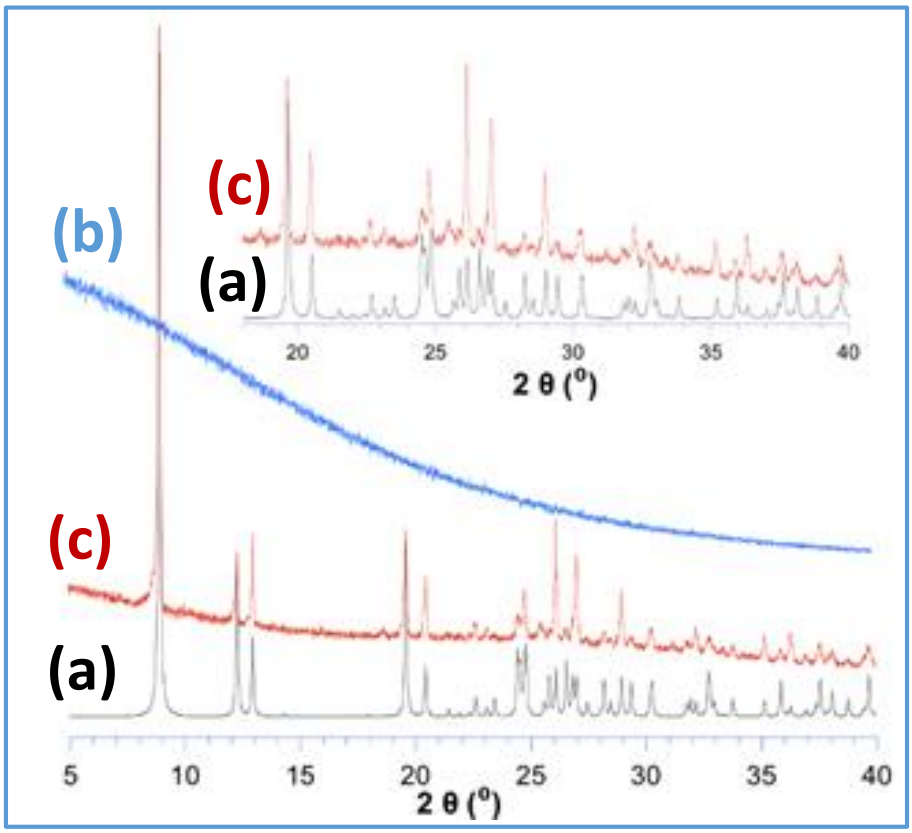

Figure 3.22. Simulated (a) and experimental X-ray powder diffractogram of a polycrystalline sample of complex **20**^{RT} immersed in acetic glacial acid (b) and after removal of the acetic acid (c). Inset shows a zoom of the 18-40º 2θ range.

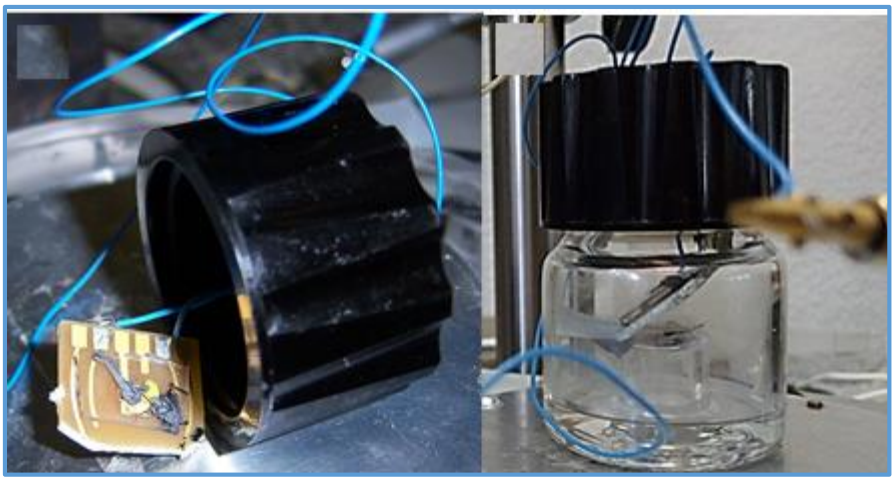

Figure 3.23. View of the yellow pellet of complex **20^{RT}** contacted with two electrodes (right) and the cell used to expose the pellet to vapours of acetic acid (left).

The conductivity increases with increasing the exposure times to acetic acid vapours (**Table 3.4**) and reaches saturation after *ca*. 45 minutes of exposure. In agreement with the Bode diagram, the semicircle representing the bulk properties of complex **20^{RT}** is shifted to higher frequencies when the HAcO exposure time increases. This fact indicates that the material/electrode interphase capacitive character becomes less important and the high conductive phase of **20^{RT}** appears (**Figure 3.25**). When saturated acetic acid pellets were exposed to air (30 min. or longer times) the Nyquist plots lost the characteristics depressed semicircle shape and a poor value of conductivity is obtained (*ca*. 10^{-11} Scm^{-1}). If we compare those results with the experiments involving different exposure times in HAcO vapour, the behaviour clearly indicates the crucial role of the HAcO molecules in establishing the conductivity pathway

In order to check the reversibility and cycling capacity of the observed drastic change in the conductivity, after 12 h in air the sample was re-exposed to HAcO vapours for 3 h. The Nyquist plot and the conductivity value (*ca*. 10^{-6} Scm^{-1}) were similar to the first ones, confirming the total reversibility of the HAcO capture/release process and its effect on the conductivity of **20^{RT}**. Successive on/off cycles (10 min in HAcO vapour followed by 70 min in air) yielded reproducible results (**Figure 3.26**) confirming the stability of the device. Furthermore, we have verified that after several weeks in air the device still presents the reproducible on/off cycles.

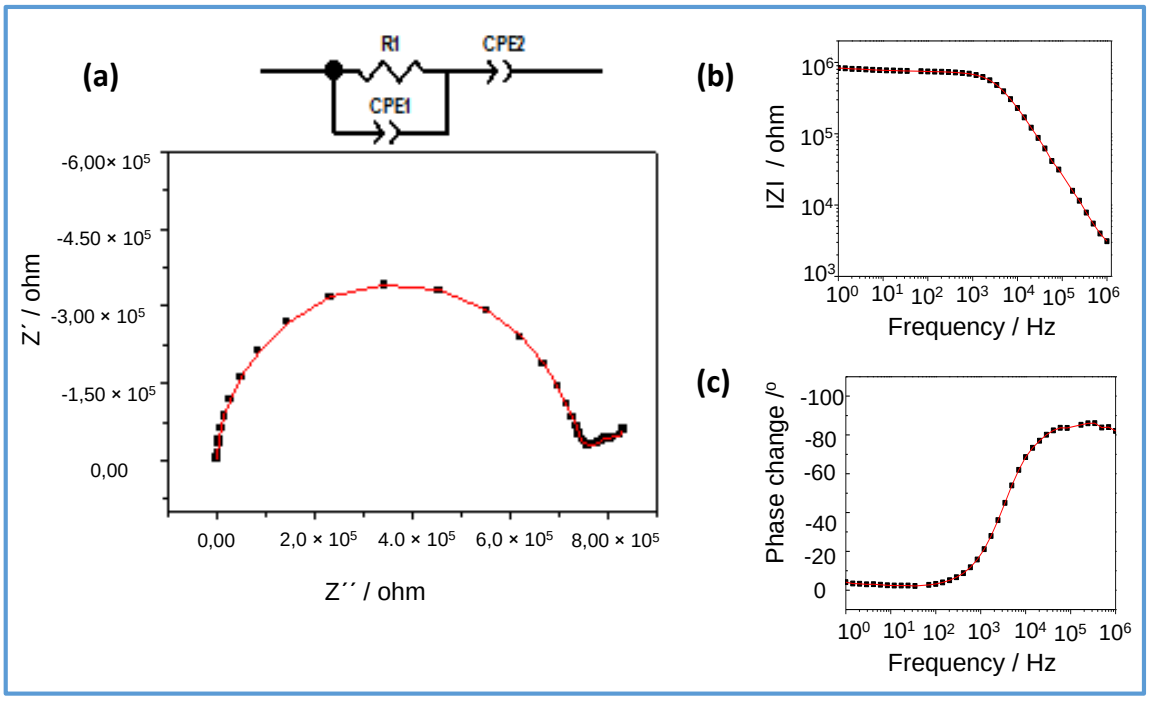

Figure 3.24. The Nyquist plot (a) and Bode plot (b, c) of complex **20**^{RT} after 24 h exposed in HAcO vapour. Experimental values (□,•), fitting values (-). The inset in (a) represent the experimental impedance plot and the fit obtained from the equivalent circuit.

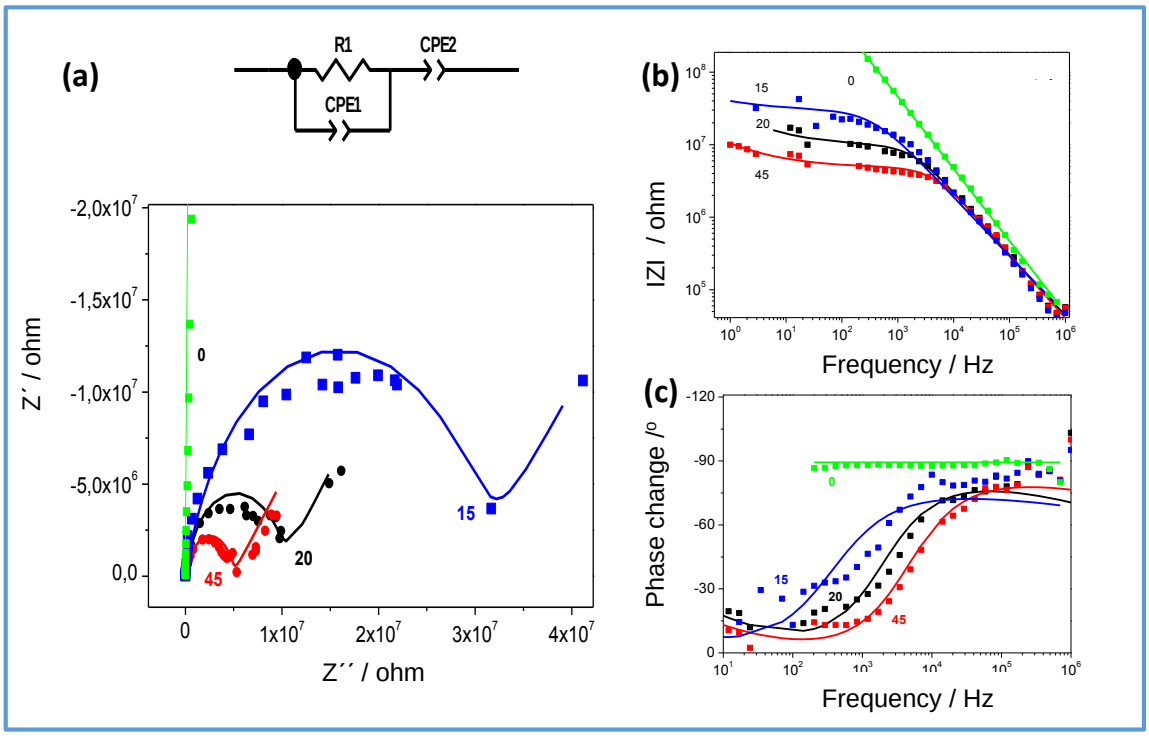

Figure 3.25. The Nyquist plot (a) and Bode plot (b, c) of complex **20**^{RT} after different exposed time (0, 45, 15, 20 min.) in HAcO (v). Experimental values (□,•), fitting values (-). The inset in (a) is the equivalent circuit.

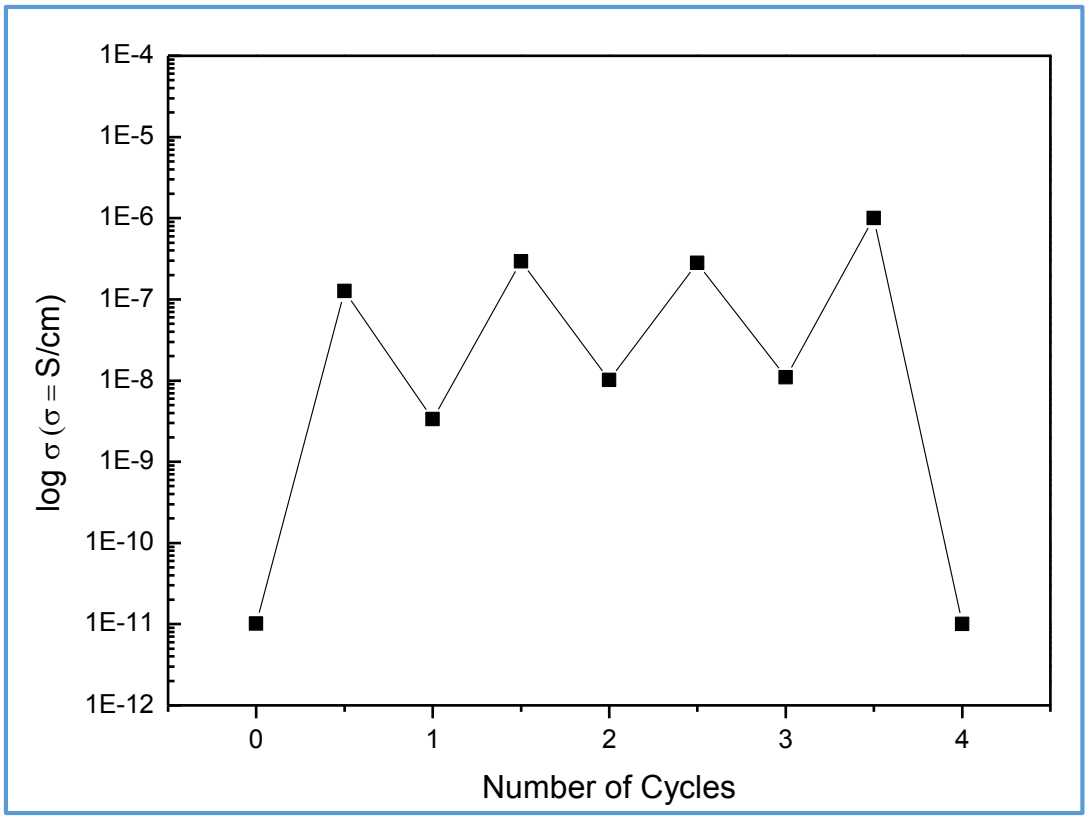

Figure 3.26. Conductivity variation *vs* on-off cycling of complex **20**^{RT} at 298K.

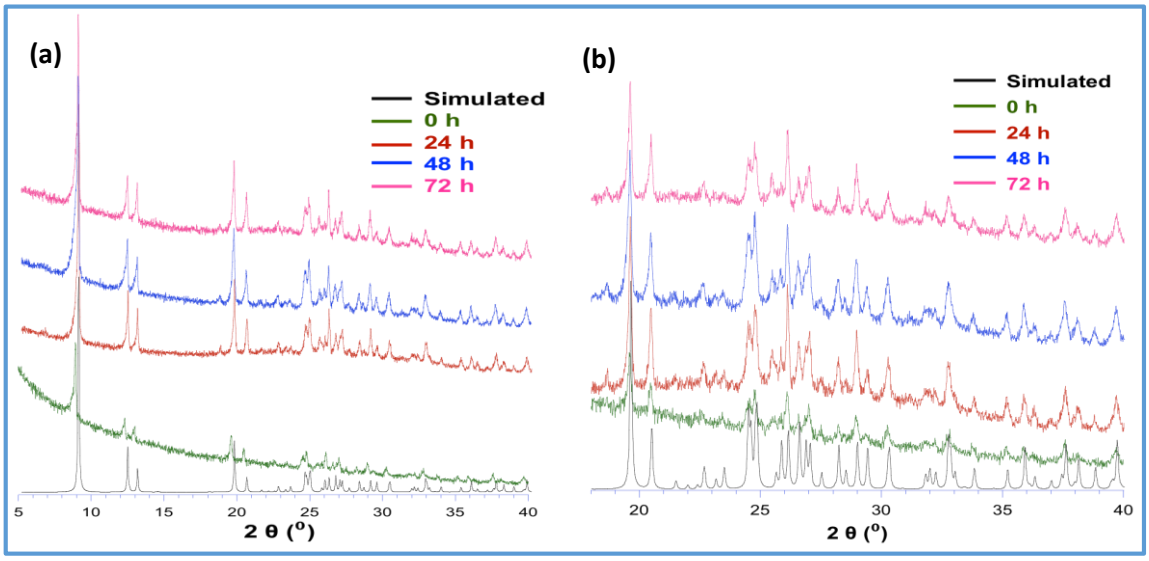

Figure 3.27. X-ray powder diffractogram in the 5-40º 2θ range (right) and in the 18-40º 2θ range (left) of a polycrystalline sample of complex **20**^{RT} exposed during 24, 48 and 72 h to HAcO vapour.

Finally, in order to confirm that the absorbed acetic acid molecules induce any relevant structural change in **20^{RT}**, we have performed a powder X-ray diffraction study with a polycrystalline sample of **20^{RT}** that was exposed to HAcO vapours during 24, 48 and 72 h. As expected, this study shows no dramatic structural changes in **20^{RT}** upon HAcO absorption (powder X-ray diffractograms remain unchanged, **Figure 3.27**), indicating that the number of absorbed HAcO molecules is low and/or that they are disordered between the chains. Obviously the adsorption should be essentially at the surface level of the pellet in a non-structurally perfect organization since these are non-porous materials, therefore desorption takes place after they are again expose to air for some time (30 min) and they recover the initial conductivity values.

In a separate experiment, a pellet of **20^{RT}** was exposed to $CHCl_3$ vapours for 24 h at 298 K (**Table 3.4**). The EIS study at 298 K shows a conductivity of *ca*. 10^{-10} Scm^{-1}, indicating the poor influence of the chloroform vapours in contrast to the HAcO ones. This results agrees with the idea that $CHCl_3$ presents a much lower capacity to interact with the ANP ligands in **20^{RT}** (it has no H-bonding capacity) and, accordingly, has a negligible ability to modify the structural parameters of the CuI chain. In contrast, HAcO has a high H-bonding capacity and, accordingly is expected to interact with the amino group of the ANP ligand and to modify the structural parameters of the CuI chain, resulting in a drastic change of the conductivity value.

In fact, these results recommend strongly the application of complex **20^{RT}** as sensor for HAcO molecules. Thus, we have decided to extend our studies to involve more solvents and other Cu_2X_2 double chains, and compare the results with the previous observations founded in **20^{RT}**. Since complexes **18** and **19** present quite similar structures and conductivity values, we have selected complexes **19** and **20^{RT}** in order to make comparative study for their electrical response versus vapors of several organic solvents. By this way, different pressed pellets of complexes **19** and **20^{RT}** have been prepared and tested in saturated vapor atmospheres of ethanol (EtOH), methanol (MeOH), diethyl ether ($(CH_3CH_2)_2O$), dimethyl methylphosphonate (DMMP) and dichloromethane (CH_2Cl_2), at 25 ºC for 1, 14, 24 and 70 h. A simple prototype device, similar to the one used to study the electrical response in complex **20^{RT}** (**Figure 3.23**), was built and used for these measurements. The initial ac conductivity values for the pristine pellets of both complexes are ca. 10^{-11} S/cm, respectively.

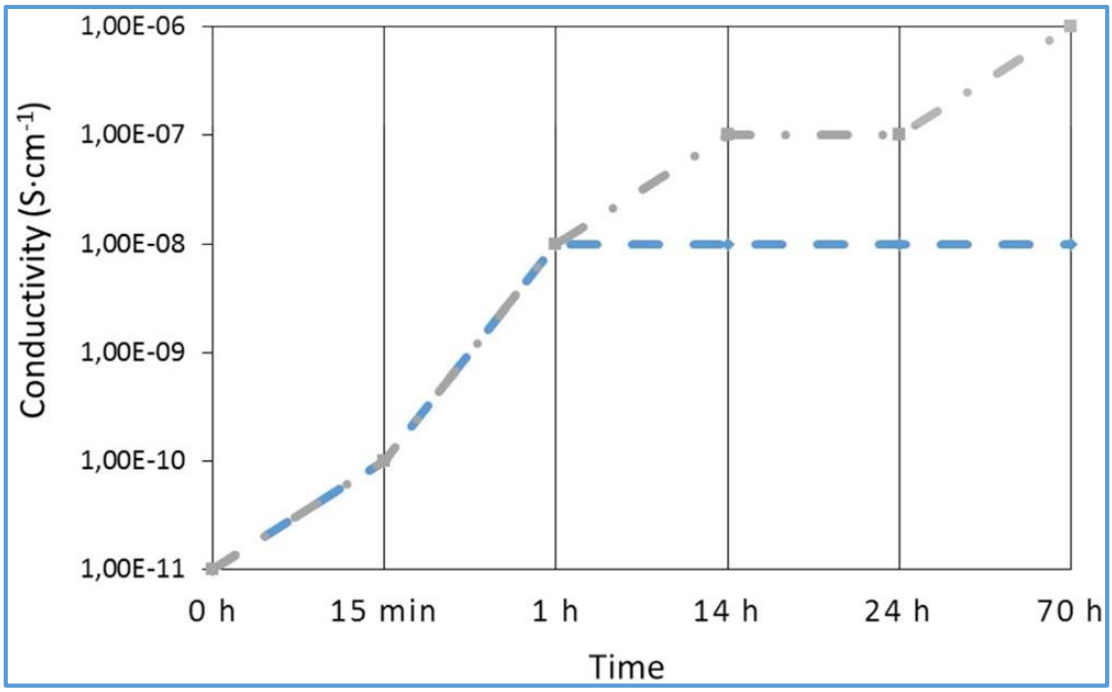

Figure 3.28. Comparison of the electrical response of complexes **19** (blue dashed line) and **20^{RT}** (gray dashed line) with different time exposition to vapors of MeOH.

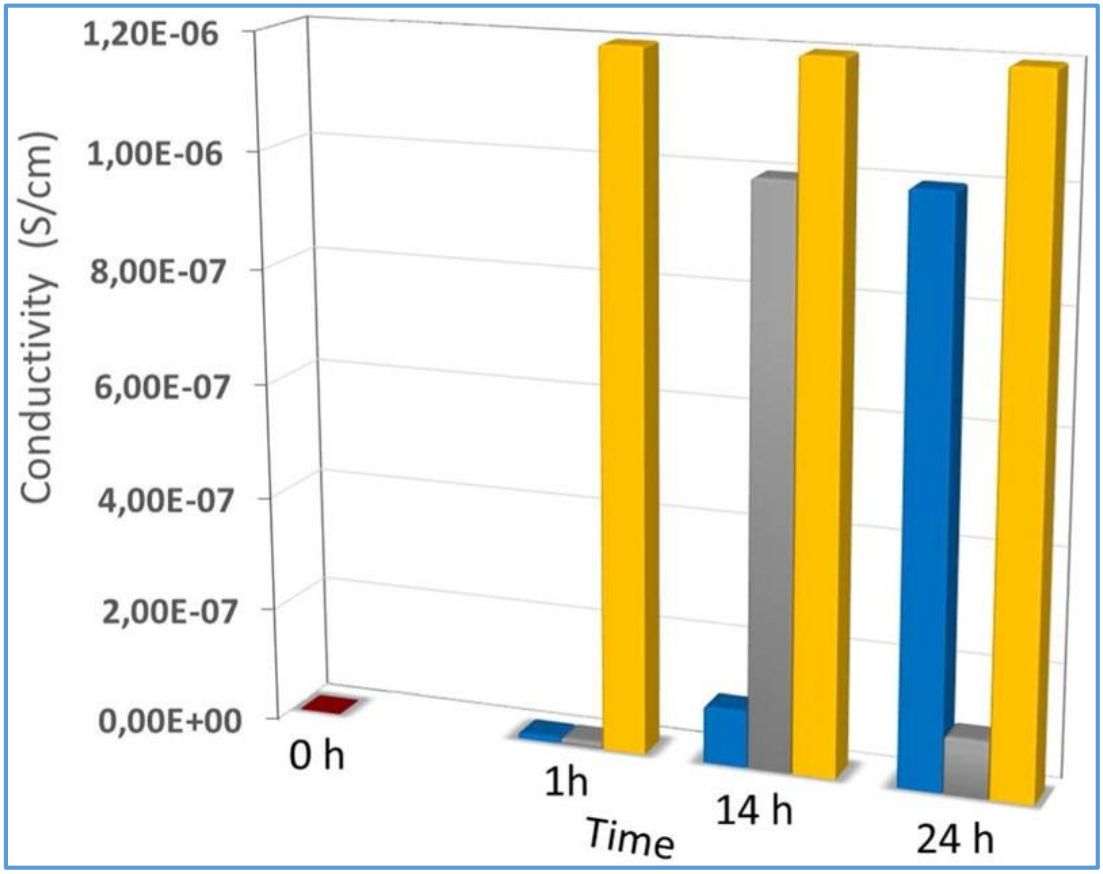

Figure 3.29. Electrical response of complex **20^{RT}** (pristine in red) with different time exposition to vapors of MeOH (blue), EtOH (gray), and acetic acid (yellow).

Table 3.5. AC conductivity values (S/cm) of complexes **19** and **20^{RT}** *versus* different solvents (g) at 25 ºC.

	σ (S/cm) of **19**		σ (S/cm) of **20^{RT}**		
Time(h)	MeOH	HAcO	MeOH	HAcO	EtOH
0.5		—	1.60 x10^{-10}	2.20 x10^{-7}	1.90 x10^{-10}
1	1.33 x10^{-8}	1.40E-08	1.00 x10^{-8}	2.20 x10^{-6}	1.51 x10^{-8}
14	1.70 x10^{-8}	5.50E-06	6.39 x10^{-8}	—	2.24 x10^{-7}
24	3.10 x10^{-8}	6.00E-06	8.80 x10^{-8}	2.50 x10^{-6}	8.00 x10^{-8}
70	—		4.14 x10^{-7}		9.00 x10^{-8}

After each exposition time, the samples were left in air for 30 min. In all the experiments, the solvent released and the samples recover the initial low conductivity values. In case of DMMP, $(CH_3CH_2)_2O$ and CH_2Cl_2, no electrical change was measured for both complexes **19** and **20^{RT}**. However, upon exposition of pellets of **19** and **20^{RT}** to vapors of MeOH or HAcO, different responds are measured (**Figure 3.28**). In both cases the presence of MeOH produce a response in *ca*. 1h enhancing the electrical conductivity in *ca*. 2 order of magnitude from the initial values. However, while in case of **19** the electrical conductivity does not undergo any significant change with longer exposition time (14h and 24h), complex **20^{RT}** enhanced *ca.* 3.5 orders of magnitude its conductivity up to 70 h of exposure to MeOH (**Figure 3.28** and **Table 3.5**).

Additionally, complex **20^{RT}** has been exposed to vapors of EtOH using the same experimental conditions that have been used for HAcO, and MeOH (**Figure 3.29**). Ethanol also produces a response in the electrical conductivity of **20^{RT}** increasing in *ca*. 2 orders of magnitude upon 1h of exposition and more than 3 orders of magnitude after 14 h (**Figure 3.29** and **Table 3.5**). We observed that longer exposition times to vapor of ethanol do not increase the electrical response but produce some disaggregation of the pellet, without any chemical degradation.

Similarly to complex **20^{RT}**, complex **19** has exposed to the vapours of HAcO for ca. 15 min showing an increase in the conductivity of 3 orders of magnitude compared with an increase of 4 orders of magnitude in case of complex **20^{RT}** (**Table 3.5** and **Figure 3.30**).The faster and stronger response founded in complex **20^{RT}** is related with

the shorter Cu-Cu distances found in its double chain and the higher flexibility of the Cu_2I_2 double chain in comparison to the Cu_2Br_2 double chain. In fact, this enhancement of conductivity induced by the absorption of such polar solvent (chemical response) can be explained by comparing the strcture parameter of complex **20b** and that of complex **20^{RT}**. According to the crystallographic data (**Figure 3.5** and **Table 3.1**) and the conductivity measurement (**Table 3.3**), we can obviously state that the hydrogen-bond interactions between the acetic acid molecules absorbed by the complex with the ANP ligand (see complex **20b** in), can slightly decrease the Cu−Cu and Cu−I distances resulting in a dramatic enhance of the conductivity. Similarly, we can suggest that the interaction with H-bonding donor molecules such as MeOH or EtOH can induce structural changes in the Cu_2X_2 double chains shortening the Cu-Cu distances and inducing an electrical response.

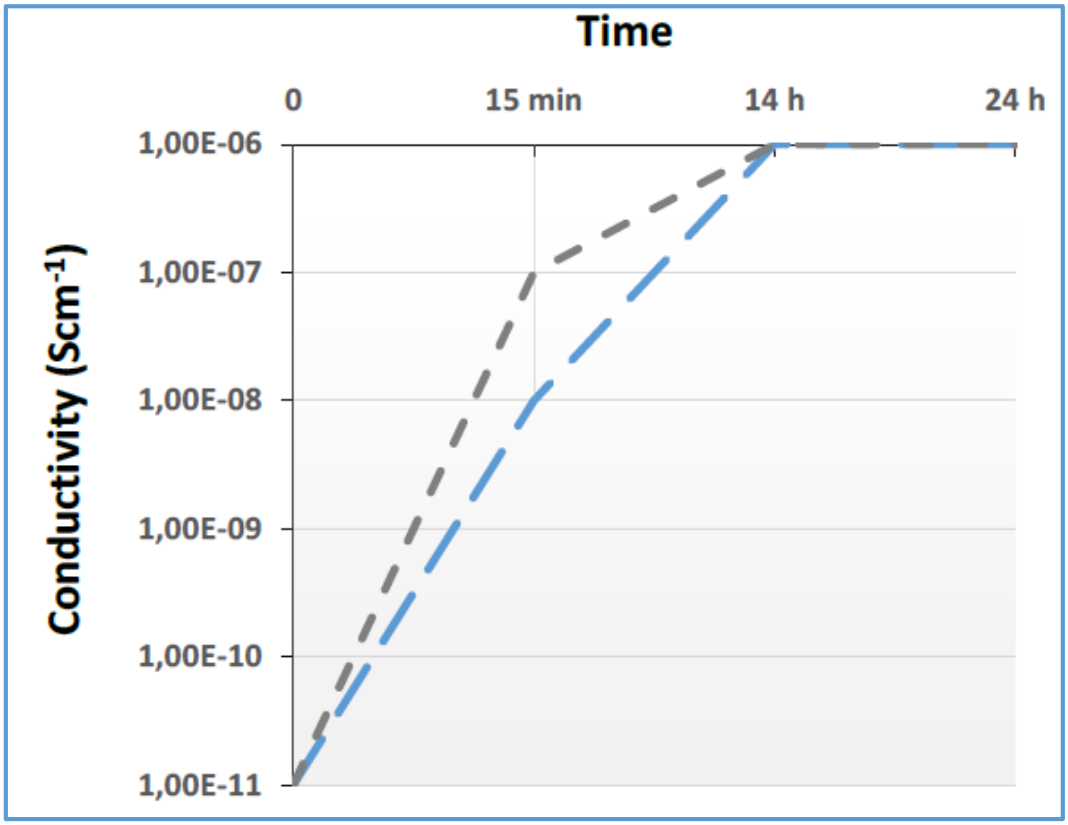

Figure 3.30. Electrical response of complexes **19** (blue dashed line) and **20^{RT}** (gray dashed line) with different time exposition to vapors of acetic acid vapors at 25 ºC.

3.2.2.3. Photoluminescence properties.

Research interest has recently focused on the luminescent properties of coordination polymers in particular, the derivatives of metal ions with d10 electronic configuration owing to their usual electronic properties.[54, 55, 18, 56]

Mostly, the luminescence emission of [Cu(I)XL] (X = halide and L = N-donor ligand) complexes can be assigned to ligand centered (LC), metal to ligand charge transfer (MLCT) ($d^{10} \rightarrow d^9\pi^*$), ligand to metal charge transfer (LMCT), halide to metal charge transfer (XMCT), metal to halide charge transfer or metal-metal (Cu-Cu) interactions.[57, 58] In this context, the solid-state luminescent properties of the complexes **18**-**24** were investigated. At room temperature, excitation of solid samples **18**-**22**, at λ = 380, produces very weak red emission with several peaks and maximum values centered at *ca*. 530, 624, and 687 nm, together with the characteristics bands due to transitions of the ANP ligand (450-520 nm range) (**Figure 3.31**). The similar emission spectra observed in the blue emission region between the ANP free ligand and the **18**-**22** complexes suggests that these transitions could be assigned to ligand-centered π→ π* transitions and/or intra-ligand transitions. The presence of a halide or pseudohalide in complexes **18**-**22** gives rise to weak low-energy red emissions that could be due to a triplet "clustercentered" (CC) excited state and might be assigned to a combination of halide-to-metal charge transfer (XMCT), and/or metal cluster centered transitions [MCC, d Cu →(s,p) Cu] in orbital parentage.[59, 57, 58] The existence of a MCC contribution could be supported by the short Cu−Cu distances observed for complexes **18**-**20,** and **22** (range: 2.764 - 2.861 Å), of the same order than twice the van der Waals radius of Cu (i.e., 2.8 Å)[45] implying strong metal-metal interactions. However, complex **22**, showing a similar spectrum but having larger Cu···Cu distances (d Cu···Cu = 4.866 Å), seems to indicate that this MCC contribution does not have a significant participation. In addition, the weaker emission observed for all complexes respect to free ligand may indicate the participation of the halides in the emissive excited states, in the form of halide-to-metal charge transfer (XMCT).[58]

The excitation of a solid sample of **23**, at λ = 380 nm produces strong emission with a slightly asymmetric single band, with maxima centered at 567 nm (**Figure 3.32**). In order to understand the photoluminescent nature of these complexes, we have compared these results with the emission spectra of the free ligand. Thus, ethyl isonicotinate shows three weak emission bands at 412, 437 and 462 nm, while **23** display just a single band at 567 nm, so the observed emission bands in **23** cannot be assigned to ligand-centered π →π*

transitions taking into account the emission of the free ligand with bands around 410−460. The low-energy emission observed at 567, are most likely originated from an iodide-to-copper charge transfer transition (IMCT) excited state. Moreover, the Cu···Cu distance found in **23** is close to the sum of the van der Waals radii (2.80 Å), therefore a MCC contribution to the emission involving the CuI skeleton, probably mixed with the transition (IMCT), can be expected. The existence of this metal–centered (d–s) (MCC) contribution is consistent with previous reported results found in related Cu_xI_y clusters.[60, 61]

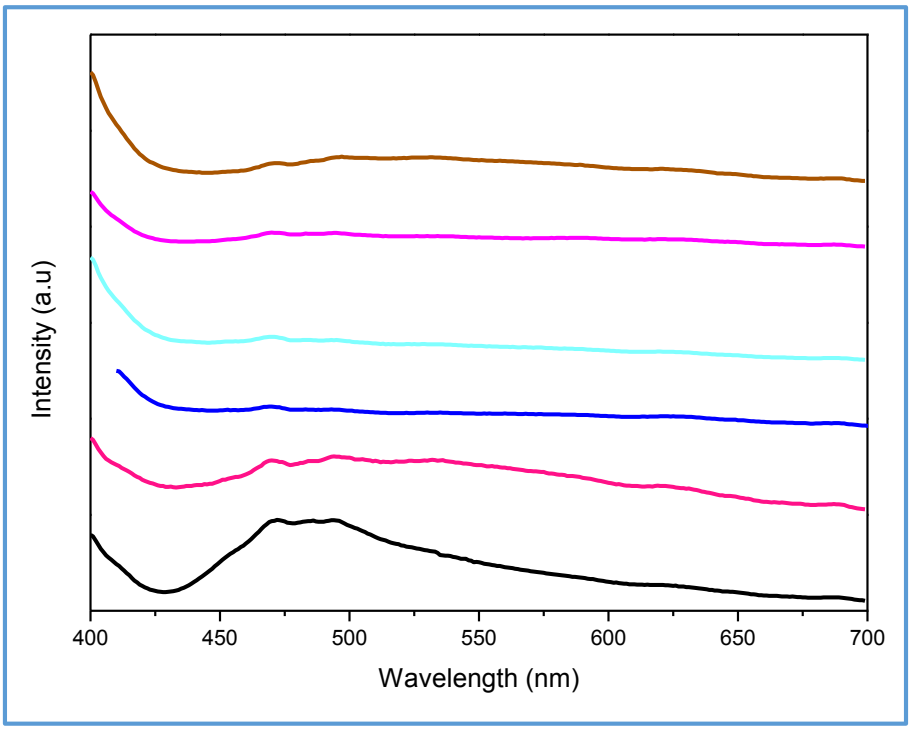

Figure 3.31. Luminescent spectra of ANP ligand (black) and complexes **18** (pink), **19** (deep blue), **20** (blue), **21** (violet) and **22** (brown) (λ_{exc}= 380 nm).

Finally, the weak emission observed at 415 nm for **24**, (**Figure 3.32**) can be assigned to intraligand transitions of the isonicotinic acid. The free ligand exhibits two broad weak emission bands at 420 and 489 nm. The significant maximum blue shift observed in **24**, relative to the free isonicotinic acid, could be due to the emission of ligand-to-metal charge transfer (LMCT) which could probably be mixed with a metal–centered (d–s) triplet state emission (CC). This last contribution, assigned to Cu–Cu interactions, is supported on the evidence that the luminescent properties can involve more than one metal center when the Cu–Cu distance is shorter than the sum of the van der Waals radii

(*ca*. 2.80 Å) as in complex **24** (with Cu–Cu distances of 2.8715(12)Å, **Table 3.2**). A similar behavior has been previously reported for the closely related coordination polymer $[CuBr(INH)]_n$.[13]

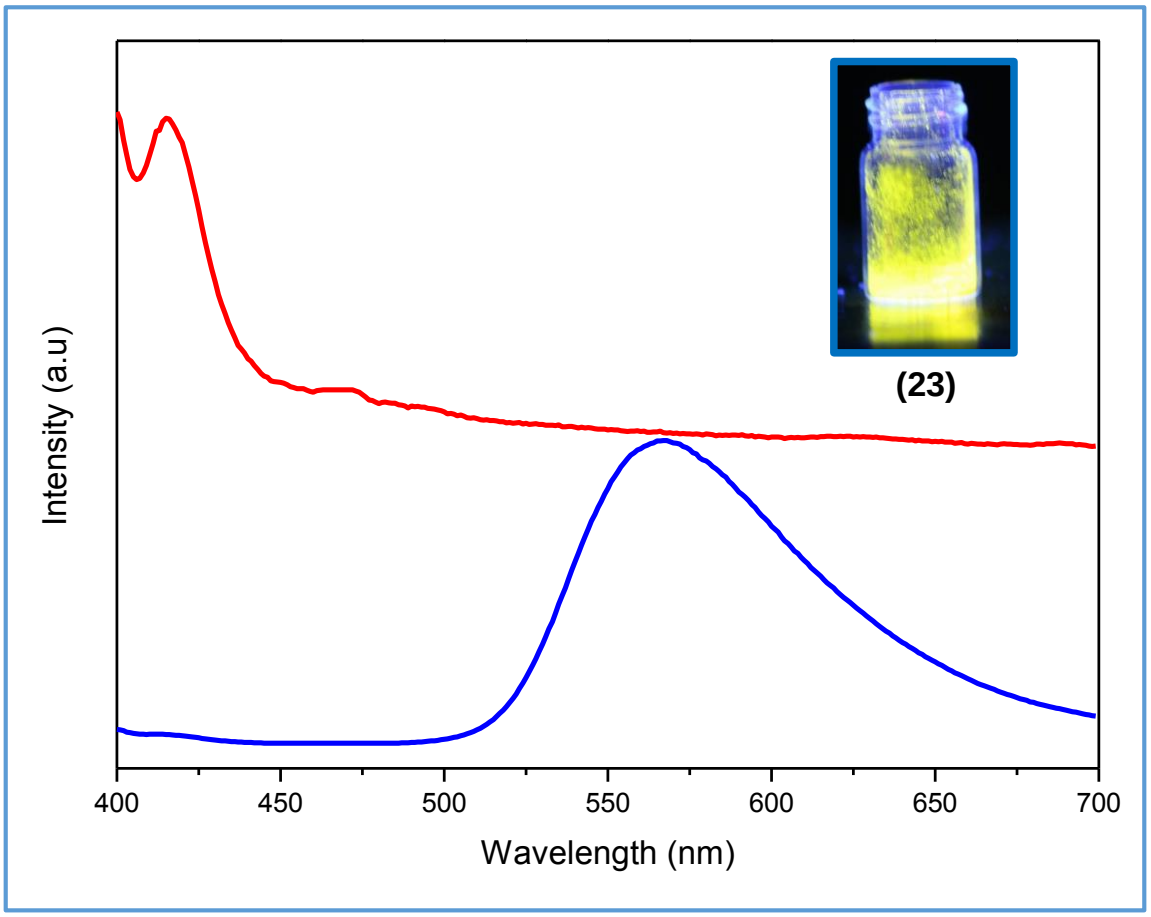

Figure 3.32. Luminescent spectra of complexes **23** (blue) and **24** (red) (λ_{exc}= 380 nm). Inset shows graphical photo for the photoluminescence emission under UV lamp (λ = 364 nm).

3.2.2.4. Theoretical calculations.

In order to rationalize, from a theoretical point of view, the electronic conductivity results obtained for the complexes **18**-**24**, we have carried out a set of first-principles density functional theory (DFT)-based calculations. For the theoretical simulations, we have used the structures obtained by X-ray diffraction for complexes (**18**-**24**). For all these CPs (complexes **18**-**24**), the residual forces acting on each atom in all the calculations were below 0.2 eV/Å, which is low enough to guarantee perfectly converged and realistic results for such complexes systems from a theoretical point of view. This noticeably good geometrical transferability between the experimental configurations and our theoretical implementation has already provided successful results for other similar polymer crystals.[62]

The electronic structure calculations yield minimum values of the transport gaps at Γ points ranging between 0.18 and 2.31 eV for all complexes (**18**-**24**) (**Figure 3.33** and **Figure 3.34**). It is important to remark the excellent agreement (and relative ordering) between the experimental and theoretical activation energies. Therefore, theory also predicts all the complexes as classical narrow band-gap semiconductors. These calculations also show that **20^{RT}** behaves as a typical p-type semiconductor with the Fermi level very close to the valence band. To check the possible influence in the electronic conduction process of the hydrogen bonds stabilizing the whole bulk-crystal structure found in complexes **20^{RT}**, **20^{LT}**, **20a** and **20b**, we have also performed electronic structure calculations of the isolated monodimensional polymeric chains for all the complexes. This strategy will permit understanding the hydrogen bonds, formed between ligands, contribution within the electronic structure calculation. The result of these calculations reveal that the electronic structure of the isolated chains does not show any significant variation with respect to the electronic structure of the bulks, except for a slight electronic gap-opening below 5% of their corresponding bulk value. These findings corroborate that the hydrogen bonds between neighbouring ligands do not contribute to the electronic conduction. To get a deeper insight on this issue, **Figure 3.35** shows the valence and conduction band orbital electron isodensities (with values of 10^{-4} $e^{-}Å^{-3}$) for the **20^{LT}** and **20^{RT}** complexes. In this **Figure 3.35**, it is possible to appreciate that the valence electron isodensity forms as a continuous hybridization band mostly located along the Cu-I skeleton, whilst the conduction electron isodensity shows a continuous orbital *side-to-side* hybridization formed between the ligands. Thus, the conduction will be produced

along the monodimensional chains exclusively. The effect of the increasing temperature will enable the charge migration from the valence band towards the conduction band, as well as a temperature-induced overlapping between both bands that will ease the carrier mobility and the electronic conduction along the chains. This effect is similarly observed for **20a** and **20b** complexes in this study but not shown in **Figure 3.35**. Similar to complex **20**, **Figure 3.36** shows the valence and conduction band orbital electron isodensities (with values of 10^{-4} $e^{-}Å^{-3}$) for the complexes **23** and **24**. According to **Figure 3.36**, the valence electron isodensity is mostly located along the Cu-I skeleton, whilst the conduction electron isodensity shows a continuous orbital *side-to-side* hybridization formed between the ligands. Thus, the conduction will be produced mainly along the monodimensional chains and increasing temperature will enable the charge migration from the valence band towards the conduction band, as well as a temperature-induced overlapping between both bands that will ease the carrier mobility and the electronic conduction along the chains.

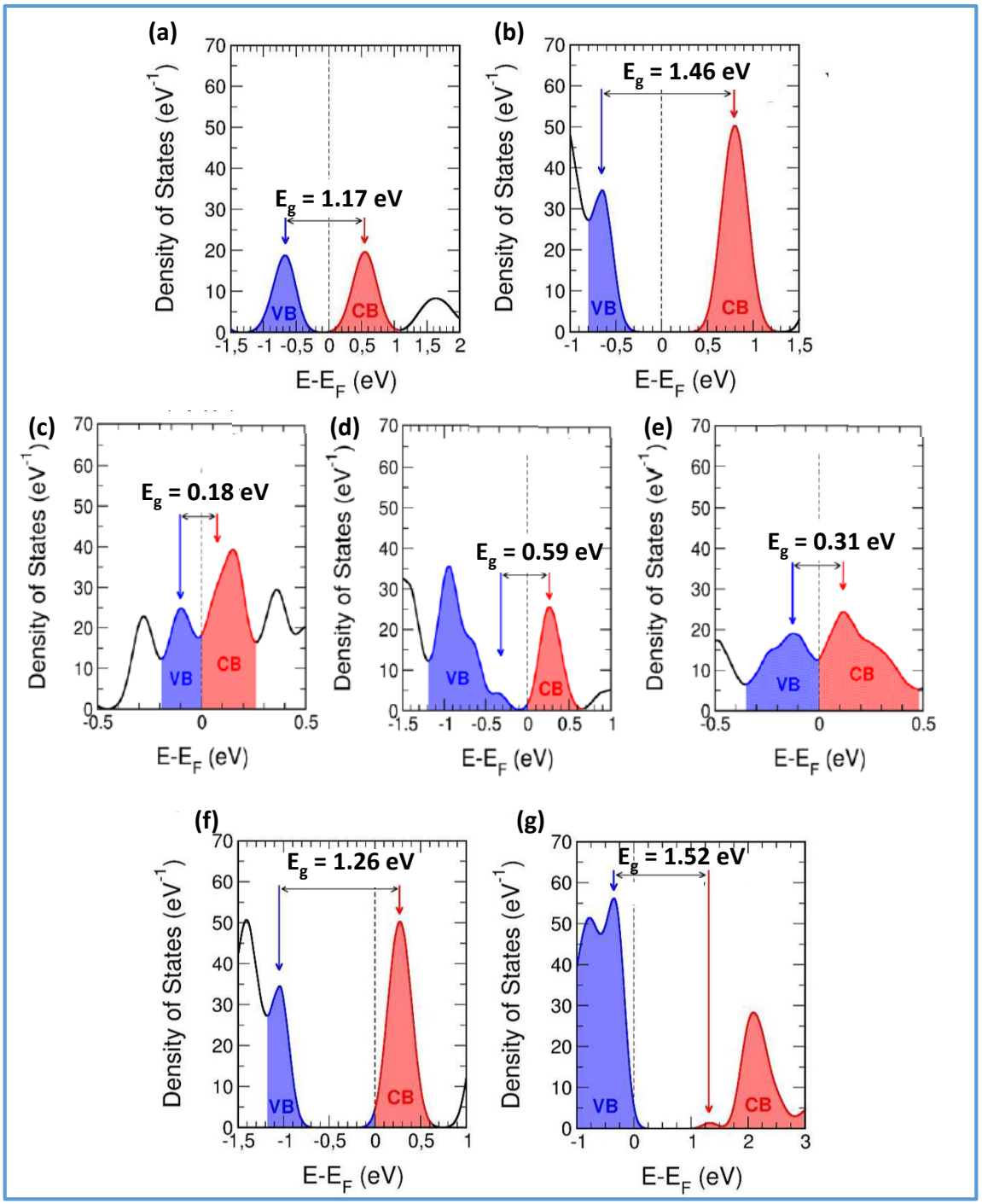

Figure 3.33. Calculated density of electronic states (in eV^{-1}) for the coordination polymers **18** (a), **19** (b), **20^{LT}** (c), **20^{RT}** (d), **20a** (e), **20b** (f), **21** (f) and **22** (h) as a function of the energy, relative to the Fermi level. Each energy level has been broadened by a Lorentzian profile with a line-width of 0.2 eV, and the valence and conduction bands for all the polymers have been shaded in blue and red, respectively. Transport gap is also indicated in each panel.

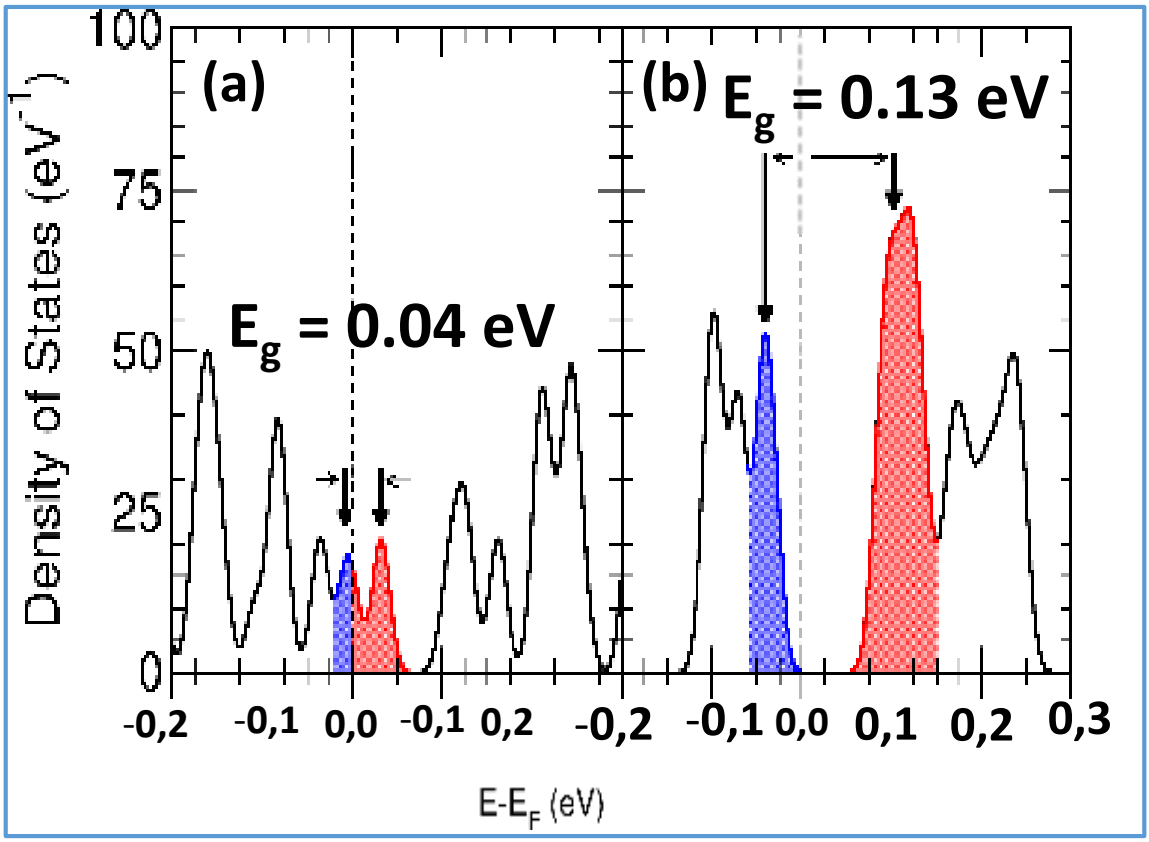

Figure 3.34. Calculated density of electronic states (in eV-1) for the coordination polymers **23** (a) and **24** (b) as a function of the energy, relative to the Fermi level. Each energy level has been broadened by a Lorentzian profile with a line-width of 0.01 eV, and the valence and conduction bands for all the polymers have been shaded in blue and red, respectively. Transport gap is also indicated in each panel.

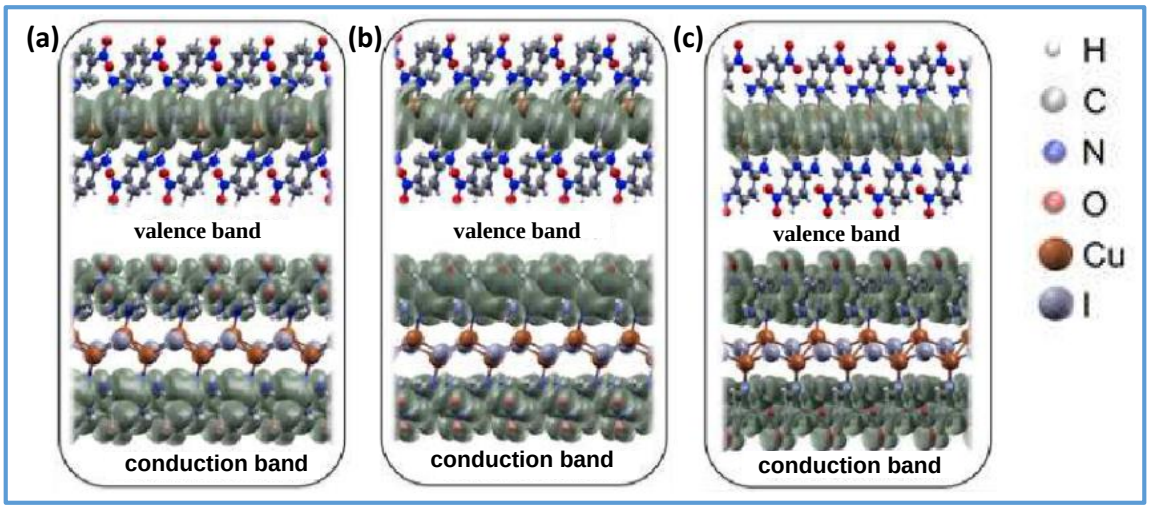

Figure 3.35. Computed valence (up) and conduction (down) band orbital electron isodensities (10^{-4} $e^{-}Å^{-3}$) for the complexes **21**^{LT} (a), **21**^{RT} (b), and **21a** (c).

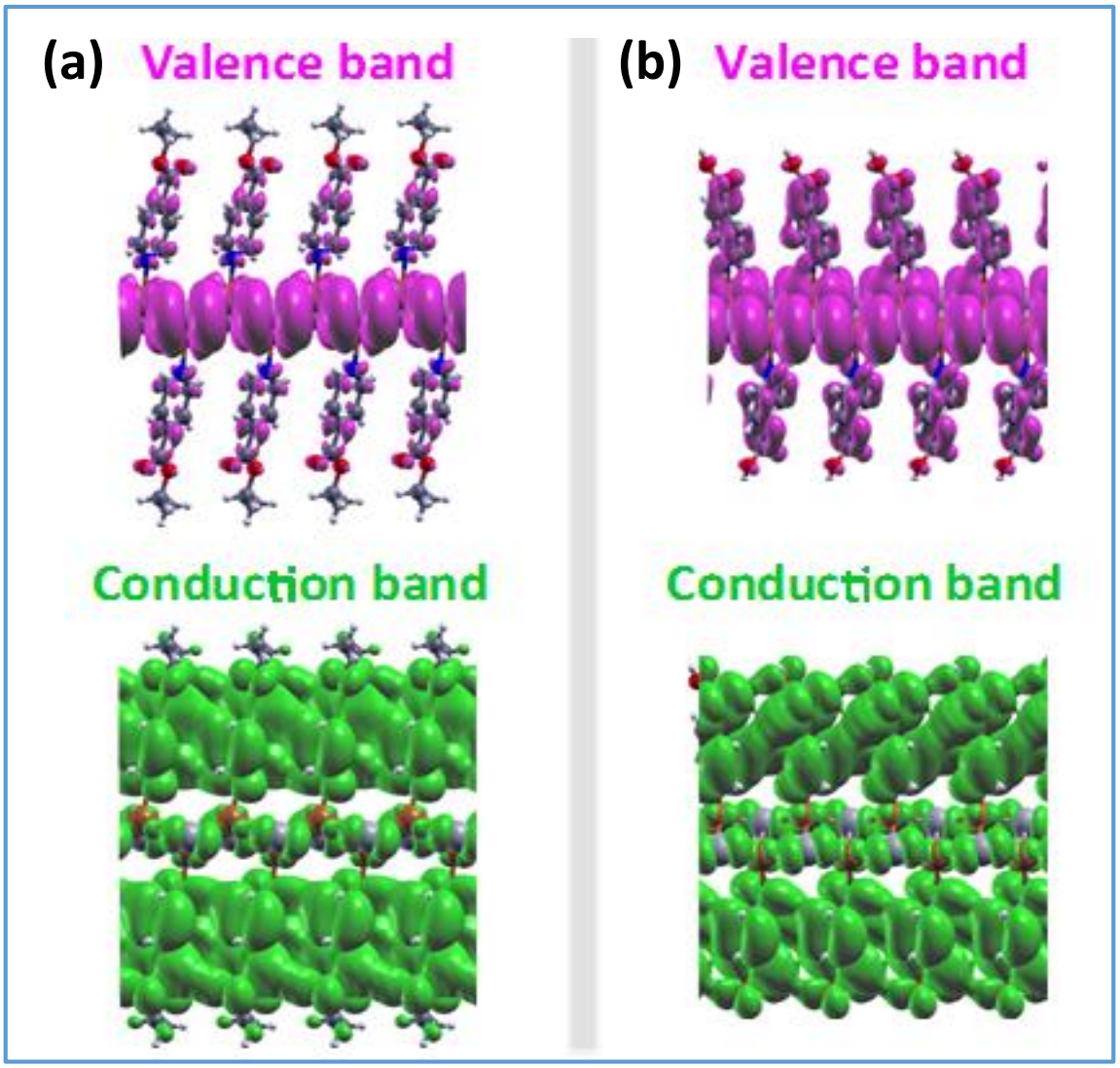

Figure 3.36. Computed valence (up panels) and conduction (down panels) band orbital electron isodensities (10^{-4} $e^{-}Å^{-3}$) for the complexes **23** (a) and **24** (b).

3.2.3. Nano-processability of complex $[CuI(ANP)]_n$ (20^{RT}).

The processability of 1D-CPs is restricted by their lack of solubility being a major drawback for the formation of nanomaterials.[63] One of the objectives of this thesis is to scale down the obtained electrical conductive 1D-CPs with the aim to form suitable nano-wires with potential molecular recognition with final goal to be attached to DNA or DNA nanostructures to produce new hybrid conductive structures (see the objectives).

To this end, we have been able to prepare very long coordination polymer nanoribbons of complex **20^{RT}** by controlling the kinetics of its formation (bottom-up technique) under ambient conditions (for further information, see section 5.3). The nanofibers were prepared by fast precipitation strategies using water as anti-solvent (**Figure 3.37**).

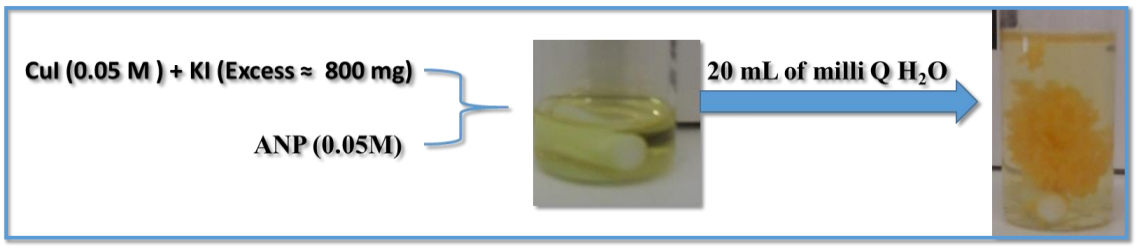

Figure 3.37. Schematic representation of the synthetic method of complex **20^{RT}** nanofibers.

The sample uniformity and narrow diameter distribution were confirmed by field emission scanning electron microscopy (FESEM). **Figure 3.38 a-c**, shows a typical FESEM images of a nanofibers obtained from a colloidal suspension of complex **20^{RT}** (**Figure 3.38a**). According to the FESEM images, the nanoribbons have diameters between 100 and 200 nm, and lenghth of several hundreds of µm. In order to get more insights on the size and morphology of the nanofibers, AFM image of diluted colloidal suspension of complex **20^{RT}** was obtained upon drop casting on SiO_2 substrate. **Figure 3.38 d-f**, shows an AFM topography image of nanofibers with a heights ranged between *ca*. 5 to 16 nm, suggesting that these nanofibers composed of few polymeric chains ca 4-12.

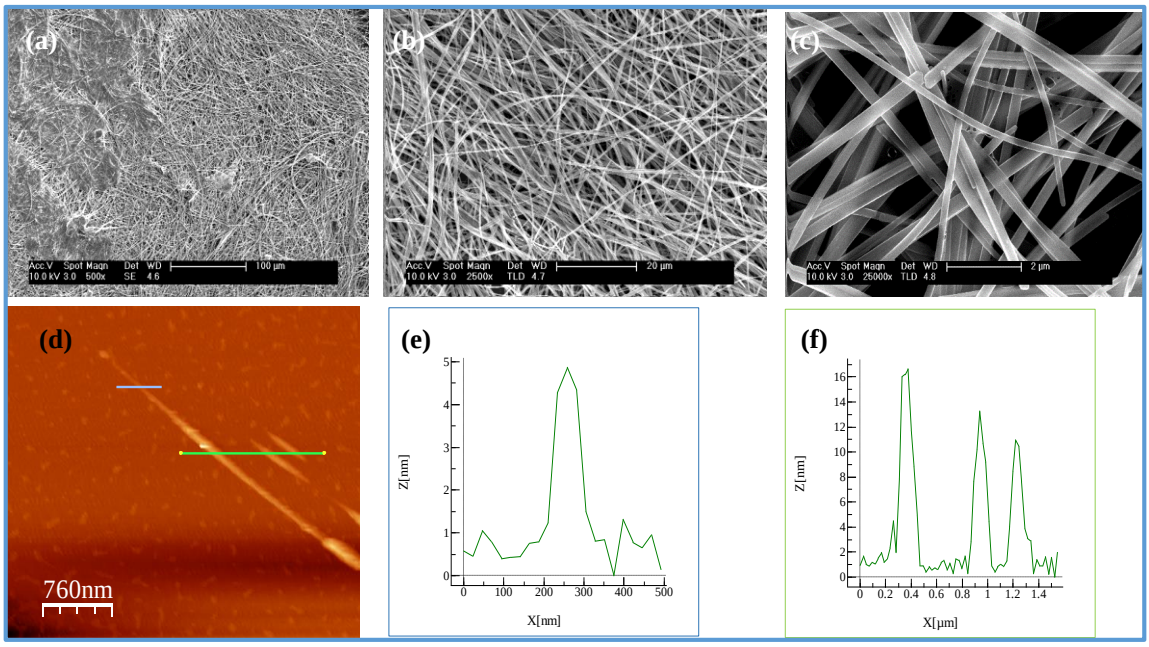

Figure 3.38. FESEM images of complexes **20^{RT}** nanofibers at different magnifications (b-d). Representative AFM topographic image of complexes **20^{RT}** nanofibers(d) and their heights profiles (e and f) obtained upon drop-casting adsorption, on mica, of the diluted colloidal suspension formed by diluted 15 µL of **20^{RT}** suspensions by dilution factor = 6.

.

References

1. O. Hietsoi, C. Dubceac, A. S. Filatov and M. A. Petrukhina, **Insulated copper(i) "wires": structural variations and photoluminescence**, *Chemical Communications*, **2011**, 47, 6939-6941, http://dx.doi.org/10.1039/C1CC11000D.
2. V. W.-W. Yam and E. C.-C. Cheng, **Highlights on the recent advances in gold chemistry-a photophysical perspective**, *Chemical Society Reviews*, **2008**, 37, 1806-1813, http://dx.doi.org/10.1039/B708615F.
3. C. Latouche, Y.-R. Lin, Y. Tobon, E. Furet, J.-Y. Saillard, C.-W. Liu and A. Boucekkine, **Au-Au chemical bonding induced by UV irradiation of dinuclear gold(i) complexes: a computational study with experimental evidence**, *Physical Chemistry Chemical Physics*, **2014**, 16, 25840-25845, http://dx.doi.org/10.1039/C4CP03990D.
4. H. Schmidbaur and A. Schier, **Argentophilic Interactions**, *Angewandte Chemie International Edition*, **2015**, 54, 746-784, http://dx.doi.org/10.1002/anie.201405936.
5. H. Schmidbaur and A. Schier, **Aurophilic interactions as a subject of current research: an up-date**, *Chemical Society Reviews*, **2012**, 41, 370-412, http://dx.doi.org/10.1039/C1CS15182G.
6. J. Beck and J. Strähle, **Complexes of 1,5-Di(p-tolyl)-1,4-pentaazadien-3-ide, Crystal Structures of [Cu(tolylNNNNNtolyl)]3 and [Ni(tolylNNNNNtolyl)2]2**, *Angewandte Chemie International Edition in English*, **1985**, 24, 409-410, http://dx.doi.org/10.1002/anie.198504091.
7. C.-M. Che, Z. Mao, V. M. Miskowski, M.-C. Tse, C.-K. Chan, K.-K. Cheung, D. L. Phillips and K.-H. Leung, **Cuprophilicity: Spectroscopic and Structural Evidence for Cu−Cu Bonding Interactions in Luminescent Dinuclear Copper(I) Complexes with Bridging Diphosphane Ligands**, *Angewandte Chemie*, **2000**, 112, 4250-4254, http://dx.doi.org/10.1002/1521-3757(20001117)112:22<4250::AID-ANGE4250>3.0.CO;2-C.
8. H. L. Hermann, G. Boche and P. Schwerdtfeger, **Metallophilic Interactions in Closed-Shell Copper(I) Compounds—A Theoretical Study**, *Chemistry – A European Journal*, **2001**, 7, 5333-5342, http://dx.doi.org/10.1002/1521-3765(20011217)7:24<5333::AID-CHEM5333>3.0.CO;2-1.
9. U. Siemeling, U. Vorfeld, B. Neumann and H.-G. Stammler, **Cuprophilicity? a rare example of a ligand-unsupported CuI-CuI interaction**, *Chemical Communications*, **1997**, 1723-1724, http://dx.doi.org/10.1039/A702793A.
10. F. A. Cotton, X. Feng, M. Matusz and R. Poli, **Experimental and theoretical studies of the copper(I) and silver(I) dinuclear N,N'-di-p-tolylformamidinato complexes**, *Journal of the American Chemical Society*, **1988**, 110, 7077-7083, http://dx.doi.org/10.1021/ja00229a021.
11. E. Kühnel, I. V. Shishkov, F. Rominger, T. Oeser and P. Hofmann, **Synthesis and Structures of Copper(I) Complexes with Phosphino-Functionalized N-Heterocyclic Carbenes (NHCP) and Bis-N-Heterocyclic Carbenes (Bis-NHC)**, *Organometallics*, **2012**, 31, 8000-8011, http://dx.doi.org/10.1021/om300701u.
12. J.-F. Liu, X. Min, J.-Y. Lv, F.-X. Pan, Q.-J. Pan and Z.-M. Sun, **Ligand-Controlled Syntheses of Copper(I) Complexes with Metal–Metal Interactions: Crystal Structure and Relativistic Density Functional Theory Investigation**, *Inorganic Chemistry*, **2014**, 53, 11068-11074, http://dx.doi.org/10.1021/ic5015797.
13. P. Amo-Ochoa, L. Welte, R. Gonzalez-Prieto, P. J. Sanz Miguel, C. J. Gomez-Garcia, E. Mateo-Marti, S. Delgado, J. Gomez-Herrero and F. Zamora, **Single**

layers of a multifunctional laminar Cu(i,ii) coordination polymer, *Chemical Communications*, **2010**, 46, 3262-3264, http://dx.doi.org/10.1039/B919647A.
14. H. Araki, K. Tsuge, Y. Sasaki, S. Ishizaka and N. Kitamura, **Luminescence Ranging from Red to Blue: A Series of Copper(I)−Halide Complexes Having Rhombic {Cu2(μ-X)2} (X = Br and I) Units with N-Heteroaromatic Ligands**, *Inorganic Chemistry*, **2005**, 44, 9667-9675, http://dx.doi.org/10.1021/ic0510359.
15. F. De Angelis, S. Fantacci, A. Sgamellotti, E. Cariati, R. Ugo and P. C. Ford, **Electronic Transitions Involved in the Absorption Spectrum and Dual Luminescence of Tetranuclear Cubane [Cu4I4(pyridine)4] Cluster: a Density Functional Theory/Time-Dependent Density Functional Theory Investigation**, *Inorganic Chemistry*, **2006**, 45, 10576-10584, http://dx.doi.org/10.1021/ic061147f.
16. P. C. Ford, E. Cariati and J. Bourassa, **Photoluminescence Properties of Multinuclear Copper(I) Compounds**, *Chemical Reviews*, **1999**, 99, 3625-3648, http://dx.doi.org/10.1021/cr960109i.
17. A. Gallego, O. Castillo, C. J. Gómez-García, F. l. Zamora and S. Delgado, **Electrical conductivity and luminescence in coordination polymers based on copper (I)-halides and sulfur-pyrimidine ligands**, *Inorganic Chemistry*, **2011**, 51, 718-727, http://pubs.acs.org/doi/abs/10.1021/ic202255w.
18. J. Pospisil, I. Jess, C. Nather, M. Necas and P. Taborsky, **Luminescence properties of "double-stranded staircase" copper(i) halide coordination polymers with N-containing ligands**, *New Journal of Chemistry*, **2011**, 35, 861-864, http://dx.doi.org/10.1039/C0NJ00809E.
19. J. P. Safko, J. E. Kuperstock, S. M. McCullough, A. M. Noviello, X. Li, J. P. Killarney, C. Murphy, H. H. Patterson, C. A. Bayse and R. D. Pike, **Network formation and photoluminescence in copper(i) halide complexes with substituted piperazine ligands**, *Dalton Transactions*, **2012**, 41, 11663-11674, http://dx.doi.org/10.1039/C2DT31241G.
20. P. M. Graham, R. D. Pike, M. Sabat, R. D. Bailey and W. T. Pennington, **Coordination Polymers of Copper(I) Halides**, *Inorganic Chemistry*, **2000**, 39, 5121-5132, http://dx.doi.org/10.1021/ic0005341.
21. R. Peng, M. Li and D. Li, **Copper(I) halides: A versatile family in coordination chemistry and crystal engineering**, *Coordination Chemistry Reviews*, **2010**, 254, 1-18, http://www.sciencedirect.com/science/article/pii/S0010854509002653.
22. E. Cariati, E. Lucenti, C. Botta, U. Giovanella, D. Marinotto and S. Righetto, **Cu(I) hybrid inorganic–organic materials with intriguing stimuli responsive and optoelectronic properties**, *Coordination Chemistry Reviews*, **2016**, 306, 566–614, http://www.sciencedirect.com/science/article/pii/S0010854515000922.
23. A. Kobayashi, K. Komatsu, H. Ohara, W. Kamada, Y. Chishina, K. Tsuge, H.-C. Chang and M. Kato, **Photo- and Vapor-Controlled Luminescence of Rhombic Dicopper(I) Complexes Containing Dimethyl Sulfoxide**, *Inorganic Chemistry*, **2013**, 52, 13188-13198, http://pubs.acs.org/doi/abs/10.1021/ic402104q.
24. G. Zeng, S. Xing, X. Han, B. Xin, Y. Yang, X. Wang, G. Li, Z. Shi and S. Feng, **Reversible photoluminescence switching behavior and luminescence thermochromism of copper(I) halide cluster coordination polymers**, *RSC Advances*, **2015**, 5, 40792-40797, http://dx.doi.org/10.1039/C5RA05157F.
25. S. Cho, Y. Jeon, S. Lee, J. Kim and T. H. Kim, **Reversible Transformation between Cubane and Stairstep Cu4I4 Clusters Using Heat or Solvent Vapor**, *Chemistry – A European Journal*, **2015**, 21, 1439-1443, http://dx.doi.org/10.1002/chem.201405800.

26. D. Sun, S. Yuan, H. Wang, H.-F. Lu, S.-Y. Feng and D.-F. Sun, **Luminescence thermochromism of two entangled copper-iodide networks with a large temperature-dependent emission shift**, *Chemical Communications*, **2013**, 49, 6152-6154, http://dx.doi.org/10.1039/C3CC42741B.
27. Q. Benito, X. F. Le Goff, S. Maron, A. Fargues, A. Garcia, C. Martineau, F. Taulelle, S. Kahlal, T. Gacoin, J.-P. Boilot and S. Perruchas, **Polymorphic Copper Iodide Clusters: Insights into the Mechanochromic Luminescence Properties**, *Journal of the American Chemical Society*, **2014**, 136, 11311-11320, http://dx.doi.org/10.1021/ja500247b.
28. E. Cariati and J. Bourassa, **Luminescence response of the solid state polynuclear copper(I) iodide materials [CuI(4-picoline)] to volatile organic compounds**, *Chemical Communications*, **1998**, 1623-1624, http://dx.doi.org/10.1039/A802805B.
29. K. Chen, J. Shearer and V. J. Catalano, **Subtle Modulation of Cu4X4L2 Phosphine Cluster Cores Leads to Changes in Luminescence**, *Inorganic Chemistry*, **2015**, 54, 6245–6256, http://dx.doi.org/10.1021/acs.inorgchem.5b00443.
30. D. Braga, F. Grepioni, L. Maini, P. P. Mazzeo and B. Ventura, **Solid-state reactivity of copper(i) iodide: luminescent 2D-coordination polymers of CuI with saturated bidentate nitrogen bases**, *New Journal of Chemistry*, **2011**, 35, 339-344, http://dx.doi.org/10.1039/C0NJ00547A.
31. D. M. Zink, M. Bächle, T. Baumann, M. Nieger, M. Kühn, C. Wang, W. Klopper, U. Monkowius, T. Hofbeck, H. Yersin and S. Bräse, **Synthesis, Structure, and Characterization of Dinuclear Copper(I) Halide Complexes with P^N Ligands Featuring Exciting Photoluminescence Properties**, *Inorganic Chemistry*, **2012**, 52, 2292-2305, http://dx.doi.org/10.1021/ic300979c.
32. E. Mateo-Marti, L. Welte, P. Amo-Ochoa, P. J. Sanz Miguel, J. Gomez-Herrero, J. A. Martin-Gago and F. Zamora, **Direct evidence of nanowires formation from a Cu(i) coordination polymer**, *Chemical Communications*, **2008**, 8, 945-947, http://dx.doi.org/10.1039/B711416H.
33. R. Mas-Balleste, J. Gomez-Herrero and F. Zamora, **One-dimensional coordination polymers on surfaces: towards single molecule devices**, *Chemical Society Reviews*, **2010**, 39, 4220-4233, http://dx.doi.org/10.1039/C001965H.
34. W.-W. Zhou, W. Zhao, X. Zhao, F.-W. Wang and B. Wei, **A New 1-D Cu(I) Pyridinate Complex [CuBr(anp)] n (anp = 2-amino-5-nitropyridine)**, *Synthesis and Reactivity in Inorganic, Metal-Organic, and Nano-Metal Chemistry*, **2013**, 43, 1171-1174, http://dx.doi.org/10.1080/15533174.2012.756899.
35. R. Barman, S. Singh and B. Das, **Synthesis and structural properties of a 1-D copper(I) coordination polymer**, *Journal of Chemical Crystallography*, **2002**, 32, 369-375, http://dx.doi.org/10.1023/A%3A1020284803511.
36. M.-M. Liu, J.-J. Hou, Z.-k. Qi, L. N. Duan, W.-J. Ji, C.-y. Han and X.-M. Zhang, **Tuning of Valence States, Bonding Types, Hierarchical Structures, and Physical Properties in Copper/Halide/Isonicotinate System**, *Inorganic Chemistry*, **2014**, 53, 4130-4143, http://dx.doi.org/10.1021/ic5001232.
37. J. Y. Lu, **Crystal engineering of Cu-containing metal–organic coordination polymers under hydrothermal conditions**, *Coordination Chemistry Reviews*, **2003**, 246, 327-347, http://www.sciencedirect.com/science/article/pii/S0010854503001449.
38. J. Y. Lu, A. B. Schauss and M. Julve, **A mixed-valence Cu(I)–Cu(II) and metal–metal bond containing coordination polymer obtained from an in situ**

oxidation reaction route, *Inorganica Chimica Acta*, **2006**, 359, 2565-2568, http://www.sciencedirect.com/science/article/pii/S0020169306000454.
39. T. Wu, D. Li and S. W. Ng, **Solvent control in the hydrothermal synthesis of two copper(i) iodide-benzimidazole coordination polymers**, *CrystEngComm*, **2005**, 7, 514-518, http://dx.doi.org/10.1039/B506273J.
40. E. Cariati, D. Roberto, R. Ugo, P. C. Ford, S. Galli and A. Sironi, **X-ray Structures and Emissive and Second-Order Nonlinear Optical Properties of Two Inorganic−Organic Polymeric Adducts of CuI with 4-Acetylpyridine. The Role of Both "Intrastrand" Charge Transfers and Structural Motifs on the Nonlinear Optical Response of Cu(I) Polymeric Adducts with Pseudoaromatic η1-Nitrogen Donor Ligands**, *Chemistry of Materials*, **2002**, 14, 5116-5123, http://dx.doi.org/10.1021/cm020640w.
41. S.-M. Fang, Q. Zhang, M. Hu, B. Xiao, L.-M. Zhou, G.-H. Sun, L.-J. Gao, M. Du and C.-S. Liu, **Controllable assembly of copper(i)-iodide coordination polymers by tecton design of benzotriazol-1-yl-based pyridyl ligands: from 2D layer to 3D self-penetrating or homochiral networks**, *CrystEngComm*, **2010**, 12, 2203-2212, http://dx.doi.org/10.1039/C002030N.
42. R.-F. Song, Y.-B. Xie, J.-R. Li and X.-H. Bu, **Syntheses and crystal structures of the copper(i) complexes with quinoline-based monothioether ligands**, *CrystEngComm*, **2005**, 7, 249-254, http://dx.doi.org/10.1039/B419374A.
43. Y. Takemura, T. Nakajima and T. Tanase, **Interconversion between ladder-type octanuclear and linear tetranuclear copper(i) complexes supported by tetraphosphine ligands**, *Dalton Transactions*, **2009**, 10231-10243, http://dx.doi.org/10.1039/B909252H.
44. F. Thébault, S. A. Barnett, A. J. Blake, C. Wilson, N. R. Champness and M. Schröder, **Control of Copper(I) Iodide Architectures by Ligand Design: Angular versus Linear Bridging Ligands**, *Inorganic Chemistry*, **2006**, 45, 6179-6187, http://dx.doi.org/10.1021/ic052130k.
45. A. Bondi, **van der Waals Volumes and Radii**, *The Journal of Physical Chemistry*, **1964**, 68, 441-451, http://dx.doi.org/10.1021/j100785a001.
46. G. R. Desiraju, **Supramolecular Synthons in Crystal Engineering—A New Organic Synthesis**, *Angewandte Chemie International Edition in English*, **1995**, 34, 2311-2327, http://dx.doi.org/10.1002/anie.199523111.
47. J. Bernasconi, P. Büesch, D. Kuse and H. R. Zeller, **Ultraviolet to far infrared optical properties of the one-dimensional conductor K2Pt(CN)4Br0·3. 3H2O**, *Journal of Physics and Chemistry of Solids*, **1974**, 35, 145-157, http://www.sciencedirect.com/science/article/pii/0022369774900286.
48. L. B. Coleman, M. J. Cohen, D. J. Sandman, F. G. Yamagishi, A. F. Garito and A. J. Heeger, **Superconducting fluctuations and the peierls instability in an organic solid**, *Solid State Communications*, **1973**, 12, 1125-1132, http://www.sciencedirect.com/science/article/pii/0038109873901270.
49. J. Ferraris, D. O. Cowan, V. Walatka and J. H. Perlstein, **Electron transfer in a new highly conducting donor-acceptor complex**, *Journal of the American Chemical Society*, **1973**, 95, 948-949, http://dx.doi.org/10.1021/ja00784a066.
50. R. E. Peierls, *Quantum Theory of Solids*, Clarendon Press, 1955.
51. F. Wudl, G. M. Smith and E. J. Hufnagel, **Bis-1,3-dithiolium chloride: an unusually stable organic radical cation**, *Journal of the Chemical Society D: Chemical Communications*, **1970**, 1453-1454, http://dx.doi.org/10.1039/C29700001453.

52. G. Givaja, P. Amo-Ochoa, C. J. Gómez-Garcia and F. Zamora, **Electrical conductive coordination polymers**, *Chemical Society Reviews*, **2012**, 41, 115-147, http://dx.doi.org/10.1039/C1CS15092H.
53. R. A. Huggins, **Simple method to determine electronic and ionic components of the conductivity in mixed conductors a review**, *Ionics*, **2002**, 8, 300-313, http://dx.doi.org/10.1007/BF02376083.
54. F. Dumur, **Recent advances in organic light-emitting devices comprising copper complexes: A realistic approach for low-cost and highly emissive devices?**, *Organic Electronics*, **2015**, 21, 27-39, http://www.sciencedirect.com/science/article/pii/S1566119915000890.
55. W. Liu, Y. Fang, G. Z. Wei, S. J. Teat, K. Xiong, Z. Hu, W. P. Lustig and J. Li, **A Family of Highly Efficient CuI-Based Lighting Phosphors Prepared by a Systematic, Bottom-up Synthetic Approach**, *Journal of the American Chemical Society*, **2015**, 137, 9400-9408, http://dx.doi.org/10.1021/jacs.5b04840.
56. V. W.-W. Yam, V. K.-M. Au and S. Y.-L. Leung, **Light-Emitting Self-Assembled Materials Based on d8 and d10 Transition Metal Complexes**, *Chemical Reviews*, **2015**, 115, 7589-7728, http://dx.doi.org/10.1021/acs.chemrev.5b00074.
57. M. Vitale* and P. C. Ford*, **Luminescent mixed ligand copper(I) clusters (CuI)n(L)m (L=pyridine, piperidine): thermodynamic control of molecular and supramolecular species**, *Coordination Chemistry Reviews*, **2001**, 219–221, 3-16, http://www.sciencedirect.com/science/article/pii/S0010854500004148.
58. V. Wing-Wah Yam and K. Kam-Wing Lo, **Luminescent polynuclear d10 metal complexes**, *Chemical Society Reviews*, **1999**, 28, 323-334, http://dx.doi.org/10.1039/A804249G.
59. L. Han, M. Hong, R. Wang, B. Wu, Y. Xu, B. Lou and Z. Lin, **Red luminescent polymeric cuprous organosulfide generated by solvothermal redox reaction**, *Chemical Communications*, **2004**, 2578-2579, http://dx.doi.org/10.1039/B409000D.
60. E. Cariati, D. Roberto, R. Ugo, P. C. Ford, S. Galli and A. Sironi, **New Structural Motifs, Unusual Quenching of the Emission, and Second Harmonic Generation of Copper(I) Iodide Polymeric or Oligomeric Adducts with Para-Substituted Pyridines or trans-Stilbazoles**, *Inorganic Chemistry*, **2005**, 44, 4077-4085, http://dx.doi.org/10.1021/ic050143s.
61. J. Zhou, G.-Q. Bian, J. Dai, Y. Zhang, Q.-Y. Zhu and W. Lu, **Luminescent 2-D Double-layered Polymer, [(CuI)4(CH3SCH3)3]∞, Containing Helical Chains Constructed by Flower-Basket-Shaped Cu4I4 Clusters**, *Inorganic Chemistry*, **2006**, 45, 8486-8488, http://dx.doi.org/10.1021/ic060972t.
62. J. Troyano, J. Perles, P. Amo-Ochoa, J. I. Martinez, F. Zamora and S. Delgado, **Reversible recrystallization process of copper and silver thioacetamide-halide coordination polymers and their basic building blocks**, *CrystEngComm*, **2014**, 16, 8224-8231, http://pubs.rsc.org/en/content/articlelanding/2014/ce/c4ce00480a.
63. C. Janiak, **Engineering coordination polymers towards applications**, *Dalton Transactions*, **2003**, 2781-2804, http://dx.doi.org/10.1039/B305705B.

4. Chapter 4; Conclusions

1. We have been able to prepare different coordination complexes, ranged between mononuclear (**1** and **2**), dimetallic (**3**-**8**), and extended coordination complexes (one dimensional coordination polymers, **9**-**12**), using modified nucleobases such as TAcOH and /or UAcOH as organic ligands and Cu(II) ion as metal centre,. The obtained 1D-CPs (**9**-**12**) only when TAcOH has been used as ligand and these 1D-CPs can be divided into two groups depending on the coordination nature of TAcOH to the Cu(II) ions. In complexes **9** and **10**, the $TAcO^-$ ligand has been participated as bridging ligand while, in case of complexes **11** and **12**, the $TAcO^-$ ligand has been participated as terminal ligand and the copper ions have been bridged using 4,4'-bipyridine as linear ligand.

2. We have measured the physical properties of the obtained complexes in particular, the electrical and magnetic properties. The electrical conductivity founded in complexes **9** and **10** have shown semiconductor behaviour. On the other hand, the magnetic properties study of complexes **3**-**11** have shown that these materials present magnetic behaviour ranged from strong antiferromagnetic to weak ferromagnetic behaviour.

3. We have studied the interactions of the same modified nucleobases (TAcOH or UAcOH) as organic ligands but with Co(II) ion, instead of Cu(II) ion, as metal centre with the aim to prepare 1D-CPs with good electrical properties. All the attempts have led to the formations of mononuclear complexes (**13** and **14** respectively). In order to obtain 1D-CPs, we have used an additional ligand such as 2,6-diaminopurine (Hdap) but we have obtained mononuclear complexes (**15** and **16** respectively). Finally, the reactions of Co(II) ion with TAcOH in the presence of the linear ligand (4,4'-bipyridine) have led to the formation of a mononuclear complex (**17**).

4. We have been able to prepare nanoribbons of complex **11**, **$[Cu(TAcO)_2(4,4'\text{-bipy})(H_2O)]_n \cdot 2H_2O$**, using fast precipitation method. We have studied the morphology of these nanoribbons using FESEM and AFM techniques. The

FESEM images confirm a nanoribbon-like structure with *ca*. 100-150 nm width and length of microns. The AFM images show a height of *ca*. 3.5 nm which is in agreement with the isolation of a ribbon consisting of just one-two molecules. We explore the potential applications of such materials in biomedical applications by studying the interaction of complex **11** nanoribbons with several oligonucleotides sequences. We have demonstrated that nanoribbons of complex **11** show higher selectivity for PolyA with respect to other oligonucleotides. These properties can allow the integration of such system for biomedical applications such as DNA detection and/or DNA delivery.

5. The interactions of copper(I) halide with pyridine derivatives ligands, that show free functional groups available for supramolecular interactions, gave rise to a family of one dimensional coordination polymers with general formula **[CuXL]$_n$**, where X is halide ions and L are pyridine derivatives ligands known as 2-amino-5-nitropyridine, isonicotinic acid and Ethyl isonicotinate. In all the cases, the copper ion showed oxidation state Cu^{+1}, which encourage us to study their luminescent properties beside the electrical conductivity.

6. Working with copper(I) halide, we have been able to prepare a series of 1D-CPs with semiconductor behaviour and relevant electrical value up to 10^{-3} S/cm (complex **24**, **[CuI(HIN)]$_n$**). Strong photoluminescence emission has been observed in case of complex **25**, **[CuI(EtIN)]$_n$**.

7. We have been able to prepare nanoribbons of complex **20^{RT},** with formula **[CuI(ANP]$_n$**, using water as anti-solvent to control the growth of the nanoribbons. the morphology studies of these nanoribbons, using FESEM and AFM techniques. The FESEM imagies show that these nanoribbons present lenghth several hundreds of µm and diameter between 100 and 200 nm. The AFM imagies of these nanoribbons show that the heights ranged between *ca*. 5 to 16 nm.

8. We have demonstrated that using organic ligands that provide molecular recognition capacity (nucleobases and pyridine derivatives) may lead to dynamic complexes thanks to the interaction flexibility offered by the H-bond interaction sites in the selected ligands and the flexible and reversible nature of the coordination bond.

In that regard,

I. We have studied structure transformations involve the interconversion between monomeric, dimetallic and one dimensional polymers that have been obtained from the reaction of Cu(II) and TAcOH and UAcOH acid. These structural transformations are followed by change in the magnetic properties.

II. Complexes **19** (**[CuBr(ANP]$_n$**) and **20^{RT}** (**[CuI(ANP]$_n$**) have shown stimuli responsive properties for temeprature change (**20^{RT}**), and gas of different volatile solvents (**19** and **20$^{RT)}$**. The study of the electrical response of complexes **19** and **20^{RT}** to the vapor of different solvents, open the door for this class of materials as sensors for the harmful organic solvents, which has great environmental and social impact.

Capítulo 4; Conclusiones

1. Hemos sido capaces de preparar diferentes complejos de coordinación, mononucleares (complejos **1** y **2**), bimetálicos (complejos **3**-**8**), y complejos de coordinación extendidos (polímeros de coordinación monodimensionales, **9**-**12**), mediante el uso de nucleobases modificadas tales como TAcOH y / o UAcOH como ligandos orgánicos, y Cu (II) como metal central. Los 1D-CPs (**9**-**12**) se han obtenido utilizado TAcOH como ligando y estos se puede dividir en dos grupos dependiendo de la naturaleza de la coordinación TAcOH al Cu(II). En los complejos **9** y **10**, el ligando TAcO- ha participado como puente ligando, mientras que, en el caso de los complejos **11** y **12**, como ligando terminal y los iones de cobre están conectados mediante un puente 4,4'-bipiridina como ligando lineal.

2. Hemos medido las propiedades físicas de los complejos obtenidos, en particular, las propiedades eléctricas y magnéticas. La conductividad eléctrica obtenida en los complejos **9** y **10** muestra un comportamiento semiconductor. Por otro lado, el de estudio de las propiedades magnéticas de los complejos **3**-**11** han demostrado que estos materiales presentan un comportamiento magnético variable entre un fuerte comportamiento antiferromagnético y débil comportamiento ferromagnético.

3. Hemos estudiado las interacciones de las mismas nucleobases modificadas (TAcOH o UAcOH) como ligandos orgánicos pero con el cation Co (II), en lugar de Cu (II), como centro metálico con el objetivo de preparar 1D-CPs con buenas propiedades eléctricas. Todos los intentos han conducido a las formaciones de complejos mononucleares (**13** y **14** respectivamente). Con el fin de obtener 1D-CPs, hemos utilizado un ligando adicional tal como 2,6-diaminopurina (HDAP), pero se han obtenido complejos mononucleares (**15** y **16** respectivamente). Finalmente, las reacciones de Co (II) con TAcOH en presencia del ligando lineal 4,4'-bipiridina han conducido a la formación de un complejo mononuclear (**17**).

4. Hemos sido capaces de preparar nanocintas del complejo **11**, **$[Cu(TAcO)_2(4,4'\text{-}bpy)(H_2O)]_n \cdot 2H_2O$**, utilizando el método de precipitación rápida. Hemos estudiado la morfología de estas nanocintas mediante las técnicas FESEM y AFM. Las imágenes de

FESEM confirman una estructura de nanocinta con ca. 100-150 nm anchura y longitud de micras. Las imágenes de AFM muestran una altura de ca. 3,5 nm, que está de acuerdo con el aislamiento de una cinta que consta de sólo uno a dos moléculas. Exploramos las posibles aplicaciones de estos materiales en aplicaciones biomédicas mediante el estudio de la interacción de nanocintas del complejo **11** con secuencias de varios oligonucleótidos. Hemos demostrado que las nanocintas del complejo **11** muestran una mayor selectividad a poliA con respecto a otros oligonucleótidos. Estas propiedades pueden permitir la integración de dicho sistema para aplicaciones biomédicas tales como la detección de ADN y / o suministro de ADN.

5. La interacción de halogenuros de cobre (I) con ligandos derivados de piridina, que muestran grupos funcionales libres disponibles para las interacciones supramoleculares, dieron lugar a una familia de polímeros de coordinación monodimensionales de fórmula general **[CuXL]$_n$**, donde X es haluro y L los ligandos derivados de piridina 2-amino-5-nitropiridina, ácido isonicotínico y isonicotinato de etilo. En todos los casos, el ion cobre presentaba estado de oxidación Cu^{+1}, lo que nos animó a estudiar sus propiedades luminiscentes junto a la conductividad eléctrica.

6. Trabajando con haluros de cobre (I), hemos sido capaces de preparar una serie de 1D CPs con comportamiento semiconductor con valores de conductividad eléctrica relevantes hasta 10^{-3} S/cm (**24** complejo, **[CuI (HIN)]$_n$**). Una fuerte emisión de fotoluminiscencia se ha observado en el caso del complejo de **25**, **[CuI (EtIN)]n**.

7. Hemos sido capaces de preparar nanocintas del complejo **20^{RT}**, con la fórmula **[CuI (ANP)]$_n$**, usando agua como anti-disolvente para controlar el crecimiento de las nanocintas. Los estudios de morfología de estas nanocintas, se realizaron mediante las técnicas FESEM y AFM. Las imágenes FESEM muestran que estos nanocintas presentes longitud de varios cientos de micras y el diámetro entre 100 y 200 nm. Las imágenes de AFM de estas nanocintas muestran que las alturas oscilan entre ca. 5-16 nm.

8. Hemos demostrado que el uso de ligandos orgánicos que proporcionan capacidad de reconocimiento molecular (nucleobases y derivados de piridina) puede dar lugar a complejos dinámicos gracias a la flexibilidad de interacción que ofrecen los sitios que forman enlaces de Hidrogeno en los ligandos seleccionados y de la naturaleza flexible y

reversible del enlace de coordinación.

En ese sentido,

I. Hemos estudiado las transformaciones de estructura que implican la interconversión entre complejos monoméricos, bimetálicos y un polímero monodimensional que se han obtenido de la reacción de Cu (II) y TAcOH y UAcOH. Estas transformaciones estructurales son seguidas por el cambio en las propiedades magnéticas.

II. Los complejos **19 ([CuBr(ANP]$_n$)** y **20^{RT} ([CuI(ANP]$_n$)** han demostrado propiedades tipo estímulo respuesta en función del cambio de temperatura (**20^{RT}**), y en presencia de gas de diferentes disolventes volátiles (**19** y **20^{RT}**). El estudio de la respuesta eléctrica de los complejos **19** y **20^{RT}** al vapor de diferentes disolventes, abre la puerta a esta clase de materiales como sensores de los disolventes orgánicos nocivos, que tiene un gran impacto ambiental y social.

5. Chapter 5; Experimental section

5.1. Physical techniques

5.1.1. Single crystals X-ray diffraction (SCXRD)

The crystal structures of the complexes have been realized using different diffractometers. Complexes (**1**-**3** and **9, 10, 14**-**17**) were done at 296(2) K on a Bruker Kappa Apex II diffractometer with graphite-monochromated Cu Kα radiation (λ = 1.54178 Å) at Salamanca University. Complexes (**4**-**6**) were done at 100(2) K and complexes (**7, 8**, **11**, **12**, **20**-**24**) at 296(2) K, on a Bruker Kappa Apex II diffractometer with graphite-monochromated Mo Kα radiation (λ = 0.71073 Å) at Autonomous University of Madrid. Complexes (**18** and **19**) were done at 100(2) K on an Oxford Diffraction Xcalibur with a graphite-monochromated Mo Kα radiation (λ = 0.71073 Å) at University of País Vasco.

5.1.2. Infrared spectroscopy (IR spectroscopy)

IR spectra were recorded on a PerkinElmer 100 spectrophotometer using a universal ATR sampling accessory and on a Bruker FT-IR Vector 22 model from 4000-400 cm^{-1} in KBr pellets.

5.1.3. Elemental analyses

Elemental analyses were performed on an LECO CHNS-932 Elemental Analyzer.

5.1.4. X-ray Powder diffraction (XRPD)

Powder X-ray diffraction of all the compounds, except compounds (**3**-**8**), has been done using a Diffractometer PANalyticalX'Pert PRO θ/2θ primary monochromator and detector with fast X'Celerator. The samples have been analyzed with scanning θ/2θ. Scan conditions θ/2θ, 3-50 degrees, with an angular increment of 0, 0167 and increasing time of 100 seconds. The powder X-ray diffraction of compounds **3**-**8** have been done using special cover to avoid the contact of the samples with air and all the manipulations of the samples have been done under argon gas using Atmosbag glove bag from Sigma.

5.1.5. Thermogravimetric analysis (TGA)

Thermogravimetric analysis (TGA) tests for complexes **3**, **20^{RT}**, **20a**, **23** and **24** were performed in a thermobalance oven equipped with a TA Instruments Q500. We were used Pt sample holder and N_2 as a purge gas at a flow of 90 mL/min. The samples were heated at 10 °C /min from room temperature to 1000 °C.

5.1.6. Conductivity

Preliminary direct current (DC) electrical conductivity measurements were performed on different single crystals of complexes **9**-1**2** and **19**-**25**, with carbon paint at 300 K and two contacts method. The contacts were made with wolframium wires (25 μm diameter). The samples were measured at 300 K applying an electrical current with voltages form +10 to -10 V. The measurements were performed in the complexes along the crystallographic *a* axis. The thermal dependence of the DC electrical conductivity was measured with the four or two contacts method, depending on the size of the crystals, on up to four crystals of every complex. The thermal dependence of the conductivity was performed in temperature range depending on the resistance at room temperature and hence the detection limit of the device. Complexes **9** and **10** were measured at temperature range 300-400 K. Complexes **19**-**23** were measured at temperature range 50-400 K. Complexes **24** and **25** were measured at temperature range 2-400 K. The contacts were made with Pt wires (25 μm diameter) using graphite paste. The samples were measured in a Quantum Design PPMS-9 equipment connected to an external voltage source (Keithley model 2450 source-meter) and amperometer (Keithley model 6514 electrometer). All the conductivity quoted values have been measured in the voltage range where the crystals are Ohmic conductors. The cooling and warming rates were 1 and 2 K/min respectively.

Electrochemical Impedance Spectroscopy data of complex **21** were collected at 298 K using an Autolab electrochemical system II PGSTAT30 (Ecochemie, The Netherlands) impedance analyser over the frequency range from 1 Hz to 1 MHz with an applied voltage of 0.01 V. The two-probe method was used in all the measurements. AC measurements through path and in line were performed to determine the conductivity parameters. The electrode samples were pressed pellets of thickness ranging between 1 and 2 mm. A powder sample (20 mg) was pressed by applying about 6 Tons/m^2 to form disks into a pellet with an area about 0.13-0.16 cm^2. The electrical contact between the sample and

the symmetric stainless steel disk electrodes was made by applying pressure, about 10 Tons/m^2, with a conductivity cell configuration SS/1/SS, where SS refers to stainless steel and 1 refers to the solid pellet of complex **21**.

5.1.7. Photoluminescence

Luminescence excitation and emission spectra of the solid compounds were performed, in the department of Photonic Materials at Institute of Materials Science CSIC, at 25 °C on a 48000s (T-Optics) spectrofluorometer from SLM-Aminco. A front face sample holder was used for data collection and oriented at 60° to minimize light scattering from the excitation beam on the cooled R-928 photomultiplier tube. Appropriate filters were used to eliminate Rayleigh and Raman scatters from the emission. Excitation and emission spectra were corrected for the wavelength dependence of the 450 W xenon arc excitation but not for the wavelength dependence of the detection system. Spectroscopic properties were measured by reflection (frontface mode) on finely ground samples and placed in quartz cells of 1 mm path length. No attempt was made to remove adsorbed or dissolved molecular oxygen from the materials. Reference samples that do not contain any fluorescent dopant were used to check the background and optical properties of the samples.

5.1.8. Magnetism

Magnetic measurements were performed on polycrystalline samples of the complexes taken from the same uniform batches used for the structural determinations with a Quantum Design MPMS-XL5 SQUID susceptometer in the temperature range 5−300 K with an applied magnetic field of 5000 G. The susceptibility data were corrected for the sample holder previously measured using the same conditions and for the diamagnetic contribution of the salt as deduced by using Pascal's constant tables.

5.1.9. Felid Emission Scanning Electron Microscope (SEM)

The FESEM images of complexes **11** and **20^{RT}** were taken by XL30 scanning electron microscope. The samples were prepared by drop casting the diluted suspension of the

target complex over glass substrate. Then, the samples were covered by 10 nm layer of conductive Cr to improve the resolution of the images.

5.1.10. Atomic Force Microscope (AFM)

Atomic Force Microscope (AFM) images were acquired in dynamic mode using a Nanotec Electronica system operating at room temperature in ambient air conditions. For AFM measurements, Olympus cantilevers were used with a nominal force constant of 0.75 N/m. The images were processed using WSxM. The surfaces used for AFM were Moscovita mica (E.M.S Company).

I. Surface preparations

In order to obtain reproducible results, very flat substrates were used with precisely controlled chemical functionalities, freshly prepared just before the chemical deposition. Muscovite Mica was cleaved with adhesive tape.

II. AFM Sample preparations

- **Complex 11**

  Diluted suspension of complex **11** was prepared by adding 20 ml of the original suspension of nanoribbons of complex 11 over 1mL of Milli-Q water. 15 μL of the diluted suspension were deposited by drop casting over freshly delaminated mica surface. The drop was allow to stand without movements for 15 minutes, avoid the total elimination of the solvent, then dried by argon flow.

- **Complex 20^{RT}**

  We have used the same procedure of complex **11** but using diluted suspension of complex $\mathbf{20^{RT}}$.

5.1.11. Theoretical Density Functional Theory (DFT)

DFT calculations were performed using the efficient plane-wave code QUANTUM ESPRESSO.[1] In this atomistic simulation package the Kohn-Sham equations are solved using a periodic supercell geometry. The ion-electron interaction is modeled by ultrasoft pseudopotentials,[2] and exchange-correlation (XC) effects are treated by the generalized-gradient-approximation (GGA) of Perdew, Burke, and Ernzerhof (PBE).[3] The one-electron wave-functions are expanded in a basis of plane-waves with energy cut-offs of 400 and 500 eV for the kinetic energy and for the electronic density, respectively, which have been adjusted to achieve sufficient accuracy in the total energy. The Brillouin zones of the different bulk-systems were sampled by using a **k**-space of $\Delta\mathbf{k} \leq 0.01 Å^{-1}$.[4]

5.1.12. Biological Experiment of complex 11

I. Modified oligonucleotide synthesis

The oligonucleotides were prepared using a MerMade4 DNA Synthesizer using commercial phosphoramidites (Link Technologies). After solid-phase synthesis, the solid support was transferred to a screw-cap glass vial and incubated at 55 ºC for 4 h with 2 mL of ammonia solution (33%). After the vial was cooled on ice the supernatant was transferred by pipet to microcentrifuge tubes and the solid support and the vial were rinsed with water. The combined solutions were evaporated to dryness using an evaporating centrifuge.

The samples were purified by polyacrylamide gel electrophoresis 20% and the oligonucleotides were eluted from gel fractions using an elutrap system. The solutions were desalted using a NAP-10 column and concentrated in an evaporating

II. Affinity studies.

The oligonucleotides (0.0055 µmol) were incubated with complex **11** (0.011 µmol) for 2 hours at room temperature in 600 µL in ultrapure water. Then, the mixture was centrifuged using standard dialysis eppendorfs (Amicon 10 K, 0.5 mL) to remove the unbound material.

The interaction between the nanoribbons and the oligonucleotides was monitored by absorbance at 260 nm of the mixture before, after 2 hours of reaction and the eluted

solutions. The absorbance was recorded in a Synergy H4 microplate reader, using a 96 well plate at room temperature.

III. Cell Viability Assay:

The cytotoxicity of the polymer was evaluated in MCF7 cell line using the resazurin assay. Cells were seeded onto 24-well plates at a density of 2 x 10^4 cells/well in supplemented DMEM medium (10% Fetal Bovine Serum (FBS), 1% L-Glutamine and 1% Streptomycin/Penicillin), and incubated overnight at standard conditions (37ºC, 5% CO_2). Then, the medium was replaced with fresh culture medium containing 25 µM, 50 µM, 75 µM, 100 µM, 150µM and 200µM of. After 24h of incubation, cells were washed twice with PBS, and incubated 48h more. Then, the medium was replace by fresh medium containing 1% of a resazurin reagent solution (1mg/mL of resazurin in PBS pH = 7.4). Cells were incubated for 3h, and the fluorescence was measured with excitation wavelength at 550 nm and emission wavelength at 590 nm using a plate reader Synergy H4. Cytotoxicity was expressed as a percentage of the control. All the experiments were performed in triplicates and the standar deviation is represented in the error bars.

5.2. Material

All the reagents and solvents were purchased commercially from standards and used without further purification. Uracil-1-acetic acid (UAcOH) was prepared according to the literature.[5] CuSCN was prepared according to the literature.[6] Dry DMF has been purchased from Acros Company. The rest of the solvents were dried according to standard methods.[7-9]

5.3. Synthesis

In this thesis we have been working mainly with Cu(II), Cu(I) and Co(II) metal ions. Using these as connectors, the thesis can be divided in three different blocks **A**, **B** and **C**. Block **A** and **B** involve the synthesis of the complexes described in **chapter 2** while, block **C** involves the synthesis of the complexes described in **chapter 3**.

Block A; This block involve the compounds obtained with Cu(II) and thymine-1-acetic acid (TAcOH) and/or uracil-1-acetic acid (UAcOH) as ligands where, the direct reactions of TAcOH and/or UAcOH in the presence of copper(II) salts lead to the formation of different compounds ranged between (i) mononuclear compounds, **$[Cu(TAcO)_2(H_2O)_4]\cdot 4H_2O$** ***(1)*** and **$[Cu(UAcO)_2(H_2O)_4]$** ***(2)***, (ii) dimetallic compounds, **$[Cu_2(TAcO)_4(DMF)_2]\cdot 2DMF$** ***(3)***, **$[Cu_2(TAcO)_4(DMF)_2][Cu_2(TAcO)_4(DMF)(H_2O)]$** ***(4)***, **$[Cu_2(TAcO)_4(DMSO)_2]\cdot 6DMSO$** ***(5)***, **$[Cu_2(TAcO)_4(DMA)_2]\cdot DMA$** ***(6)***, **$[Cu_2(TAcO)_2(UAcO)_2(DMF)_2]$** ***(7)*** and **$[Cu_2(UAcO)_4(DMSO)_2]\cdot 2DMSO$** ***(8)*** and (iii) 1D extended systems as **$[Cu(TAcO)_2(H_2O)_2]_n$** ***(9)*** and **$[Cu_{1.5}(TAcO)_2(H_2O)(OH)]_n\cdot 4H_2O$** (***10)***, depending on the reaction conditions. Moreover, the reactions of copper(II) nitrate trihydrate with TAcOH the presence of 4,4'-bipyridine (4,4'-bipy) as linear bridging ligand. allow the formation of new 1D coordination polymers, **$[Cu(TAcO)_2(4,4'\text{-bipy})(H_2O)]_n\cdot 2H_2O$** ***(11)*** and **$[Cu_2(TAcO)_2(4,4'\text{-bipy})]_n$** ***(12)***.

The purity of all the compounds have been confirmed by X-ray powder diffraction (see appendix **A**).

Mononuclear complexes.

$[Cu(TAcO)_2(H_2O)_4]\cdot 4H_2O$ ***(1)***

$Cu(AcO)_2\cdot H_2O$ (0.100 g, 0.50 mmol) was added over a solution of TAcOH (0.184 g, 1.0 mmol) and KOH (0.056 g, 1.0 mmol) in 10 mL of water. Then, the mixture was stirred for 3 h at 110 ºC, (pH = 5.3). Upon cooling, blue crystals of complex **1** appeared. Then the blue crystals were filtered off, washed with water, ethanol, diethyl ether, and dried by vacuum. The yield of complex **1** is 38.3 % (0.11 g, based on Cu).

Elemental analysis calculated (found) for $C_{14}H_{30}CuN_4O_{16}$ (**1**): C, 29.30 (30.09); H, 5.27 (5.07); N, 9.76 (9.71).

IR selected data (KBr, cm^{-1}): 3430 (m), 1678 (s), 1603 (w), 1479 (w), 1404 (w), 1350 (w), 1247 (w), 869 (w).

$[Cu(UAcO)_2(H_2O)_4]$ ***(2)***

A mixture of $Cu(AcO)_2\cdot H_2O$ (0.100 g, 0.50 mmol) and UAcOH (0.170 g, 1.0 mmol) was dissolved in 15 mL of water and fully stirred at 25 ºC for 3 hr, (pH = 3.7). The resulting blue solution was filtered off. Then, the blue solution was allowed to stand at 25ºC for crystallization. After 3 weeks, blue crystals of complex **2** were grown by slow evaporation of the blue solutions. The blue crystals were filtered off, washed with water, ethanol, diethyl ether, and dried by vacuum. The yield of complex **2** is 38.8 % (0.092 g, based on Cu).

Elemental analysis calculated (found) for $C_{12}H_{18}CuN_4O_{12}$ (**2**): C, 30.42 (30.74): H, 3.41 (3.87): N, 11.82 (12.52).

IR selected data (KBr, cm^{-1}): 3051 (w), 1711 (s), 1647 (m), 1592 (m), 1411 (m), 1387 (m), 1349 (m), 1326 (m), 1254 (w), 813 (w).

Dimetallic complexes.

$[Cu_2(TAcO)_4(DMF)_2]\cdot DMF$ ***(3)***

A (0.2 g, 0.35 mmol) of complex **1** was dissolved in 8 mL of dry DMF and stirred for 2 hr at 25 ºC under argon gas. Then, 20 mL of mixture of dry acetone and dry diethyl ether (1:1) has been layered over the resulting deep green solution. Green crystals of complex **3** were grown after one week. The solvents were removed under argon gas using cannula

system. The green crystals were dried under vacuum for 3 hours and have been kept under argon atmosphere. The yield of complex **3** is 6.1 % (0.0114 g, based Cu).

Elemental analysis calculated (found) for $C_{40}H_{44}Cu_2N_{12}O_{20}$ (**3**): C, 42.14 (41.35); H, 3.89 (5.20); N, 14.47 (14.35).

IR selected data (KBr, cm^{-1}): 3030 (w), 1707 (s), 1666 (s), 1630 (m), 1467 (w), 1435 (w), 1408 (m), 1384 (m), 1297 (m), 1250 (m), 1107 (m), 878 (w), 763 (w).

$[Cu_2(TAcO)_4(DMF)_2]_3[Cu_2(TAcO)_4(DMF)(H_2O)]_2$ *(4)*

$[Cu_2(TAcO)_4(DMSO)_2]\cdot 4.5DMSO$ *(5)* and **$[Cu_2(TAcO)_4(DMA)_2]\cdot DMA$** *(6)*.

Complexes **4**, **5** and **6** were prepared by the same procedure but using different solvents. In general, a mixture of $Cu(AcO)_2\cdot H_2O$ (0.050 g, 0.25 mmol) and TAcOH (0.092 g, 0.50 mmol) was dissolved in 8 mL of dry DMF (N,N-dimethylformamide) for complex **4**, DMSO (Dimethyl sulfoxide) for complex **5** and DMA (N,N-dimethylacetamide) for compound **6**. The resulting green solutions of complexes **4**, **5** and **6** were stirred for 2 h under argon gas at 25ºC. Then, 20 mL of mixture of dry acetone and dry diethyl ether (1:1) has been layered over the resulting green solutions of complexes **4**, **5** and **6**. Green crystals of complexes **4**, **5** and **6** were grown after one week. The solvents were removed under argon gas using cannula system and the green crystals of complexes **4**, **5** and **6** were dried under vacuum for 3 hours and were kept under argon atmosphere.

The yield of complex **4** is 61.3 % (0.075 g, based on Cu).

Elemental analysis calculated (found) for $C_{65}H_{79}Cu_4N_{19}O_{36}$ (**4**): C, 39.90 (41.20); H, 4.07 (4.60); N, 13.60 (14.40).

IR selected data (KBr, cm^{-1}): 3438 (w), 3164 (w), 3027 (w), 1706 (s), 1667 (s), 1626 (s), 1475 (w), 1435 (m), 1408 (m), 1384 (m), 1296 (m), 1250 (m), 1107 (w), 879 (w), 762 (w).

The yield of complex **5** is 38.8 % (0.072 g, based on the Cu).

Elemental analysis calculated (found) for $C_{44}H_{76}Cu_2N_8O_{24}S_8$ (**5**): C, 35.59 (34.76); H, 5.16 (5.14); N, 7.55 (7.30); S, 17.28 (16.59).

IR selected data (KBr, cm^{-1}): 3450 (w), 3177 (w), 3047 (w), 1692 (s), 1645 (s), 1468 (m), 1441 (m), 1414 (m), 1250 (m), 1228 (m), 1012 (s), 956 (w), 765 (w).

The yield of complex **6** is 39.25 % (0.055 g, based on Cu)

Elemental analysis calculated (found) for $C_{40}H_{55}Cu_2N_{11}O_{19}$ (**6**): C, 42.86 (43.27); H, 4.95(4.27); N, 13.74 (13.55).

IR selected data (KBr, cm^{-1}): 3421 (w), 3195 (w), 3057 (w), 1697 (s), 1602 (s), 1436 (w), 1405 (m), 1249 (w), 1229 (w), 1018 (w), 970 (w), 846 (w), 766 (w).

$[Cu_2(TAcO)_2(UAcO)_2(DMF)_2]$ *(7)*

A mixture of $Cu(AcO)_2 \cdot H_2O$ (0.050 g, 0.25 mmol), UAcOH (0.043 g, 0.25 mmol) and TAcOH (0.046 g, 0.25 mmol) was dissolved in 8 mL of dry DMF for 2 hr at 25 ºC. Then, 20 mL of mixture of dry acetone and dry diethyl ether (1:1) has been layered over the resulting green solution of complex **7**. Green crystals of complex **7** were grown after one week. The solvents were removed under argon gas using cannula system and the green crystals were dried under vacuum for 3 hr and were kept under argon atmosphere. The yield of complex **7** is 40.91 % (0.05 g, based on Cu).

Elemental analysis calculated (found) for $C_{32}H_{38}Cu_2N_{10}O_{18}$ (**7**): C, 39.31 (39.34); H, 3.92 (4.17); N, 13.32 (14.10).

IR selected data (KBr, cm^{-1}): 3298 (w), 3165 (w), 3012 (w), 1710 (s), 1648 (s), 1630 (s), 1456 (w), 1434 (m), 1400 (m), 1300 (w), 1312 (w), 1246 (w), 1105 (m), 898 (w), 820 (w), 758 (w).

$[Cu_2(UAcO)_4(DMSO)_2]$ DMSO *(8)*

The preparation of complex **8** is analogous to that described for complexes **4**-**6** but using UAcOH (0.085 g, 0.50 mmol) instead of TAcOH.

The yield of complex **8** is 47.31 % (0.066 g, based on Cu).

Elemental analysis calculated (found) for $C_{32}H_{44}Cu_2N_8O_{20}S_4$ (**8**): C, 34.44 (34.15); H, 3.97 (3.57); N, 10.04 (10.20); S, 11.49 (12.55).

IR selected data (KBr, cm^{-1}): 3428 (w) 3050 (w), 1698 (s), 1651 (m), 1459 (w), 1242 (w), 1024 (w), 809 (w).

1D extended complexes.

$[Cu(TAcO)_2(H_2O)_2]_n$ *(9)*

A mixture of $CuCl_2 \cdot 2H_2O$ (0.100 g, 0.59 mmol), TAcOH (0.216 g, 1.17 mmol) and KOH (0.066 g, 1.17 mmol) was dissolved in 20 mL of water and stirred for 3 h at 25 ºC, (pH = 4.5). The resulting blue mixture was filtered off and the resulting blue solid of complex **9** was washed with water, methanol, diethyl ether, and dried by vacuum. Blue crystals of **9**

were obtained after the filtrate was allowed to stand at room temperature for one week. The blue crystals were filtered off, washed with water, methanol, diethyl ether, and dried by vacuum.

The yield of complex **9** is 35.7 % (0.098 g, based on Cu).

Elemental analysis calculated (found) for $C_{14}H_{18}CuN_4O_{10}$ (**9**): C, 36.09 (36.20); H, 3.89 (3.89); N, 12.03 (12.39).

IR selected data (KBr, cm^{-1}): 3458 (w), 3091 (w), 1694 (s), 1647 (s), 1468 (w), 1428 (w), 1353 (m), 1254 (m), 881 (w).

$[Cu_{1.5}(TAcO)_2(H_2O)(OH)]_n \cdot 4H_2O$ ***(10)***

Complex **10** was obtained by the same procedure mentioned for complex **1** but doing the reaction at 25 ºC instead of 110 ºC, (pH = 5.3). The resulting blue suspension was filtered off to get blue solid and blue solution. The blue solution was allowed to stand at 25 ºC for crystallization. After 5 days, blue crystals of complex **10** were obtained then, the blue crystals were filtered off, washed with water, ethanol, diethyl ether, and dried by vacuum. The blue solid was a mixture of complexes **1** and **10**.

The yield of complex **10** is 34 % (0.11 g, based on Cu).

Elemental analysis calculated (found) for $C_{28}H_{42}Cu_3N_8O_{24}$ (**10**): C, 31.57 (31.10); H, 3.97 (3.92); N, 10.52 (10.82).

IR selected data (KBr, cm^{-1}): 3458 (w), 3091 (w), 1694 (s), 1647 (s), 1468 (w), 1428 (w), 1353 (m), 1254 (m), 881 (w).

$[Cu(TAcO)_2(4,4'\text{-bipy})(H_2O)]_n \cdot 2H_2O$ ***(11)*** and **$[Cu_2(TAcO)_2(4,4'\text{-bipy})]_n$** ***(12)***

A mixture of $Cu(NO_3)_2 \cdot 3H_2O$ (0.100 g, 0.41 mmol), TAcOH (0.152 g, 0.82 mmol) and 4,4'-bipy (0.065 g, 0.41 mmol) was dissolved in 18 mL of H_2O and stirred for 10 minutes at 25 ºC, (pH = 4.8). The deep blue mixture was sealed in a 23 mL Teflon-lined steel autoclave and heated at 140 ºC for 3 days then, cooled to 30 ºC in 24 hours. Blue and yellow crystals of complexes **11** and **12** respectively were obtained. The blue and yellow crystals were separated manually under lens. The crystals were washed by water, ethanol, diethyl ether, and dried by vacuum. The yield of complex **11** is 41.9 % (0.11 g, based on Cu) while the yield of complex **12** is 15.02 % (0.02 g, based on Cu).

Pure phase of complex **11** was obtained by dissolving $Cu(NO_3)_2 \cdot 3H_2O$ (0.100 g, 0.41 mmol), TAcOH (0.152 g, 0.82 mmol), NaOH (0.033 g, 0.82 mmol) and 4,4'-bipy (0.065 g, 0.20 mmol) in 18 mL of water for one hr. at 25 º C, (pH = 5.8). The blue solid obtained

(complex **11)**, was filtered off and washed with water, ethanol, diethyl ether, and dried by vacuum. The yield of complex **11** is 76.2 % (0.200 g, based on Cu).

Pure phase of complex **12** was obtained by dissolving a mixture of $Cu(NO_3)_2 \cdot 3H_2O$ (0.100 g, 0.41 mmol), TAcOH (0.076 g, 0.41 mmol) and 4,4'-bipy (0.065 g, 0.41 mmol) in 12 mL of ethanol and 1 mL of water then, the resulting blue suspension was stirred for 10 minutes at 25 ºC. The deep blue mixture was sealed in a 23 mL Teflon-lined steel autoclave and heated at 160 ºC for 4 days, then cooled to 30 ºC in 24 hours. Yellow crystals of complex **12** were isolated from the resulting yellow suspension by filtration and washed by water, ethanol, diethyl ether, and dried by vacuum. The yield of **12** is 82.61 % (0.11 g, based on Cu).

Elemental analysis calculated (found) for $C_{24}H_{28}CuN_6O_{11}$ (**11**): C, 45.04 (45.35); H, 4.41 (4.36); N, 13.13 (13.13).

IR selected data (KBr, cm^{-1}): 3446 (s), 1704 (s), 1677 (s), 1612 (s), 1471 (w), 1419 (m), 1355 (w), 1301 (w), 1247 (w), 1230 (w), 1078 (w), 1012 (w), 971 (w), 831 (w).

Elemental analysis calculated (found) for $C_{12}H_{11}CuN_3O_4$ (**12**): C, 46.68 (44.45); H, 3.59 (3.38); N, 13.61 (13.03).

IR selected data (KBr, cm^{-1}): 3471 (w), 1685 (s), 1643 (s), 1608 (s), 1473 (w), 1427 (m), 1373 (m), 1351 (w), 1282 (w), 1228 (w), 1074 (w), 1012 (w), 981 (w), 831 (w).

Preparation of nanoribbons for complex 11

A mixture of TAcOH (0.018 g) in 1 mL of water and NaOH (0.0039 g) in 1 mL of water was added to a water (1 mL) solution of 4,4'-bipy (0.0078 g) at 25ºC. The resulting clear solution was turned into a deep blue colloid upon addition of 1 mL of a water solution of $Cu(NO_3)_2 \cdot 3H_2O$ (0.0012 g). The blue colloid was stirred for 5 min., then the resulting blue colloid was collected by centrifugation and washed with H_2O, ethanol, and diethyl ether.

Block B; This block involve the compounds obtained from Co(II) salts and TAcOH or UAcOH as ligands. The direct reactions of TAcOH or UAcOH in the presence of $Co(AcO)_2 \cdot 4H_2O$ allow the formation of the mononuclear complexes, **$[Co(TAcO)_2(H_2O)_4]$** ***(13)*** and **$[Co(UAcO)_2(H_2O)_4]$** ***(14)***, respectively. On the other hand, the direct reactions of TAcOH or UAcOH with cobalt $Co(AcO)_2 \cdot 4H_2O$ in the presence of 2,6-diaminopurine (HDap) allow the formation of mononuclear complexes, **$\{[Co(Hdap)_2(H_2O)_4] \cdot (TAcO)_2 \cdot 3H_2O\}$** ***(15)*** and **$\{[Co(Hdap)_2(H_2O)_4] \cdot (UAcO)_2 \cdot 3H_2O\}$** ***(16)*** respectively. Attempts to obtain 1D extended polymers by using 4,4'-bipy as linear bridging ligand, allow the formation of a new mononuclear complex **[Co(TAcO)(4,4'-bipy)(H_2O)]** ***(17)***.

$[Co(TAcO)_2(H_2O)_4]$ ***(13)***

A mixture of $Co(AcO)_2 \cdot 4H_2O$ (0.100 g, 0.40 mmol) and TAcOH (0.148 g, 0.80 mmol) was dissolved in 15 mL of H_2O and stirred for 3 hr at 25 ºC (pH = 3.2). The resulting pink solution was filtered off and the pink filtrate was allowed to stand at 25 ºC for crystallizations. After three weeks, pink crystals of complex **13** were grown by slow evaporation of the water solvent. The pink crystals were filtered off, washed by water, ethanol, diethyl ether, and dried by vacuum. The yield of complex **13** was 47.26 % (0.094 g, based on Co).

Elemental analysis calculated (found) for $C_{14}H_{22}CoN_4O_{12}$ (**13**): C, 33.81 (33.45); H, 4.46 (4.41); N, 11.27 (11.26).

IR selected data (KBr, cm^{-1}): 3110 (m), 3108 (w), 3060 (w), 1710 (s), 1658 (s), 1415 (m), 1355 (m), 1311 (m), 1249 (m), 813 (w).

$[Co(UAcO)_2(H_2O)_4]$ ***(14)***

Complex **14** was prepared by the same method for complex **13**, but using UAcOH (0.138 g, 0.80 mmol) instead of TAcOH, pH = 3.7. After two weeks, pink crystals of complex **14** were grown by slow evaporation of the water solvent from the resulting pink solution. The pink crystals were filtered off, washed by water, ethanol, diethyl ether, and dried by vacuum. The yield of complex **14** was 38.36 % (0.072 g, based on Co).

Elemental analysis calculated (found) for $C_{12}H_{18}CoN_4O_{12}$ (**14**): C, 30.72 (30.20); H, 3.87 (3.87); N, 11.94 (11.8).

IR selected data (KBr, cm^{-1}): 3000 (w), 1697 (s), 1638 (m), 1590 (m), 1434 (m), 1386 (m), 1357 (m), 1302 (m), 1254 (m), 826 (w).

{[Co(Hdap)$_2$(H$_2$O)$_4$]·(TAcO)$_2$·3H$_2$O} ***(15)***

A mixture of $Co(AcO)_2·4H_2O$ (0.100 g, 0.40 mmol), TAcOH (0.073 g, 0.40 mmol) and KOH (0.023 g, 0.40 mmol) was dissolved in 12 mL of H_2O (pH=6.4). The resulting pink solution was added over 10 mL ethanolic solution of 2,6-diaminopurine (HDap) (0.060 g, 0.40 mmol), (pH = 6.4). The resulting pink solution was stirred for 2 hr at 80 ºC. The resulting pink solution was filtered off and the pink filtrate was allowed to stand at 25 ºC for crystallization. After one week, suitable pink crystals of complex **15** for DRX monocrystals diffraction were grown from the pink solution. The pink crystals were filtered off, washed by water, ethanol, and diethyl ether, and dried by vacuum. The yield of complex **15** was 35.23 % (0.120 g, based on Co).

Elemental analysis calculated (found) for $C_{24}H_{40}CoN_{16}O_{15}$ (**15**): C, 33.85 (33.82); H, 4.73 (4.69); N, 26.21 (27.16).

IR selected data (KBr, cm^{-1}): 3386 (w), 3139 (w), 1697 (s), 1610 (s), 1479 (m), 1423 (m), 1375 (m), 1243 (m), 1226 (w), 1006(w), 792 (w).

{[Co(Hdap)$_2$(H$_2$O)$_4$]·(UAcO)$_2$·3H$_2$O} ***(16)***

Complex **16** was prepared using the same method of complex **15** but using UAcOH (0.056 g, 0.40 mmol) instead of TAcOH, (pH = 5.8). The resulting pink solution was filtered off and the pink filtrate was allowed to stand at 25 ºC for crystallizations. After one week, suitable for DRX monocrystals diffraction pink crystals of complex **16** were grown from the pink solution. The pink crystals of **16** were filtered off, washed by water, ethanol, and diethyl ether, and dried by vacuum. The yield of complex **16** was 33.76 % (0.110 g, based on Co).

Elemental analysis calculated (found) for $C_{22}H_{34}CoN_{16}O_{14}$ (**16**): C, 32.80 (32.88); H, 4.25 (4.17); N, 27.88 (28.55).

IR selected data (KBr, cm^{-1}): 3488 (w), 3367 (w), 3147 (w), 1689 (s), 1614 (s), 1450 (m), 1417 (m), 1380 (m), 1295 (m), 1238 (w), 1160 (w), 1000(w), 698 (w).

[Co(TAcO)(4,4'-bipy)(H_2O)] ***(17)***

A mixture of $Co(NO_3)_2 \cdot 6H_2O$ (0.100 g, 0.34 mmol), TAcOH (0.063 g, 0.34 mmol) and 4,4'-bipy (0.054 g, 0.34 mmol) was sealed in a 23 mL Teflon-lined steel autoclave and heated at 120 ºC for 2 days, then cooled to 30 ºC in 1 day. Pink crystals of complex **17** were obtained. The crystals were filtered off, washed by water, ethanol, diethyl ether, and dried by vacuum. The yield of complex **17** was 53.22 % (0.14 g, based on Co).

Elemental analysis calculated (found) for $C_{34}H_{34}CoN_8O_{10}$ (**17**): C, 52.79 (52.28); H, 4.43 (4.42); N, 14.48 (14.47).

IR selected data (KBr, cm^{-1}): 3137 (w), 3018 (w), 1685 (s), 1602 (m), 1469 (m), 1427 (m), 1405 (m), 1380 (w), 1355 (w), 1317 (m), 1236 (m), 1149, 1106 (m), 1068 (m), 1045 (w), 1000 (w), 813 (w).

Block C; This block involve the complexes obtained by the reactions of Cu(I/II) salts with pyridine derivatives that allow the formation of a series of 1D-CPs based. The reactions of CuX (X = Cl, Br, I, CN, NCS ions) with 2-amino-5-nitropiridine (ANP), allow the formation of complexes (**$[Cu(ANP)Cl]_n$** ***(18)***, **$[Cu(ANP)Br]_n$** ***(19)***, **$[Cu(ANP)I]_n$** ***(20)***, **$[Cu(ANP)CN]_n$** ***(21)*** and **$[Cu(ANP)SCN]_n$** ***(22)*** respectively. While the reactions of CuI with Ethyl isonicotinate (EtIN) and Isonicotinic acid (INH) allow the formation of complexes **$[Cu(EtIN)I]_n$** ***(23)*** and **$[Cu(INH)I]_n$** ***(24)*** respectively.

$[Cu(ANP)Cl]_n$ ***(18)***

Method A; A mixture of $CuCl_2 \cdot 2H_2O$ (0.100 g, 0.58 mmol) and ANP (0.162 g, 1.17 mmol) was dissolved in 15 mL mixture of water-ethanol (1:2). The suspension was stirred for 10 minutes at 25 ºC and then sealed in a 23 mL Teflon-lined steel autoclave, heated at 160 ºC for 4 days, and finally cooled to 30 ºC at a rate of 2.71 ºC/h (48 h). Yellow crystals of complex **18** were isolated from the resulting green solution by filtration and washed with water, ethanol, acetonitrile, diethyl ether and dried by vacuum. The yield of complex **18** was 28.96 % (0.04 g, based on Cu).

Elemental analysis calculated (found) for $C_5H_5CuN_3O_2Cl$ (**18**): C, 25.22 (24.53); H, 2.12 (2.37); N, 17.65 (17.06).

IR selected data (KBr, cm^{-1}): 3452 (m), 3347 (m), 1635 (s), 1603 (m), 1572 (m), 1332 (s), 1290 (s), 826 (m), 759 (w).

Method B; A mixture of CuCl (0.100 g, 1.01 mmol) and ANP (0.141 g, 1.0 mmol) was dissolved in 15 mL mixture of water-ethanol (1:2). The suspension was stirred for 10 minutes at 25 ºC and then sealed in a 23 mL Teflon-lined steel autoclave, heated at 160 ºC for 4 days, and finally cooled to 30 ºC at a rate of 2.71 ºC/h (48 h). Yellow crystals of complex **18** were isolated from the resulting green solution by filtration and washed with water, ethanol, acetonitrile, diethyl ether and dried by vacuum. The yield of complex **18** was 16.63 % (0.040 g, based on Cu). The similarity of the crystals obtained from methods A and B was confirmed by single crystal X-ray diffraction and X-ray powder diffraction.

$[Cu(ANP)Br]_n$ ***(19)***.

Complex **19** has been reported starting from CuBr[10], but here we reported its synthesis using another methods which allow us to reduce the reaction time and improve the yield with respect to the publish one (method C).

Method A; Complex **19** was synthesized by the same method of complex **18** but using $CuBr_2$ (0.100 g, 0.45 mmol) instead of $CuCl_2 \cdot 2H_2O$ and ANP (0.124 g, 1.17 mmol). Orange/ yellow crystals of complex **19** were isolated from the resulting green solution by filtration and washed with water, ethanol, acetonitrile, diethyl ether, and dried by vacuum. The yield of complex **19** was 29.86 % (0.038 g, based on Cu).

Method B; Similar to method **B** that has been used for complex **18** but using CuBr (0.100 g, 0.68 mmol) and ANP (0.097 g, 0.68 mmol). Yellow crystals of complex **19** were isolated from the resulting green solution by filtration and washed with water, ethanol, acetonitrile, diethyl ether and dried by vacuum. The yield of complex **19** was 26.02 % (0.051 g, based on Cu).

Method C; A mixture of $CuBr_2$ (0.050 g, 0.22 mmol) and ANP (0.031 g, 0.22 mmol) was dissolved in 12 mL of (3:1) mixture of ethanol/ water, then the resulting yellow suspension was placed in a 70 mL TFM leaned vessel, sealed and placed into a microwave oven equipped with a rotor. The multimode microwave has a twin magnetron (2 x 800

W, 2.45 GHz) with a maximum delivered power of 1000 W. The temperature was increased from room temperature to 160 ℃ in 20 min. (microwave power was set at 600 W) and kept for a preset time of 4 h after which, the vessel was slowly cooled down to room temperature at a rate of 5.42 ºC/h (24 h). Orange/ yellow crystals of complex **19** were isolated from the resulting green solution by filtration and washed with water, ethanol, acetonitrile, diethyl ether, and dried by vacuum. The yield of complex **19** was 91.69 % (0.057 g, based on Cu).

The similarity of the crystals obtained from methods **A**, **B** and **C** was confirmed by single crystal X-ray diffraction and X-ray powder diffraction.

Elemental analysis calculated (found) for $C_5H_5CuN_3O_2Br$ (**19**): C, 21.25 (21.25); H, 1.78 (1.89); N, 14.87 (14.97).

IR selected data (KBr, cm^{-1}): 3471 (m), 3328 (m), 1633 (s), 1601 (m), 1570 (m), 1334 (s), 1293 (s), 826 (m), 759 (w).

$[Cu(ANP)I]_n$ ***(20^{RT})***

A mixture of CuI (0.050 g, 0.26 mmol) and ANP (0.036 g, 0.26 mmol) was dissolved in 12 mL acetonitrile. The resulting yellow solution was stirred for 2 h at 25 ºC. The final yellow solution was filtered off and left for crystallization at 25 ºC. After a week, yellow crystals of complex **20^{RT}** were filtered, washed with water, acetonitrile and diethyl ether, and dried by vacuum. The yield of complex **20^{RT}** was 44.35 % (0.038 g, based on Cu).

Elemental analysis calculated (found) for $C_5H_5CuN_3O_2I$ (**20^{RT}**): C, 18.22 (18.05); H, 1.53 (1.63); N, 12.75 (12.80).

IR selected data (KBr, cm^{-1}): 3452 (m), 3326 (m), 1626 (s), 1603 (m), 1571 (m), 1335 (s), 1290 (s), 827 (m), 759 (w).

Preparation nanofibers of compound 20^{RT} $[CuI(ANP)]_n$

We dissolved 0.05 M of CuI salt in saturated aqueous solution of KI (clear solution), then 0.05 M ethanolic solution of ANP ligand was added over the CuI solution while stirring. Yellow solution was formed. 20 mL of water were added one shot over the yellow solution to get yellow nanofibers of compound **20^{RT}.** The nanofibers were collected by centrifugation and washed twice by water and ethanol through centrifugation cycles. Then the nanofibers were redispersed in water for further studies.

[Cu(ANP)I]$_n$ ***(20a)***

A mixture of CuI (0.050 g, 0.26 mmol) and ANP (0.036 g, 0.26 mmol) was stirred in 12 mL of acetonitrile-water (2:1) for 10 min at 25 ºC. The resulting yellow solution was sealed in a 23 mL Teflon-lined steel autoclave, heated at 160 ºC for 4 days, and finally cooled to 30 ºC at a rate of 5 ºC/h (28 h). Red crystals of complex **20a** were filtered, washed with water, acetonitrile, diethyl ether, and dried by vacuum. The yield of complex **20a** was 32.68 % (0.028 g, based on Cu).

Elemental analysis calculated (found) for $C_5H_5CuN_3O_2I$ (**20a)**: C, 18.22 (17.95); H, 1.53 (1.69); N, 12.75 (12.37).

IR selected data (KBr, cm^{-1}): 3452 (m), 3326 (m), 1626 (s), 1603 (m), 1571 (m), 1335 (s), 1290 (s), 827 (m), 759 (w).

{[Cu(ANP)I]$_n$×nCH$_3$COOH} ***(20b)***

A mixture of CuI (0.100 g, 0.52 mmol) and ANP (0.036 mg, 0.26 mmol) was stirred in 12 mL acetonitrile-water (2:1) for 10 min at 25 ºC and the solution saturated with O_2 bubbling gas for 20 min. The resulting yellow solution was sealed in a 23 mL teflon-lined steel autoclave, heated at 160 ºC for 4 days and finally cooled to 30 ºC at a rate of 5 ºC/h (28 h). Three different types of crystals of complexes **20a** (red), **20b** (orange) and $[Cu_2(CH_3COO)_4(C_5H_5N_3O_2)_2]$ (green) were filtered off, washed with water, acetonitrile and diethyl ether, and air-dried. The obtained crystals were manually isolated, **20a** (0.032 g, yield 37 % based on Cu), **20b** as a by-product (in very low yield < 10 %) and $[Cu_2(CH_3COO)_4(C_5H_5N_3O_2)_2]$ (0.012 g, yield 9 % based on Cu).

IR selected data (KBr, cm^{-1}): 3437 (m), 3380 (m), 1654 (s), 1605 (m), 1507 (m), 1394 (s), 1339 (s).

[Cu(ANP)CN]$_n$ ***(21)***

A mixture of CuCN (0.150 g, 1.67 mmol) and ANP (0.233 g, 1.67 mmol) was dissolved in 20 mL of acetonitrile. The mixture was refluxed for 3 hours at 80 ºC. The resulting yellow suspension was filtered off to get yellow solid of complex **21** mixed with small yellow crystals of **20** then, the yellow solid was washed with water, ethanol, acetonitrile, diethyl ether, and dried by vacuum. Suitable crystal for single crystal X-ray diffraction was separated manually under lens from the mixture of yellow solid and crystals. The yield of complex **21** was 70.69 % (0.270 g, based on Cu).

Elemental analysis calculated (found) for $C_6H_5CuN_4O_2$ (**21**): C, 31.51 (30.70); H, 2.20 (2.56); N, 24.50 (23.95).

IR selected data (KBr, cm^{-1}): 3439 (m), 3341 (m), 2114 (s), 1625 (s), 1573 (s), 1339 (s), 1285 (s).

[Cu(ANP)SCN]$_n$ ***(22)***

A mixture of CuSCN (0.075 g, 0.62 mmol), ANP (0.086 g, 0.62 mmol) and NH_4SCN (140 mg, 1.8 mmol) was dissolved in 10 mL of acetonitrile. The mixture was stirred for 3 hours at 25 ºC and the resulting red/orange solution was filtered off and left to crystallize by slow evaporation at 4 ºC. Yellow crystals of complex **22** were grown at 4 ºC. The crystals were filtered off, washed with water, ethanol, acetonitrile, diethyl ether, and dried by vacuum. The yield of complex **22** was 71.14 % (0.115 g, based on Cu).

Elemental analysis calculated (found) for $C_6H_5CuN_4O_2S$ (**22**): C, 27.64 (25.98); H, 1.93 (1.98); N, 21.49 (20.60); S, 12.30 (12.80).

IR selected data (KBr, cm^{-1}): 3438 (m), 3336 (m), 2165 (s), 1625 (s), 1572 (m), 1338 (s), 1288 (s).

[Cu(EtIN)I]$_n$ ***(23)***.

Method A; Ethyl-isonicotinate (EtIN) (0.157 g, 1.04 mmol) was added over a solution of CuI (0.200 g, 1.04 mmol) in 12 mL of acetonitrile at 25 ºC. Immediately, the solution turned into yellow mixture. Yellow solid of complex **23** was filtered of, washed with ethanol, diethyl ether and dried by vacuum. Yellow crystals of complex **23** were grown at 25 ºC in 2 days. The yellow crystals were filtered of, washed with ethanol, diethyl ether and dried by vacuum. The yield of complex **23** was 71.77 % (0.255 g, based on Cu).

Elemental analysis calculated (found) for $C_8H_9CuO_2I$ (**23**): C, 28.13 (28.20); H, 2.66 (2. 44); N, 4.10 (4.02).

IR selected data (KBr, cm^{-1}): 3421 (w), 1716 (m), 1556 (w), 1413 (s), 1395 (w), 1363 (m), 1322 (m), 1292 (s), 1259 (m), 1224 (w), 1135 (w), 1110 (w), 1060 (m), 1018 (m), 856 (w), 800 (m), 759 (m), 698 (m).

Method B; A mixture of CuI (0.100 mg, 0.52 mmol) and INH (0.064 mg, 0.52 mmol) was dissolved in 12 mL mixture of water-ethanol (1:1). Then, the yellow solution was sealed in a 23 mL Teflon-lined steel autoclave, heated at 160 ºC for 3 days and finally

cooled to 30 ºC at a rate of 5.4 ºC/h (26 h). The resulting suspension was filtered off to give a solid consisting of a mixture of yellow and blue solid. The solid was treated with 10 mL of acetonitrile and the remaining insoluble blue solid filtered-off and the yellow filtrate (yellow solution) was left for crystallization at 25 ºC. Yellow crystals of complex **23** were obtained upon standing the clear solution at 25 ºC for 3 days. The yellow crystals were washed with ethanol, diethyl ether, and dried by vacuum. The yield of complex **23** was 37.34 % (0.04 g, based on Cu). The similarity of the obtained crystals from methods **A** and **B** was confirmed by single crystal X-ray diffraction and powder X-ray diffraction

[Cu(INH)I]$_n$ ***(24)***

A mixture of INH (0.129 g, 1.05 mmol) and CuI (0.200 g, 1.05 mmol) was dissolved in 60 mL of a mixture of acetonitrile-ethanol (1:1). The mixture was stirred for 2 h at 25 ºC. The volume of the resulting yellow solution was reduced by rotary system until a red solid of **24** was appeared. The red solid of complex **24** was filtered of, washed with ethanol, acetonitrile, diethyl ether, and dried by vacuum. Suitable red crystals for single crystal X-ray diffraction of complex **24** were grown by slow evaporation of the yellow solution (filtrate) at 25 ºC in 2 days. The red crystals were filtered of, washed with ethanol, acetonitrile, diethyl ether and dried by vacuum. The yield of complex **24** was 45.56 % (0.150 g, based on Cu).

Elemental analysis calculated (found) for $C_6H_5CuNO_2I$ (**24**): C, 22.98 (22.88); H, 1.61 (1.65); N, 4.47 (4.47).

IR selected data (KBr, cm^{-1}): 3444 (w), 1697 (s), 1604 (m), 1556 (m), 1411 (s), 1324 (m), 1292 (s), 1209 (m), 1133 (s), 1058 (w) 917 (w), 825 (w), 759(m), 696 (m), 676 (m).

References

1. G. Paolo, B. Stefano, B. Nicola, C. Matteo, C. Roberto, C. Carlo, C. Davide, L. C. Guido, C. Matteo, D. Ismaila, C. Andrea Dal, G. Stefano de, F. Stefano, F. Guido, G. Ralph, G. Uwe, G. Christos, K. Anton, L. Michele, M.-S. Layla, M. Nicola, M. Francesco, M. Riccardo, P. Stefano, P. Alfredo, P. Lorenzo, S. Carlo, S. Sandro, S. Gabriele, P. S. Ari, S. Alexander, U. Paolo and M. W. Renata, **QUANTUM ESPRESSO: a modular and open-source software project for quantum simulations of materials**, *Journal of Physics: Condensed Matter*, **2009**, 21, 395502, http://stacks.iop.org/0953-8984/21/i=39/a=395502.
2. D. Vanderbilt, **Soft self-consistent pseudopotentials in a generalized eigenvalue formalism**, *Physical Review B*, **1990**, 41, 7892-7895, http://link.aps.org/doi/10.1103/PhysRevB.41.7892.
3. J. P. Perdew, K. Burke and M. Ernzerhof, **Generalized Gradient Approximation Made Simple**, *Physical Review Letters*, **1996**, 77, 3865-3868, http://link.aps.org/doi/10.1103/PhysRevLett.77.3865.
4. H. J. Monkhorst and J. D. Pack, **Special points for Brillouin-zone integrations**, *Physical Review B*, **1976**, 13, 5188-5192, http://link.aps.org/doi/10.1103/PhysRevB.13.5188.
5. J. Xiong, M.-C. Liu and J.-X. Yuan, **1-(Carboxymethyl)uracil**, *Acta Crystallographica Section E*, **2005**, 61, o2665-o2667, http://dx.doi.org/10.1107/S1600536805022774.
6. M. A. S. Goher and F. A. Mautner, **Dimeric and polymeric copper(I) complexes. Synthesis and characterization of copper(I) complexes of di-2-pyridyl ketone oxime (DPKox) and crystal structures of [Cu(DPKox)Cl]** 3425-3431, http://dx.doi.org/10.1016/S0277-5387(99)00250-8.
7. D. R. Burfield, K.-H. Lee and R. H. Smithers, **Desiccant efficiency in solvent drying. A reappraisal by application of a novel method for solvent water assay**, *The Journal of Organic Chemistry*, **1977**, 42, 3060-3065, http://pubs.acs.org/doi/abs/10.1021/jo00438a024.
8. D. R. Burfield and R. H. Smithers, **Desiccant efficiency in solvent drying. 3. Dipolar aprotic solvents**, *The Journal of Organic Chemistry*, **1978**, 43, 3966-3968, http://dx.doi.org/10.1021/jo00414a038.
9. D. R. Burfield and R. H. Smithers, **Drying of grossly wet ether extracts**, *Journal of Chemical Education*, **1982**, 59, 703, http://dx.doi.org/10.1021/ed059p703.
10. W.-W. Zhou, W. Zhao, X. Zhao, F.-W. Wang and B. Wei, **A New 1-D Cu(I) Pyridinate Complex [CuBr(anp)] n (anp = 2-amino-5-nitropyridine)**, *Synthesis and Reactivity in Inorganic, Metal-Organic, and Nano-Metal Chemistry*, **2013**, 43, 1171-1174, http://dx.doi.org/10.1080/15533174.2012.756899.

Appendix A; crystallographic tables

Appendix **A** shows the crystallographic data obtained by single X-ray diffractions

Table A. 1. Crystallographic data of complexes **1** and **2**.

Complexes	**1**	**2**
Empirical formula	$C_{14}H_{30}CuN_4O_{16}$	$C_{12}H_{26}CuN_4O_{16}$
MW (g mol^{-1})	573.96	545.91
Crystal system	Monoclinic	triclinic
Space group	P21/c	$P2_1/c$
a (Å)	8.3932(2)	8.341(3)
b (Å)	12.4324(4)	11.823(4)
c (Å)	11.1965(3)	11.097(5)
α (º)	90	
β (°)	93.938(1)	92.73(2)
γ (º)	90	
V (Å^3)	1165.57(6)	1093.1(7)
Z	2	2
T (K)	296(2)	296(2)
λ (Å)	1.54180	1.659
ρ_{calcd} (g cm^{-3})	1.635	2.218
μ (mm^{-1})	2.111	2307
Reflections collected	5227	1187
Unique data/restraints/parameter	1877/0/161	71
R_{int}	0.0191	0.0576
Goodness of fit (S)[a]	1.091	3.137
R_1[b]/wR_2[c] [I>2□(I)]	0.0313/0.0869	0.3137/0.6100
R_1[b]/wR_2[c] [all data]	0.0323/0.0879	0.4213/0.7221

Table A. 2. Selected bond lengths (Å) and angles (º) for complexes **1** and **2**.

Complex **1**			
Cu1–O1	1.9595(13)	O1-Cu1-O1w^{i}	90.76
Cu1–O1w	1.9413(14)	O1-Cu1-O2w	96.50
Cu1–O2w	2.5309(14)	O1-Cu1-O2w^{i}	83.50
O1-Cu1-O1w	89.24		
Complex **2**			
Cu1–O1	1.867(15)	O1-Cu1-O1w^{i}	91.28
Cu1–O1w	1.94(2)	O1-Cu1-O2w	88.53
Cu1–O2w	2.59(2)	O1-Cu1-O2w^{i}	82.53
O1-Cu1-O1w	91.28		

Symmetry codes for complex **1**: (i) -x, -y, -z. Symmetry codes for complex **2**: (i) -x, -y, -z.

Table A. 3. Hydrogen bond distances [Å] and bond angles [°] for complex **1**.

D─H···A	D─H	H···A	D···A	∠D─H···A
N3─H···O3w^{i}	0.86	2.01	2.864(2)	176.3
O1w─H···O3w	0.84	1.86	2.696(2)	174.2
O1w─H···O4w	0.86	1.81	2.664(2)	168.8
O2w─H···O2	0.91	1.82	2.705(2)	164.2
O2w─H···O4^{ii}	0.80	2.24	3.029(2)	169.0
O3w─H···O2`^{iii}	0.71	2.16	2.837(2)	159.4
O3w─H···O2^{iv}	0.84	1.85	2.689(2)	176.5
O4w─H···O2w^{v}	0.90	2.00	2.878(2)	166.1
O4w─H···O4^{vi}	0.91	2.04	2.841(2)	146.4

Table A. 4. Crystallographic data of complexes **3**-**5**.

Complexes	**3**	**4**	**5**
formula	$C_{40}H_{44}Cu_2N_{12}O_{20}$	$C_{65}H_{79}Cu_4N_{19}O_{36}$	$C_{44}H_{76}Cu_2N_8O_{24}S_8$
MW (g mol^{-1})	1139.95	1956.63	1484.69
crystal system	monoclinic	monoclinic	triclinic
space group	$P2_1/n$	$P2_1/n$	P-1
a (Å)	13.4524(4)	18.997(4)	9.4516(9)
b (Å)	11.3654(3)	24.852(6)	13.4558(12)
c (Å)	16.6721(4)	27.646(6)	14.2802(11)
α (º)	90	90	64.204(3)
β (º)	94.674(2)	104.45(1)	89.820(3)
γ (º)	90	90	79.094(3)
V (Å^3)	2540.55(12)	12639(5)	1599.2(2)
Z	2	4	1
T (K)	296(2)	100(2)	100(2)
ρ_{calcd} (g cm^{-3})	1.490	1.028	1.542
μ (mm^{-1})	0.924	0.730	1.007
reflections collected	11872	181794	21745
unique data/parameters	3786/338	23084/1125	5790/339
R_{int}	0.0297	0.0756	0.0456
Goodness of fit (S)[b]	1.058	0.966	1.049
R_1[c]/wR_2[d] [I>2σ(I)]	0.0498/0.1517	0.0770/0.2187	0.0779/0.2049
R_1[c]/wR_2[d] [all data]	0.0568/0.1589	0.1142/0.2365	0.1104/0.2280

Table A. 5. Crystallographic data of complexes **6**-**8**.

Complexes	**6**	**7**	**8**
formula	$C_{40}H_{55}Cu_2N_{11}O_{19}$	$C_{32}H_{38}Cu_2N_{10}O_{18}$	$C_{32}H_{44}Cu_2N_8O_{20}S_4$
MW (g mol^{-1})	1121.03	977.80	1116.07
crystal system	triclinic	triclinic	triclinic
space group	P-1	P-1	P-1
a (Å)	11.1990(3)	9.3071(2)	9.4621(5)
b (Å)	15.5475(5)	10.7239(2)	11.1133(4)
c (Å)	15.6884(5)	11.2475(2)	12.3040(5)
α (º)	80.724(2)	81.814(1)	65.178(2)
β (º)	74.6220(10)	65.581(1)	78.605(2)
γ (º)	71.103(2)	83.654(1)	89.604(2)
V (Å^3)	2483.35(13)	1010.10(3)	1146.94(9)
Z	2	1	1
T (K)	100(2)	296(2)	296(2)
ρ_{calcd} (g cm^{-3})	1.499	1.607	1.616
μ (mm^{-1})	0.941	1.142	1.194
reflections collected	45426	38704	17213
unique data/parameters	9033/658	3690/283	4145/297
R_{int}	0.0381	0.0278	0.0387
Goodness of fit (S)[b]	1.145	1.129	1.122
R_1[c]/wR_2[d] [I>2σ(I)]	0.0475/0.1359	0.0479/0.1413	0.0557/0.1555
R_1[c]/wR_2[d] [all data]	0.0626/0.1562	0.0540/0.1474	0.0825/0.1881

Table A. 6. Selected bond lengths (Å) for complexes **3**-**8**.

Complex **3**			
Cu1-O191	2.018(2)	Cu1-O291	1.958(2)
Cu1-O192^{i}	1.975(3)	Cu1-O292^{i}	1.955(3)
Cu1···Cu1^{i}	2.6701(9)		
Complex **4**			
Cu1-O191	1.959(3)	Cu2-O192	1.990(3)
Cu1-O291	1.982(3)	Cu2-O292	1.953(3)
Cu1-O391	1.967(3)	Cu2-O392	2.031(3)
Cu1-O491	1.992(4)	Cu2-O492	1.958(3)
Cu1-O1	2.134(4)	Cu2-O2	2.134(3)
Cu1···Cu2	2.6484(9)		
Cu3-O591	1.979(3)	Cu4-O592	1.987(4)
Cu3-O691	1.968(3)	Cu4-O692	1.967(3)
Cu3-O791	1.998(3)	Cu4-O792	1.975(3)
Cu3-O891	1.963(3)	Cu4-O892	1.986(4)
Cu3-O3	2.142(4)	Cu4-O1w	2.144(4)
Cu3···Cu4	2.6530(9)		
Complex 5			
Cu1-O191	1.972(4)	Cu1-O291	1.982(4)
Cu1-O192^{i}	1.968(4)	Cu1-O292^{i}	1.960(4)
Cu1···Cu1^{i}	2.6749(14)		
Complex **6**			
Cu1-O191	1.992(2)	Cu1-O291	1.958(2)
Cu1-O192^{i}	1.974(2)	Cu1-O292^{i}	1.952(2)
Cu1···Cu1^{i}	2.6824(8)		
Cu2-O391	1.959(3)	Cu2-O491	1.994(3)
Cu2-O392^{ii}	1.956(3)	Cu2-O492^{ii}	1.964(3)
Cu2···Cu2^{ii}	2.6712(9)		
Complex **7**			
Cu1-O191	1.971(3)	Cu1-O291	1.962(3)
Cu1-O192^{i}	1.958(3)	Cu1-O292^{i}	1.985(2)
Cu1···Cu1^{i}	2.6648(7)		
Complex **8**			

Cu1-O181	1.982(3)	Cu1-O281	1.978(3)
Cu1-O182^{i}	1.964(3)	Cu1-O282^{i}	1.961(4)
Cu1···Cu1^{i}	2.6766(11)		

Symmetry codes for complex **3**: (i) –x+1, -y, -z; for complex **5**: (i) –x,-y+1,-z+1; for complex **6**: (i) –x,-y+1,-z; (ii) –x+2,-y,-z+1; for complex **7**: (i) –x+1,-y+2,-z+1; for complex **8**: (i) –x+1,-y+1,-z.

Table A. 7. Hydrogen bond and π–π stacking interactions (Å, º) of complexes **3**-**8**.[a]

Complex **3**					
D─H···A		H···A	D···A		D–H···A
N13–H13···O62^{i}		2.08	2.931(7)		163.8
N23–H23···O54^{i}		2.05	2.910(7)		165.9
N33–H33···O34^{ii}		1.97	2.846(5)		171.2
N43–H43···O84^{iii}		1.93	2.802(5)		169.7
N53–H53···O22^{iv}		2.03	2.895(8)		167.8
N63–H63···O14^{iv}		1.99	2.856(6)		169.9
N73–H73···O72^{ii}		2.07	2.910(5)		160.2
N83–H83···O44^{v}		1.92	2.798(5)		172.0
Complex **4**					
D─H···A		H···A	D···A		D–H···A
N13–H13···O191^{i}		2.36	3.133(4)		149.0
N23–H23···O41^{ii}		1.99	2.835(5)		167.1
π–π interactions[a]	Angle	DC	α	DZ	DXY
Thy2–Thy2^{iii}	0.0	3.5150(1)	14.6	3.4014	0.887
Complex **5**					
D─H···A		H···A	D···A		D–H···A
N13–H13···O4^{i}		1.97	2.827(8)		165.7
N23–H23···O4^{ii}		1.96	2.820(7)		164.9
π–π interactions[b]	Angle	DC	α	DZ	DXY
Thy1–Thy1^{iii}	0.0	3.6873(4)	25.0	3.3409	1.560
Thy2–Thy2^{iv}	0.0	3.4979(3)	15.2	3.3749	0.919
Complex **6**					
D─H···A		H···A	D···A		D–H···A
N13–H13···O191^{i}		2.19	3.002(4)		154.0

N23–H23···O24[ii]	1.96	2.835(4)	173.9		
N33–H33···O71[iii]	1.89	2.735(5)	160.7		
N43–H43···O4[iv]	2.37	3.167(5)	150.4		
π–π interactions[b]	Angle	DC	α	DZ	DXY
Thy1–Thy1[iv]	0.0	3.9593(1)	37.2	3.1526	2.395
Complex **7**					
D–H···A	H···A	D···A	D–H···A		
N13–H13···O14[i]	1.98	2.837(5)	175.2		
N23–H23···O292[ii]	2.30	3.081(4)	150.5		
π–π interactions[b]	Angle	DC	α	DZ	DXY
Ura1–Ura1[iv]	0.0	4.0705(1)	38.9	3.1695	2.554
Complex **8**					
D–H···A	H···A	D···A	D–H···A		
N13–H13···O12[i]	2.10	2.955(6)	170.0		
N23–H23···O24[ii]	1.91	2.771(6)	177.2		

[a]Symmetry for complex **3**: (i) x+1, y, z; (ii) –x+1, -y+2, -z; (iii) x+1/2, -y+3/2, z+1/2; (iv) x-1, y, z; (v) x-1/2, -y+3/2, z-1/2; for complex **4**: (i)-x+1, -y-1, -z; (ii) –x+2, -y-1, -z;(iii) –x+1, -y+1, -z+1; for complex **5**: (i) x-1, y-1, z; (ii) –x+1, -y+1, -z+1; (iii) –x, -y, -z+2; (iv) –x, -y, -z+1; for complex **6**: (i) –x+1, -y+1, -z; (ii) –x, -y+1, -z+1; (iii) –x+1, -y+1, -z+1; (iv) –x+1, -y, -z+1; for complex **7**: (i) –x, -y+1, -z+2; (ii) –x+1, -y+2, -z; (iii) –x+1, -y, -z+2; for complex **8**: (i) –x+1, -y+1, -z+1; (ii) –x, -y+2, -z. [a]Angle: Dihedral angle between planes I and J (°), DC: Distance between ring centroids (Å), α: Angle Cg(I) —> Cg(J) vector and normal to plane I (°), DZ: Perpendicular distance of Cg(I) on ring J (Å), DXY: Slippage. [b] Complex **4**: Thy2 (N21, C22, N23, C24, C25, C26); complex **5**: Thy1 (N11, C12, N13, C14, C15, C16); Thy2 (N21, C22, N23, C24, C25, C26); complex **6**: Thy1 (N41, C42, N43, C44, C45, C46); complex **7**: Ura1 (N21, C22, N23, C24, C25, C26).

Table A. 8. Crystallographic data of complexes **9** and **10**.

Complexes	**9**	**10**
Empirical formula	$C_{14}H_{30}CuN_4O_{16}$	$C_{14}H_{18}CuN_4O_{10}$
MW (g mol^{-1})	573.96	465.86
Crystal system	Monoclinic	Monoclinic
Space group	P21/c	P21/c
a (Å)	8.3932(2)	12.9460(9)
b (Å)	12.4324(4)	4.5896(3)
c (Å)	11.1965(3)	14.6110(12)
α (º)	90	90
β (°)	93.938(1)	100.140(8)
γ (º)	90	90
V (Å^3)	1165.57(6)	854.58(11)
Z	2	2
T (K)	296(2)	296(2)
λ (Å)	1.54180	1.54180
ρ_{calcd} (g cm^{-3})	1.635	1.810
μ (mm^{-1})	2.111	2.451
Reflections collected	5227	4236
Unique data/restraints/parameter	1877/0/161	1700/0/135
R_{int}	0.0191	0.0422
Goodness of fit (S)[a]	1.091	1.062
R_1[b]/wR_2[c] [I>2□(I)]	0.0313/0.0869	0.0547/0.1640
R_1[b]/wR_2[c] [all data]	0.0323/0.0879	0.0604/0.1720

Table A. 9. Selected bond lengths (Å) and angles (º) for complexes **9** and **10**.

Complex **9**			
Cu1–O1	1.945(2)	Cu1–O1w	1.950(2)
Cu1–O2^{ii}	2.624(2)	Cu1···Cu1^{ii}	4.5896(3)
Complex 10			
Cu1–O1	1.963(3)	Cu2-O1	1.965(2)
Cu1–O11	1.991(2)	Cu2–O12	1.930(2)
Cu1–O21	2.348(2)	Cu2–O21	2.395(3)
Cu1···Cu2	3.003(2)	Cu2–O11^{i}	2.680(3)
Cu1···Cu2^{ii}	3.302(2)	Cu2···Cu2^{ii}	2.9734(14)

Table A. 10. Hydrogen bond distances [Å] and bond angles [°] for complexes **9** and **10**.

Complex **9**				
D─H···A	D─H	H···A	D···A	∠D─H···A
N3─H···O4^{i}	0.86	1.99	2.835(3)	168.4
O1w─H···O2`^{ii}	0.87	1.87	2.682(3)	153.9
O1w─H···O2	0.87	1.84	2.621(3)	148.5
Complex **10**				
D─H···A	D─H	H···A	D···A	∠D─H···A
N13─H···O22^{i}	0.86	1.96	2.793(4)	162.0
N23─H···O27^{ii}	0.86	2.01	2.843(4)	164.3
O1─H···O3w^{iii}	0.78	1.96	2.695(4)	158.0
O1w─H···O17^{i}	0.85	1.85	2.703(4)	177.9
O1w─H···O22^{iv}	0.85	1.81	2.616(4)	157.8
O2w─H···O28	0.85	1.96	2.805(4)	169.9
O2w─H···O21^{v}	0.86	2.19	3.005(4)	158.1
O3w─H···O28^{ii}	0.85	2.15	2.904(4)	147.1
O3w─H···O2w^{v}	0.85	1.98	2.668(5)	137.6

Symmetry codes for complex **9**: (i) –x+1, –y, –z+1, (ii) –x+1, –y, –z+2, (iii) –x, –y, –z+1, (iv). Complex **10**: (i) –x-1, –y-1, –z+1, (ii) –x+y, –x, z+2. (iv) x-1, y, z, (v) –x, –y, –z+2.

Table A. 11. Crystallographic data of complexes **11**and **12**.

Complexes	**11**	**12**
formula	$C_{24}H_{28}CuN_6O_{11}$	$C_{12}H_{11}CuN_3O_4$
MW (g mol^{-1})	640.06 g/mol	324.78
crystal system	monoclinic	triclinic
space group	P 1 21/n 1 (14)	P -1
a (Å)	6.5300(1)	4.93330(10)
b (Å)	22.2196(5)	9.7064(2)
c (Å)	18.7306(4)	13.1365(3) Å
α (º)	9	73.8950(10)
β (º)	96.996(1)	82.7070(10)
γ (º)	90	89.0080(10)
V ($Å^3$)	2697.46(9)	599.35(2)
Z	4	2
T (K)	296(2)	296(2)
ρ_{calcd} (g cm^{-3})	1.57597	1.800
μ (mm^{-1})		0.0888
reflections collected		19698
unique data/parameters		
R_{int}		0.0330
Goodness of fit (S)[b]		1.000
R_1[c]/wR_2[d] [I>2σ(I)]		0.0247/0.0843
R_1[c]/wR_2[d] [all data]		0.0301/0.0979

Table A. 12. Selected bond lengths (Å) and angles (º) for complex **11**.

Complex **11**					
Cu1-N4	2.005(6)	N4-Cu1-N4i	171.13(17)	N4i-Cu1-O1i	88.02(18)
Cu1-N4i	2.008(6)	N4-Cu1-O1	91.01(18)	N4i -Cu1-O1w	94.7(2)
Cu1-O1	1.970(3)	N4-Cu1-O1i	88.87(19)	O1-Cu1- O1i	172.40(14)
Cu1-O1i	2.020(4)	N4-Cu1-O1w	94.1(2)	O191-Cu1-O1w	88.14(15)
Cu1-O1w	2.307(5)	N4i-Cu1-O191	90.98(18)	O1i-Cu1-O1w	99.45(15)

Table A. 13. Crystallographic data of complexes **13**–**16**.

Complexes	**13**	**14**	**15**	**16**
formula	$C_{14}H_{22}CoN_4O_{12}$	$C_{12}H_{18}CoN_4O_{12}$	$C_{24}H_{40}CoN_{16}O_{15}$	$C_{22}H_{34}CoN_{16}O_{14}$
MW (g mol^{-1})	497.29	469.23	851.65	805.58
crystal system	monoclinic	monoclinic	triclinic	triclinic
space group	$P2_1/c$	$P2_1/c$	$P\bar{1}$	$P\bar{1}$
a (Å)	4.8757(2)	12.3732(5)	7.4544(2)	7.6802(2)
b (Å)	10.4569(5)	5.0780(2)	8.4452(2)	8.0454(2)
c (Å)	18.8851(8)	14.1462(6)	14.2169(5)	13.6231(3)
α (º)	90	90	79.096(2)	73.127(1)
β (º)	92.780(3)	99.031(3)	80.811(2)	88.691(1)
γ (º)	90	90	89.143(2)	89.355(1)
V (Å^3)	961.72(7)	877.80(6)	867.46(4)	805.32(3)
Z	2	2	1	1
T (K)	296(2)	296(2)	100(2)	296(2)
λ (Å)	1.54056	1.54056	1.54184	0.71073
ρ_{calcd} (g cm^{-3})	1.717	1.775	1.630	1.661
μ (mm^{-1})	7.697	8.392	4.716	0.627
Data/parameters	3529/144	1332/133	2681/254	2956/241
Rint	0.0572	0.0261	0.0183	0.0233
Goodness of fit (S)[a]	1.438	1.089	1.117	1.141
R_1[b]/wR_2[c] [I>2σ(I)]	0.0997/0.2898	0.0349/0.0992	0.0427/0.1237	0.0249/0.0742
R_1[b]/wR_2[c] [all data]	0.1837/0.3633	0.0383/0.1017	0.0457/0.0427	0.0274/0.0849

Table A. 14. Hydrogen bonding interactions (Å, º) found in complexes **13-16**.

Complex 13			
D─H···A	H···A	D···A	D–H···A
O1w–H···O4^{i}	1.80	2.638(5)	167.5
O1w–H···O92	1.75	2.598(6)	157.4
O2w–H···O91^{ii}	1.96	2.752(5)	153.9
O2w–H···O1w^{iii}	1.96	2.731(5)	146.3
N3–H···O2w^{iv}	2.08	2.930(6)	170.1
Complex 14			
D─H···A	H···A	D···A	D–H···A
O1w–H···O2^{i}	2.05	2.871(3)	162.3
O1w–H···O92	1.89	2.715(2)	153.1
O2w–H···O91^{ii}	1.80	2.650(2)	176.4
O2w–H···O2^{iii}	1.91	2.753(3)	169.1
N3–H···O4^{iv}	1.94	2.805(3)	178.9
Complex 15			
D─H···A	H···A	D···A	D–H···A
O1w–H···N3^{i}	1.97	2.816(3)	172.8
O1w–H···O191^{i}	1.90	2.743(3)	159.8
O2w–H···O192	1.87	2.718(3)	172.8
O2w–H···O192^{ii}	1.89	2.739(3)	174.5
N2–H···O12^{iii}	2.35	3.052(4)	139.1
N2–H···O4w^{iv}	2.60	3.164(12)	124.5
N6–H···N1^{v}	2.13	2.989(4)	172.3
N6–H···O3w^{vi}	1.98	2.839(6)	176.9
N6–H···O5w^{vii}	2.09	2.907(12)	157.7
N7–H···O191^{vi}	2.13	2.790(3)	133.2
N7–H···O3w^{vi}	2.44	3.183(6)	144.9
N13–H···O14^{viii}	2.01	2.866(3)	170.9

Complex 16			
D–H···A	H···A	D···A	D–H···A
O1w–H···O192^{i}	1.91	2.7689(19)	173.8
O1w–H···N3^{ii}	2.14	2.9605(19)	153.8
O2w–H···O191^{iii}	1.89	2.6495(18)	167.6
O2w–H···O191^{iv}	1.82	2.6545(19)	173.5
O3w–H···O12	2.26	2.931(2)	145.7
O3w–H···N3^{v}	2.48	3.107(2)	144.9
N2–H···O12^{vi}	2.64	3.245(2)	128.1
N2–H···O12^{vii}	2.22	3.075(2)	176.8
N6–H···O14^{vii}	1.96	2.816(2)	176.9
N6–H···O3w^{viii}	2.12	2.961(2)	167.3
N7–H···O3w^{ix}	2.20	2.982(2)	150.6
N13–H···N1^{viii}	2.13	2.990(2)	177.7

Symmetry for compound **13**: (i) x, -y+1/2, z+1/2; (ii) -x, -y, -z+1; (iii) x-1, y, z; (iv) x, -y+1/2, z-1/2; for compound **14**: (i) x, -y+5/2, z-1/2; (ii) x, y+1, z; (iii) -x+1, y+1/2, -z+3/2; (iv) -x+2, -y+2, -z+2; for compound **15**: (i) -x+1, -y+1, -z+1; (ii) -x, -y+1, -z+1; (iii) x+1, y, z; (iv) -x+1, -y+1, -z+2; (v) -x+1, -y, -z+2; (vi) x, y-1, z; (vii) -x, -y, -z+2; (viii) -x, -y+2, -z+2; for compound **16**: (i) -x+1, -y+1, -z+1; (ii) -x+2, -y+2, -z+1; (iii) -x+2, -y+1, -z+1; (iv) x+1, y+1, z; (v) x-1, y-1, z; (vi) x, y+1, z; (vii) -x+1, -y+1, -z+2; (viii) -x+1, -y+1, -z+2; (ix) x+1, y, z.

Table A. 15. Crystallographic data of complexes **17**.

Complex	**17**
formula	$C_{34}H_{34}CoN_8O_{10}$
MW (g mol^{-1})	773,61
crystal system	monoclinic
space group	P 1 21/n 1 (14)
T (K)	296(2) K
a (Å)	12.4464(2)
b (Å)	7.9407(2)
c (Å)	18.0313(4)
α (º)	90
β (º)	102.426(1)
γ (º)	90
V (Å^3)	1740.34(6)
Z	4
μ (mm^{-1})	3.185
Reflections collected	31005
Unique data/parameters	3188 / 2 / 250
Rint	0.0337
Goodness of fit (S)[a]	1.004
R_1[b]/wR_2[c] [I>2σ(I)]	0.0266/0.0903
R_1[b]/wR_2[c] [all data]	0.0360/0.1119

Table A. 16. Crystallographic data of complexes **18** and **19**.

Complexes	**18**	**19**
Empirical formula	$C_5H_5ClCuN_3O_2$	$C_5H_5BrCuN_3O_2$
MW (g mol^{-1})	238.11	282.57
λ (Å)	0.71073	0.71073
T (K)	100(2)	100(2)
Crystal system	monoclinic	monoclinic
Space group	$P2_1/c$	$P2_1/c$
a (Å)	3.7060(2)	3.7808(1)
b (Å)	15.378(1)	7.2375(2)
c (Å)	13.3228(8)	28.815(1)
α (º)	90	90
β (°)	92.006(5)	92.565(3)
γ (º)	90	90
V ($Å^3$)	758.81(8)	787.69(4)
Z	4	4
ρcalcd (g cm^{-3})	2.084	2.383
μ (mm^{-1})	3.185	7.802
Reflections collected	5237	4998
Unique data/parameters	2934/110	1704/109
Rint	0.0376	0.0260
Goodness of fit (S)[a]	0.985	1.374
R_1[b]/wR_2[c] [I>2σ(I)]	0.0399/0.0885	0.0406/0.0789
R_1[b]/wR_2[c] [all data]	0.0590/0.0927	0.0441/0.0802

Table A. 17. Crystallographic data of complexes of **20^{LT}**, **20 ^{RT}**, **20a** and **20b**.

Complex	**20^{LT}**	**20^{RT}**	**20a**	**20b**
Empirical formula	$C_5H_5CuIN_3O_2$	$C_5H_5CuIN_3O_2$	$C_5H_5CuIN_3O_2$	$C_7H_9CuIN_3O_4$
MW (g mol^{-1})	329.56	329.56	329.56	389.61
λ (Å)	0.71073	0.71073	0.71073	0.71073
T (K)	200(2)	298(2)	296(2)	296(2)
Crystal system	monoclinic	monoclinic	monoclinic	triclinic
Space group	Pn	$P2_1/n$	$P2_1/c$	P-1
a (Å)	4.1982(1)	4.2284(1)	4.0708(1)	4.1444(1)
b (Å)	14.3433(3)	14.3638(7)	7.5386 (2)	11.3403(2)
c (Å)	13.6017(3)	13.6840(5)	28.2779(7)	15.0851(3)
α (º)	90	90	90	108.660(1)
β (°)	94.707(2)	95.241(3)	90.880(1)	93.975(1)
γ (º)	90	90	90	98.533(1)
V (Å^3)	816.28(3)	827.64(5)	867.69(4)	659.10(2)
Z	4	4	4	2
ρ_{calcd} (g cm^{-3})	2.682	2.645	2.523	1.963
μ (mm^{-1})	6.417	6.329	6.036	4.001
Reflections collected	16183	3768	12161	11658
Unique data/parameters	2861/233	1418/129	1560/109	2344/146
Rint	0.0579	0.0294	0.0242	0.0298
Goodness of fit (S)[a]	0.956	1.244	1.121	1.117
R_1[b]/wR_2[c] [I>2σ(I)]	0.221/0.0472	0.0482/0.0943	0.0201/0.0365	0.0212/0.0587
R_1[b]/wR_2[c] [all data]	0.0234/0.0479	0.0593/0.1005	0.0268/0.0395	0.0243/0.0615

Table A. 18. Crystallographic data of complexes **21** and **22**.

Complexes	**21**	**22**
Empirical formula	$C_{12}H_{10}Cu_2N_8O_4$	$C_6H_5CuN_4O_2S$
MW (g mol^{-1})	457.36	260.74
λ (Å)	0.71073	0.71073
T (K)	296(2)	296(2)
Crystal system	monoclinic	monoclinic
Space group	P2/n	$P2_1/n$
a (Å)	14.6169(3)	5.8985(1)
b (Å)	7.2367(2)	14.2513(3)
c (Å)	16.1212(3)	10.8843(2)
α (º)	90	90
β (°)	110.554(1)	105.129(1)
γ (º)	90	90
V (Å^3)	1596.72(6)	883.24(3)
Z	4	4
ρcalcd (g cm^{-3})	1.903	1.961
μ (mm^{-1})	2.703	2.684
Reflections collected	20974	16366
Unique data/parameters	2932/253	1614/127
Rint	0.0377	0.0265
Goodness of fit (S)[a]	1.003	1.000
R_1[b]/wR_2[c] [I>2σ(I)]	0.0279/0.0880	0.0221/0.0620
R_1[b]/wR_2[c] [all data]	0.0433/0.1133	0.0244/0.0637

Table A. 19. Crystallographic data of complexes **23** and **24**.

Complexes	**23**	**24**
Empirical formula	$C_8H_9CuINO_2$	$C_6H_5CuINO_2$
MW (g mol^{-1})	341.60	313.55
λ (Å)	0.71073	0.71073
T (K)	296(2)	296(2)
Crystal system	monoclinic	monoclinic
Space group	$P2_1/n$	$P2_1/c$
a (Å)	4.1577(1)	14.6503(7)
b (Å)	27.9294(6)	4.1198(2)
c (Å)	9.0620(2)	14.3078(7)
β (º)	100.708(1)	104.892(2)
V (Å^3)	1033.97(4)	834.56(7)
Z	4	4
ρ_{calcd} (g cm^{-3})	2.194	2.496
μ (mm^{-1})	5.065	6.263
Reflections collected	11168	11064
Unique data/parameters	1864/119	1526/101
R_{int}	0.0206	0.0514
Goodness of fit (S)[a]	1.000	1176
R1[b]/wR2[c] [I>2σ(I)]	0.0212/0.0867	0.0286/0.0668
R1[b]/wR2[c] [all data]	0.0268/0.0987	0.0515/0.0998

Appendix B; X-ray powder diffraction figures

Appendix **B** shows the X-ray powder diffraction figures for complexes **1-24**.

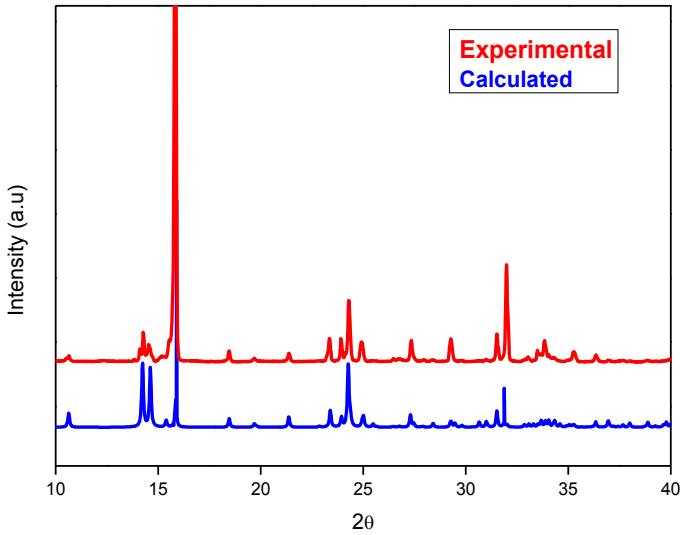

Figure B. 1. Experimental and calculated powder diffractogram of complex **1**.

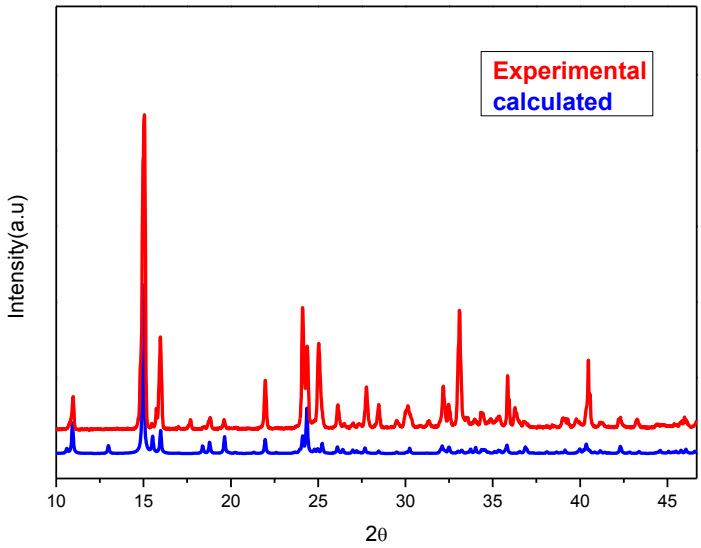

Figure B. 2. Experimental and calculated powder diffractogram of complex **2**.

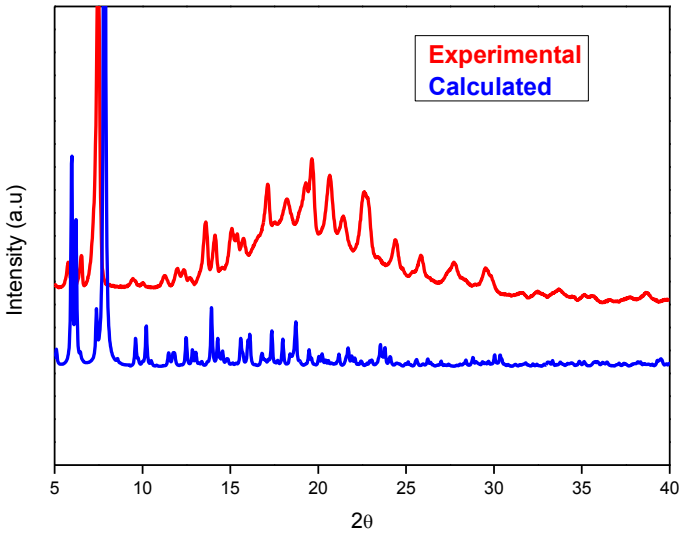

Figure B. 3. Experimental and calculated powder diffractogram of complex **4**.

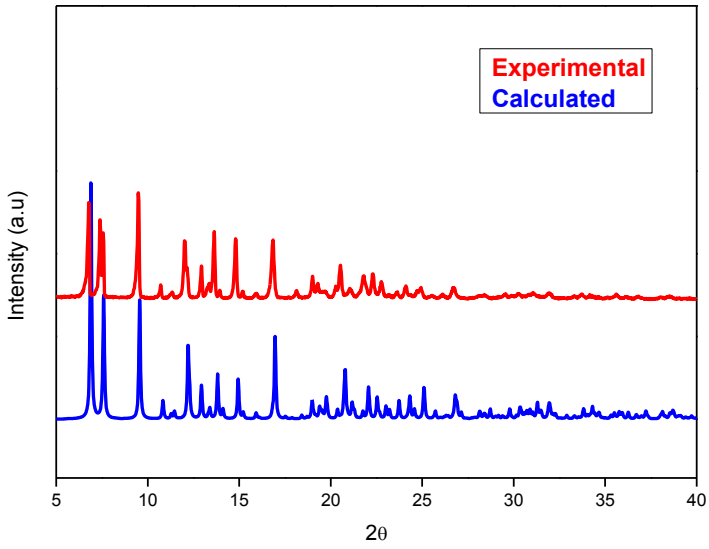

Figure B. 4. Experimental and calculated powder diffractogram of complex **5**.

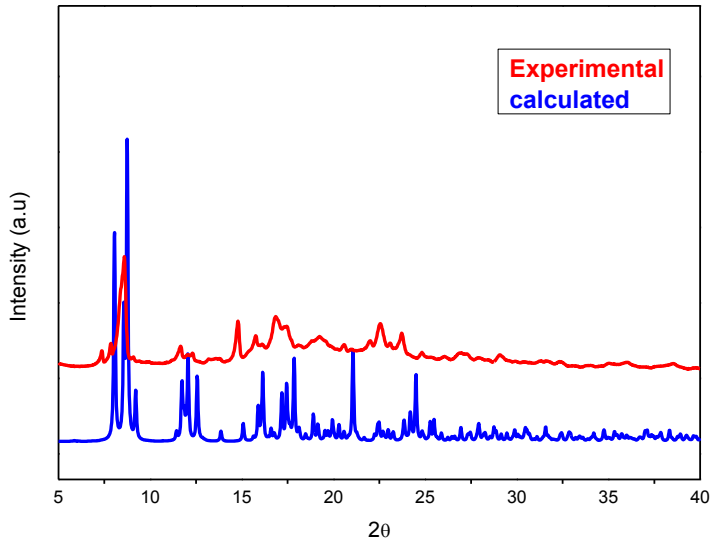

Figure B. 5. Experimental and calculated powder diffractogram of complex **6**.

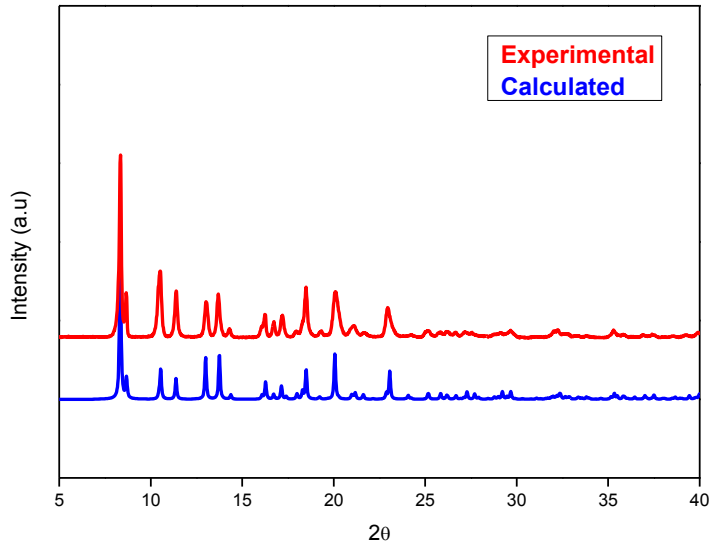

Figure B. 6. Experimental and calculated powder diffractogram of complex **7**.

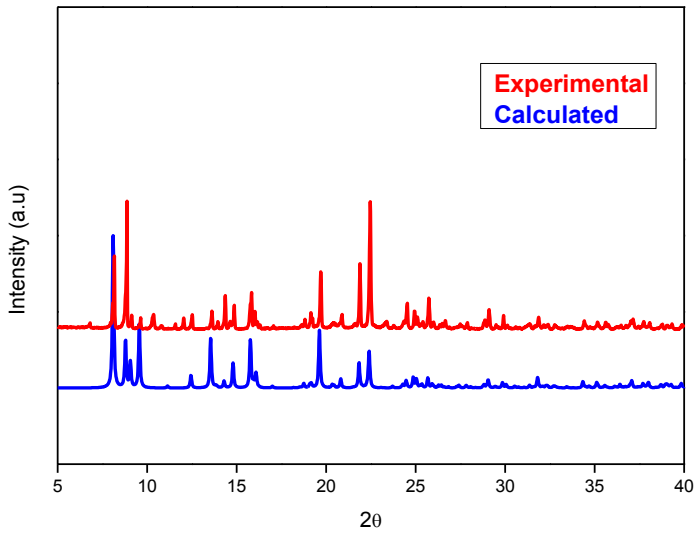

Figure B. 7. Experimental and calculated powder diffractogram of complex **8**.

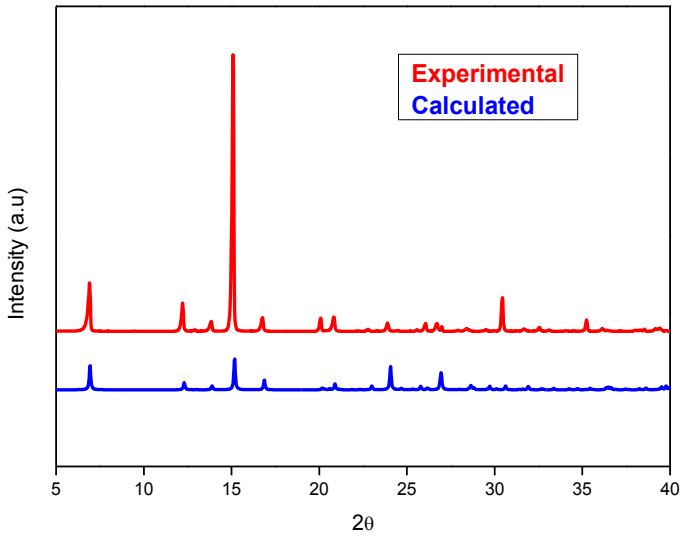

Figure B. 8. Experimental and calculated powder diffractogram of complex **9**.

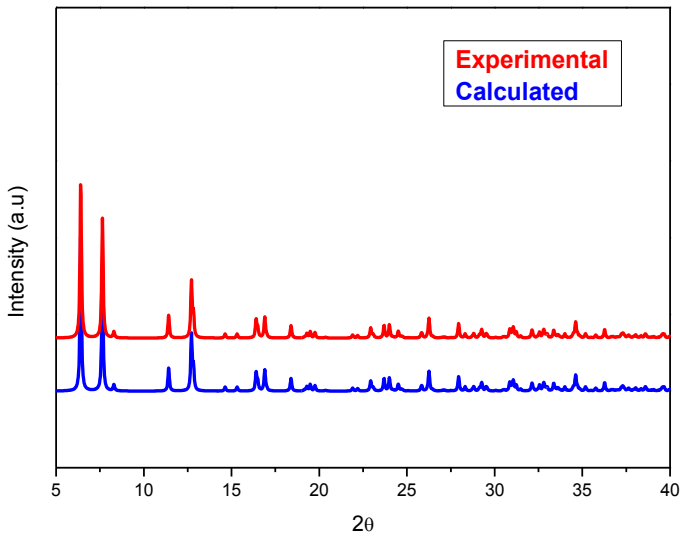

Figure B. 9. Experimental and calculated powder diffractogram of complex **10**.

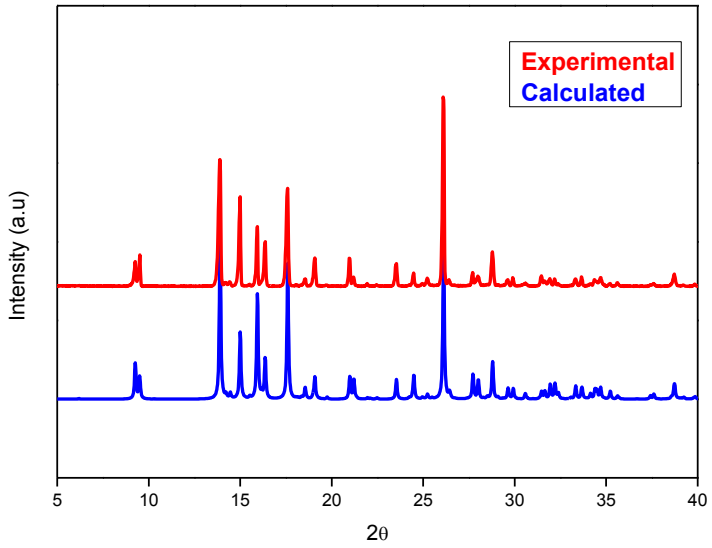

Figure B. 10. Experimental and calculated powder diffractogram of complex **11**.

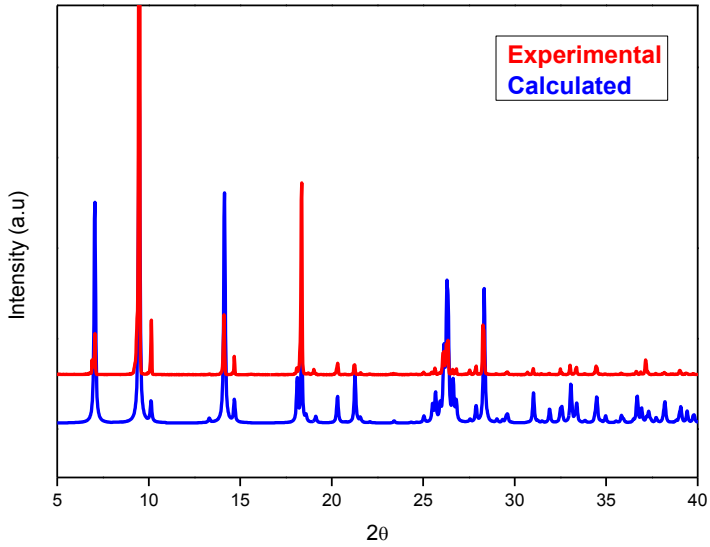

Figure B. 11. Experimental and calculated powder diffractogram of complex **12**.

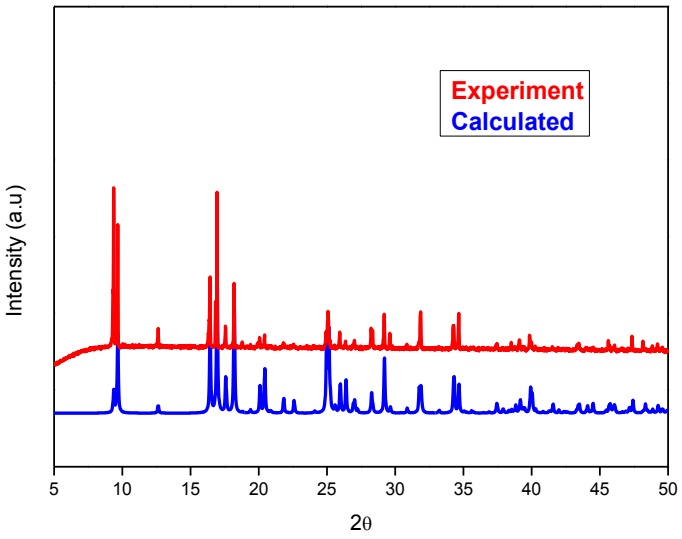

Figure B. 12. Experimental and calculated powder diffractogram of complex **13**.

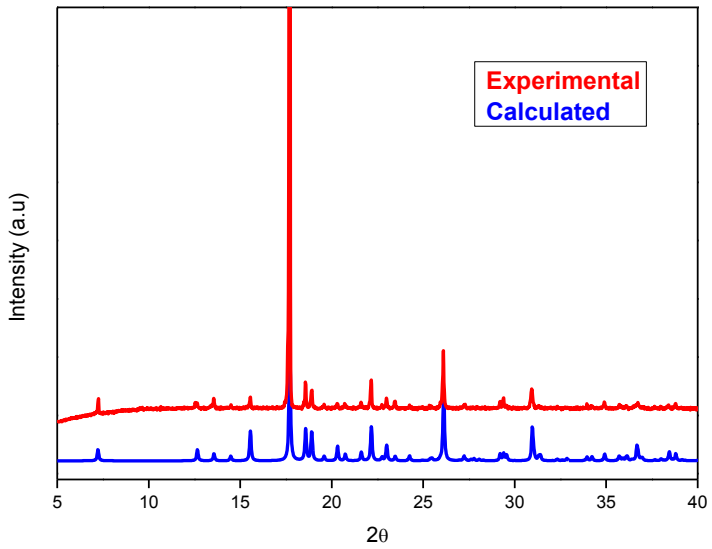

Figure B. 13. Experimental and calculated powder diffractogram of complex **14**.

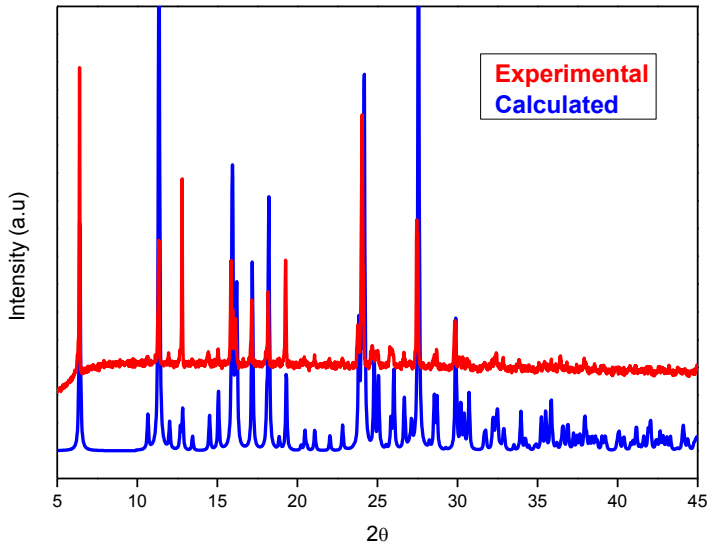

Figure B. 14. Experimental and calculated powder diffractogram of complex **15**.

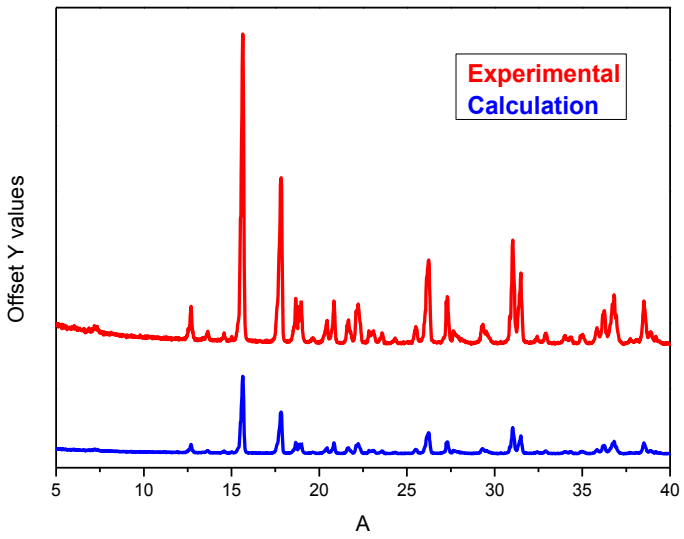

Figure B. 15. Experimental and calculated powder diffractogram of complex **16**.

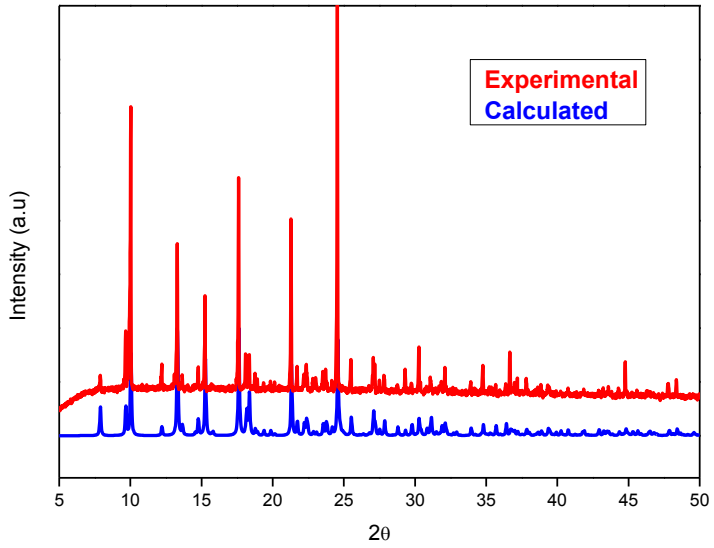

Figure B. 16. Experimental and calculated powder diffractogram of complex **17**.

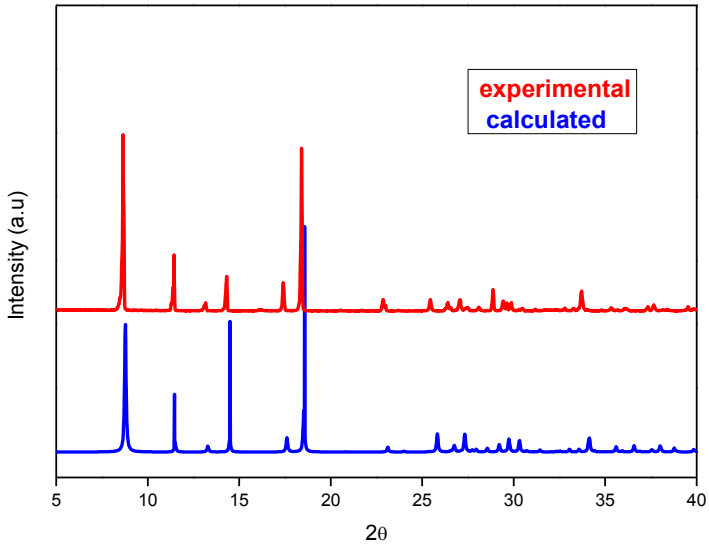

Figure B. 17. Experimental and calculated powder diffractogram of complex **18**.

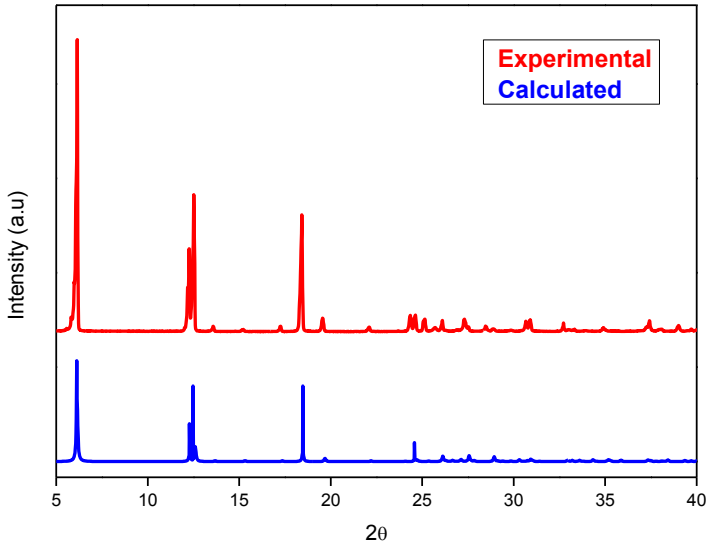

Figure B. 18. Experimental and calculated powder diffractogram of complex **19**.

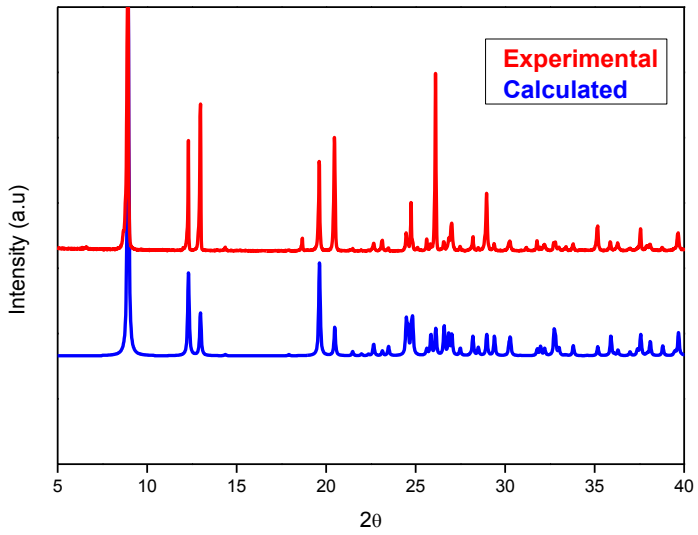

Figure B. 19. Experimental and calculated powder diffractogram of complex **20**^{RT}.

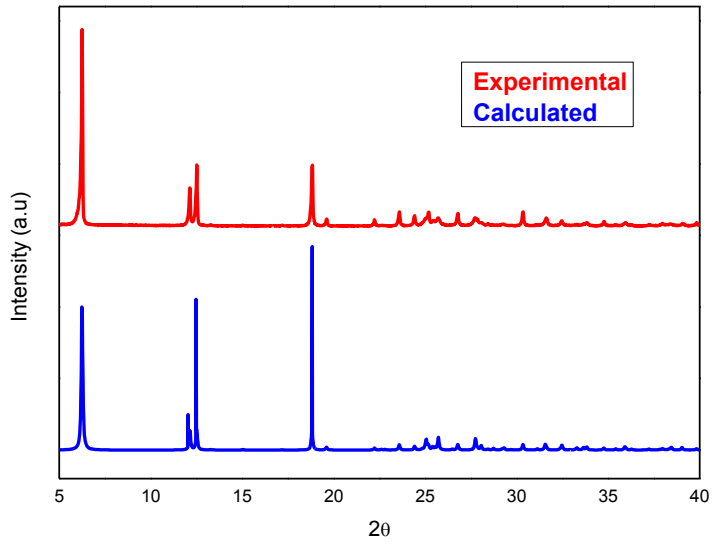

Figure B. 20. Experimental and calculated powder diffractogram of complex **20a**.

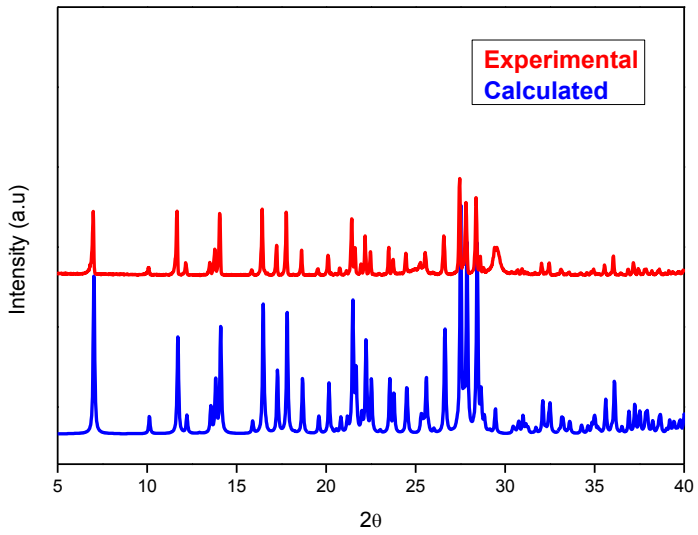

Figure B. 21. Experimental and calculated powder diffractogram of complex **21**.

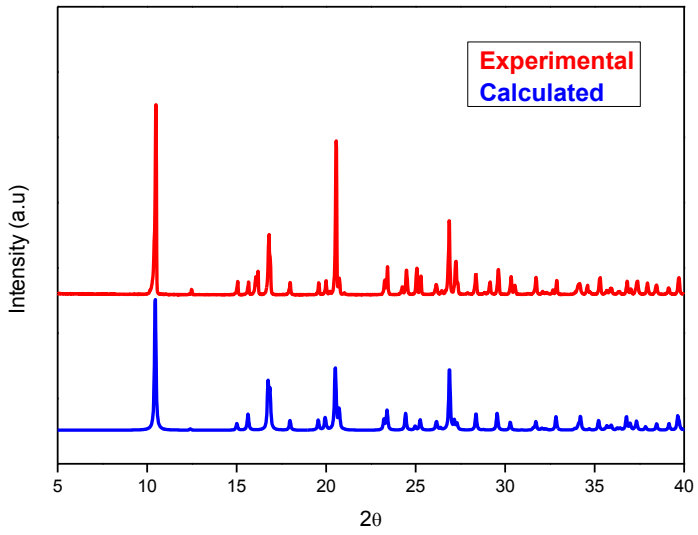

Figure B. 22. Experimental and calculated powder diffractogram of complex **22**.

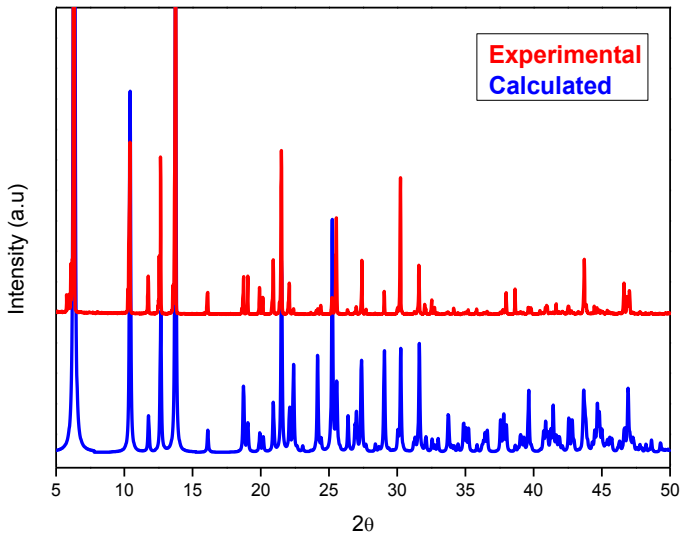

Figure B. 23. Experimental and calculated powder diffractogram of complex **23**.

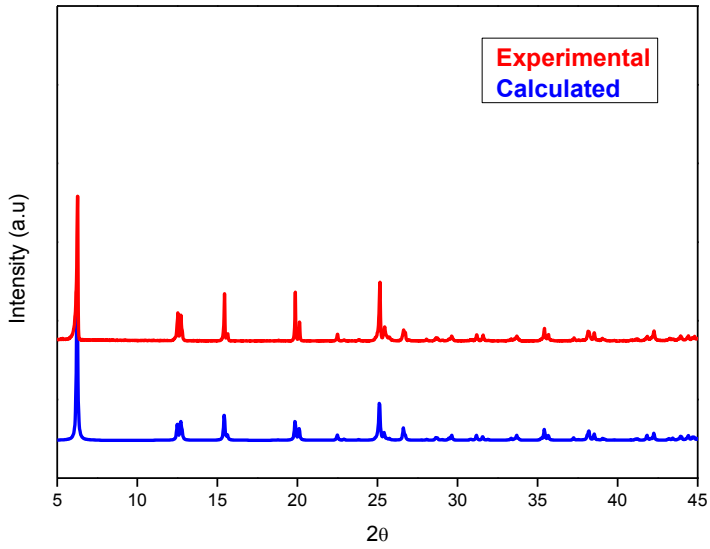

Figure B. 24. Experimental and calculated powder diffractogram of complex **24**.